

University of Warwick institutional repository: <http://go.warwick.ac.uk/wrap>

**A Thesis Submitted for the Degree of PhD at the University of Warwick**

<http://go.warwick.ac.uk/wrap/3542>

This thesis is made available online and is protected by original copyright.

Please scroll down to view the document itself.

Please refer to the repository record for this item for information to help you to cite it. Our policy information is available from the repository home page.



Optical Instrumentation for Fluid Flow  
in  
Gas Turbines

By

Mark Burnett

Submitted for the Degree of Doctor of Philosophy in Engineering at the  
University of Warwick

School of Engineering  
University of Warwick

September 2000



## SUMMARY

Both a novel shearing interferometer and the first demonstration of particle image velocimetry (PIV) to the stator-rotor gap of a spinning turbine cascade are presented. Each of these techniques are suitable for measuring gas turbine representative flows.

The simple interferometric technique has been demonstrated on a compressor representative flow in a 2-D wind tunnel. The interferometer has obvious limitations, as it requires a clear line of sight for the integration of refractive index along an optical path. Despite this, it is a credible alternative to schlieren or shadowgraph in that it provides both qualitative visualisation and a quantitative measurement of refractive index and the variables to which it is dependent without the vibration isolation requirements of beam splitting interferometry.

The 2-D PIV measurements have been made in the stator-rotor gap of the MT1 high-pressure turbine stage within DERA's Isentropic Light Piston Facility (ILPF). The measurements were made at full engine representative conditions adjacent to a rotor spinning at 8200 rpm. This is a particularly challenging application due to the complex geometry and random and periodic effects generated as the stator wake interacts with the adjacent spinning rotor. The application is further complicated due to the transient nature of the facility. The measurements represent a 2-D, instantaneous, quantitative description of the unsteady flow field and reveal evidence of shocks and wakes. The estimated accuracy after scaling, timing, particle centroid and particle lag errors have been considered is  $\pm 5\%$ . Non-smoothed, non-time averaged measurements are qualitatively compared with a numerical prediction generated using a 2-D unsteady flow solver (prediction supplied by DERA). A very close agreement has been achieved.

A novel approach to characterising the third component of velocity from the diffraction rings of a defocusing particle viewed through a single camera has been explored. This 3-D PIV technique has been demonstrated on a nozzle flow but issues concerning the aberrations of the curved test section window of the turbine cascade could not be resolved in time for testing on the facility. Suggestions have been made towards solving this problem.

Recommendations are also made towards the eventual goal of revealing a temporally and spatially resolved 3-D velocity distribution of the stator wake impinging on the passing rotor.

# Contents

Summary	i
Contents	ii
List of Figures	viii
List of Tables	xvii
Nomenclature	xviii
Acknowledgements	xxiii
Declaration	xxiv
<b>Part 1: Introduction &amp; Literature Review</b>	
<b>1.0 Introduction</b>	<b>1</b>
1.1 Introducing the Problem	1
1.2 Aims & Objectives	2
1.3 Description of Thesis	2
1.4 Novel Contribution	5
1.4.1 Velocity Measurements in the Stator-Rotor Gap of a Turbine Cascade	5
1.4.2 Determination of the Out-of-Plane Component of Velocity from Defocusing	6
1.4.3 Development and Application of a Simple Shearing Interferometer to Phase Objects	6
<b>2.0 Review of Optical Methods for Fluid Flow &amp; Combustion in Gas Turbines</b>	<b>7</b>
2.1 Introduction to the Review	8
2.2 Velocity & Visualisation	9
2.2.1 Laser Doppler Anemometry (LDA)	9
2.2.2 Doppler Global Velocimetry (DGV)	15
2.2.3 Hot Wire Anemometry (HWA)	19
2.2.4 Laser Two Focus (L2F)	20
2.2.5 Shadowgraphy	23
2.2.6 Schlieren	23
2.2.7 Interferometry	25

2.3 Temperature	27
2.3.1 Coherent Anti-Stokes Raman Spectroscopy (CARS)	27
2.3.2 Degenerate Four-Wave Mixing (DFWM)	28
2.3.3 Optical Pyrometers	29
2.3.4 Thermographic Phosphors	31
2.3.5 Temperature Sensitive Paint (TSP)	32
2.3.6 Thermal Paints (Irreversible)	33
2.4 Speciation	34
2.4.1 Fourier Transform Infrared Spectroscopy (FTIR)	35
2.4.2 Non-Disperse Infrared (NDIR) Analyser	36
2.4.3 Laser Induced Fluorescence (LIF)	37
2.4.4 Laser Induced Incandescents (LII) & Planar Laser Induced Incandescence (PLII)	39
2.5 Particle & Drop Sizing	41
2.5.1 Phase Doppler Anemometry (PDA)	41
2.5.2 Laser Sheet Drop Sizing (LSD)	44
2.5.3 Light Obscuration	47
2.5.4 Diffraction Methods	48
2.5.5 Time of Flight Particle Sizing	49
2.5.6 Intensity Methods	50
2.6 Summary of Optical Instrumentation for Fluid Flow in Gas Turbines	51
2.6.1 Compressors & Turbines	51
2.6.2 Combustion	53
Part 2: The Application of PIV to a Spinning Turbine Cascade	
<b>3.0 Introduction &amp; Background</b>	56
3.1 Introduction	57
3.1.1 Background	57
3.1.2 Novel Requirements of the Measurements	59
3.2 The isentropic Light Piston Facility (ILPF) & MT1 Turbine Stage	61

<b>4.0 Particle Image Velocimetry (PIV) – Review of Theory for Application</b>	<b>64</b>
4.1 Introduction	65
4.2 Operating Principle	68
4.3 Flow Tracing Seed & Scattered Intensity	71
4.3.1 Requirements of the Seed	71
4.3.2 Dynamics of Spherical Seed in a Moving Fluid	72
4.3.3 Light Scattering from Spherical Seed	75
4.4 Analysis Techniques	78
4.4.1 Correlation Techniques	78
4.4.2 Particle Pairing	79
4.4.3 Directional Ambiguity	80
4.4.4 Centroid Estimation	82
4.5 3-D PIV	87
4.5.1 Holographic PIV	87
4.5.2 Stereoscopic PIV	88
4.5.3 Defocusing Mask PIV	94
4.6 Summary of Chapter	96
<b>5.0 System Definition &amp; Testing</b>	<b>98</b>
5.1 Introduction	99
5.2 The PIV Systems	99
5.2.1 Interlaced Camera System	99
5.2.2 Cross Correlation Camera System	100
5.3 2-D Measurements of a Free Air Jet	101
5.3.1 Experimental Method	101
5.3.2 Results	103
5.3.3 Discussion of Results	104
5.3.4 Conclusions of the 2-D PIV Measurements of the Nozzle Flow	107
5.4 Third Component Characterisation	109
5.4.1 Stereo PIV	109
5.4.2 Three Component PIV by Defocusing	111
5.4.3 Defocusing Calibration	117
5.5 3-D Measurement of a Free Air Jet by Defocusing	120

5.5.1 Experimental Method	120
5.5.2 Results	122
5.5.3 Discussion of Results	123
5.5.4 3D-PIV by Defocusing Through a Contoured Test Section Window	124
5.6 Summary of Chapter	128
<b>6.0 Experimental Arrangement</b>	<b>130</b>
6.1 Optical Access	131
6.2 Light Sheet delivery	133
6.3 Image Acquisition	137
6.4 The PIV System	140
6.5 Seeding	141
6.6 Summary of Chapter	143
<b>7.0 Results</b>	<b>144</b>
<b>8.0 Discussion</b>	<b>153</b>
8.1 Vector Extraction	154
8.1.1 Particle Tracking	154
8.1.2 Auto-Correlation	154
8.1.3 Comparison of Results generated using Particle Tracking & Auto-Correlation	155
8.1.4 Post Processing	157
8.2 Description of Results	160
8.2.1 Trailing edge of NGV to leading edge of rotor	161
8.2.2 Stator passage	163
8.2.3 Suction surface of NGV to leading edge of rotor	165
8.2.4 Comparison with Numerical Prediction	167
8.2.5 Accuracy, Resolution & Sources of Errors	168
8.3 Recommendations for Further Work	172
8.3.1 Optimisation for a Cross-Correlation camera	172
8.3.2 Measurements Close to Mechanical Surfaces	173
8.3.3 Time averaged measurements	174

8.3.4 3-D PIV in the ILPF	175
8.4 Summary of Chapter	178
<b>Part 3 Development &amp; Application of a Novel Shearing Interferometer to Compressible Flows</b>	
9.0 Shearing Interferometer –Theory for Application	180
9.1 Introduction	181
9.2 Optical Path Difference	182
9.3 Interferometry	183
9.4 The Shearing Interferometer	183
9.5 The Fourier Transform Method of Fringe Analysis	190
9.6 Tomographic Reconstruction of Density Fields	198
9.6.1 Axial Tomography	198
9.6.2 Abel Inversion	201
9.6.3 Application of Abel Inversion to a Propane Flame	202
9.6.4 Algebraic Reconstruction Technique (ART)	206
9.6.5 Overview of other Reconstruction techniques	212
9.7 Summary of Chapter	215
10.0 Application to a 2-D Transonic Wind Tunnel	217
10.1 Introduction	218
10.2 2-D Wedge Rig	219
10.3 Experimental Arrangement	221
10.4 Results	223
10.5 Interpretation of Results	225
10.5.1 Analysis of the Fringe Patterns	225
10.5.2 Description of the Results, Mass Flow Rate 0.66 kg/s	227
10.5.3 Resolution in Density	228
10.5.4 First Order Approximation of Refraction	228
10.6 Discussion	229
10.7 Summary of Chapter	232

11.0 Application to a Shock-Tube Exhausting into Ambient Air	233
11.1 Introduction	234
11.1.1 Introducing the Problem	234
11.1.2 Aims & Objectives	235
11.1.3 Overview of Experiment	236
11.2 The MIT Shock Tube	238
11.3 Experimental Arrangement	243
11.4 Results – Shock Tube	245
11.5 Interpretation of Results	247
11.5.1 Description of Results	247
11.5.2 Comparison with Mie-Scattering and Schlieren Measurements	248
11.5.3 Tomographic Reconstruction	249
11.5.4 Optical Path difference at Nozzle Exit	249
11.5.5 Resolution in Density	250
11.5.6 First Order Approximation of Refraction	251
11.6 Discussion	252
11.7 Summary of Chapter	253
Conclusions	255
References	262
Appendix A	283
Appendix B	288

## List of Figures

Figure 2.1. Fringe model. The intensity of the scattered light produced as a particle passes through a series of interference fringes contained within a measurement volume defined by the intersection of two coherent beams.	12
Figure 2.2. Laser Doppler Anemometer – backscatter configuration.	13
Figure 2.3. Three component LDA system with beams launched from separate heads. Measurement volume defined by intersection of three beam pairs.	14
Figure 2.4. The direction of the measured component of velocity in relation to the direction of the light sheet and the observation point.	16
Figure 2.5. The Doppler Global Velocimeter	17
Figure 2.6. Shadowgraphy arrangement	23
Figure 2.7. The Schlieren arrangement	24
Figure 2.8. Orientation of launch head and detectors of a PDA system	43
Figure 2.9. Particle sizing by diffraction	48
Figure 2.10. Intensity method of particle sizing	50
Figure 3.1 The Isentropic Light Piston Facility (ILPF)	63
Figure 4.1 Particle centroid estimation	86
a. Using the pixels of greatest intensity	
b. Diagonals of a bounding box that are assumed to intersect at the particle's centroid. Grey level threshold needed to determine perimeter of particle image.	
c. Centre of mass approximation where the centroid is determined from the sum of the products of the pixel intensities and their distance from a datum. Again a grey level threshold is required.	
d. Gaussian fit to the image's pixel intensity profile.	



Figure 4.2. Stereoscopic PIV arrangement – Translation	89
Figure 4.3. Stereoscopic PIV Arrangement – Angular Displacement	90
Figure 4.4. Stereoscopic PIV arrangement – angular displacement method that satisfies the Scheimpflug condition.	92
Figure 4.5. Scheimpflug Configuration	93
Figure 4.6 The use of a defocusing mask to determine the out-of-plane position of a scatterer. Three defocused images produced using 5mm apertures at a 10 mm PCD. 12 mm displacement in the out-of-plane direction between exposures	95
Figure 5.1. The optical arrangement.	101
Figure 5.2. Field of view, 1400 mm from the nozzle.	101
Figure 5.3. PIV and LDA measurements of the nozzle flow. Centreline of the nozzle is at 7.5 mm on the x axis.	
a. PIV vectors processed using an auto-correlation (32 x 32, 50% overlap)	
b. PIV vectors solved using particle pairing	
c. LDA vectors (144 points)	
d. PIV vectors (3000 vectors from combined frames)	
e. Top: Scatter of the PIV ‘.’ And the LDA ‘o’ data	
Bottom: Mean velocity profile (PIV dotted, LDA continuous)	103
Figure 5.4. Disparity between particle pairs viewed through stereo cameras.	110
Figure 5.5 Diffraction rings at incremental depths	112
Figure 5.6. Schematics of dimensions for equations 5.1 to 5.10.	

a.	Geometrical image for an out-of-focus particle.	
b.	Geometry of an aberration free optical system	114
Figure 5.7. Experimental arrangement used in the 3-D calibration		117
Figure 5.8. Calibration curves for theoretical and measured estimations. (Figure taken from Udrea <sup>[125]</sup> )		118
Figure 5.9. Experimental measurements of the defocused point source. A. ½ ring, $\epsilon_0 \approx 40 \mu\text{m}$ b. 1 ring, $\epsilon_0 \approx 120 \mu\text{m}$ c. 1 ½ ring, $\epsilon_0 \approx 200 \mu\text{m}$ d. 2 rings, $\epsilon_0 \approx 300 \mu\text{m}$ e. 2 ½ rings, $\epsilon_0 \approx 400 \mu\text{m}$ f. 3 rings, $\epsilon_0 \approx 500 \mu\text{m}$ g. 3 ½ rings, $\epsilon_0 \approx 600 \mu\text{m}$ h. 4 rings, $\epsilon_0 \approx 700$		118
Figure 5.10. Defocused particles of the nozzle flow tilted at 30° to the plane of the light sheet. Triple exposure.		120
Figure 5.11 Displacements vector plots of the nozzle flow tilted from the y axis		122
Figure 5.12 a. Diffraction image recorded through test-section window of turbine cascade (inverted).		
b. Single diffraction image recorded through window after partial correction with cylindrical lenses (inverted).		
c. Diffraction image taken from calibration for comparison (inverted).		127
Figure 6.1 The test section window		
a.	Photograph of window, periscope and light sheet incident on the rotor.	
b.	The periscopes and windows fitted to the cavities within the nozzle guide vanes.	
c.	Window removed from facility. Note ngvs form part of the window assembly. Rule included for scale.	132
Figure 6.2 Schematic of the periscopes inserted into hollowed out nozzle guide vanes. Used to form and project a light sheet into the test section.		134

Figure 6.3. Fibre delivery system with circular bundle at input and fibres stacked in a line at the output to project a light sheet. 135

Figure 6.4 The rigid optical system used to relay the beam from the laser to the test section. Designed to accommodate axial movement of the ILPF during the run time. 136

Figure 6.5 Schematic of the PIV system 140

Figure 7.1. Example of the data set recorded between the ngvs. Colour bar is in  $\text{ms}^{-1}$ , Coordinates are in mm. Processed using autocorrelation (64 x 64 pixels).

- a. Region of interest between the ngvs
- b. Velocity surface generated using a delaunay triangulation overlaying the raw piv image
- c. Velocity vectors overlaying the raw piv image. Colour and magnitude represent the magnitude of the velocity 145

Figure 7.2. Example of the data set recorded between the ngvs. Colour bar is in  $\text{ms}^{-1}$ , Coordinates are in mm. Processed using autocorrelation (64 x 64 pixels).

- a. Region of interest between the ngvs
- b. Velocity surface generated using a delaunay triangulation overlaying the raw piv image
- c. Velocity vectors overlaying the raw piv image. Colour and magnitude represent the magnitude of the velocity 146

Figure 7.3. Example of the data set recorded between the ngvs. Colour bar is in  $\text{ms}^{-1}$ , Coordinates are in mm. Processed using autocorrelation (64 x 64 pixels).

- a. Region of interest between the ngvs
- b. Velocity surface generated using a delaunay triangulation overlaying the raw piv image
- c. Velocity vectors overlaying the raw piv image. Colour and magnitude represent the magnitude of the velocity 147

Figure 7.4. Example of the data set recorded between the ngvs. Colour bar is in  $\text{ms}^{-1}$ , Coordinates are in mm. Processed using autocorrelation (64 x 64 pixels).

a. Region of interest between the ngvs

b. Velocity surface generated using a delaunay triangulation overlaying the raw piv image

c. Velocity vectors overlaying the raw piv image. Colour and magnitude represent the magnitude of the velocity

148

Figure 7.5. Example of the data set recorded between the ngvs. Colour bar is in  $\text{ms}^{-1}$ , Coordinates are in mm. Processed using autocorrelation (64 x 64 pixels).

a. Region of interest between the ngvs

b. Velocity surface generated using a delaunay triangulation overlaying the raw piv image

c. Velocity vectors overlaying the raw piv image. Colour and magnitude represent the magnitude of the velocity

149

Figure 7.6. Example of the data set recorded between the ngvs. Colour bar is in  $\text{ms}^{-1}$ , Coordinates are in mm. Processed using autocorrelation (64 x 64 pixels).

a. Region of interest between the ngvs

b. Velocity surface generated using a delaunay triangulation overlaying the raw piv image

c. Velocity vectors overlaying the raw piv image. Colour and magnitude represent the magnitude of the velocity

150

Figure 7.7. Example from the brief data set recorded from the higher of the two optical periscopes. Solutions from a single image shown in the background. Colour bar in  $\text{ms}^{-1}$

a. The region of interest and the approximate rotor phase

b. Velocity surface generated using a delaunay triangulation overlaid the raw piv image

c. Velocity vectors overlaid the raw piv image. Colour and magnitude represent the magnitude of the velocity

151

Figure 7.8 Measurement and prediction. Colour bar shows both Mach number and velocity in  $\text{ms}^{-1}$ .

a. Measured, two combined frames that slightly overlap. Individual images shown in figures 7.2 and 7.6.

b. Predicted, unsteady and 2-D.(Unslow). Taken from Giles <sup>[128]</sup>. 152

Figure 8.1 Scatter of the PIV data processed by particle tracking and auto-correlation

a. 'x' component of displacement in pixels versus 'x' co-ordinate

b. 'y' component of displacement in pixels versus 'y' co-ordinate 156

Figure 8.2 The affect of the smoothing over a velocity plot. Red line is the interpolation between red dots that represent the original vectors. Blue dots represent interpolated velocity at centroids. Green dots represent interpolation between centroids at the original vector locations. 158

Figure 8.3. Post processing of the velocity data

a. Location of the sparse vectors produced using particle pairing (turb5\_27)

b. Delaunay triangulation of the sparse vectors (edges over 50 pixels removed).

c. Refined delaunay mesh. Additional nodes at centroids of original triangles.

Linear interpolation along triangle edges, Surface interpolated with respect to all three nodes 159

Figure 9.1. Using mirrors and a beam splitter as a beam-shearing device. 184

Figure 9.2. The Shearing Interferometer 185

Figure 9.3. Beam shear 'd' produced using a back-silvered mirror 186

Figure 9.4. Measurement of a CO<sub>2</sub> jet using a shearing interferometer

a. The raw interferogram

b. The unwrapped phase map of the interferogram

c. Plot of the normalised intensity, equivalent to fringe order number, through the cross-section of the CO<sub>2</sub> jet indicated in 'b'.

188

Figure 9.5. The shearing interferometer used as a fringe projection system for surface contouring.

a. The fringes projected onto the eye of a manikin. Camera placed at an angle to the optical path of the illumination.

b. The fringe pattern solved using the FFT approach. A reference image (fringes projected onto a flat surface) has been subtracted to remove distortions in the image due to non-straight reference fringes.

189

Figure 9.6. The FFT method of extracting the phase information from finite fringe interferograms

a. Intensity data of one raster of pixels and weighting window.

b. Intensity data weighted by window.

c. Power spectrum of raster with carrier frequency and deformation.

d. Side lobe after weighting by Hanning window and translated by the carrier frequency to the origin.

e & f. Wrapped phase produced by selecting different carrier frequencies, f is correct, e has a gradient due to incorrect carrier frequency

195

Figure 9.7. Axial tomography

199

Figure 9.8. Projection coordinate system

200

Figure 9.9. Optical path through a radially symmetric refractive index field

197

Figure 9.10. The analysis of a tilted wave interferogram projected through a propane flame.

a. The tilted wave interferogram.

b. The unwrapped phase map of half the interferogram (highlighted in red).	
c. Cross section through the propane flame calculated using an Abel inversion.	
Highlighted areas contain localized failures discussed in text.	204

Figure 9.11. Testing of the discretisation of the Abel Inversion, equation 9.19, using a synthetic density field

a. The synthetic density field	
b. Original cross section plotted against reconstructions at successively higher resolutions	205

Figure 9.12. Example of the multiplicative algebraic reconstruction technique. 207

Figure 9.13. A ray passing through a domain, partially overlapping some of the elements 210

Figure 9.14. Comparison of multiplicative reconstructions of a synthetic domain using two and four views. 211

Figure 9.15. Diagrammatic explanation of Fourier Slice theorem 213

Figure 10.1 The test section of the wedge rig 220

Figure 10.2 The shearing interferometer applied to the wedge rig. 222

Figure 10.3 Fringes projected through the wedge rig

a. Reference image in the absence of the flow	
b. Flow on, mass flow rate of 0.66 kg/s, Mach 1.5 at inlet, flow from left to right	223

Figure 10.4 Processed fringe pattern from the wedge rig

a. Unwrapped phase map. Colour bar in $\text{kg/m}^3$ relative to sheared point (refer to text for description of highlighted regions)	
b. Solution for raster of pixels highlighted in 'a'. Flow on and off relative	

densities, and integrated density with unknown offset and offset estimated from oblique shock theory.	224
Figure 10.5 The power spectrum of the raster of pixels considered in figure 10.4b	230
Figure 11.1. Exhaust core jet and mixing region of a compressible jet	234
Figure 11.2. Lobe type suppressor nozzle <sup>[103]</sup>	235
Figure 11.3. The Gas Dynamics of the Shock Tube	
a. The three sections of the Shock Tube	
b. Primed for firing	
c. Diaphragms rupture and shock wave progresses towards exhaust nozzle	
d. Shock is reflected, leaving a high pressure, high temperature reservoir in its wake	239
Figure 11.4. Shock propagation in the shock tube with respect to time <sup>[105]</sup> .	242
Figure 11.5a. The raw interferogram of the 20 <sup>th</sup> scale (2 inch diameter) nozzle, NPR=2.3, TTR=2.3.	
b. The fringe order height map representing the bending of the fringes relative to a reference picture (reference not shown).	245
Figure 11.6. Seeded with 0.59 $\mu\text{m}$ seed, NPR 2.5, 12 millisecond delay from pressure transducer trigger.	246
Figure 11.7. Focused schlieren image. Diamond pattern can just be seen.	246
Figure 11.8. Refraction of a ray passing through a circular region of higher refractive index than its surroundings	251



## List of Tables

Table 4.1 Dynamic velocity and spatial ratios for different forms of recording media. Calculations under autocorrelation assume that resolvable paired exposures can not overlap. Correlation spot size of $64 \times 64$ pixels, giving a maximum resolvable displacement of 16 pixels. Particle diameter of 2 pixels, centroid can be located to $1/10^{\text{th}}$ of the diameter.	70
Table 5.1 calculations and measurements of the out-of-plane component of the nozzle flow	121
Table 8.1 Parameters for the PIV data in the stator-rotor gap	162
Table 8.2 Parameters for the PIV data in the stator passage	164
Table 8.3 Parameters for the PIV data between the suction surface of the NGV and the leading edge of the rotor	166
Table 8.4 Parameters used to assess the resolution of 3-D PIV by defocusing through aperture masks	177
Table 10.1 Dimensions of the wedge rig	220
Table 10.2 Pre and post shock densities and Mach numbers	227

# Nomenclature

## Chapter 2

<b>Symbol</b>	<b>Definition</b>
$v_p$	Velocity of a particle
$s$	Distance
$t$	Time
$\Delta\nu$	Doppler shift in frequency
$\nu_o$	Laser frequency
$\nu$	Scattered light frequency
$c$	Speed of light
$\vec{V}$	Particle velocity
$\vec{l}$	Light sheet direction
$\vec{o}$	Direction of observation
$\theta$	Angle between light sheet and direction of observation (DGV), half angle between converging beams (PDA)
$Re$	Reynolds Number
$\varepsilon$	Emissivity
$\varphi$	Angle of detector from z axis in y-z plane
$\psi$	Elevation of detector from y-z plane
$D$	Diameter of a droplet
$C$	Constant representing scattering angle, solid angle of collection optics, droplet refractive index, polarisation etc.
$S_{mie}$	Scattered light intensity
$S_{fluo}$	Fluorescent light intensity
$N_i$	Number of droplets per pixel

## Chapter 4

<b>Symbol</b>	<b>Definition</b>
$U$	Fluid Velocity
$M$	Magnification

$\Delta x_{max}$	Maximum particle displacement
$c_{\tau}$	Constant that describes the ability to which a particle centroid can be located (%)
$d_{\tau}$	Mean diameter of the particle image
$\sigma_u$	Minimum resolvable velocity
$L_x$	Dimension defining the format of the recording media
$d_p$	Diameter of particle
$\rho_p$	Density of particle
$U_p$	Velocity of the particle
$\rho_f$	Density of the fluid
$U_f$	Velocity of the fluid
$A$	Cross sectional area of the particle
$\mu_f$	Viscosity
$C_D$	Drag coefficient
$F_e$	External potential force
$Re_p$	Reynolds number of a particle
$\nu_f$	Kinematic viscosity
$t_l$	Time constant
$d_s$	Diameter of image of Airy function
$f^{\#}$	$f$ -number
$\lambda$	Wavelength of light
$d_e$	Approximation of particle image diameter (to first zero).
$\bar{\epsilon}$	Mean exposure (mean energy per unit area)
$W$	Energy of a pulse of light
$D_a$	Lens aperture
$n$	Scattering power law exponent
$d_o$	Object distance
$d_i$	Image distance
$\Delta y_o \Delta z_o$	Cross sectional area of light sheet
$E(x,y)$	Grey scale intensity distribution of a particle image
$(x_o, y_o)$	Centroid of a particle image
$A$	Amplitude of a Gaussian profile

$\sigma$	Variance of a Gaussian profile
$n(x,y)$	Additive noise
$\delta z$	Focal depth
$\alpha$	Rotation of image plane relative to the lens
$\theta$	Angle between normal to light sheet and angle of observation
$M_n$	Nominal magnification
$b$	Image separation owing to an aperture mask
$f$	Focal length
$d$	Pitch Circle Diameter of apertures in an aperture mask
$z$	Out-of-plane displacement of a particle from object plane

## Chapter 5

<b>Symbol</b>	<b>Definition</b>
$d_1$	Projection of particle displacement viewed from angle $\theta_1$
$d_2$	Projection of particle displacement viewed from angle $\theta_2$
$d_o$	3-D Particle displacement
$U_i(x_i, y_i)$	Image Amplitude distribution
$U_o(x_o, y_o)$	Object Amplitude distribution
$h(x_i, y_i)$	Point spread function
$h_\varepsilon(\rho_I, \theta_I)$	Point spread function of a defocused system in polar coordinates
$x_o, y_o$	Cartesian coordinates in plane object plane (or plane of defocused particle)
$x_i, y_i$	Cartesian coordinates in the image plane
$x, y$	Cartesian coordinates in plane of aperture
$\varepsilon$	Path length difference for defocusing
$\rho_I, \theta_I$	Image polar coordinates
$\rho_o, \theta_o$	Object polar coordinates
$a$	Diameter of circular aperture
$P(x, y)$	Pupil function of the lens
$P_W(x, y)$	Complex pupil function
$I(x_i, y_i)$	Image intensity
$W(x, y)$	Aberration function introduced by defocusing

$\epsilon_l$	Image defocusing
$\epsilon_o$	Object defocusing

## Chapter 9

<b>Symbol</b>	<b>Definition</b>
$\mu$	Refractive Index
$\rho$	Density
$\Delta\psi$	Optical Path Difference
$C$	Gladstone-Dale constant
$\Delta\rho(x,y)$	2-D Change in density distribution
$N$	Fringe order number
$l$	Path length through a 2-D phase object
$(x_1, y_1, z_1),$ $(x_2, y_2, z_2)$	Optical paths of two interfering rays
$(x, y, z)$	Cartesian coordinates in a phase object
$d$	Shear distance
$\theta_l$	Angle of incidence
$\theta_t$	Angle of transmissivity
$\mu_l$	Refractive index of air
$\mu_t$	Refractive index of glass
$t$	Thickness of shearing mirror
$G(u)$	Fourier transform of $g(x)$
$G(n)$	Discrete Fourier Transform of $g(k)$
$A(x,y)$	Background amplitude
$B(x,y)$	Modulation noise
$f_o$	Carrier frequency in the $x$ direction
$\phi(x,y)$	Phase distribution
$g(x,y)$	Intensity distribution of interferogram
$c(x,y)$	Complex valued interferogram with zero order removed
$c^*(x,y)$	Complex conjugate
$f,y$	spatial frequency coordinates

$\Im[]$	Imaginary component
$\Re[]$	Real component
$\theta$	Projection angle
$f(x,y)$	Source function
$f_r(p,\theta)$	Projection of source function at angle $\theta$ transverse coordinate $p$
$q$	Coordinate along ray path
$\delta$	Dirac delta function
$n$	Refractive index
$\psi_x$	Differential of $\psi$ with respect to $x$
$w_{ij}$	Weighting coefficient of the $I,j$ element
$\Im\}$	Fourier Transform
$b(x,y)$	Back projection of projections at increments in $\theta$

## Chapter 10

Symbol	Definition
$\rho_1$	Pre shock density
$\rho_2$	Post shock density
$\theta$	Angle of leading edge of shock
$\beta$	Half angle of wedge
$\gamma$	Ratio of specific heats
$M$	Mach number

## Chapter 11

Symbol	Definition
$\alpha$	Refraction of a ray passing through a circular region of higher refractive index than its surroundings

## Acknowledgements

I've composed this section of my thesis many times whilst drunk but unfortunately I can never remember these pearls of wisdom in the morning. I'll endeavour to finish this version before I go to bed....

First of all I'd like to thank my supervisor, Prof. Peter Bryanston-Cross, for making the Ph.D. happen in the first place. Like all good supervisors he can be inspiring at times, infuriating at others. You've opened many doors for me. Cheers Pete. PS: You still owe me that drive down Newbury Street in a Union Jack clad Jaguar on the 4<sup>th</sup> July.

Thanks to the OEL long termers, Daci and Leo, who I worked in cahoots with for the first couple of years of my Ph.D. Hope both Daci and baby (Alex) are doing fine n' dandy. The OEL newcomers, Paul, Phil, Keith, Gordon, Claire and Trevor deserve a mention for making work feel more like a social, owing to the office banter. The technicians, Steve, Hue, Dave and Tony also deserve a big thank you for being extremely helpful and a source of wisdom over the years. Profs. Carpenter & Chetwynd deserve a big thank you for proof reading this document and correcting the smelling pistakes.

I would like to acknowledge the assistance of James Anderson and Bill Corbett at DERA Pyestock, and Doug Creviston, Dan Kirk and Prof. Ian Waitz at MIT in gathering some of the data that are presented here. I would also like to acknowledge Rolls-Royce SRC for granting access to their 2-D wind tunnel.

EPSRC funded my studentship and the Corporation of London sponsored me to go to MIT, under the Robert Blair Fellowship. I hope their investment proves worthwhile.

I've had the pleasure of meeting a lot of people during my Ph.D., none more curious than Martin Fisher – a person whom I initially thought was a posh vagrant who had infiltrated the University. Since these humble beginnings Martin has become a very close friend and partner in crime. We've saved the world many times during the drunken haze called Top Banana. He couldn't have done it with out me!

Finally, I'd like to thank the love and support of Faye. Nothing's a problem and everything is so easy when you're around. Love you.

## Declaration

I hereby declare that the work contained in this thesis is the author's own work. Papers that have been published from the work contained in this thesis are attached in Appendix B. The thesis has not been submitted for a degree at any other university.



# CHAPTER 1

## INTRODUCTION

### 1.1 INTRODUCING THE PROBLEM

The advent of sophisticated numerical methods to study and predict flows has enhanced, rather than diminished, the requirement for experimental measurements. An increased level of understanding of the physical flow requires more detailed measurements for verification, especially in separated and turbulent flows.

The gas turbine is a technically mature product. As the compressor and turbine sections are already highly efficient, their performance converging to an asymptote, the engineering need has been targeted towards manufacturing improvements and cost reductions coupled with increased reliability by, for instance, reducing the number of turbine blades. In contrast the combustors are largely considered to be black boxes, the output response of a change in input is known but little is known about the internal behavior of the combustor, especially when running off condition. The range and scope of this thesis from velocity measurements in a gas turbine to a simple, quantitative interferometric technique for compressible flows reflects the perceived engineering need.

## 1.2 AIMS & OBJECTIVES

The aim of this work is to provide improved diagnostic techniques to increase the fundamental understanding, and to verify numerical models, of the engines and their flows. The innovative objectives of the work are to push forward the practical performance of the measurements techniques and in the case of the PIV measurements of the turbine, demonstrate how the technique can be applied in a hostile environment with a complex geometry. The interferometric measurements show how quantitative density measurements can be made using a combination of a novel optical arrangement and analysis software that is no more complex and no more sensitive to vibration than a schlieren arrangement.

## 1.3 DESCRIPTION OF THESIS

The literature survey is not intended to provide details of current commercial systems, but rather the general properties, uses and limitations of a number of key measurement techniques. The survey is deliberately broad, covering measurements of temperature, velocity, pressure and molecular species. It is intended to allow gaps in instrumentation relevant to the two studies included in this thesis to be identified. The literature survey has also aided a separate, ongoing, project to reconstruct tomographically the location of heat release within a combustor operating at its stability limit. The shearing interferometer and some of the tomographic algorithms presented in part 3 (multiplicative algebraic reconstruction and Abel transform) have also been used in this ongoing project.

Part 2 describes velocity measurements in an axial flow turbine mounted in a transient test facility. The measurements have been made using a planar imaging technique called particle image velocimetry (PIV).

The velocity measurements are of interest to the turbine engineer as the flow is inherently unsteady, mainly due to the relative motion between the stationary nozzle guide vanes (NGV) and the rotating rotor blades. The rotor blades periodically pass through the wake and shock structure of the preceding nozzle guide vane row, modulating the flow field over the blades. Fluctuations in pressure change the loading on the blades and can cause vibrations. Changes in heat flux can give rise to thermal fatiguing of the blades and variations in the angle of incidence of the rotor to the flow direction can cause the blades to operate off the design condition.

This stator-rotor gap region is dominated by a complex three-dimensional flow owing to the periodic interaction between the stator wake and the passing rotor. This region represents a substantial loss within a turbomachine, but it is not well modeled by current analysis methods. Nor has the instantaneous structure of the flow been previously recorded, although extensive point measurements have been made using Laser Doppler Anemometry (LDA) and Laser 2 Focus (L2F). The instantaneous structures revealed by the PIV measurements are required in order to increase the fundamental understanding of this region and to provide a test case to validate further calculations.

For the turbine measurements the emphasis is placed on gathering time-resolved, accurate, velocity measurements at engine representative conditions to validate fledgling time-varying calculations. Suggestions are also made towards realizing the

maximum permissible spatial resolution and improving the signal-to-noise ratio in the presence of glare from mechanical surfaces in the field of illumination.

Part 3 describes the development and application of a simple shearing interferometer to compressible flow fields. The shearing interferometer shears a single beam to produce a finite fringe interferogram. It is less susceptible to vibration, in comparison to a beam splitting interferometer, as the sheared beams are incident off common components. The constraint on mechanical isolation from such sources is relaxed to a level equivalent to that of a schlieren arrangement. It is envisaged that the shearing interferometer would be applied either where a schlieren or beam splitting interferometer would normally be used. The shearing interferometer would give a quantitative measurement of refractive index or its dependent variables. In each case only a few, relatively inexpensive, components are required to make the measurement.

The shearing interferometer has been applied to a two-dimensional transonic wind tunnel and a shock-tube exhausting into ambient air. The measurements of the two-dimensional wind tunnel were used both to evaluate the technique and to provide a first pass characterization of the wind tunnel that was to be used for the calibration of anemometry equipment. The purpose of the measurements on the shock-tube was to provide flow visualization to aid the acoustic evaluation of jet-exhaust noise-suppressor nozzles, or mixer-ejectors. The nozzles are designed to suppress noise by increasing the contact area, and hence the interaction, between the exhaust jet and its ambient surroundings. The visualisation of this interaction is intended to aid the mixer-ejector designer by revealing the features that give rise to the acoustic signal. Such features

may be accelerated mixing-layer growth, the scale of eddies within it, or the length of the exhaust core.

Conclusions, part 4, discuss the outcome of both these studies and reviews the new knowledge generated.

## 1.4 NOVEL CONTRIBUTION

### 1.4.1 Velocity Measurements in the Stator-Rotor Gap of a Turbine Cascade

The velocity measurements in the stator-rotor gap of a turbine cascade represent both a new application of the PIV technique and a synthesis of new knowledge generated since the previous velocity measurements, presented by Towers et al. <sup>[113]</sup> on the same facility prior to the fitting of a spinning rotor. The flow measurement is far more spatially resolved, in comparison with this previous study, with approximately five times as many velocity vectors per unit area. The measurements were originally intended to be phase locked to the rotor. Unfortunately, this could not be demonstrated owing to equipment failure. The development of the flow with respect to the phase of the rotor was therefore constructed by selecting the appropriate frames from a large data set (approximately 200 frames of data).

## 1.4.2 Determination of the Out-of-Plane Component of Velocity from Defocusing

A novel defocusing method of determining the out-of-plane component of velocity has been explored on a free air jet exhausting into air. The accuracy to which the out-of-plane component can be measured was found to be comparable to that of the in-plane component if the particle's diffraction pattern can be resolved. These preconditions dictate that diffraction-limited optics and either a high-resolution camera, or small field-of-view, are required. The former precondition could not be satisfied on application to the turbine cascade as the compound curvature and small-scale aberrations of the window could not be corrected. Recommendations have been made to overcome this problem.

## 1.4.3 Development and Application of a Simple Shearing Interferometer to Phase Objects

A simple, low cost, shearing interferometer has been developed and demonstrated with application to compressible flow fields and flames. The original idea was conceived to be a teaching aid to demonstrate the principle of phase by projecting a series of interference fringes. This thesis describes its development from an educational toy into a measurement tool capable of revealing quantitative information of compressible flow fields. This has been achieved by identifying the variable that is being measured by the interferogram and creating strategies that can be used to extract it. Tomographic algorithms have been used to reconstruct the phase object where necessary. The shearing interferometer can be used to reveal quantitative information about the density distribution of a flow field where either schlieren photography or shadowgraphs would traditionally be used.

## Chapter 2

# REVIEW OF OPTICAL METHODS FOR FLUID FLOW

### *Description of Chapter*

*This chapter presents and discusses some of the optical techniques that are used to measure fluid flow and combustion in gas turbines. The intent is to give some idea of the range of measurands and the techniques that can be used to measure them. This knowledge has been used to identify gaps in optical instrumentation required to increase the understanding of the fluid flow and to verify fledgling numerical models.*

*The field of optical flow diagnostics is very wide so such a survey cannot possibly be exhaustive. It does, however, include a discussion of both well established techniques, some of which have been implemented into commercial systems, and some, highly specialized, laboratory curiosities that may come of age in the future.*

## 2.1 INTRODUCTION TO THE REVIEW

The optical diagnostics discussed in this chapter can be split into two categories, those that measure a flow parameter directly and those that measure the dynamics of a body carried by the fluid flow. This body can either be a flow tracing marker, such as a bubble, particle or condensation, or even a seed gas or dopant that can be provoked into giving a fluorescence signature indicative of its surroundings. All the techniques require optical access, either from one direction, or from two typically orthogonal directions, or by a line of sight clear through the region of interest. The interrogated area can either be a volume, two-dimensional plane, point or line integral. All have preconditions that need to be satisfied prior to their successful application. Gaps in the current instrumentation for combustion and fluid flow in gas turbines are identified at the end of the chapter. The discussion makes reference to the need to increase the understanding of the fluid flow and to verify numerical predictions.



## 2.2 VELOCITY & VISUALISATION

### 2.2.1 Laser Doppler Anemometry (LDA)

Laser Doppler Anemometry is a non-intrusive optical technique for measuring the velocity of a fluid at a point. Since its invention in 1964 by Yeh and Cummins <sup>[1]</sup> it has matured into a now well-established optical technique that is commonly used in industry. A concise explanation of LDA is given by Dantec <sup>[2]</sup> whilst a more rigorous explanation is given by Durst et al <sup>[132]</sup>.

LDA allows up to three components of velocity to be measured at any one time over a small volume, the size of which is determined by the intersection of two or more beams of coherent light <sup>[2]</sup>. The interference of the intersecting beams generates fringes within the measurement volume through which flow tracing particles can pass, see figure 2.1. The intensity of the light scattered by the particle as it passes through the measurement volume is modulated according to the spacing of the fringes and the component of velocity of the particle normal to the plane of the fringes. The frequency of the pulses in the scattered intensity is equal to the velocity of the particle divided by the spacing of the fringes.

Figure 2.2 shows a schematic of a typical laser Doppler anemometer in the backscatter configuration. The anemometer consists of two sections, the transmitting and receiving systems respectively. The former consists of a coherent laser source, the beam of which is split and launched into polarization-maintaining single-mode fibers that relay the beams to the launch head. Each of the emerging beams is collimated and focused within the measurement volume. Each beam converges onto a common point that defines the extent of the measurement volume. The two overlapping beams interfere to produce

fringes perpendicular to the plane of the converging beams, see figure 2.1. The fringe spacing can be calculated if the direction and wavelength of the two intersecting beams is known. The measurement of velocity is therefore absolute.

As the measurement volume has dimensions of the order a 100  $\mu\text{m}$  the spatial resolution is potentially very high, although in practical applications it can be limited by the prolonged time periods required to traverse and map large areas. The close proximity of surfaces, to within a millimetre of the center of the measurement volume, can mask the Doppler signal. In turbomachinery applications it is often the case that the beam is 'chopped' in phase to the passing rotor to avoid saturation of the photo-multipliers <sup>[3]</sup>.

The measurement of each additional component of velocity requires a further pair of intersecting beams. In a two-component system the second pair of beams is usually launched from the same launch head as the first but from an orthogonal orientation. The interference fringes are therefore also orthogonal to the first set. A different illuminating wavelength is used to distinguish the multiple channels. For a three-component system the third channel is often launched from a separate head remote from the first, see figure 2.3 <sup>[4, 5, 116 & 131]</sup>. The measurement volume is defined by the overlap of three pairs of beams, reducing the size of the volume and increasing the spatial resolution. LDA systems that measure three components from five beams launched from a single launch head are commercially available, but the accuracy in the out-of-plane component is reduced for long focal distances <sup>[6]</sup>. However, they are mechanically stable and easy to align owing to the single launch head, and are particularly useful where optical access is limited, such as for in-cylinder IC engine applications <sup>[7,8 & 9]</sup>.

Each of the channels must intersect within the same measurement volume to resolve the three-dimensional vector of a single particle. The alignment of the three beams can be verified by projecting each of the three channels through a pinhole placed in the centre of the measurement volume. A power meter behind the pinhole can be used to *walk* (a process of translating the beam and recording the power behind the pinhole in an iterative manner until a peak power is achieved) the beams into a common volume.

Accuracies from  $\pm 1\%$  to  $\pm 0.1\%$  have been claimed for prolonged acquisition periods in time-invariant flows <sup>[133]</sup>. Velocities ranging from less than  $1\text{ms}^{-1}$  to hypersonic speeds have been measured with LDA <sup>[98]</sup>. In order to maintain a sufficient data rate there needs to be an abundance of seeding material. Data rates inevitably suffer in boundary layers or areas of recirculation where there may be little seed. High refractive-index gradients, such as those found in flame fronts and boundary layers, refract the intersecting beams, either displacing or destroying the measurement volume <sup>[8 & 9]</sup>.

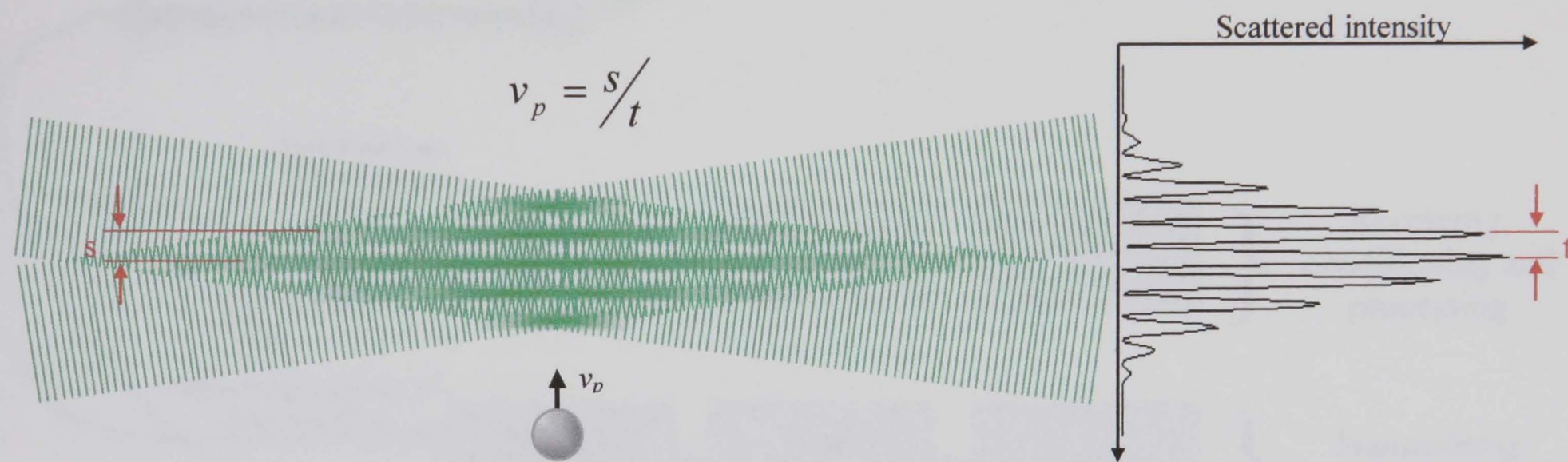


Figure 2.1. Fringe model. The intensity of the scattered light produced as a particle passes through a series of interference fringes contained within a measurement volume defined by the intersection of two coherent beams.

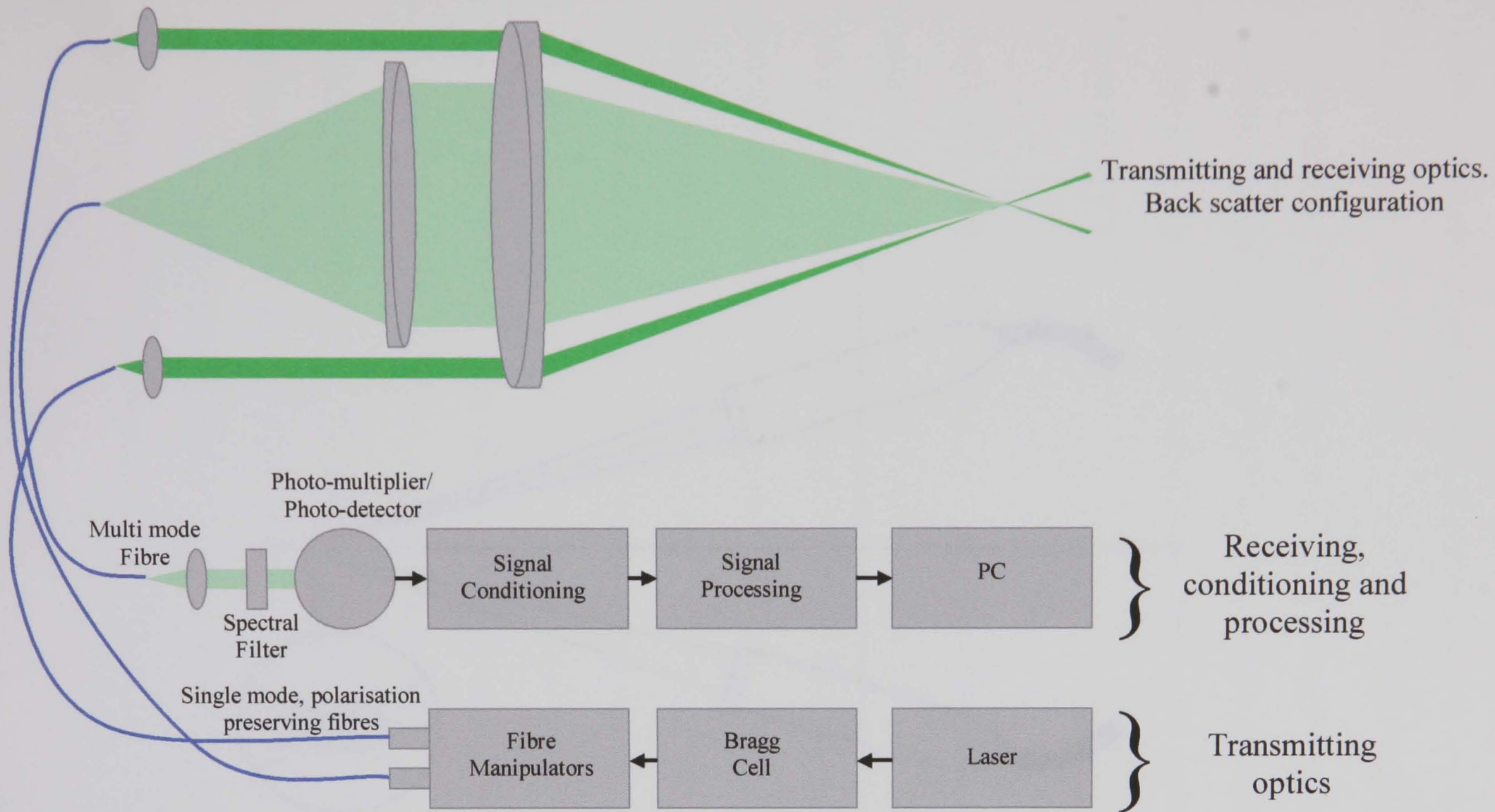


Figure 2.2. Laser Doppler Anemometer – backscatter configuration.



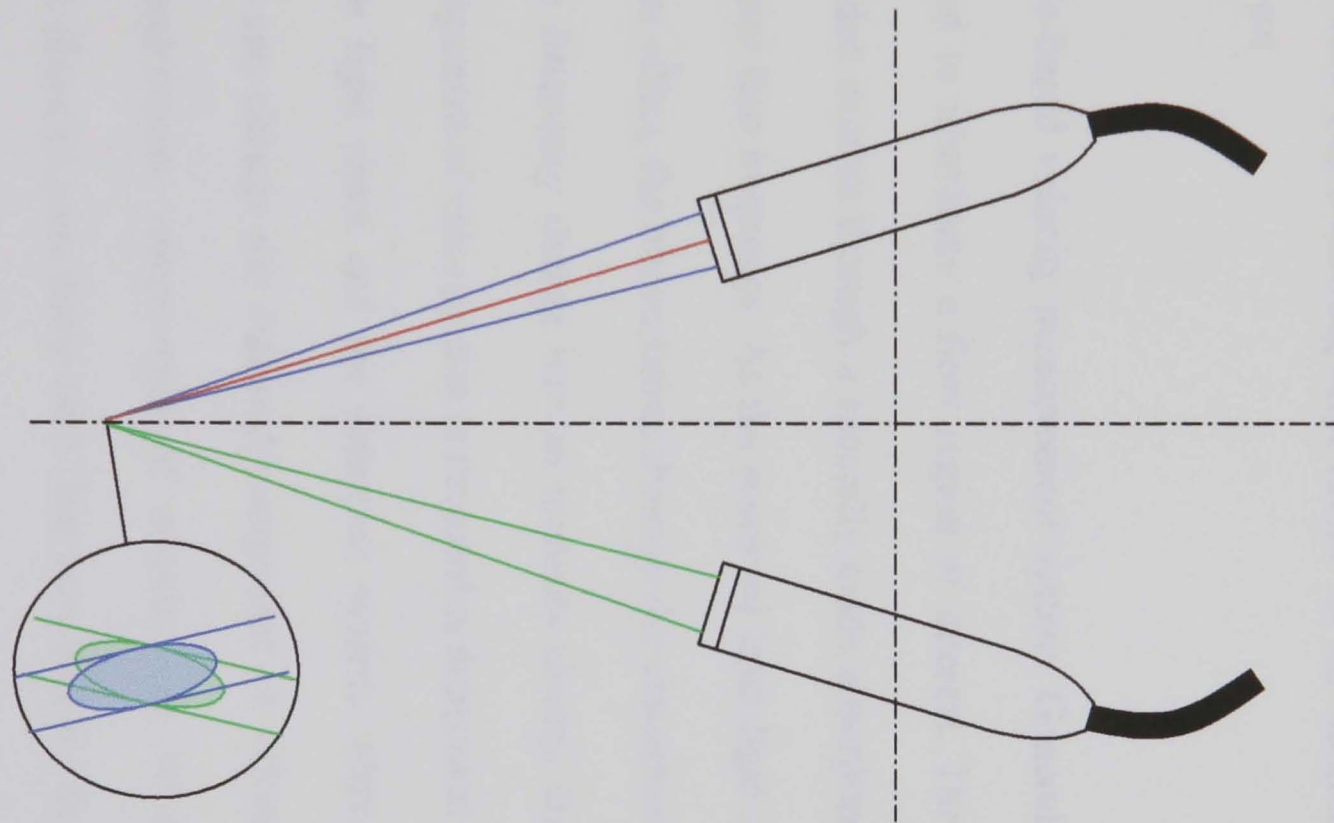


Figure 2.3. Three component LDA system with beams launched from separate heads. Measurement volume defined by intersection of three beam pairs.

### 2.2.2 Doppler Global Velocimetry (DGV)

Doppler Global Velocimetry, DGV, is an imaging anemometer that gives a spatially resolved, mean velocity measurement over a plane. Velocity is determined from the Doppler shift of light scattered by seed suspended in the flow. H. Komine <sup>[10]</sup>, Northrop Research Center first invented the technique, but it was Meyers and Komine <sup>[11]</sup> at NASA Langley who turned it into a practical tool for Fluid Mechanics. DGV is also known as Planar Doppler Velocimetry, PDV, and Global Doppler Velocimetry, GDV, but DGV was the name given by Meyers and Komine and will be used throughout the remainder of this text. The following brief review of the method follows the approach given by Roehle <sup>[13]</sup>.

DGV is a particle-based velocity measurement system. Generally, in this technique a laser sheet is used to illuminate a flow region of interest. The illuminated region is imaged onto a video camera through a specially made absorption cell that has a sharp cutoff near the laser line frequency. As the scattered laser light is shifted in frequency, due to the Doppler effect, the transmission through the absorption cell will also change. This converts the frequency change into an intensity change that can be more readily detected. The component of velocity that is detected is dependent upon the angle formed between the laser light sheet and the detection system. Altering the light sheet or detector location can change the detected component of velocity. By replicating the system three simultaneous components of velocity can be acquired over a two-dimensional field. Since its conception DGV has been steadily developed into a credible tool for fluid mechanics. Difficulties in laser stabilisation and detecting the Doppler signal have hampered the packaging of the technique. However, DGV is finally coming

of age as demonstrated by the measurements in turbo-machinery presented by Roehle et al <sup>[12]</sup>.

The velocity is determined from the frequency shift of the scattered light from a moving particle due to the Doppler effect <sup>[13]</sup>,

$$\Delta\nu = \nu - \nu_0 \quad (2.1)$$

where  $\nu_0$  is the laser frequency,  $\nu$  the scattered light frequency. The shift depends on the particle velocity,  $\vec{V}$ , the speed of light,  $c$ , the light sheet direction,  $\vec{l}$ , and the direction of observation,  $\vec{o}$ , thus

$$\Delta\nu = \nu_0 \frac{(\vec{o} - \vec{l}) \cdot \vec{V}}{c} \quad (2.2)$$

One component of velocity is measured from each observation point. The direction of the component of velocity is  $\vec{o} - \vec{l}$ , the bisector of the angle formed by the direction of the light sheet and the direction of observation, see figure 2.4.

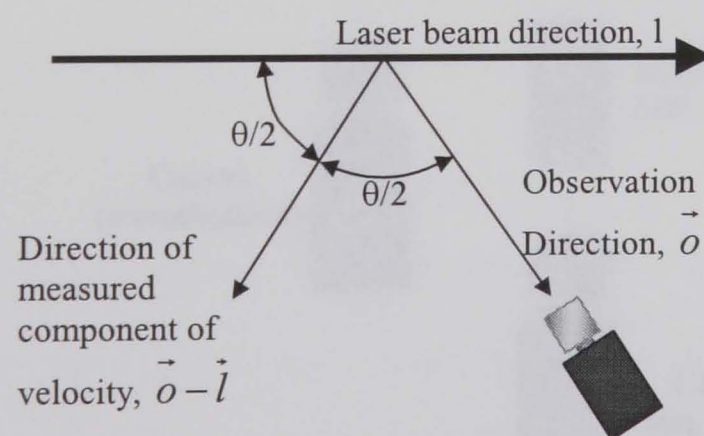


Figure 2.4. The direction of the measured component of velocity in relation to the direction of the light sheet and the observation point.



The frequency shift due to the Doppler effect is typically too small to be measured directly. The shifted light is filtered from the illuminating light by capturing the scattered light through a spectroscopic cell. The absorption line of the spectroscopic cell is identical to the frequency of the illuminating light. If the absorption line has a slightly larger bandwidth than the illuminating light the Doppler shift will cause a change in the transmission through the spectroscopic cell. Frequency variations will manifest themselves as changes in intensity when viewed through the spectroscopic cell.

Intensity variations will also be created by local variations in seeding number density. Two cameras are used to capture the scattered light, one looking through a spectroscopic cell, and the other looking directly at the scattered light, see figure 2.5. A pixel-wise division of the two camera intensities, together with additional post-processing, will reveal a map of the velocity component.

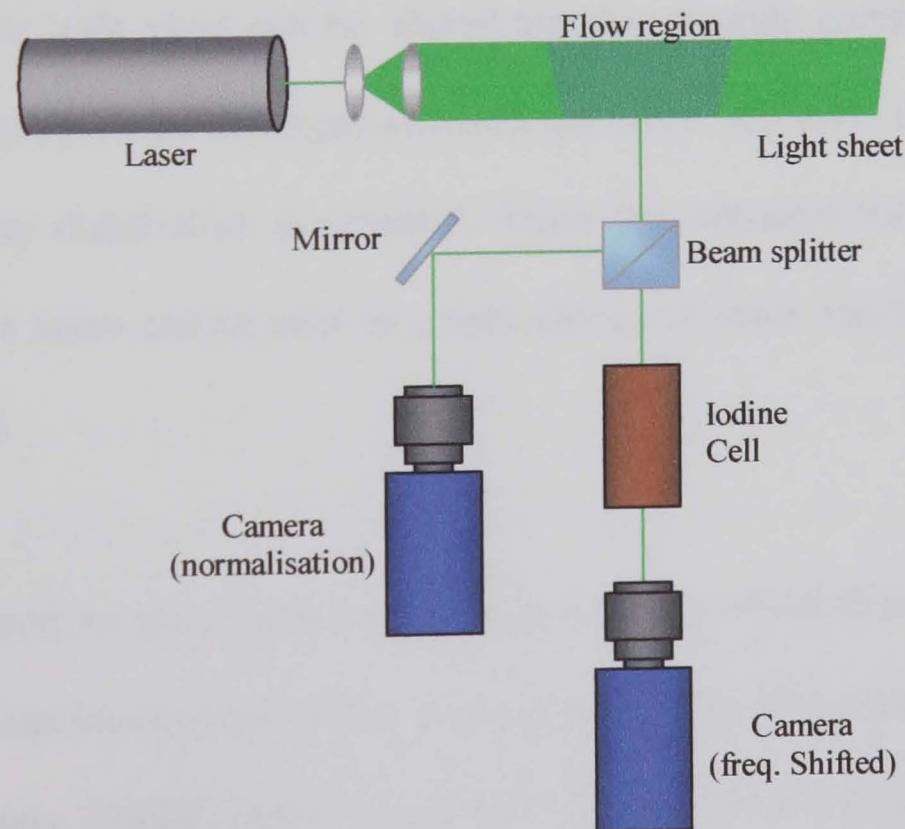


Figure 2.5. The Doppler Global Velocimeter

As the absorption line filter can discriminate between increases and decreases in frequency there is no ambiguity in the sign of the velocity. A calibration procedure is required to establish the transmission profile of the spectroscopic cell. The laser frequency must also be stable to coincide with the absorption line of the spectroscopic cell. Iodine vapour is commonly used in the spectroscopic cell, as it has well-known strong absorption lines in the visible spectrum. These absorption lines interfere with the 514 and 532 lines of Argon Ion and frequency-doubled Nd:YAG lasers respectively, and so is used as a frequency-to-transmission converter for these lasers.

The further components of velocity can be determined in either of two ways depending on whether a snapshot or a time-averaged measurement is required. Firstly, three camera systems can be imaged onto a common area of a light sheet from different directions of observation. The three cameras are triggered simultaneously to reveal a near-instantaneous measurement of the three-dimensional flow field. Secondly, the orientation of the light sheet can be altered and the separate components of velocity measured in sequence. As the measurements are taken one after the other the time-averaged velocity distribution is revealed. Since the exposure times can be longer, continuous wave lasers can be used as a light source. A lower seeding number density can also be used.

DGV can be used to give pseudo-continuous velocity distributions of fluids. As a velocity vector can be encoded within a single pixel even low-resolution cameras can give approximately 250000 vectors per image. The results are given almost online as the processing consists of little more than a pixel-wise division of intensities. The image intensity is generated from an ensemble of seed rather than individually resolved

particles. The compromise on the size of seed can therefore be relaxed in favour of its flow-following capabilities. Measurements can also be made at standoff distances of several metres, light levels permitting. As the particles do not need to be resolved, nor the scattered phase information preserved, the quality of the optical access does not need to be perfect. Test section windows can be curved and not of optical quality. Endoscopes <sup>[13]</sup> can be used in applications where optical access is restricted.

### 2.2.3 Hot Wire Anemometry (HWA)

Although not an optical technique hot wire anemometry has been included in this review due to its ability to measure time-resolved flow <sup>[14]</sup>, and hence its extensive application to fluid studies. No other equivalent technique offers such a high frequency response <sup>[134]</sup>. The basis for hot wire anemometry is the heat balance equations, which can be applied to the anemometric signal to calculate the flow velocity <sup>[15]</sup>. The anemometric probes consist of a thin wire held across the tips of two prongs that may also be operated as thermometric sensors or fine-wire resistance thermometers. The sensing element is a couple of mm long and typically 10  $\mu\text{m}$  in diameter. Although this is fairly large, implying a relatively poor frequency response, the probe must be strong enough to survive particularly harsh environments such as combustion chambers. Hot film probes are generally more robust than hot wire probes and are therefore used in more hostile environments. The criteria for the dimensions of the probe are based on strength, spatial resolution and the frequency response of the prong and wire combination.

The heat exchange between the hot wire and the fluid affects the output voltage of the anemometric signal. For hot wire anemometry it is necessary to measure both the gas temperature and prong tip temperature in addition to the anemometric signal. This is so that during flow measurements the thermal capacity and thermal inertia of the hot wire and prongs are taken into account and may be balanced by a feedback system when processing anemometric data. The feedback system keeps the mean temperature and resistance of the wire constant. Partially shielded probes may be used to resolve any directional ambiguity in the signal.

HWA can detect perturbations as small as 0.01% of the mean velocity assuming that velocity can be isolated from temperature. Further errors can arise due to contaminants on the wire, eddy shedding from wire ( $Re \approx 50$ ), and probe vibration. Neglecting sampling frequency, the frequency response is dictated by the dimensions of the hot wire itself. Typical dimensions of the sensing elements are approximately 2 mm long, 10  $\mu\text{m}$  diameter giving a frequency response of 100 kHz<sup>[14]</sup>. HWAs are intrusive to the flow and delicate. They do, however, give a time-history signal rather than a measurement punctuated by the absence of a flow tracing seed. Their very high frequency response and sensitivity is unsurpassed by any other measurement technique. This, together with their relatively low cost, has attributed them to turbulence studies [16].

#### 2.2.4 Laser Two Focus (L2F)

An L2F anemometer creates a probe volume containing two parallel focussed beams. A particle travelling along the focal plane of the two beams will produce two successive

scattered light pulses as it passes through this 'light gate.' The elapsed time between these two pulses yields the component of velocity perpendicular to the optical axis. The anemometer is sensitive to particles travelling in all directions. Spurious measurements result when independent particles pass through only one of the beams <sup>[17 & 18]</sup>. A correct measurement will result when the beams are orientated parallel to the flow direction and a particle passes through both beams. Prolonged acquisition times are required to orientate the beams approximately to the mean flow direction and to statistically determine the correct measurement. The result is a two-dimensional probability density function containing information about the velocity components in the plane perpendicular to the optical axis, eg: mean flow vector, turbulence intensities and Reynolds shear stresses etc.

Three-component systems can either consist of two two-dimensional systems typically separated by 30°. Alternatively, the 3rd component can be determined from the measurement frequency as a function of the off-axis component <sup>[18]</sup> when the focal point of the beams of a multi-colour system can be displaced (different colours focussed at different axial depths owing to achromatic aberration of focussing lens).

L2F has a typical accuracy of approximately  $\pm 1\%$  or better for mean velocity depending on the amount of data collected and 5-10% for turbulent intensity depending on beam diameter/separation ratio <sup>[18]</sup>. However, errors increase close to surfaces or in highly fluctuating flows or velocity gradients as the probability of successful dual beam transit decreases with high turbulent intensities. Sensitivity to turbulent intensities depends on the ratio of beam diameter to beam separation. Typical limit on turbulent intensity is 30% for a single colour system, although systematic errors increase depending on

whether the particle contacts the periphery or centre of the beams – different path lengths. L2F has been demonstrated in turbomachinery applications up to Mach 2.

The probe volume again determines the spatial resolution. Beam diameters are typically  $\approx 10 \mu\text{m}$ , axial length  $0.5 \mu\text{m}$ . Vectors can be measured in the backscatter configuration to within 2 to 3 mm of surfaces, but the photo-multipliers can be saturated when a mechanical surface ‘touches’ the probe volume. The distance from the *light gate* to the surface can be reduced to half a millimetre if fluorescent markers are used.

The primary limitation of the technique is the time-consuming measurement procedure. Schodl and Forster <sup>[17]</sup> describe 6 to 8 probe angle settings with about 2000 particles at each setting for accurate calculation of mean flow vector and turbulence intensities. This equated to approximately 5 minutes for each measurement point, although they subsequently reduced the sampling time by a factor of ten using modified mathematical models, automated measuring procedures and modest improvements in optics and electronics <sup>[17]</sup>.

High-quality optics are required to focus the two beams and gather the light scattered by the particles. Greater precision allows improved spatial filtering of the signal to give a greater tolerance to surfaces adjacent to the probe volume. Schodl <sup>[18]</sup> also describes a three-dimensional, two-colour, L2F system that has been packaged into a small rotatable optical head connected to a laser and photo-multipliers via fibre optics, enabling 3 components to be measured from a narrow viewing angle.

### 2.2.5 Shadowgraphy

Shadowgraphy is a non-intrusive technique that is based on the refraction of light passing through strong density gradients <sup>[76]</sup>. A collimated beam of light is projected through the flow field onto a screen to reveal an intensity distribution. Dark areas will appear representing regions where the light has been deflected away from its original unperturbed path.

Opaque objects in the flow will appear blurred in the shadow image. This can be improved by decreasing the diameter of the light source. Shadowgraphy is sensitive to changes in the second derivative of the gas density. It is therefore well suited for visualising shock waves and turbulent compressible flow fields as well as the mixing of gasses of differing refractive indices.

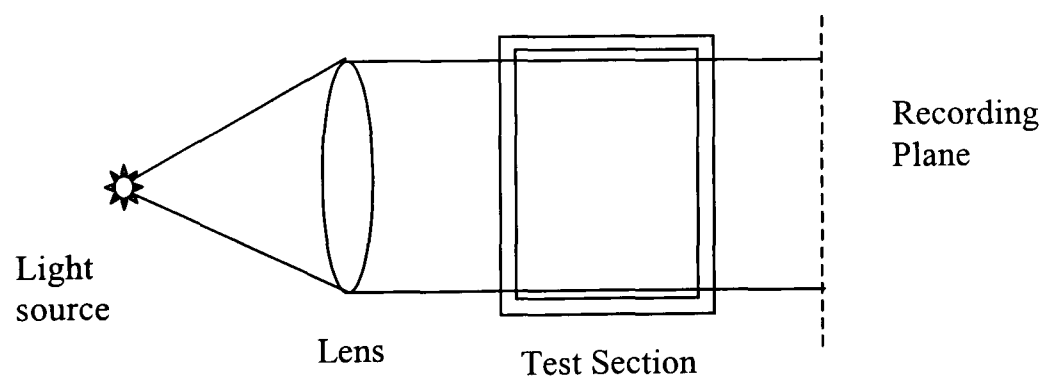


Figure 2.6. Shadowgraphy arrangement

### 2.2.6 Schlieren

Schlieren technique is also based on the deflection of light, but now the deflection angle of the ray at the end of the test volume is measured <sup>[19 & 76]</sup>. The resolution is higher than that of shadowgraphy, but the set-up is more complicated and more difficult to use.

The collimated beam is sent through the flow field, after which it is made convergent by passing through a lens or reflecting off a concave mirror. An image of the light source is formed in the focal plane of this lens or mirror. When the collimated beam is deflected, the deflected light is imaged slightly displaced in the focal plane. By placing a so-called schlieren filter in the focal plane this deflection can be made visible. E.g. knife-edge filters or coloured filters can be used to visualise the magnitude and/or direction of the gradient in the flow field by intensity or different colours. For this the light source should either be a point source or a slit source parallel to the knife edge direction. A lens is used to form an image of the section, which eliminates shadow effects.

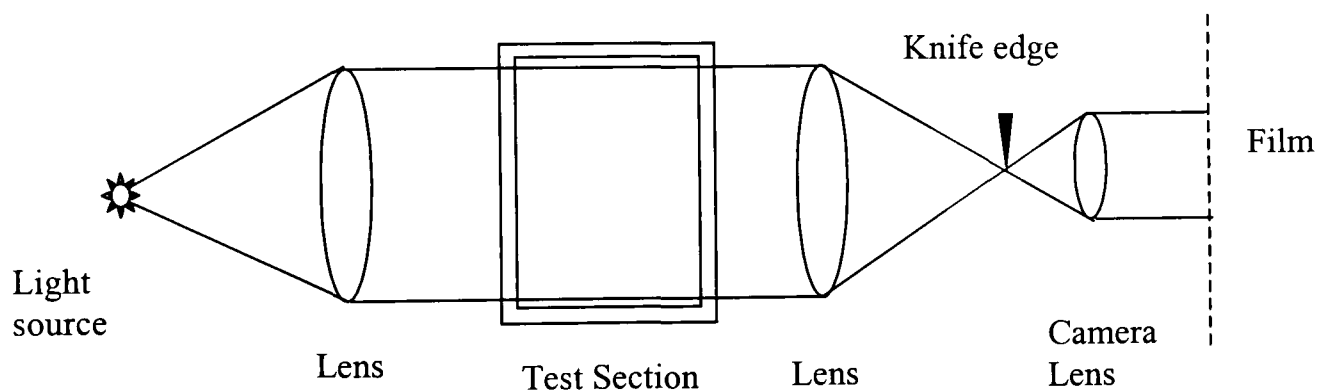


Figure 2.7. The Schlieren arrangement

In general, the intensity change is proportional to the component of the density gradient normal to the knife-edge. The schlieren system is thus, sensitive to changes in the first derivative of density. For high sensitivity it is advantageous for the second lens to have a larger focal length.

Both schlieren and shadowgraphy work well for visualising 2-D flow characterised by the large refractive index gradients. They do not work well with low refractive indexes.



Quantitative results from shadowgraph and schlieren images suffer severely because they only measure the second and first derivatives respectively of the density field. Despite these drawbacks both Schlieren and Shadowgraphs are commonly used owing to their simplicity and readily digestible qualitative results. Their usefulness can be improved when coupled to high-speed cameras and light sources to study the transit of shocks within aerodynamic facilities <sup>[20]</sup>.

### 2.2.7 Interferometry

Interferometry can be used for non-intrusive visualisation and to give quantitative results concerning the density distribution in a compressible flow <sup>[19,21,22 & 23]</sup>. Neither probes nor seed need to be introduced into the flow. The interferogram typically consists of a series of interference fringes that portray a contour map of the two-dimension projection of the density <sup>[22]</sup>, or relative density <sup>[21]</sup>, distribution. Interferometry is sensitive to absolute changes in density. It is based on the retardation that a light ray experiences when crossing an inhomogenous refractive index (density) field with respect to an undisturbed ray. When a collimated beam crosses a field that is homogeneous in the x- and y- direction the wave front remains plane. When it traverses an inhomogeneous field the wave front is deformed owing to local retardations.

By using interferometry the phase delay of the light beam passing through the flow field can be measured. This phase delay is proportional to a line integral of the density along the light path through the flow field. Once the phase delay is known

the average density of the flow can be determined. The density distribution can then be used, in some cases, to derive information on velocities <sup>[21 & 22]</sup>.

To exclude phase-disturbing effects of dust and non-ideal optical apparatus the interfering beams may be stored, and reconstructed, holographically. The holographic medium also allows the three-dimensional effects of the flow to be recorded <sup>[19]</sup>.

Large changes in pressure and temperature can greatly affect density. If the density change is non-orthogonal to the beam it will be deflected by refraction. This can present problems when measuring compressible flows where large density gradients such as shocks and boundary layers are present <sup>[21 & 22]</sup>.

In nominally two-dimensional wind tunnels the phase object can be assumed to be constant in the  $z$  direction, greatly simplifying the analysis and improving accuracy. Measurement of highly three-dimensional flows largely depends on the ability to deconvolve the 3-D information. Interferometry requires both mechanical and laser (SLM and TEM<sub>00</sub>, single longitudinal mode and transverse electric and magnetic modes) stability for beam splitting interferometers <sup>[22 & 19]</sup>, although this restraint is greatly relaxed for beam-shearing arrangements where the two beams are incident off common components and share common optical paths <sup>[21]</sup>.

Interferometry has undergone a renaissance owing to the advent of Electronic Speckle Pattern Interferometry (ESPI) that exploits the speckle effect of light scattered from diffuse surfaces, an attribute which was historically the bane of the art <sup>[135]</sup>.

## 2.3 TEMPERATURE

### 2.3.1 Coherent Anti-Stokes Raman Spectroscopy (CARS)

CARS is a non-linear Raman technique used to measure temperature and species concentration in hostile particle-laden, turbulent and highly luminescent environments. Two laser beams are utilized to stimulate Raman scattering of the molecules <sup>[24]</sup>. The signal is produced in a coherent "laser-like" beam that can be readily separated both physically and spectrally from interference. The amount of scattered light is dependent upon the number of molecules present, thereby allowing the molecular number density to be measured <sup>[25 & 26]</sup>. In addition, the frequency of the signal is dependent upon the Boltzman distribution, which is governed by the temperature. An analysis of the frequency content gives a measurement of temperature. CARS data can be obtained in a "broadband" mode that allows the spectra to be obtained instantaneously (10 nsec). A 100-500 mJ, spectrally narrow, pulse pumped laser is required as is a broadband Stokes laser (Dye) for broadband CARS. A multi-channel detector is required to receive the CARS signal. The typical accuracy for molecular number density is 10%, whilst that of temperature 5% for single shot for N<sub>2</sub>, 1% for continuous wave excitation. Other species that have been investigated include H<sub>2</sub>, H<sub>2</sub>O, and CO<sub>2</sub> <sup>[25]</sup>.

CARS is complex to set up and the signal is difficult to analyse. The signal intensity is non-linearly dependent on temperature, species concentration, Raman line width and pressure. Computer models of species spectra are required before a measurement can be extracted. The apparatus itself, pump and Stokes lasers and detector, are also expensive. CARS remains a highly specialized technique that is neither widespread in industry or research institutions.

### 2.3.2 Degenerate Four-Wave Mixing (DFWM)

DFWM uses a resonant interaction of a frequency of light with a molecular transition frequency to measure temperature, species or velocity. The experimental arrangement is similar to CARS, but is potentially more sensitive owing to the use of a resonant interaction <sup>[27]</sup>.

Typically, three laser beams cross (to define a localized sample volume) and interact to generate a fourth laser beam that becomes the detected optical signal. An alternative physical picture of this process is to imagine that two of the input beams interfere to create an interference pattern and associated index of refraction grating. The third input beam is diffracted from this index grating to become the fourth or signal beam. Versions using one wavelength or multiple wavelengths are possible, as well as versions that use the non-resonant susceptibility or a particular absorption resonance of a given molecule. Non-intrusively measured flow quantities that have, so far, been demonstrated include total density, individual species density, temperature, velocity, and the speed of sound <sup>[27]</sup>. Variations of this technique are also called, for example, Laser-Induced Gratings Spectroscopy (LIGS) and Transient Grating Spectroscopy (TGS) <sup>[28]</sup>. DFWM has shown to be accurate to 5% for temperature over a range from 300 to 2300 K for N<sub>2</sub> <sup>[27]</sup>. As quenching problems are less compared to Laser-Induced Fluorescence (LIF), both major and minor species are accessible. Its application requires dual-ended optical access, but the highly directional signal requires only a small detector. Larger windows are required if interrogation spot is to be traversed. DFWM, like CARS, is a complex and immature technique that remains in the realm of a few specialised laboratories.

### 2.3.3 Optical Pyrometers

The thermal radiation of a material or gas depends on the radiating properties of the emitter <sup>[29]</sup>. The radiance emitted from a black body, at any wavelength, is solely a function of absolute temperature and is described by Planck's law or, integrated over all wavelengths, by the Stefan-Boltzmann law.

The spectral radiance of a non-black-body emitter depends on emissivity that varies with temperature, wavelength and microstructure. For solids the emissivity is also a function of the surface macrostructure, e.g.  $\epsilon \approx 0.95$  for black carbon  $\epsilon \approx 0.02$  for polished aluminium. The reliance on the radiance intensity at a given wavelength to measure temperature can be misleading as the emissivity can change with surface finish or if the surface oxidises. Various comparative radiometric methods can be used to reduce the dependence on emissivity. These methods are described in detail by Lawton and Klingenberg <sup>[29]</sup> but can be summarised thus,

*Total or integrated method:* Radiance integrated over spectrum – radiance temperature

*Spectral Emission:* Spectral radiance – brightness temperature

*Colour Temperature:* Based on two or more brightness temperatures

*Differential Colour Temperature:* Comparison of emission contour to that of a black body over a limited range.

*Reversal Method:* Comparison of the emission of an unknown source to that of a source at a known temperature.

If the dependence of emissivity on wavelength is removed the optically measured temperature is identical to the true temperature, but these techniques can become inaccurate where the emissivity is much less than 1. They are therefore more suitable for soot-laden combustion environments. The basis of this pyrometry method in combustion applications is that some of the soot particles escape oxidation. The incandescent particles are at temperatures similar to the surrounding gas, emitting electromagnetic radiation in the form of visible light and infrared energy.

The reversal method allows both the brightness temperature, emission and absorption coefficients to be equated and located using a tomographic approach. The reversal method consists of nulling the emission and absorption of an unknown source against that of a reference [29,30 & 31]. Either a small measurement volume or an integrated line of sight can be measured depending on the set-up. Transient measurements can be made either by strobing the known source or by recording the unknown source emission local to the reversal signal. For the former a laser (Argon Ion or Nd:YAG) can be used as the known source, if calibrated against a black-body emitter. The reversal principle can also be exploited to determine the emission and absorption of individual spectral lines of a flame to spatially specify a flame.

Most commercial pyrometers use colour temperatures to reduce the dependence on emissivity. Typical accuracy is  $\approx 1\%$  with temperatures varying from  $-50$  to  $3000^{\circ}\text{C}$ . The spatial temperature distribution can be revealed by ratioing the grey-level

intensities of two images recorded at different wavelengths <sup>[32]</sup>. The signal can be attenuated by windows and emission/absorption in optical path but, gives non-intrusive spatial temperature distribution if pre-conditions are satisfied.

#### 2.3.4 Thermographic Phosphors

This non-intrusive optical technique utilises the temperature-sensitive emission properties of certain luminescent inorganic chemicals known as thermographic phosphors <sup>[33]</sup>. When excited with ultra-violet light these phosphors produce fluorescence whose properties are temperature dependent in terms of its emission lifetime and in terms of the relative intensity of emission at various discrete wavelengths. Utilising these characteristics a thin layer of the phosphor can be applied to a surface to measure the instantaneous surface temperature distribution <sup>[33]</sup> or incorporated in a static or dynamic sensor <sup>[34 & 35]</sup>.

The primary advantage of phosphors is that they can be painted onto entire surfaces or integrated into a point sensor such as the phosphor-tipped fibre optics with UV excitation and recipient photodiode described by McGee <sup>[36]</sup>. The phosphors exhibit high sensitivity ( $\approx 0.05^\circ\text{C}$ ), robustness and stability, and have been demonstrated at temperatures from  $-100$  to almost  $2000^\circ\text{C}$ . Systems can be adapted to make remote measurements of pressure, heat flux, shear stress and strain. They can exhibit frequency responses up to a kilohertz depending on whether a radiative or lifetime mode is used. They are non-contact and emissivity independent unlike pyrometers and thermocouples. However, the coating thickness can affect aerodynamic qualities of the substrate, for example coating of turbine blades can alter their geometry and hence their efficiency <sup>[37]</sup>.

### 2.3.5 Temperature Sensitive Paint (TSP)

Temperature is a cause for uncertainty with pressure-sensitive paints (PSP). However, the sensitivity to pressure can be decoupled from that of temperature by covering the PSP with a non-permeable coating preventing the diffusion of oxygen into the paint <sup>[38]</sup>. The physics of the temperature-sensitive paints is similar to that of PSP in that an active molecule is excited by a specific wavelength of light except that quenching occurs as a result of molecular collisions giving rise to a non-radiative de-excitation rather than the presence of oxygen <sup>[39]</sup>. Such paints have been demonstrated over ranges of approximately 10 to 70 °C with a resolution of 1°C at pressures ranging from zero to ambient. The magnitude of luminescence is related to luminophore concentration, source irradiance, and paint temperature. Therefore an image ratio method is employed to isolate the influence of temperature. An accuracy of  $\approx \pm 0.3^\circ\text{C}$  have been demonstrated by Cattafesta et al <sup>[40]</sup> on swept cylinder and swept-wing models in a supersonic flow. Relative motion between model and illumination source or model deformation and deflection between wind-on and wind-off states are usually the cause of the dominant error term.

Although images can be realigned the effect of the deformation on the illumination is difficult to correct. However, this error can be corrected using a two-colour paint that contains both reference and temperature luminophores. The paint can be applied using conventional spraying equipment. The surface can be sanded or sprayed over with a suitable lacquer to achieve an acceptable surface roughness. The TSP must have surface properties that do not alter the aerodynamic characteristics of the substrate and must remain attached. Surface contaminants can also degrade measurements e.g. oil deposits may also fluoresce.



TSPs allow the remote measurement of surface temperature distribution up to a range of approximately 200°C with high spatial resolution, and accuracy comparable to conventional temperature sensors. As their temperature range is limited they are only suitable for *cold* applications.

### 2.3.6 Thermal Paints (Irreversible)

Thermal paints applied to a substrate change colour upon reaching a predetermined threshold temperature. As the colour change is irreversible they can only be used once. Single or multi-change paints are available over ranges of 135 to 635°C and 160 to 1270°C respectively with accuracies of  $\pm 5\%$  <sup>[41]</sup>. Single-change paints indicate whether a single temperature threshold has been reached. Multi-change paints go through a range of colours according to a defined temperature range. Both are colour fast in direct sunlight, resistant to oil, steam and water, and provide a clear line colour change. No primer is required for most surfaces.

## 2.4 SPECIATION

Optical Spectroscopy (UV/Visible/IR) is employed as a non-intrusive flowfield diagnostic for combustion research <sup>[25]</sup>. Techniques include absorption/emission in the UV and IR, laser induced fluorescence (LIF) of both naturally occurring and seeded species, and a number of scattering techniques including Rayleigh, spontaneous Raman, and several coherent Raman spectroscopies. Temperatures can be derived from spectroscopic measurements applying emission/absorption methods according to Planck's or Wien's and Kirchhoff's laws, provided there is local thermal equilibrium in the system <sup>[29]</sup>. The emissivity and absorption of radiating gases vary strongly with wavelength. Therefore spectroscopic temperature measurements are based on the radiative quantities at specific wavelengths. The temperature of soot can be found because it is almost a blackbody source (the emissivity  $\sim 1$ ). The temperature can be found using Planck's law that relates spectral radiance of a blackbody radiator to the temperature. For flame temperature measurements the temperature of the soot is often assumed to be equivalent to the flame temperature <sup>[29]</sup>.

The evolving spectroscopic techniques are species specific and often measure the internal state distribution of the probed molecules. These measurements require a detailed knowledge of the collision physics and reaction dynamics as an integral part of their interpretation, and, therefore, represent a revolution of sorts in that they are leading to an understanding of aerodynamic phenomena from the molecular level rather than from the traditional bulk-properties approach.

## 2.4.1 Fourier Transform Infrared Spectroscopy (FTIR)

Many atmospheric species have IR activity that can be measured with high sensitivity using FTIR Spectroscopy. FTIR allows many gases to be monitored simultaneously and non-intrusively, a desirable quality where there is no prior knowledge of the molecular species that may be present. Typical molecular species measured are CO<sub>2</sub>, CO, NO and H<sub>2</sub>O. FTIR has been successfully applied to gas turbine exhaust plumes <sup>[42,43 & 44]</sup>, gas-fired, power-plant plumes and in-cylinder IC engine measurements <sup>[45]</sup>. Fourier Transform Spectroscopy (FTS) can be categorised into either active or passive systems depending on whether the absorption of a reference source or the emission of the subject gas itself is measured. Gas samples can be probed actively by passing a beam of modulated IR radiation through the gas and measuring the spectral absorption. Using a multi-pass system, where the reference IR radiation is reflected through the gas more than once, can increase the sensitivity of such systems. Alternatively FTIR can be used to measure the spectral emissions of hot gases using single-ended access where access to the far side of the target gas is difficult. The target gas needs to be hotter than its surroundings for it to be a net emitter rather than a net absorber.

The basis of the instrument is a Michelson interferometer. A heated ceramic that approximates a black body is used as a reference source of IR radiation. The collimated radiation is split into two optical paths by a beam splitter. One of the beams is incident on a fixed corner cube reflector whilst the other is incident on a second corner cube that can be translated along the optical axis. Corner cubes are used as they allow for misalignment of the mirrors, always returning the light along its incident path. The movable mirror modulates the signal on the detector by changing the optical path length between the two beams. The amplitude modulation is proportional to the wave number

of each spectral component. Path differences of integral wavelengths give maximum intensities, vice-versa for half wavelengths.

The energy throughput of an FTIR spectrometer is higher than that of a comparable scanning monochromator allowing faster acquisition and better signal-to-noise ratio. Calibration entails simply counting the interference fringes produced by projecting the beam of a He Ne laser through the interferometer.

#### 2.4.2 Non-Disperse Infra Red (NDIR) Analyser

Non-Disperse Infrared Spectroscopy can be used to measure carbon monoxide, carbon dioxide and nitric oxide although the accuracy for low levels of nitric oxide is not high<sup>[46]</sup>. The infrared spectra of many gases are characterised by narrow, non-overlapping absorption bands. Thus, the measurement of absorption within a defined wavelength band can uniquely identify the presence and concentration of a particular gas. In NDIR gas sensors, an infrared optical 'sample' filter with a narrow band of transmission is selected to overlap with the absorption band of interest, the position of the filter determines the gas to be measured and the amount of absorption determines the gas concentration present. The infrared filter is chosen to ensure that the sensor is totally gas specific and will not exhibit cross sensitivity with other gases. A reference filter at a different pass band can be used as a datum. Concentrations of CO, CO<sub>2</sub> and CH<sub>4</sub>. from 0-2000 ppm to 0-100% can be measured with a typical accuracy of  $\pm 2\%$  of full scale.

### 2.4.3 Laser Induced Fluorescence (LIF)

LIF has the capability to detect species in smaller concentrations than those required for Raman-based approaches. Raman approaches cannot be used at concentrations less than 0.1%. Flame radicals in combustion, such as OH, CH etc., are often only present in concentrations less than 0.01%. They are therefore inaccessible to the inherently weak Raman-based techniques <sup>[25]</sup>.

Specific molecules can become electronically excited by absorbing laser light at specific wavelengths causing them to fluoresce <sup>[54]</sup>. Lasers are the preferred source of excitation as they are spectrally and spatially specific. The chemical species that can be excited is determined by the presence of an electronic absorption band within the spectral range covered by tunable laser (200–1500 nm approx.). The fluorescence wavelength is usually, but not always, red shifted (Stokes shifted) from the excitation wavelength unless resonance fluorescence occurs (same excitation fluorescence wavelength). This allows the fluorescence signal to be sifted from spurious interference from Mie scatter, glare etc <sup>[25]</sup>. There are several preconditions that need to be satisfied to perform fluorescence measurements on a molecule. Firstly, the molecule must have an absorption wavelength that is accessible by laser. The molecule must also have a known emission spectrum and rate of radiative decay. The fluorescence power is proportional to the rate of decay. Corrections need to be made for collision quenching in the presence of other species and temperature if accurate species number density measurements can be made.

Fuel flow and dispersion measurements can be made by adding a tracer to the fuel or intake of a combustion engine that is not affected by the combustion process. The

molecules of the tracer fluoresce when exposed to laser light at certain wavelengths, revealing the fuel distribution <sup>[47 & 55]</sup>. Dopants are selected according to their fluorescent properties for visualisation purposes these are good absorption of the laser wavelength, quantum yield, low quenching by oxygen, sufficient red shift (Stokes-shift), similar boiling point and solubility in fuel <sup>[48]</sup>. The large Stokes shift is required to separate the fluorescent signal from the elastically scattered stray light. Dopant with a similar boiling point to fuel is used to ensure that the dopant vaporises with the fuel and is a good tracer in both liquid and gas phases.

Velocity can be determined either by measuring the Doppler shift on the fluorescence signal or by adopting a similar approach to PIV by strobing the excitation light source. Temperature can be measured using a variety of approaches <sup>[25]</sup>. Firstly, excitation or fluorescence scans can be used to reveal vibration/rotation energy level of the ground electronic state. Secondly, the relative populations of two states can be measured and the temperature calculated from the Boltzmann expressions <sup>[49,50,51 & 52]</sup>. Lastly, a single-excitation, thermally assisted approach can be used in instances where collisions rapidly distribute the population throughout the upper state manifold. The fluorescence reflects the population distribution from which the temperature can be calculated. Temperatures are typically inferred from rotational population ratios. The typical accuracy in number density measurements is 5 to 10%, and 10% for temperature (based on simultaneous imaging of NO (seeded) and OH at combustion temperatures ranging from 1000 to 2200 K) <sup>[51]</sup>. The use of fluorescent flow tracing markers in a PIV application would not necessarily improve the accuracy, but would allow the measurements in the presence of glare from surfaces, windows etc.

LIF can be implemented in a variety of configurations. Reeves and Musculus excited and imaged a small measurement volume from common optical access <sup>[56]</sup>. Alternatively planar arrangement can be used to measure 2-D spatial information. Ninety-degree, dual optical access would be required together with a high-energy laser system and ICCD. Tunable (dye) lasers are desirable to allow the excitation of specific bands or the choice of a laser line with a lower absorption when absorption is a problem. However, high-power XeCl excimer lasers (typically higher energy than dye lasers) can be used to produce low-noise images in larger flow fields. Saturation can be achieved, removing the laser energy and quenching dependence of the signal, at the cost of a non-linear relation between fluorescence and population fraction <sup>[53]</sup>.

#### 2.4.4 Laser Induced Incandescence (LII) & Planar Laser Induced Incandescence (PLII)

Planar LII can be used to provide a planar measurement of soot volume fractions and soot particle size <sup>[57,58,59 & 61]</sup>. LII involves heating soot particles with a laser beam so that they achieve a much higher temperature than the gas within which they are suspended. The laser heating produces a considerable increase in the black-body radiation, or incandescence of the soot. Soot vapourisation/fragmentation occurs at laser fluences above  $0.45 \pm 0.05 \text{ J/cm}^2$  at 1064 nm <sup>[60]</sup>. Laser intensities need to be greater than  $10 \text{ MW cm}^{-2}$ , otherwise signal will not be independent of intensity. Above this threshold the particle temperature will not increase significantly but at high laser fluences the particle will loose mass rapidly. The net result is a signal that is largely proportional to the soot volume fraction and slightly dependent on particle diameter, yet nearly independent of laser fluence assuming certain preconditions are met <sup>[3]</sup>. The primary

limitation is that it can be difficult to distinguish the signal from high luminescent backgrounds. Broadband incandescents can be far more intense than Raman signatures of other species.

Particle size is determined either from ratio of the LII signals produced by a single pulse, but recorded at separate wavelengths, or from the signal ratios at different time gates <sup>[57]</sup>. The measurement of particle size relies on an energy conservation model to describe the heating of the soot particle from the laser pulse and its subsequent cooling due to radiation, conduction and vapourisation.

Typical accuracy is 10% for volume fraction for moderate ranges of particle sizes and flame temperatures. Errors can be reduced by careful selection of wavelength, detector gating (duration and delay to coincide when vaporisation is dominant) and laser intensity <sup>[57]</sup>. For particle sizing the accuracy is  $\pm 2$  nm over a 10 to 40 nm range over a temperature difference of 1000 K using the two-colour method. The time gate method is sensitive to temperature and is only applicable where the temperature distribution is known to  $\pm 50$  K. The spatial resolution is determined by resolution of the camera, as individual particles do not need to be resolved.



## 2.5 PARTICLE & DROP SIZING

### 2.5.1 Phase Doppler Anemometry (PDA)

A seed's ability to follow a fluid flow is a function of its size. Combining the measurement of size with that of velocity reduces the uncertainty in the data. A large particle will scatter more light than a small particle. The result is either a skewed spectrum from an LDA measurement or a bright particle in a PIV image that misguides correlation algorithms<sup>[127]</sup>. PDA allows both the size and velocity of a spherical particle to be determined simultaneously. The process has also been extended to irregularly shaped particles<sup>[62]</sup>. Both PDA and LDA share a common principle for determining velocity in that it is calculated from the Doppler shift in the frequency of the light scattered by a particle as it passes through a small measurement volume. PDA extends this principle by also considering the phase difference between the scattered light at different detectors to determine the particle diameter.

PDA can be used to measure particle diameters from 0.5  $\mu\text{m}$  to several millimeters where there is sufficient optical access, usually from two directions<sup>[66]</sup>. The refractive index of the particle and of the medium within which it is suspended are also required as the optimum scatter angle is a function of refraction<sup>[63,64 & 65]</sup>. This calculation relies on the assumption that the particle medium is homogeneous, although slight inhomogeneities can be tolerated where the diameter of the inhomogeneous seed is approximately equal or less than the wavelength of the illuminating light. The number concentration of the particles is also limited, as only one particle must be present in the measurement volume at any one time.

Despite these preconditions PDA has seen successful application to spray and liquid atomisation processes, powder production and bubble dynamics such as cavitation, aeration and multiphase mass transfer <sup>[66]</sup>. The technique is commonly used to characterise fuel sprays where both the drop size and velocity of the fuel is required. The drop size is a function of the shear within the liquid, which can be determined from the velocity. As larger droplets have greater momentum they can be propelled further. Smaller droplets evaporate quicker. Knowledge of the drop size and velocity allows the fuel distribution in the combustion environment to be studied.

Figure 2.8 shows the layout of a typical PDA system <sup>[66]</sup> that is essentially the same as that for an LDA system, except that two detectors are used so that the phase difference between the two can be calculated. The detectors are often positioned off the axis of the transmitting components so that diffracted light is largely responsible for the scattered signal. If only one scattering mode dominates, a linear phase difference/curvature relationship exists and no calibration is required. If additional scattering modes of comparable intensity are simultaneously recorded this linear relationship will be lost.

As the phase difference between two detectors is encapsulated within a modulo  $2\pi$  there remains a phase ambiguity between particle sizes that generate a phase difference exceeding  $2\pi$ . This ambiguity is often overcome by employing a third detector to identify the integer multipliers of  $2\pi$ . Increasing the separation between the detectors can also extend the measurement range. The intersection of two or more focussed beams and the projection of a slit-shaped spatial filter mounted in front of the receiving fibres define the measurement point. A single particle passes through the measurement volume and scatters light from each of the individual beams with a Doppler frequency

shift. The multiple sources of scattered light interfere to produce a beat frequency. The beat signal at each of the detectors is converted into a Doppler burst with a frequency that is linearly dependent on the particle's velocity. The phase delay between the Doppler signals of the detectors is a direct measure of the particle diameter.

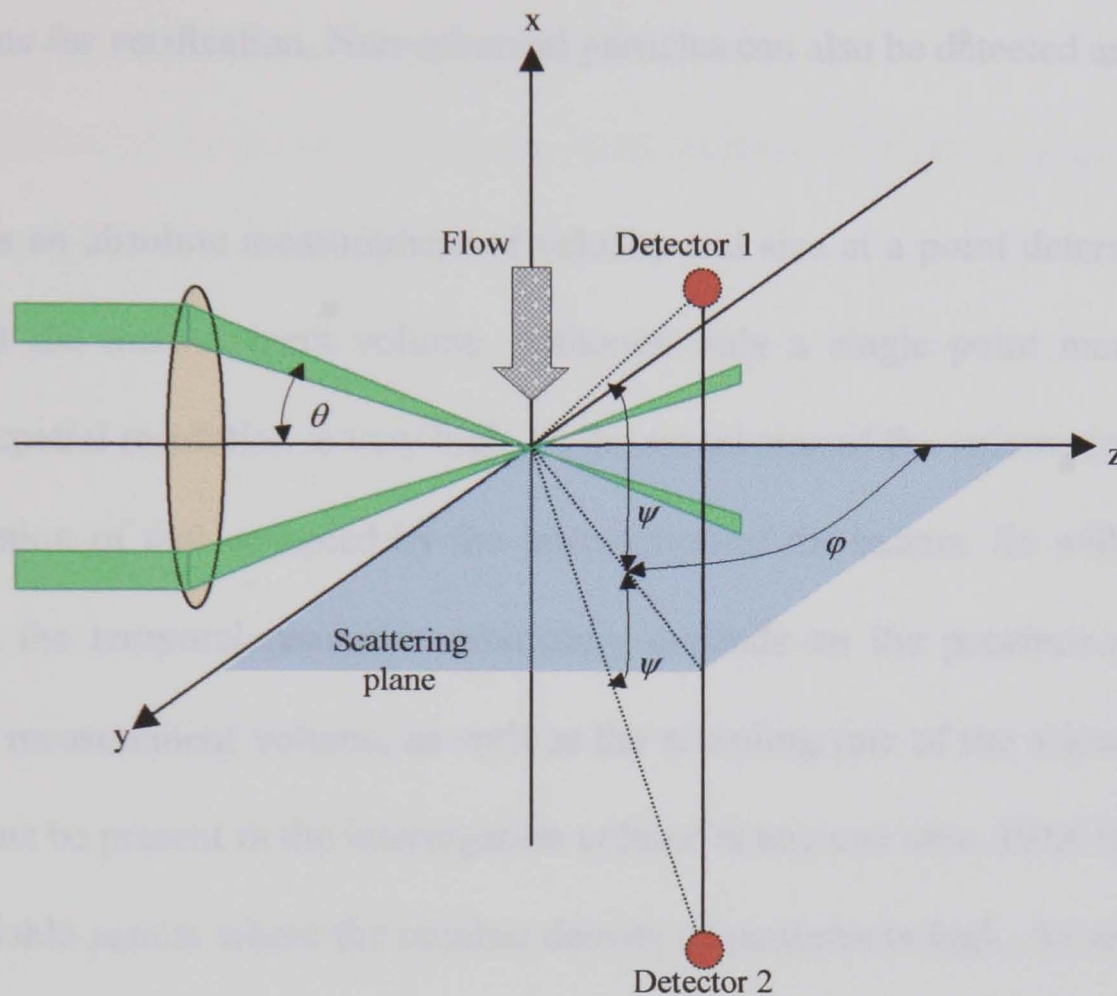


Figure 2.8. Orientation of launch head and detectors of a PDA system.

There are several sources of uncertainty that can degrade the quality of the data. Erroneous phase information can result from oscillations in the spatial coherence of the illuminating light, irregular particle shapes, inhomogeneous particles and multiple scattering effects. The signal to noise ratio can vary owing to variations in intensity and extinction. The former can be generated by a particle trajectory across the Gaussian profile of the illuminating light, which can vary the ratio of reflected and refracted light incident on the detector <sup>[66]</sup>. This effect becomes noticeable for transparent particles with a diameter exceeding half the measurement volume diameter. Further anomalies

arise where the slit aperture ahead of receiving fibers can filter out the required mode of scattering, leaving a different scattering mode dominant. Both the Gaussian and slit-effect problems can be addressed using a dual PDA system. A dual PDA system uses the phase information given by an additional pair of intersecting beams and detectors in the y-z plane for verification. Non-spherical particles can also be detected and rejected.

PDA offers an absolute measurement of velocity and size at a point determined by the location of the measurement volume. Although only a single point measurement is made, the spatial resolution is very high, as the actual size of the volume interrogated is only a fraction of that occupied by the intersection of the beams. As with all seeding techniques the temporal resolution ultimately depends on the presence of a particle within the measurement volume, as well as the sampling rate of the system. Only one particle must be present in the interrogation volume at any one time. PDA therefore fails to give reliable results where the number density of particles is high. As with all point-measurement techniques its spatial resolution can be compromised by the need to map an area over a realistic acquisition period.

### 2.5.2 Laser Sheet Drop Sizing (LSD)

Laser sheet drop sizing, or planar drop sizing as it is also known, is a relatively new technique and there are few references for it. This review follows the description given by Le Gal et al <sup>[67]</sup>. Laser sheet drop sizing uses the ratio of the laser induced fluorescence and Mie signals to calculate the Sauter Mean Diameter, SMD, information from sprays.

The SMD represents the ratio of volume to surfaces area. It is of consequence to the study of sprays as it is a measure of the ease with which it will vaporise. Large SMD implies that the spray will vaporise poorly, a small SMD implies it will vaporise readily.

LSD is a planar technique that gives a two-dimensional SMD map of a spray and has been successfully applied to a pressure swirl atomiser <sup>[67]</sup>. It is a complementary technique to PDA in that it can be used to measure dense sprays where PDA fails to give reliable results. As it is a planar technique it gives a two-dimensional representation of the spray rather than the point-wise measurement. LSD relies on two assumptions that act as a precondition to the technique. Firstly, it is assumed that the Mie scattering signal obeys a  $D^2$  relationship and secondly, that the fluorescence signal obeys a  $D^3$  relationship, where  $D$  is the diameter of the droplet.

The first assumption can be encapsulated in equation 2.3 where  $C$  is a constant representing the scattering angle, solid angle of collection optics, droplet refractive index, polarisation etc. and  $S_{mie}$  is the scattered intensity. This relationship has been shown to be accurate for spherical absorbing droplets greater than 1  $\mu\text{m}$  in diameter although the  $D^2$  dependence deteriorates above 80  $\mu\text{m}$  <sup>[68]</sup>.

$$S_{Mie} = C_{Mie} D^2 \quad (2.3)$$

Fluorescence occurs when the liquid spray contains a fluorophore that absorbs part of the illuminating laser light, which is commonly emitted with a strong red shift that can be spectrally filtered from the Mie signal. The fluorophore can either be naturally occurring or added to the liquid in low concentrations. For transparent droplets the

fluorescence signal,  $S_{Fluo}$ , is largely proportional to the concentration of the fluorescing molecules and thus can be described by the  $D^3$  relation, equation 2.4.

$$S_{Fluo} = C_{Fluo} D^3 \quad (2.4)$$

However, the index of the dependence can vary when strongly absorbing dyes are used and thus a careful characterisation of both the elastic and inelastic scattering of the droplets as a function of their diameter is required.

Le Gal et al. <sup>[67]</sup> characterised the Mie and fluorescence signal by illumination of the fog of mineral spirit (kerosene) doped with p-Terphenyl (PTP) from a droplet generator using the second and fourth harmonics of an Nd:YAG laser respectively (532 and 266 nm). The droplet diameters were measured using a two-component PDA system. A good correlation with the  $D^2$  dependence of the Mie scattering signal was found, although the dye concentration was found to have a profound influence on the absorption and hence also the fluorescence signal. Only ‘highly dilute’ dye concentrations were found to follow the  $D^3$  dependence.

If the preconditions are correctly adhered to, and more than one droplet is sampled per pixel, the intensity ratio of the fluorescence and Mie signals at a pixel gives the Sauter Mean Diameter,

$$\frac{S_{Fluo}}{S_{Mie}} = \frac{C_{Fluo} \sum_i N_i D_i^3}{C_{Mie} \sum_i N_i D_i^2} \propto \frac{\sum_i D_i^3}{\sum_i D_i^2} = SMD \quad (2.5)$$

where  $N_i$  is the number of droplets per pixel with diameter  $D_i$ . LSD gives a two-dimensional map of the relative Sauter Mean Diameter of sprays. The measurements can be made absolute using a single point measurement of droplet diameter that can be provided using a PDA system. LSD can be applied to dense sprays and gives a high spatial resolution determined the number of picture elements and magnification of the imaging system.

A calibration procedure is required to determine the correct dye-liquid combination and dye concentration in order to establish a  $D^3$  dependent fluorescence signal. This is most easily achieved in water-based sprays where many dyes are available that can be excited using visible light. Even in the absence of a calibration the technique can be used to give qualitative patternation data as a precursor to mapping the SMD. The technique has the potential to be extended into high-temperature combustion environments where a dye of similar boiling point and evaporation rate to the liquid fuel would be required.

### 2.5.3 Light Obscuration

It is possible to measure particle cross-section from the shadow cast by an individual particle. A simple system would consist of a photo-detector and a laser diode. Particles passing through the beam obscure some of the light incident on the photo-detector. High number densities can present a problem, as only one particle must be in the beam at any one time <sup>[69]</sup>. Alternatively particle sizes can be established using a process called Back-Lit Imaging where, as the name suggests, the particle diameters are established by interrogating an image of the particles <sup>[70]</sup>. The images can reveal irregular particle shapes, inclusions in droplets etc. A sequence of frames can reveal velocity and



qualitative information such as jet break-up and ligament growth. Back-Lit imaging can be limited in its application owing to the confusion generated by out-of-focus particles outside the image plane. This problem becomes worse in sprays of high number densities.

#### 2.5.4 Diffraction Methods

The angular distribution of the light diffracted by an ensemble of particles can be used to determine their mean diameter. The majority of the diffracted light is concentrated towards the forward direction of the incident laser beam and is collected using a Fourier transform lens, see figure 2.9. Smaller particles diffract a larger portion of their incident light away from the forward direction than larger particles.

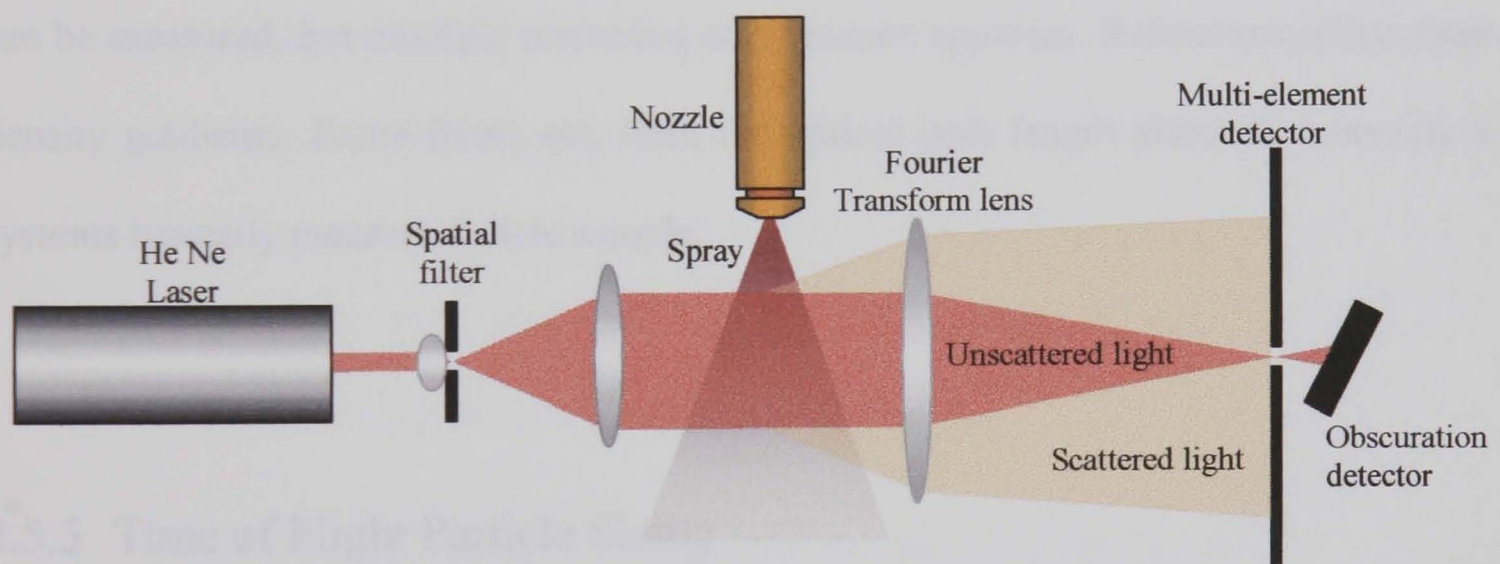


Figure 2.9. Particle sizing by diffraction

The angular distribution can be interrogated by traversing a photo-multiplier in the back focal plane of the transform lens.



This principle forms the basis of the commercially available Malvern particle sizer that can be used to measure particle diameters ranging from 0.02-3500  $\mu\text{m}$  in wet or dry suspension <sup>[71 & 72]</sup>. The spatial resolution is defined by the thickness of beam and working distance of the Fourier Transform lens (1.5 times focal length of Fourier Transform lens to give a suitable capture angle). The measurement is an integration of the mean diameter along the optical path of the beam. The results therefore need to be de-convolved to give spatial size distributions. As particles diffract at a given angle regardless of velocity, the technique can be applied to high-speed flows. The particle, in effect, gives a signal all the time it is in the measurement volume.

In dense sprays the result can also be skewed owing to smaller particles falling within the shadow of larger particles. Low concentrations right up to 95% beam obscuration can be measured, but multiple scattering may become apparent. Refraction effects from density gradients, flame fronts etc, limit the optical path length although commercial systems typically measure remote sample.

### 2.5.5 Time of Flight Particle Sizing

Time-of-flight particle sizing consists of accelerating a particle or aerosol through the path of two laser beams <sup>[69 & 73]</sup>. The transit time of the particle across the two beams is correlated against the particle's aerodynamic diameter. Larger, heavier particles are slower to respond to the accelerating flow field, vice-versa for smaller, lighter particles. A second size distribution can be established from the side scatter of the two illuminating beams. Concentration can be determined from the signal counts. This kind

or particle sizer is typically used for particle diameters in excess of  $0.5 \mu\text{m}$  in concentrations up to  $10\,000$  particles per  $\text{cm}^3$ .

### 2.5.6 Intensity Methods

Particle sizes can be calculated from the amplitude of the light scattered by a particle as it passes through an illuminating beam [74 & 75]. The absolute intensity is compared against either Mie or Rayleigh theory to ascertain the particle diameter. Typical particle sizes range from a fraction to tens of microns. Light scattering intensity is dependent on particle shape, complex index of refraction, lens geometry, and photo-detector spectral characteristics as well as particle size. A calibration is required, usually with ideal, non-absorbing, spherical aerosols, although they may not be representative of non-ideal, light absorbing, irregular particles, eg: soot. Errors occur where intensity variations are present at either the source or in the optical path and owing to the particle trajectory through a Gaussian beam profile. Either defining the measurement volume as the intersection of two separate colour beams or by sampling intrusively at a known location can solve these problems. The Knollenberg probe [75] is an example of a commercial system that uses this principle, see figure 2.10.

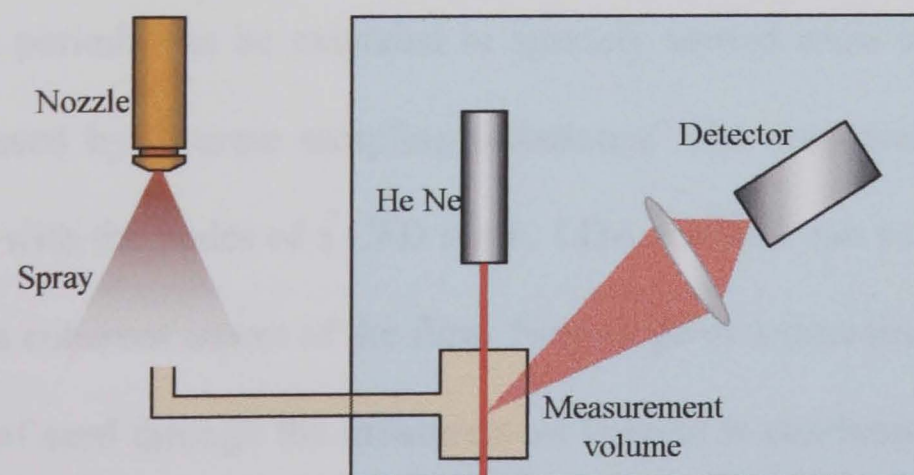


Figure 2.10. Intensity method of particle sizing

## 2.6 SUMMARY OF OPTICAL INSTRUMENTATION FOR FLUID FLOW IN GAS TURBINES

### 2.6.1 Compressors & Turbines

As compressor and turbine performances converge to an asymptote an ever-improving knowledge of the detailed flow-field is required to improve them. Detailed numerical predictions rely on accurate diagnostic instrumentation to validate them.

If the compressor or turbine blades are considered to be two-dimensional a simple transmitted-light technique such as interferometry can be used to provide quantitative flow data such as density and the location of shocks. Such data are obviously insufficiently accurate where three-dimensional profiles, and predictions, are considered.

LDA and L2F have been successfully applied to both compressors and turbines to ascertain velocity and its fluctuations <sup>[116 & 136]</sup>. Both are intrinsically point-wise techniques where a volume or plane is traversed over a period of time. The vectors can be established from an ensemble or a single particle passing through the measurement volume. Sampling periods can be extended in sparsely seeded areas to record vectors that would be missed by discrete sampling techniques. The measurement points can therefore coincide with the nodes of a CFD mesh. LDA and L2F can be phase locked to a passing rotor or a coherent aspect of the flow. Neither gives a time history of the flow, unless the stream of seed through the measurement volume is continuous, necessitating a very high seeding number density that, if achievable, could leave deposits on the blades. In each case the spatially irregular, incoherent aspect of the flow would be lost.

The compressors and turbines are made up of stages of stationary and rotating blades. The rotors are mounted on typically two or three shafts that rotate at different angular velocities. The flow between the stators and rotors is inherently unsteady due to the relative motion between them. The rotors either side of a stator may not be rotating at the same angular velocity nor have the same number of blades. In the strictest sense successive measurements would need to coincide with the correct phase of both of the rotors, not just the phase of a single rotor to spatially map a plane or volume. If spatial and time accurate predictions of this unsteady flow are to be verified, a plane or volume needs to be measured in an instant. The acquisition of simultaneous vectors is obviously desirable where a facility is transient, the cost of running high, or where it is difficult to maintain a constant run condition over a period of time.

Both DGV and PIV allow the acquisition of simultaneous vectors in high-speed flows. DGV is obviously the more elegant of the two but is also at a less advanced stage than PIV. It is doubtful whether a sufficient seeding number density could be achieved in turbomachinery to realize the potential spatial resolution of DGV, one vector per pixel, if it were to be used in single shot mode, unless the seeding was injected locally. In addition to this, two cameras are required for each component of velocity to be measured. In the application of PIV to the turbine cascade, described in part 2, the optical access and the space available to accommodate the camera arrangement is minimal. This, combined with complexity and expense of hardware required, stabilized and spectrally narrow lasers, temperature controlled iodine cells etc, bode against the use of DGV, especially in the presence of a more mature, simpler alternative such as PIV.

## 2.6.2 Combustion

Non-laminar flows are typically modeled using the time-averaged Navier-Stokes equation or by direct numerical simulation. The former makes the assumption that the instantaneous velocity is made up of a mean and a fluctuating term that generates the Reynolds or turbulent stresses <sup>[137]</sup>. This premise generates six more unknowns than there are equations, so an approximation model is used to solve the closure problem. The predictions can be highly accurate where a suitable turbulence model is used, but can also bear no relation to the flow where the model is unsuitable. Experimental verification is required to assess both the quantitative accuracy and the qualitative resemblance to the measured flow.

A direct numerical simulation represents the flow at a resolution that includes all the scales of instantaneous velocity. Such an approach is obviously very computationally intensive owing to the temporal and spatial resolution required. The problem is exacerbated where a reacting flow is considered as the reactions occur at a molecular scale over very short reaction times. The problem is further compounded due to the transport of different phases and particles within the fluid. Combustion modeling is therefore at a far less advanced state than that of non-reacting flows. Direct numerical simulation will not be feasible for most flows of engineering interest for the foreseeable future.

The combustion chamber is largely considered to be a black box where the general relationship between the inputs and outputs of the combustion chamber are known, but little is understood about its internal behaviour. Still less is known when the combustor is taken to the limits of, and beyond, its stability loop. Combustion can become unstable

if the AFR is increased. Further problems can ensue if the combustion instability couples with the acoustic mode of the combustion chamber or other mechanical components. Such a phenomenon would be difficult to model owing to interaction (energy transfer) between the fluid and a mechanical surface. Likewise the interaction, and acoustic signal, of the exhaust jet mixing with its ambient surroundings is also problematic.

Part 3 describes the development and application of a shearing interferometer. It has initially been applied to a compressor representative transonic flow in a 2-D wind tunnel. The shearing interferometer has also been used to visualise a compressible exhaust jet mixing with its ambient surroundings, a flow that would be difficult to model due to the interaction between the mixing fluids. This visualization was secondary to acoustic measurements of the exhaust jet so was to be inexpensive and not interfere with these primary measurements.

The application of the shearing interferometer also includes a tomographic reconstruction of a natural gas flame. This reconstruction is to be used in a separate project, not described in this thesis, as a comparison against emission/absorption measurements of the flame made using the reversal principle described in section 2.3.3. The reversal principle will be used to spatially map the emission and absorption coefficients of a single spectral line, (308 nm, bright OH in a CH<sub>4</sub> flame) within a natural gas flame.

Many optical methods for combustion already exist but their application is severely hampered by the harsh, multi-phase, particle-laden, often optically dense, and highly

luminous environment. These methods will undoubtedly become more accurate as spectral sources and detectors become more precise and as spectral models of combustion improve, but until then a void remains in the understanding of combustion within the gas turbine.

## *Chapter 3*

# APPLICATION OF PIV TO A SPINNING TURBINE CASCADE

-

## INTRODUCTION & BACKGROUND

### *Description of Chapter*

*The rationale for applying particle image velocimetry, rather than other velocimetry techniques, to the stator-rotor gap in a short duration turbine cascade is described. The novel requirements of the PIV measurements undertaken here are highlighted.*

*A previous PIV measurement made in this cascade, prior to the fitting of the rotor, is discussed, since it defines the fundamental parameters to this experiment, such as the choice of seed and general approach. Improvements regarding the recording of the data, data reduction and vector yield per image are identified.*

*Finally, the turbine cascade and turbine stage are described.*



## 3.1 INTRODUCTION

### 3.1.1 Background

Turbomachines are typically technically mature products and are used in a variety of engineering applications from power generation to marine and aero-propulsion. Improving their efficiency, and reducing their operation and acquisition costs, relies on either calculating or measuring the flow regimes within them.

Detailed investigations in turbomachinery have been performed using LDV for over two decades. Moore et al <sup>[141]</sup> (1981) and Edmunds et al <sup>[116]</sup> (1998) give an account of the development of LDV with regard to high-speed turbomachinery applications over this period. LDV is a point measurement technique that can be used to reveal stationary spatial flow structures by time and ensemble averaged over all the blades passages. As numerical predictions are typically time-averaged the results are well suited for comparison. Further to this, the LDV measurement points can coincide with the CFD mesh nodes for a direct, non-reconstructed, comparison.

CFD is a science in its infancy. As fluid models improve and more processing power becomes commercially available it will become a credible design tool independent of experimental validation. As the numerical solutions improve so must the experimental results used to validate them.

PIV gives a series of instantaneous spatial velocity measurements. It can reveal the unsteady, incoherent aspects of a flow as well as the time-mean flow by combining frames <sup>[77]</sup>. As each frame can yield many velocity vectors the data acquisition times are much shorter than with traditional LDV techniques. Where the cost of producing a

turbomachinery representative flow is high, or if the flow is transient, the use of point measurement techniques can become undesirable. This problem can be exacerbated where the working conditions of facility, temperature variations, seeding concentrations etc., have to be kept constant over the acquisition period.

The stator-rotor gap region of a turbine stage is a challenging application both to measure and to model owing to the complex interaction of a series of stationary and rotating blades. The region contains both coherent and unsteady components generated as the stator wake impinges on the passing rotor. The measurements are further complicated due to the transient nature of the facility.

Many of the issues encountered during the application of LDV to turbomachinery apply to PIV. As with a backscatter LDV system, only one window is required for PIV. A clear line of sight similar to that used for transmitted light methods is not necessary. The light sheet must also be introduced without significantly perturbing the flow. Gaining optical access is not trivial where the viscous or thermal flow is not to be perturbed by a window. An ideal window would not compromise the casing annulus shape nor aberrate the field-of-view through it. Its heat transfer properties would also be identical to the rest of the casing in order to maintain a correct gas and wall temperatures ratio. It must also withstand the mechanical and thermal loadings imposed upon it.

Typically, sub-micron seeding particles are needed to follow the high frequency perturbations and abrupt changes in velocity found in high-speed flows <sup>[87 & 117]</sup>. As the

amount of backscatter from such particles is small, either high-powered pulsed light sources ( $\approx 100$  mJ/pulse) or image-intensified cameras are required to see them.

### 3.1.2 Novel Requirements of the Measurements

The novel contribution of the work undertaken here is the instantaneous measurement of the 2-D velocity distribution of the flow through the stator-rotor region of a short duration turbine cascade operating at engine representative conditions. The feasibility of a novel method for recording 3-D vectors has also to be explored and demonstrated on a free air jet but not applied to the turbine. The 2-D PIV data have been recorded digitally and the necessary algorithms implemented to facilitate the data reduction required for the automatic extraction of the velocity vectors. This work represents a logical progression from the previous measurements made on this facility described by Bryanston-Cross and Towers et al <sup>[139 & 113]</sup>, in that a rotor has since been fitted to the facility. It is the interaction of the stator wake with the passing rotor that has been measured rather than flow between the nozzle guide vanes in the absence of a rotor. The flow through the nozzle guide vanes has also been measured here, except with the presence of the rotor. The vector yield per image of the data presented here is an order of magnitude higher than the previous work despite the lower resolution of digital cameras in comparison to photographic film. The requirement for manual pairing of the particle exposures during the analysis stage and need for wet processing of photographic films has also been obviated. The measurements are to be used to validate time accurate numerical predictions and to demonstrate a velocity measurement capability on this facility.

The choice of instrumentation, and the early direction of the project, had largely been defined by the previous work by Bryanston-Cross & Towers et al <sup>[139 & 113]</sup>. They describe the velocity measurement in the nozzle guide vane passage made using PIV. The results were recorded photographically, scanned and processed by manual identification of the particle pairs. Each photograph yielded approximately 100 vectors and took three hours to process. The accuracy of the measurements was estimated to be 6% after cosine errors, aberrations and analysis tolerances etc. had been considered. However, as Bryanston-Cross and Towers had already defined the correct seeding and general approach, the benefits of their work for the current project should not be underestimated.

## 3.2 THE ISENTROPIC LIGHT PISTON FACILITY (ILPF) & MT1 TURBINE STAGE

The ILPF is a short duration wind tunnel for testing full size, high pressure turbine stages <sup>[140, 142, 143 & 144]</sup>. It is capable of matching all the non-dimensional parameters relevant to turbine fluid mechanics and heat transfer. This is achieved by exhausting a nearly isentropically compressed, and hence heated, volume of air through a spinning rotor. The rotor speed is kept constant throughout the valid run-time by an aerodynamic turbobrake operating on a common shaft to the rotor. The ILPF can simulate full engine representative conditions for run times ranging from a few hundred milliseconds to a couple of seconds, depending on the conditions required.

The ILPF consists of three sections. In the centre of the facility is the working section containing the MT1 unshrouded, high-pressure turbine stage. The stage consists of 32 nozzle guide vanes and 60 rotor blades. The rotor operates on a common hollow shaft to an aerodynamic turbobrake downstream of the rotor. The hollow shaft houses signal conditioning circuitry for instrumented blades and is supported on two sets of oil-lubricated bearings.

Upstream of the working section is a pump tube containing a lightweight piston. The pump tube is separated from the working section by a fast acting plug valve. Downstream of the working section is an exhaust tank separated from the movement of the rest of the facility by a sliding joint.

Prior to the run the lightweight piston is positioned at the upstream end of the pump tube and the volume ahead of the piston is filled to a predetermined pressure. The

exhaust tanks and working section are evacuated and the rotor assembly is spun up to speed.

The run is initiated by introducing high-pressure air behind the lightweight piston to nearly isentropically compress the volume ahead of it. When the desired pressure and temperature have been reached the plug valve is opened, releasing a steady flow of air through the working section. A second throat at the stage's exit determines the pressure ratio across it. It is an annular variable device that maintains axisymmetry in the exhaust flow. The throat acts as a choke and isolates the stage from disturbances originating downstream. The flow through the turbobrake can be reduced by fitting blockage rings over its diameter. Its performance can be further fine tuned by regulating the amount of exhaust flow that bypasses it.

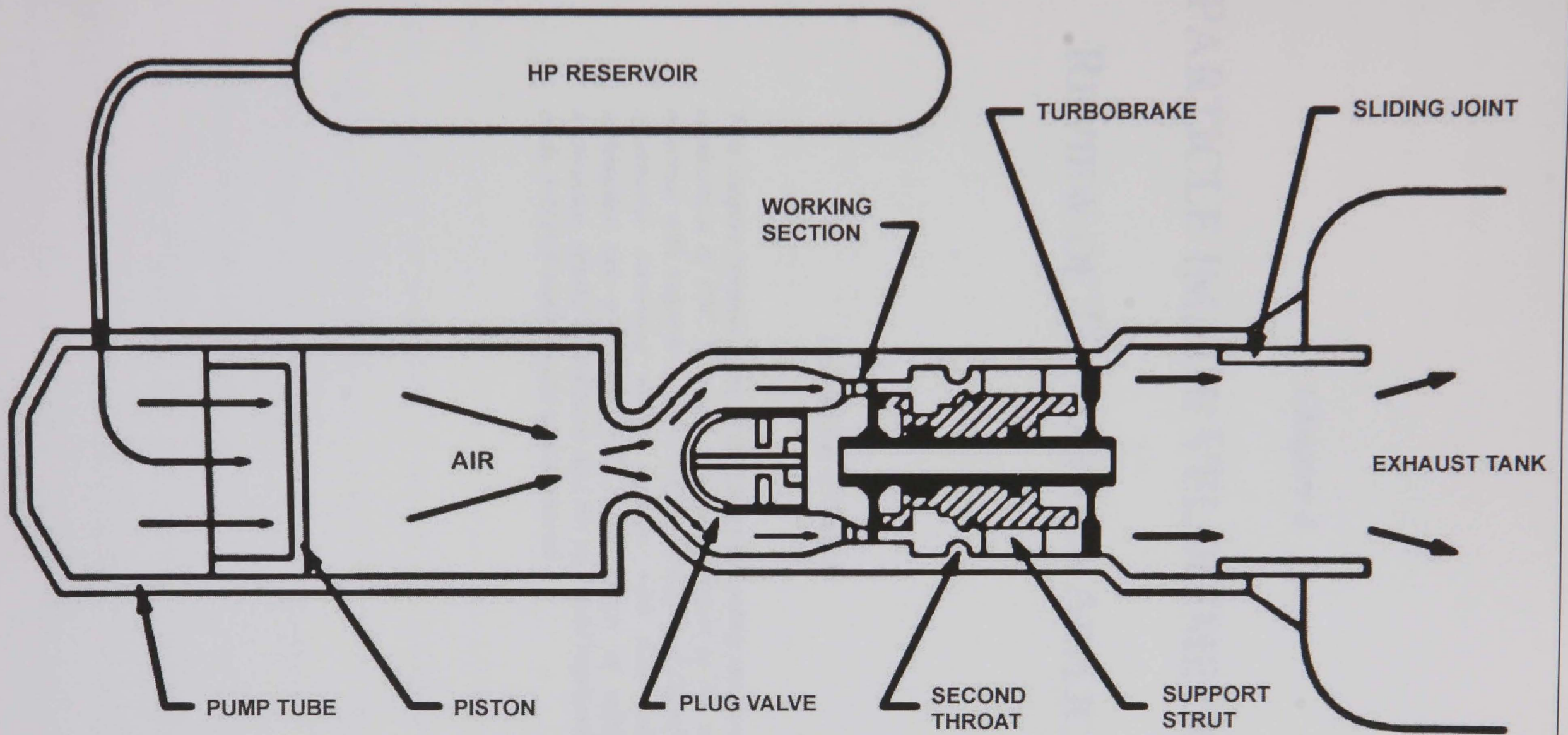


Figure 3.1 The Isentropic Light Piston Facility (ILPF)  
 (Taken from [140])

## *Chapter 4*

# PARTICLE IMAGE VELOCIMETRY (PIV)

—

## REVIEW OF THEORY FOR APPLICATION

### *Description of Chapter*

*This chapter reviews some of the issues regarding the successful application of PIV. It covers the requirements of the seeding material with regards to flow tracing ability and detectability. Alternative recording media together with data reduction techniques are presented with a discussion of achievable accuracies, spatial resolutions and the practical implications of each. 3-D PIV methods are also reviewed.*



## 4.1 INTRODUCTION

The most salient characteristic of PIV is the measurement of two components of velocity within a plane <sup>[77, 79 & 84]</sup>. The fundamental principle of PIV is the determination of the displacement of a flow-tracing particle with respect to time. The measurement is made by projecting a two-dimensional light sheet into the region of interest. Naturally occurring particulates or artificially introduced 'seed' are illuminated as they pass through the light sheet.

If a continuous light source is used, streaks of length proportional to the integration time of the camera and the velocity of the particle will be evident at a camera orthogonal to the plane of the light sheet. If the light source is strobed at a known frequency the velocity of the particle can be calculated from the displacement between the subsequent exposures of the same particle. The latter is the principle that is predominantly used in quantitative PIV and is the crux of most commercial PIV systems.

PIV images can be captured on video, photographic or holographic media, each having its merits and drawbacks. The spatial resolution available is fundamental to PIV. For instance, the accuracy of the analysis can be improved if the distance between particle pairs is described by as many 'pixels' as possible. The estimation of particle image centres can also improved if the image contains a sufficient number of pixels to allow the fitting of a theoretical intensity profile <sup>[118]</sup>. To increase the number of pixels between particle pairs either the magnification or the pulse separation can be increased. The former presents difficulties in the optics as simple geometric aberrations of the lenses are amplified, thus diffracting (enlarging) the particle images. The signal-to-noise ratio also deteriorates. The combination of increased pulse separation and turbulence

increases the probability of single particle images making it difficult to establish particle pairs.

Towers et al <sup>[86]</sup> describe how photography was used to make PIV images at a standoff distance greater than two metres in a large-scale transonic wind tunnel. The film used was 35 mm Kodak TMAX 3200 with a resolution of 100 lines/mm, ASA/ISO rating of 3000 that represented the best speed/resolution compromise at the time, as described in by Bryanston-Cross <sup>[87]</sup>. Processing the data involved digitising the photographs with a flat bed scanner and manually pairing the sparse particle exposures.

Photography is still the best cost/resolution option compared with digital methods of imaging. Digital PIV becomes desirable where the inaccuracies and time lost owing to 'wet' processing and digitising the data is unacceptable <sup>[88]</sup>. A digital camera has advantages in that the image is immediately digitally stored allowing instant viewing and manipulation. The number of images stored is dependent on the communications speed and memory of the system.

Bryanston-Cross et al <sup>[88]</sup> measured an area 0.1m by 0.1m, again in a large scale transonic wind tunnel, using a CCD camera of resolution 512 by 512 by 'tiling' the area of interest, the final measurement being a mosaic of inevitably time-averaged tiles.

Bryanston-Cross et al <sup>[89]</sup> describe the combination of holography and PIV to facilitate the measurement of three-dimensional vectors. Previously holography has been used for whole field measurements <sup>[90,91 & 119]</sup> over two-dimensional compressor and turbine profiles, though the complexity of deconvolving and tomographically reconstructing

refractive index fields, and the need for a clear line of sight, has hampered its application to three-dimensional profiles. Rather than measuring refractive index the holographic plate is used to store the three-dimensional positions of the particles within a 50 mm high, 2 mm wide light sheet, with the illumination supplied by a Ruby laser. This was achieved with a conventional pulsed laser PIV set up, although an additional reference beam was created using a beam splitter to separate less than 1% of the light. Upon re-illuminating the hologram a CCD camera could be focused to the required depth in the virtual image to make two-dimensional images at will. Holographic plates have a resolution approximately two orders of magnitude greater than a 512 by 512 CCD, so the hologram was studied 'tile by tile' as described previously. Furthermore, by rotating the camera about an axis through the virtual image the data could be observed at an angle to the normal of the plate allowing orthogonal measurements.

Apart from allowing the orthogonal measurement, using holography as a three-dimensional, particle image storage media has further advantages. Firstly the optical resolution of holographic plates is considerably higher than that of photographic films. Secondly, optical phase as well as intensity is stored. The phase front is due to the Mie scattering characteristics of the particle<sup>[92]</sup> and not those of the imaging lens.

Gogineni et al., 1998<sup>[120]</sup>, describes the evaluation of a high-resolution (3060 x 2036 pixel) colour CCD camera for turbomachinery applications. An Nd:YAG and Dye laser are used to provide pulses of different colours to allow the first and second particle exposures to be identified. This arrangement was applied to a 20 inch diameter axial fan and allowed the instantaneous measurements to be made at spanwise positions.

Wernet <sup>[121]</sup> describes the application of a novel ‘frames-straddling’ camera to centrifugal and axial compressor fans. The camera allows two frames to be recorded with an interframe gap of the order of a microsecond. Although the camera only contains 1000 x 1000 pixels the vector yield per image pair is high as each frame contains only one exposure. The frames are cross-correlated to remove a directional ambiguity and realise a high spatial resolution owing to the small interrogation region required during the analysis compared to autocorrelation.

## 4.2 OPERATING PRINCIPLE

The displacement of the particle between exposures must be sufficiently small so that  $\delta x/\delta t$  is a good approximation of the velocity  $U$ . This is satisfied if  $\delta x$  can be assumed to be a straight line in a stationary frame of reference. The accuracy of the measurement of the displacement of the particle is partly determined by the finite uncertainty in locating the centre of a particle image or correlation peak. Scaling errors, optical aberrations and fluctuations in the pulse separation are also sources of uncertainty. The error of the centroid estimation relative to the distance between paired exposures determines the accuracy to which the particle displacement can be measured. This directly limits the temporal and spatial resolution of the system as without this constraint  $\delta t$  could be reduced to realize a higher particle response.

Adrain <sup>[78]</sup> suggests two quantities to define the capabilities of a PIV system and its image-recording medium. The quantities are the Dynamic Velocity Ratio (*DVR*) and Dynamic Spatial ratio (*DSR*). The DVR is defined as the ratio of the maximum velocity to the minimum resolvable velocity that is given by

$$DVR = \frac{u_{\max}}{\sigma_u} = \frac{M\Delta x_{\max}}{c_\tau d_\tau} \quad (4.1)$$

where  $M$  is the magnification,  $\Delta x_{\max}$  is the maximum displacement,  $c_\tau$  is a constant that describes the ability to locate a particle's centroid (typically 1 to 10%),  $d_\tau$  is the mean diameter of the particle image. The Dynamic Spatial Ratio ( $DSR$ ) is the ratio of the largest and smallest observable length scales and is given by

$$DSR = \frac{L_x/M}{\Delta x_{\max}} \quad (4.2)$$

where  $L_x$  is one of the dimensions defining the format of the recording media. The product of these ratios, see equation 4.3, gives a benchmark with which to compare various forms of recording media. Typical values of these benchmarks are given in table 4.1 for different forms of recording media and processing techniques.

$$(DSR)(DVR) = \frac{L_x}{c_\tau d_\tau} \quad (4.3)$$

Obviously high values of  $DSR$  and  $DVR$  are preferable for flows with high turbulent intensities. The maximum resolvable displacement is usually considered to be  $\frac{1}{4}$  the interrogation spot area for correlation analysis to avoid aliasing in the correlation plane [77]. The particle displacements are therefore typically between 10 and 20 pixels with interrogation spots covering areas of typically 32 x 32 or 64 x 64 pixels. The maximum displacement for particle tracking is determined by the ability of the analysis algorithms to pair exposures across which largely depends on the seeding concentration.

Recording Media	Autocorrelation			Cross correlation		
	DVR	DSR	DVR×DSR	DVR	DSR	DVR×DSR
768×576	7.27	48	349	80	48	3840
1000×1000	7.27	62.5	454	80	62.5	5000
35mm film, 100 lines/mm	7.27	218.75	1590	80	218.75	17500

Table 4.1 Dynamic velocity and spatial ratios for different forms of recording media. Calculations under autocorrelation assume that resolvable paired exposures can not overlap. Correlation spot size of  $64 \times 64$  pixels, giving a maximum resolvable displacement of 16 pixels. Particle diameter of 2 pixels, centroid can be located to  $1/10^{\text{th}}$  of the diameter.

## 4.3 FLOW TRACING SEED & SCATTERED INTENSITY

### 4.3.1 Requirements of the Seed

The important properties of a scattering seed are its light scattering ability and aerodynamic size. These two properties determine the signal generated by the particle and its ability to follow a flow. If the seed is too small it will not be measurable. If it is too large it may not accurately follow the flow <sup>[78 & 94]</sup>.

An ideal seed would have an identical density to the fluid within which it was suspended and a large effective area to increase its scattering power. All seed in a 'batch' would be identical and easily dispensed in a controlled concentration. It would also be inexpensive. Not all these criteria can be met but adequate compromises have been achieved using liquid droplets (vegetable and mineral oils, water etc.) and powders (titanium dioxide, aluminium oxide etc) ranging from a fraction of micron to a couple of microns in low to moderate speed flows. Gaseous bubbles or solid particles are used in liquid flows, whilst solid particles or liquid droplets are typically used in gases. Styrene spheres are available in sizes ranging from 0.6 to several  $\mu\text{m}$ , albeit at high cost (£500 per litre) <sup>[113]</sup>. The styrene seed is usually suspended in water after manufacture. Bespoke atomizers are required to evaporate the residue water and to avoid agglomeration of the seed when it is launched into the flow. The required monodisperse seed (single particle size with no agglomerates) can be separated by exploiting the principle of the time-of-flight particle sizer discussed in section 2.5.5.

### 4.3.2 Dynamics of Spherical Seed in a Moving Fluid

For the flow tracer to follow the flow accurately the viscous forces carrying it must be greater than its inertial forces resisting a change in direction [95 & 96]. This problem is heightened in unsteady or rotational flows where changes in direction are frequent. The motion of a particle within a fluid of variable velocity is given by equation 4.4 [96]

$$\begin{aligned} \frac{\pi d_p^3}{6} \rho_p \frac{dU_p}{dt} = \frac{1}{2} C_D \rho_f (U_f - U_p)^2 A + \frac{\pi d_p^3}{6} \rho_f \frac{dU_f}{dt} + \frac{1}{2} \frac{\pi d_p^3}{6} \rho_f \left( \frac{dU_f}{dt} - \frac{dU_p}{dt} \right) \\ + \frac{3}{2} d_p^2 \sqrt{\pi \rho_f \mu_f} \int_{t_0}^t \frac{\frac{dU_f}{dt} - \frac{dU_p}{dt}}{\sqrt{t-t'}} dt + F_e \end{aligned} \quad (4.4)$$

Where,  $d_p$  is the diameter of the particle,

$\rho_p$  is the density of the particle,

$U_p$  is the particle velocity,

$\rho_f$  is the density of the fluid,

$U_f$  is the velocity of the fluid,

$A$  is the cross sectional area of the particle,

$\mu_f$  is the fluid viscosity,

$C_D$  is the drag coefficient,

$t$  is time,

$F_e$  is any external potential force.



Each term represents a force that can be described as follows:

Mass  $\times$  acceleration of particle = drag force

- + Mass  $\times$  acceleration of fluid displaced by particle, ie:  
pressure gradient on particle due to fluid's acceleration
- + force to accelerate added mass of particle compared to  
mass of fluid displaced
- + drag force due to turbulent deviations (time history of  
acceleration).
- + body force, i.e.: gravity, centripetal, electrostatic

The first term on the right hand side is expressed in a general manner to accommodate different expressions of the drag coefficient. Towers <sup>[113]</sup> presents a numerical comparison of Stoke's, Melling's, Neilson and Gilchrist's and Meyer's drag coefficients against a normal shock wave and a forced vortex.

Equation 4.4 is valid if,

- The particle size is smaller than the scales of turbulence present in the fluid.
- The particle does not overshoot the motion of the fluid.
- The particles are in dilute suspension ie: no interaction between particles.
- The turbulence is homogeneous and statistically stationary.

Initially equation 4.4 appears rather daunting but fortunately it can be approximated to a much simpler form. Even for the least dense seeding the ratio of fluid density to particle

density is less than 0.001 therefore the terms proportional to the fluid density can be neglected <sup>[95]</sup>. Using the Reynolds number for the particle,

$$R_{ep} = \frac{(U_f - U_p)d_p}{\nu_f} \quad (4.5)$$

and neglecting external forces, equation 4.4 becomes

$$\frac{dU_p}{dt} = \frac{3\nu_f}{4d_p^2} \frac{\rho_f}{\rho_p} R_{ep} C_D (U_f - U_p) \quad (4.6)$$

where  $\nu_f$  is the kinematic viscosity of the fluid and  $U_f - U_p$  is the particle slip. The acceleration of the particle can therefore be maximised by using a smaller, less dense particle.

A particle's response to a change in velocity of the fluid is often described in terms of a flow velocity and a frequency of oscillation. The particle slip is a function of the applied acceleration and a benchmark is required to determine when an unacceptably large error occurs. Feller and Meyers <sup>[97]</sup> describe a first-order model of a particle's response to a step change in acceleration applicable to 1 to 2 micron diameter seed within gases (particle density  $\gg$  gas density). The time constant is defined as

$$t_1 = \frac{d_p^2 \rho_p}{18\mu_f} \quad (4.7)$$

The 3 dB frequency at which the particle would follow a sinusoidal variation in the velocity with an amplitude of 0.707 of the original amplitude is  $f_{3dB} = 1/2\pi t_1$ . This

frequency should be larger the Lagrangian frequency (the motion of the particle is approximately Lagrangian) fluctuation to be measured. In slow flows the primary limitation may be the seeding settling velocity. For air the settling velocity is  $9.8 t_l$  ( $\text{ms}^{-1}$ )<sup>[98]</sup>.

Styrene microspheres are typically used as a seeding material in transonic or supersonic flows. Polystyrene has a relatively low density, is non-toxic and the microspheres can be manufactured in a range of discrete sizes from 0.6 to 2.7 microns. The microspheres also have a high reflectivity thus aiding the imaging process.

### 4.3.3 Light Scattering from Spherical Seed

The diameter of the image of an illuminated seed is dependent on the diameter of the particle and the magnification and point spread function of the system. If the system is diffraction limited the point response will be an Airy function of diameter

$$d_s = 2.44(1 + M)f\lambda \quad (4.8)$$

The image is a convolution of the Airy disk with the geometric image of the seed<sup>[99]</sup>. These functions can be approximated using a Gaussian profile to give an estimation of the image diameter<sup>[100]</sup>,

$$d_e = (M^2 d_p^2 + d_s^2)^{1/2} \quad (4.9)$$

For seed diameters less than 10  $\mu\text{m}$   $d_e$  will be largely independent of the particle diameter. Conversely, for particle diameters greater than 50 microns  $d_e$  will be approximately equal to the product of the magnification and particle diameter.

The scattering efficiency as a function of seed diameter varies erratically about a mean that generally increases with the seed diameter. The mean energy increases with a  $(d_p/\lambda)^4$  in the Rayleigh region,  $d_p \ll \lambda$ , and  $(d_p/\lambda)^2$  where  $d_p \gg \lambda$ . The ratio of the refractive indices of the seed and fluid greatly affect the scattering efficiency. The refractive index of water is 1.33 times that of air. Equivalent seed are typically 10 times more effective at scattering in air than in water. Fortunately, water flows are usually slow and large seeding can be used to compensate.

The optical density recorded on a photographic film or the electrical output of a photo-detector is proportional to the optical exposure defined as energy per unit area. The mean exposure over a particle image is defined as <sup>[100]</sup>

$$\bar{\varepsilon} \propto \frac{\lambda^2 W d_p^n D_a^2}{\lambda^n d_o^2 \left( M^2 d_p^2 + \frac{2.44^2 d_i^2 \lambda^2}{D_a^2} \right) \Delta y_o \Delta z_o} \quad (4.10)$$

where  $W$  is the energy of the pulse,  $D_a$  is the lens aperture,  $n$  the scattering power law exponent,  $d_o$  and  $d_i$  the object and image distances respectively and  $\Delta y_o \Delta z_o$  is the cross sectional area of the light sheet assumed to be of uniform intensity.

For seed in the range of 1 to 10  $\mu\text{m}$   $n$  is of the order three and diffraction blurring, rather than the geometric image of the seed, dominates the seed image. The denominator therefore reduces to give

$$\frac{-}{\varepsilon} \propto \frac{Wd_p^3 D_a^4}{\lambda^3 d_o^2 d_i^2 \Delta y_o \Delta z_o} \quad (4.11)$$

This relation implies that if the system is increased in size, ie  $d_o$ ,  $d_i$  and  $\Delta y_o$  are scaled up by a factor  $m$  the intensity of the image decreases by a factor of  $m^{-5}$ . There are also  $\lambda^{-3}$  and  $d_p^3$  dependence. Shorter wavelengths and larger seed are therefore preferable.

As the seed increase in size beyond 5 to 10  $\mu\text{m}$   $n$  is of the order 2 and the geometric image, rather than the diffraction image becomes dominant and equation 4.10 reduces to

$$\frac{-}{\varepsilon} \propto \frac{WD_a^2}{d_o^2 M^2 \Delta y_o \Delta z_o} \quad (4.12)$$

This relation implies that the image intensity becomes independent of seed diameter (above approximately 100  $\mu\text{m}$ ) as both the scattered light intensity and the image area increase by  $d_p^2$ .

## 4.4 ANALYSIS TECHNIQUES

### 4.4.1 Correlation Techniques

The method of analysis depends on the seeding number density. If the seeding density is high a fringe analysis method can be adopted. This technique was developed to overcome the requirement for large amounts of computer processing power to evaluate the flow data. By interrogating a small spot with a coherent light source each particle image acts like an individual light source, allowing interference to occur between the pairings<sup>[77]</sup>. If the spot is small the displacement of the particle images will be equal so that the probability of the mean displacement is high and the probability of the random displacement is low. Therefore interference from the random displacements is small in comparison to interference from the mean displacements. In other words the random image pairings produce interference that averages to zero whilst the pairings associated with the displacement produce interference fringes with spacing inversely proportional and perpendicular to the displacement of the pairs. In effect this procedure is a spatial correlation at the speed of light.

The same result can be achieved computationally using the Fourier Domain approach<sup>[100]</sup>. The mean frequency of the particle images corresponds to the mean displacement within a spot and will show as a peak in the Fourier domain significantly larger than the random frequencies. If the seeding density is low the Fourier process can be applied to a larger area to acquire sufficient data although such a process simply averages over a larger area. By considering a larger area small scale features such as shocks and wakes can be averaged out.

#### 4.4.2 Particle Pairing

The use of the fringe analysis method, described earlier, requires the use of either photographic or holographic recording to allow the interrogation of the negative by laser to produce interference fringes. In practice producing a high enough seeding density for fringe analysis to be successful can be difficult in high-speed turbulent flows. It is usually the case that in high-speed applications the seeding number density is low, allowing the brute-force approach of considering each individual particle image to be applied, a process which is computationally intensive.

To get the images in a digital format either a CCD camera can be used or a photograph can be scanned. The major difference between these two types of media is the number of picture elements available. CCD cameras generally have around 1000 x 1000 picture elements. A scanned photograph, recorded with 35 mm film, can have over an order of magnitude more picture elements. Once in the digital form the images can be analysed using either statistical methods to establish the probability distribution of the displacements, or a spatial correlation between the first and second images can be applied. Once the image pairs have been established the image processing software calculates the distance between successive particle images, a time consuming process that has only become practical as powerful computers have become available. If the seeding density is low, image pairs will be separated by large voids making the pairing process trivial.

Warwick's analysis software, APWin<sup>[109]</sup>, is designed for sparsely seeded flows in that it considers each particle and its neighbours individually to establish particle pairs. A statistical mean over a predetermined area is used in further iterations to delete

erroneous pairings. A yield of 300 particle pairs over an image of 768 by 576 pixels was found to be the upper limit of the software.

#### 4.4.3 Directional Ambiguity

There remains a directional ambiguity in velocity if the order of the first and second exposures of a particle on a single image is not known. This may not be a problem in flows with high mean velocity, as intuition can suggest the correct sign convention, but it is for recirculating or turbulent flows. The exposures can be distinguished either by using different pulse colours or intensities, to code the pulse sequence <sup>[120 & 122]</sup>, or by using fluorescent seed that leaves a decay streak after excitation. Each can prove problematic during analysis as the commonly used autocorrelation analysis is conjugate symmetric regardless of pulse configuration, giving two peaks at equal displacements from the dc term. Further analysis is required to identify the correct correlation peak, unless the first and second exposures are separated and cross-correlated to give a single correlation peak.

Image shifting allows the addition of a positive bias to the velocity in a similar manner to the Bragg cell of an LDA system. The image can be shifted by placing a rotating mirror between the plane of the light sheet and camera, polarization optics between the imaging lens and image plane or by shifting the pixels on a CCD array between exposures. In each case the second pulse is shifted by a known displacement relative to the first. The bias is subtracted after the analysis to reveal the underlying velocity field.

An alternative to image shifting is to record the 1<sup>st</sup> and 2<sup>nd</sup> exposures on separate frames to reveal their order. Cross-correlating between the two frames will give an



unambiguous velocity direction. Unlike the autocorrelation the cross correlation is not conjugate symmetric and there will be only one valid peak displaced from the dc term. Recording the 1<sup>st</sup> and 2<sup>nd</sup> exposures has further benefits, in that a higher seeding density can be used to improve the spatial resolution. As successive exposures can be closer without obscuration and no image shifting is required, the dynamic velocity range of the recording medium is extended in comparison to a double exposure image. The particles can be paired more efficiently as 1<sup>st</sup> exposures of two different particles cannot be paired.

The adoption of interrogation spot shifting during cross-correlation analysis allows a higher spatial resolution to be achieved in comparison to an autocorrelation without compromising the accuracy of the measurement <sup>[123]</sup>. If the full-scale particle displacement in a 1024 x 1024 image is 16 pixels the correlation interrogation spot size needs to be 64 x 64 pixels according to Adrian's 1/4 rule <sup>[77]</sup>. If each of the interrogation spots has a 50% overlap the vector yield will be a grid 32 x 32 vectors. If the interrogation spot is shifted by the mean displacement it will contain more pairs and the visibility of the correlation peak will improve. The correlation peak will now be nearer the centre of the correlation plane so the interrogation spot size is reduced to avoid aliasing. The shifting of the interrogation spot reduces the amount of spatial averaging and increase the number of vectors in the example described to 64 x 64 without compromising accuracy.

The major drawback of recording the exposures on separate frames is that long pulse separations are required to allow for the inter-frame periods of conventional CCD cameras. For example RS-170 cameras have an inter-frame time of 33 ms that is

impractical for most flow regimes. Inter-frame periods of fractions of a millisecond, or indeed microseconds in turbomachinery applications, are usually needed.

Various commercial systems use a bespoke fast image transfer cameras that allow the image to be discharged from the CCD array in a few microseconds. By adopting a frame-straddling strategy whereby the 1<sup>st</sup> exposure occurs at the end of the 1<sup>st</sup> frame, the 2<sup>nd</sup> exposure at the beginning of the 2<sup>nd</sup> frame, the dynamic velocity range can be extended into the transonic region<sup>[80]</sup>.

#### 4.4.4 Centroid Estimation

Particle images made of large pixel clusters can be beneficial in particle tracking applications where a large dynamic velocity range is not required. Large clusters of pixels allow the centroids to be estimated with sub-pixel accuracy from the grey scale of the pixels. Smaller clusters are required for correlation analysis as the self correlation peak will be twice as broad, further reducing the dynamic velocity range.

Having established particle pairs or correlation peaks the accuracy of the displacement measurement depends on the certainty to which their centres can be located. The accuracy to which this can be achieved depends on the resolution of the system and the range that is being considered. For example, if the particle image or correlation peak centroids can be located to half a pixel over a displacement of 16 pixels the probable accuracy to which the displacement can be measured is  $\pm 3\%$ . If the particle centres can be located with greater accuracy for a given resolution the error will be reduced.

The centre of the particle can be estimated in one of four ways, see figure 4.1. Firstly, the pixel of highest intensity can be considered to be the particle centre. Assuming a noise and distortion free image the centre can only be located to within a pixel in each of the x and y directions. The error can therefore be up to 1.41 pixels. Secondly, the image can be enclosed by a bounding box, where the diagonals of the box are assumed to intersect at the centroid <sup>[109]</sup>. Edge detection techniques are required to find the image periphery, a process that requires a careful choice of threshold for noisy images. A symmetrical image is also assumed. The particle centre can be located to an estimated half a pixel in each of the x and y directions giving a total possible error of 0.705 pixels. Thirdly the center-of-mass of the intensity distribution can be calculated using equation 4.13,

$$(x_0, y_0) = \left[ \frac{\sum_i \sum_j (x_i, y_j) E(x_i, y_j)}{\sum_i \sum_j E(x_i, y_j)} \right] \quad (4.13)$$

where

$E(x, y)$  is the intensity distribution of the image.

$(x_0, y_0)$  is the centroid.

As with the bounding box a careful choice of threshold is required to distinguish the particle from the noise, typically locating the particle centre to within approximately a fifth of a pixel. Fourthly, if the theoretical intensity profile of a particle is known and the number of sampling points, i.e. pixels, is sufficient, the best fit theoretical profile can be assigned to the particle image, to give its true centre of mass. Owing to the limited resolution of the optical system the image of the particle appears as an Airy Disk Pattern. For micron sized particles this intensity profile can be closely approximated

using a Gaussian profile <sup>[99 & 118]</sup>. For a two-dimensional particle image the intensity is approximated using

$$E(x,y) = A \exp\left\{-\left[\frac{(x-x_0)^2 + (y-y_0)^2}{2\sigma^2}\right]\right\} + n(x,y) \quad (4.14)$$

where

$A$  is the amplitude of the Gaussian profile,

$\sigma$  is the variance of the Gaussian profile,

$(x_0, y_0)$  is the centre of the Gaussian profile,

$n(x,y)$  is the additive noise.

Udrea et al., 1996 <sup>[118]</sup> claims that the Gaussian fit approach can be used to locate particle centroids to  $1/10^{\text{th}}$  of a pixel when applied to particle tracking. In order to achieve this the pixel clusters would need to be at least 4 to 5 pixels in diameter. Particles need only be sampled by 2 picture elements to satisfy the Nyquist's criterion and to distinguish them from pixel noise. Over sampling wastes the capacity of the recording medium and reduces the available Dynamic Velocity Range. It is expected that  $1/10^{\text{th}}$  of a pixel could only be achieved in the absence of optical aberrations and where the particle images are clearly visible. However, incomplete particle images, such as those produced from interlacing faults or saturation, can be corrected and it is expected that peak locking (bias towards integer pixel values) would be less significant in comparison to the techniques described earlier.

Variations in the diameter of particle images and velocity within an interrogation spot broaden the correlation peaks. Particle images of 1 to 2 pixels in diameter produce

correlation peaks of 2 to 3 pixels in diameter. As the correlation peak is broader than the pixel image, an estimator that approximates the correlation peak shape can more readily be applied without over sampling, as described by Westerweel <sup>[123]</sup>.

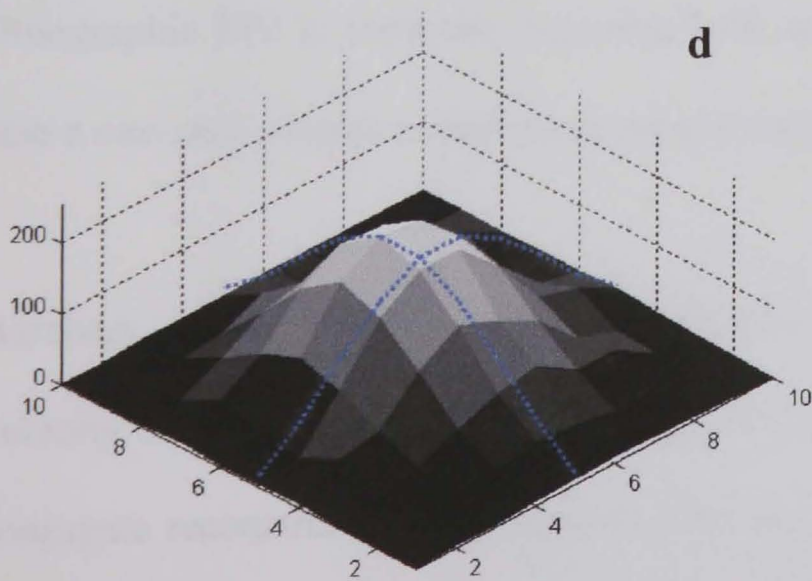
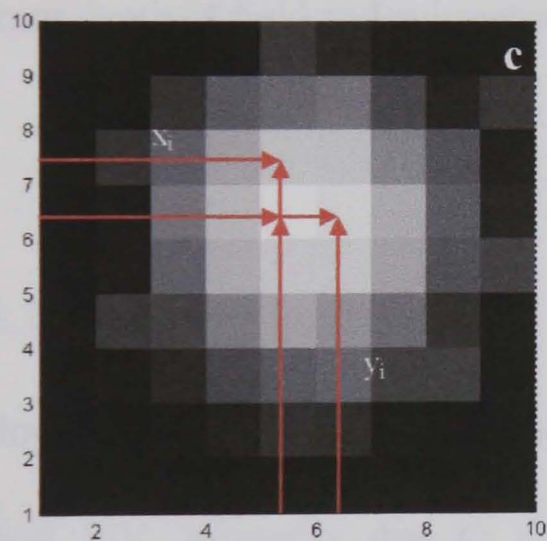
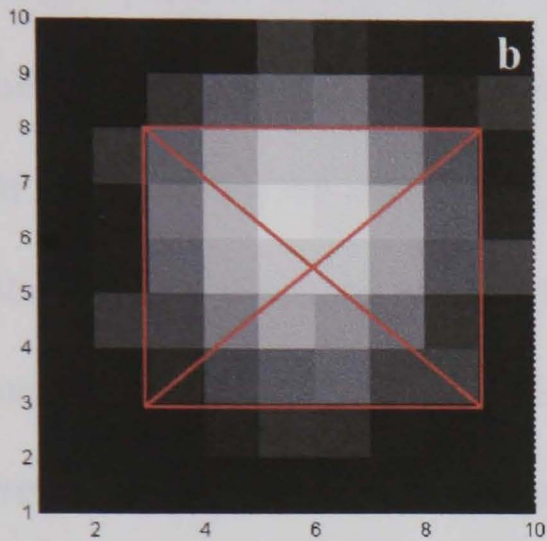
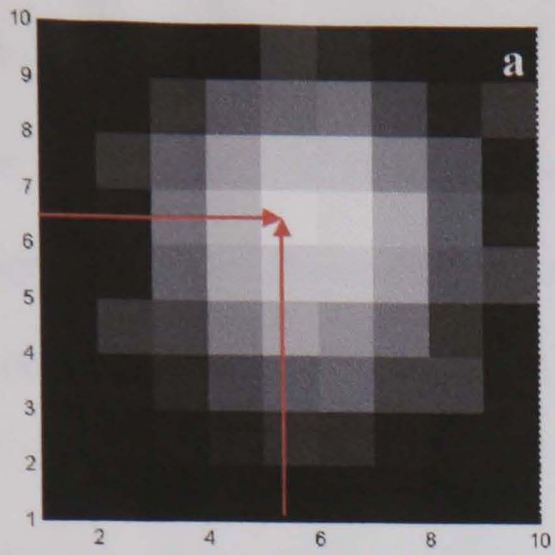


Figure 4.1 Particle centroid estimation

- Using the pixels of greatest intensity
- Diagonals of a bounding box that are assumed to intersect at the particle's centroid. Grey level threshold needed to determine perimeter of particle image.
- Centre of mass approximation where the centroid is determined from the sum of the products of the pixel intensities and their distance from a datum. Again a grey level threshold is required.
- Gaussian fit to the image's pixel intensity profile.

## 4.5 3-D PIV

The development of three-dimensional PIV systems would appear to be a logical progression from planar PIV. Three-dimensional measurements also allow the in-plane velocities to be corrected where they are contaminated by an out-of-plane component.

A large aperture is required if one seeks to image small seed with a high spatial resolution. This prerequisite defines a narrow depth of field. Ideally the thickness of the light sheet would be kept approximately equal to the depth of field to avoid this contamination but cannot always be achieved (eg:  $f^{\#}=8$ ,  $\lambda=0.6993$  gives a depth of focus of only 0.7 mm). Measuring all three components of velocity allows this error to be corrected. The thicker light sheets required for volumetric recording necessitate a greater depth of field and subsequently produce larger image diameters <sup>[100]</sup>.

### 4.5.1 Holographic PIV

Holographic PIV allows substantially more information to be gathered per image than digital PIV, primarily due to the data being stored in a volumetric domain <sup>[81]</sup>. Holographic PIV is complex, requiring both an imaging and reconstruction stage. It is also a *one-shot* process as wet processing is required.

Barnhart et al., 1998 <sup>[81]</sup> employed reflection holography to make three-dimensional velocity measurements within an IC engine with extensive optical access. A phase conjugate reconstruction was used to eliminate the gross image distortions created by transparent cylinder block. The hologram was interrogated using an optical correlation to determine the velocity vectors.

Owing to these complexities holographic PIV remains a highly specialized measurement technique whose application is difficult to generalize in the presence of generic digital 3-D PIV systems that would potentially allow the acquisition of many frames of data, and automated analysis, that would allow a statistic analysis of the cycle-by-cycle variability in an IC engine.

#### 4.5.2 Stereoscopic PIV

The fundamental principle of stereoscopic PIV is that two cameras are used to image the illuminated plane at different angles. The two projections of the particle displacement allow it to be characterized in three dimensions. Stereoscopic PIV initially appears to be straightforward, but successful applications can require optimum camera configuration, evaluation and correction of the perspective distortion and a camera calibration procedure depending on the camera orientation used. The 3-D vectors are calculated from the triangulation of the two projections. There are two basic stereoscopic techniques, the translation and angular displacement methods, that differ in the alignment of their optical set-up. A concise description of both of these arrangements is given by Van Oord, 1997 <sup>[82]</sup>.



## Translation Method

The translation method uses two cameras with parallel axes orthogonal to the plane of the light sheet<sup>[82 & 83]</sup>, see figure 4.2. As the camera array is parallel to the object plane the magnification is constant across the field-of-view.

The overlap between the two angular fields, called the joint field, is largely determined by the offset between the cameras. Increasing the offset reduces the joint field but improves the accuracy the out-of-plane measurement. These two parameters are in direct conflict, but the relation can be relaxed by introducing an additional lateral offset to the camera array relative to the lens to improve the sensitivity to  $z$ . The offset is made as big as possible within the resolution and distortion limits of the lens.

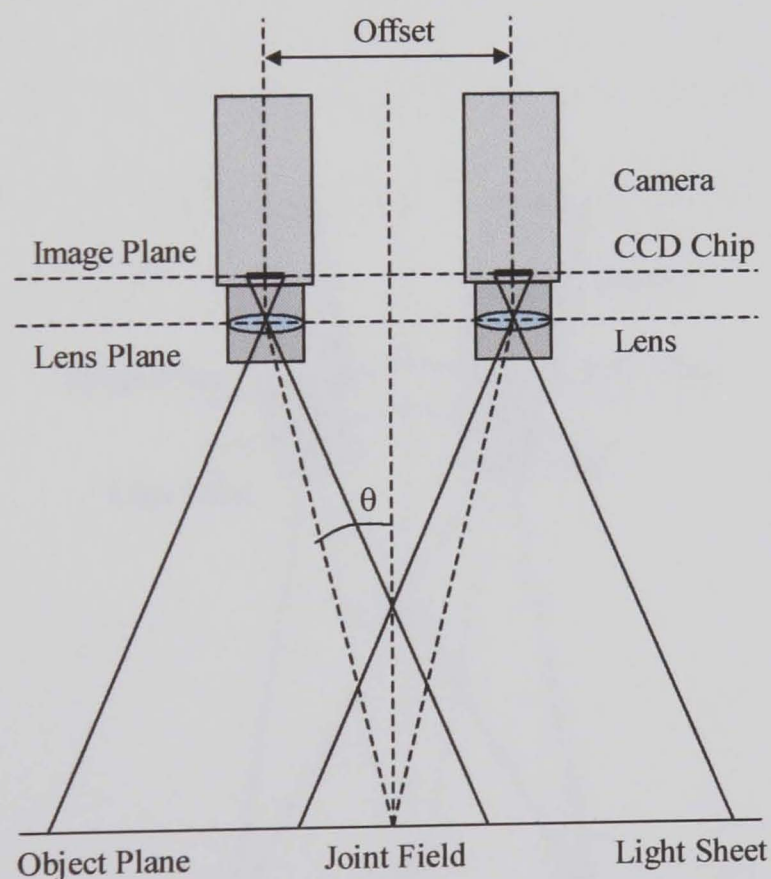


Figure 4.2 Stereoscopic PIV arrangement – Translation

### Angular Displacement Method

An alternative to the translation method is the angular displacement method. It is more complicated to align than the translation method and an extensive calibration error is required to remove a perspective error. However, it does not suffer from the compromise between the size of the joint field and the sensitivity to the out-of-plane component of displacement<sup>[82 & 85]</sup>.

The angular displacement arrangement consists of two cameras with optical axis that converge onto a single point in the object plane, see figure 4.3. As the cameras are no longer parallel to the object plane the magnification will not be uniform across the image but much larger viewing angles can be realized. This allows the sensitivity to the out-of-plane component to be increased without greatly compromising the size of the joint field.

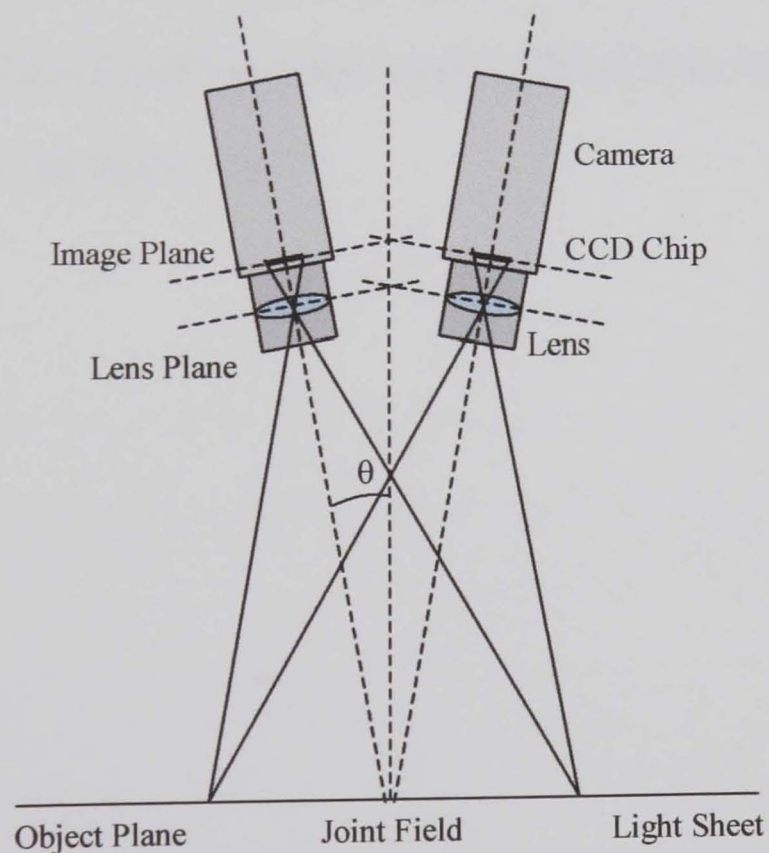


Figure 4.3. Stereoscopic PIV Arrangement – Angular Displacement

Only a small area of the field-of-view will be in focus as the camera array is no longer parallel to the object plane. The size of the area in focus can be improved by increasing the depth of field. The focal depth is described by the parameter  $\delta z$  where

$$\delta z = 4(1 + M^{-1})^2 f\#^2 \lambda \quad (4.15)$$

and  $M$  is the magnification,  $\lambda$  is the wavelength of the illuminating light, and  $f\#$  is focal distance of the lens divided by the diameter of the aperture <sup>[100]</sup>. Outside this range the seed image by an amount exceeding 20% of the in focus diameter. From this relation the focal depth can be increased, within limits, by reducing the size of the camera aperture, but this inevitably reduces the amount of light incident on the camera array. This is far from desirable in limited light applications. Van Oord <sup>[82]</sup> found that rotating the image plane with respect to the lens plane, satisfying the Scheimpflug condition, allowed him to achieve an equivalent sharp image at  $f\#4$  to that of a parallel image and lens plane combination, see figure 4.4.



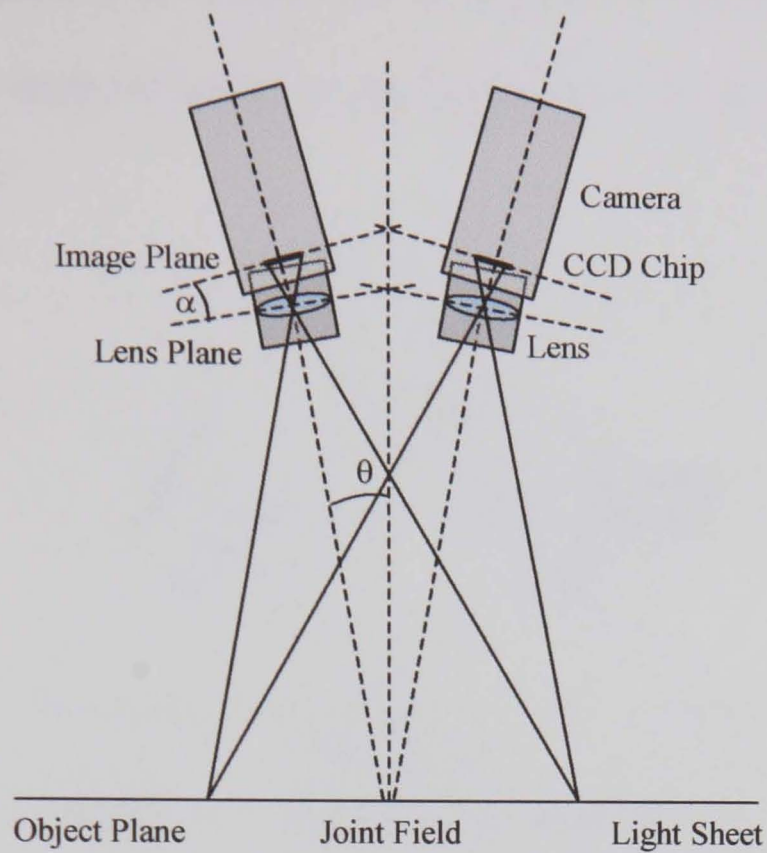


Figure 4.4. Stereoscopic PIV arrangement – angular displacement method that satisfies the Scheimpflug condition.

Rotating the image plane relative to the lens improves the focus of the image but introduces a non-uniform magnification across the image. The nominal magnification is defined as

$$M_n = \frac{d_i}{d_o} \quad (4.16)$$

where  $d_i$  and  $d_o$  are the image and object distances respectively. In order to achieve a complete focus the Scheimpflug conditions needs to be satisfied, i.e.

$$M_n = \frac{\tan \alpha}{\tan \theta} \quad (4.17)$$

where  $\alpha$  is the rotation of the image plane with respect to the lens plane and  $\theta$  is the viewing angle, the angle subtended by the nominal ray and the normal to the object plane, see figure 4.5.

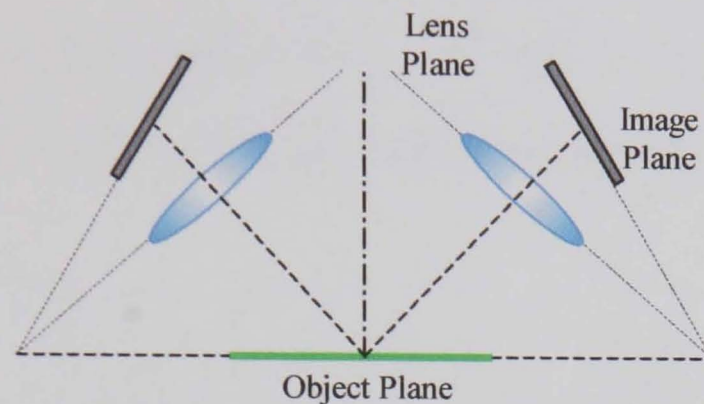


Figure 4.5. Scheimpflug Configuration

The stereoscopic procedure as outlined by Van Oord consisted of analysing the two 2-D velocity fields in the same way as conventional 2-D PIV. The 2-D vectors were back projected onto the object plane either by using a mathematical warping procedure or by a geometrical optics reconstruction to compensate for the non-uniform magnification. The corrected 2-D vectors were interpolated to common grid points and combined to give the 3-D vectors.

The 3-D vector is calculated from the triangulation of two 2-D vectors. Each of those 2-D vectors will have a percentage error associated with it due to the uncertainty in locating the particle centres. The error will be smaller than in conventional 2-D PIV as the two vectors take into account the particle's component of displacement normal to the plane of the light sheet. However, the measurement of the out-of-plane component is a function of, in effect, two in-plane measurements so the error will inevitably be compounded.

If the out-of-plane component of velocity is small in comparison to the in-plane, it may not be significantly larger than this error. If there is a strong out-of-plane component of velocity the particle may not be present in the light sheet for both exposures. This can largely be remedied by either misaligning the light sheet with the mean flow direction or by increasing the thickness of the light sheet at the expense of the power density of the light sheet.

### 4.5.3 Defocusing Mask PIV

Gharib et al (1998) <sup>[124]</sup> presents a novel method of locating a seed in three dimensions using defocusing masks. A defocusing mask containing three apertures at an equal pitch circle diameter is placed before the camera lens to obtain three images for each scattering centre. The out-of-plane component is determined by the image separation caused by the off axis apertures, the separation increasing as the scattering centre moves away from the object plane. The image separation,  $b$ , is given by <sup>[124]</sup>

$$b = \frac{f d d_o}{d_o - f} \left( \frac{1}{d_o - z} - \frac{1}{d_o} \right) \quad (4.18)$$

where  $f$  is the focal length of the lens and the other dimensions are given in figure 4.6. Gharib's system uses separate CCDs behind each aperture to overcome the overcrowding that would occur over a single CCD. The system was applied to a 5 x 5 x 5 cm<sup>3</sup> measurement volume in a two-phase bubbly flow.



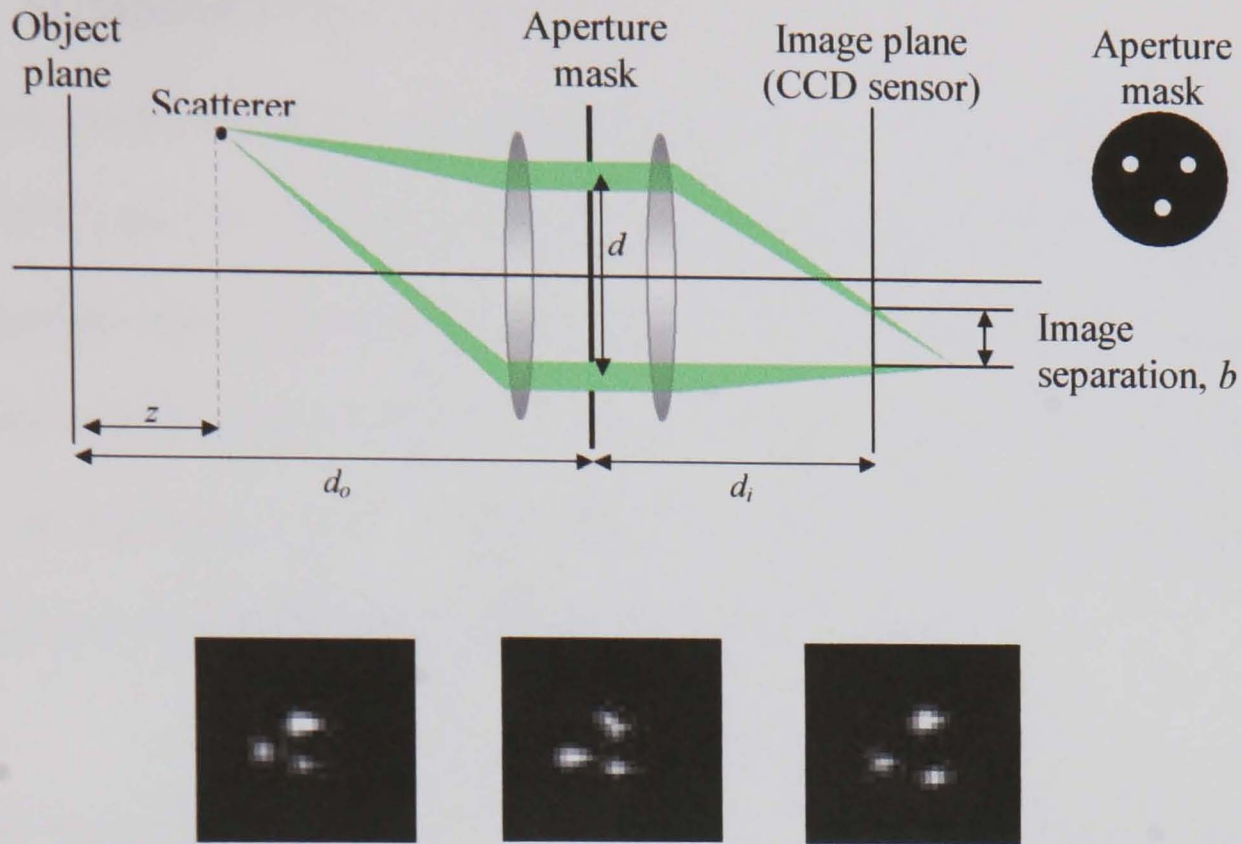


Figure 4.6 The use of a defocusing mask to determine the out-of-plane position of a scatterer. Three defocused images produced using 5mm apertures at a 10 mm PCD. 12 mm displacement in the out-of-plane direction between exposures

The sensitivity of defocusing mask PIV to out-of-plane displacements is low compared to typical light sheet thickness of the order of 1mm. As a consequence a wide light sheet is required at the cost of the power density through its cross section. The technique would appear to be more applicable to water flows where large (bright) seeding can be used or where low speed wind tunnels are seeded with neutrally buoyant bubbles.

## 4.6 SUMMARY OF CHAPTER

PIV data can be recorded by holographic, photographic or digital means. Photographic films still offer the best resolution per unit cost, although CCD cameras of near photographic resolution have been demonstrated in turbomachinery applications. Cross-correlation CCD cameras allow two images to be recorded with an inter-frame gap of only 1  $\mu$ s. The images can be cross-correlated to remove the directional ambiguity in the data and achieve a higher vector yield per image pair.

Styrene microspheres, of less than 1  $\mu$ m in diameter, have been identified as a suitable seed for transonic flows (flow temperature below 100°C approx.). The scattering efficiency of such seed has a  $(d_p/\lambda)^3$  dependence so shorter wavelengths of illuminating light are favoured. The image of the seed will be due to diffraction blurring rather than a geometric image. The approximate diameter of the diffraction-limited particle is expected to be 18  $\mu$ m for a magnification of 0.25 and an  $f$ -number of 11. If the optical arrangement,  $d_o$ ,  $d_i$  and  $\Delta y$  are scaled up by a factor  $m$ , the mean exposure of the particle decreases by a factor of  $m^{-5}$ . Short standoff distances are therefore required to improve the brightness of the particle images.

The PIV data can be processed either by correlation or particle tracking. The former correlates over an interrogation spot to give the strongest local velocity. The minimum spot size is typically 4 times the largest displacement between exposures although larger areas need to be considered where the seeding is sparse. Correlation analysis is therefore suitable for high seeding concentrations. Particle tracking can be used in sparsely seeded flows to establish up to approximately 300 vectors over a  $576 \times 768$  pixel image.



The centroids of particle images can be located with sub-pixel accuracy if the image contains a large cluster of pixels (4 to 5 pixels in diameter). The centroid can be estimated either from the grey scale of the cluster or by fitting a Gaussian profile to the intensity profile of the cluster. Large clusters are suitable for pairing but not for correlation as the correlation peak will be twice as broad. Clusters of 1 to 2 pixels are used for correlation analysis to give a 3 to 4 pixel diameter correlation peak to which the centroid, again, can be located with sub-pixel accuracy.

The in-plane displacement can be contaminated by an out-of-plane component where large depths of field and thick light sheets are used. The out-of-plane component can be measured by using either holographic recording, triangulation of stereo cameras, or by measuring defocusing effects viewed through an aperture mask. Holographic recording is a one-shot technique whilst stereo cameras require wide optical access. The defocusing approach only requires a single camera but is less sensitive to the out-of-plane than in plane, so is used in a volumetric rather than planar configuration.

## Chapter 5

# THE APPLICATION OF PIV TO A SPINNING TURBINE CASCADE

-

## SYSTEM DEFINITION & TESTING

### *Description of Chapter*

*This chapter describes the evaluation of the available hardware and analysis algorithms as a precursor to the test on the ILPF. A novel 3-D PIV technique that determines the out-of-plane displacement from defocusing effects through a single camera has also been investigated.*

*Two camera systems were tried. The first used an interlaced  $768 \times 576$  camera that acted as a timing master for the whole PIV system. The second used a  $1000 \times 1000$ , triggerable 'frame straddling' camera, identical to that used by Wernet<sup>[121]</sup>. Unfortunately the latter failed and could not be replaced in time for tests on the ILPF. The results shown here were therefore gathered with the first camera system.*

*A  $30 \text{ ms}^{-1}$  nozzle flow (circular exit of area  $120 \text{ mm}^2$ ) has been used as a subject for both the 2-D and 3-D tests. A good agreement has been achieved with equivalent velocity measurements of the nozzle, supplied by a third party, made using a 2-D LDA system.*

*3-D measurements have been made of the nozzle flow after an initial calibration exercise. The out-of-plane resolution was shown to be  $\pm 20 \mu\text{m}$  at a standoff distance of  $140 \text{ mm}$ . The measurements were successful, but issues regarding the correction of the gross distortions of the test section window of the ILPF could not be resolved in time for the test. Recommendations are made regarding its successful application.*

## 5.1 INTRODUCTION

## 5.2 THE PIV SYSTEMS

The same Q-switched frequency doubled Nd:YAG laser and laser firing system previously used on the ILPF by Bryanston-Cross formed the basis of the PIV system used here <sup>[139]</sup>. The laser firing system controls the programming of the laser firing, sequence, one-shot etc. and the appropriate voltage conversion required to interface the laser. The laser itself can provide two 50 mJ, 532 nm, pulses at 25 Hz but only for limited periods otherwise the laser over heats. The laser can be operated on open-lase mode to allow the beam to be aligned in a relatively low power condition.

### 5.2.1 Interlaced Camera System

The interlaced camera system consisted of two 768 by 576 pixel, 8 bit monochrome cameras that could be used in a stereo configuration if the clock signals of the two cameras were connected together. The laser needed to be pulsed whilst both the odd and even fields of the cameras were integrating to avoid an interlaced image (operating in frame mode). The cameras could be triggered but there remained varying period of several milliseconds before the next full frame could be recorded. The cameras were therefore used as a timing master for the PIV system with the vertical sync. signal used as a trigger for the laser firing system. A triggered sequence consists of waiting until the next full frame is available after the trigger signal, a period of up to 30 milliseconds. The inter-frame time was approximately 30 milliseconds, so only very slow flows can be cross-correlated.

### 5.2.2 Cross correlation Camera System

The second camera system consisted of a commercially available 1000 by 1000 Kodak es:1 camera modified to operating in the 'frame straddle' configuration <sup>[85]</sup>. This configuration allows two frames to be captured in quick succession separated only by a few microseconds to allow the charge on the CCD chip to be discharged, a period called the transfer time. The first and second frames take 255 microseconds and 33 milliseconds respectively. This cycle is triggerable and can be repeated at up to 15 Hz.

The transfer time is a function of the amount of charge on the CCD chip. If the image is brightly illuminated and saturated the transfer time can be in excess of 10 microseconds. However, it was found that if the mean background grey level is low and the image is sparsely seeded the transfer time can be reduced to approximately a microseconds.

To synchronise the camera and laser accurately, the camera feedback was used as a trigger for the laser firing system. This feedback signal was used in preference to the camera trigger as the 'camera ready' period flutters slightly owing to thermal effects making it difficult to fire both just before and just after the transfer time. The firing sequence was initiated by sending a trigger to the camera.

## 5.3 2-D MEASUREMENTS OF A FREE AIR JET

### 5.3.1 Experimental Method

A commercially available, variable velocity, low turbulence free air jet from a nozzle unit designed for the calibration of anemometry systems was used to evaluate the PIV system. The pressure within the nozzle was measured using a water manometer connected to a pressure tapping on the nozzle body. Half micron styrene particles suspended in water were injected into the flow using a six jet atomiser. The seeding was injected into the nozzle body prior to a flow straightening honeycomb so that higher seeding pressures could be used to increase the seeding density without altering the characteristics of the flow. The nozzle was mounted to the optical table, see figure 5.1, via a series of translation stages that allowed the nozzle to be rotated and translated relative to the camera and light sheet.

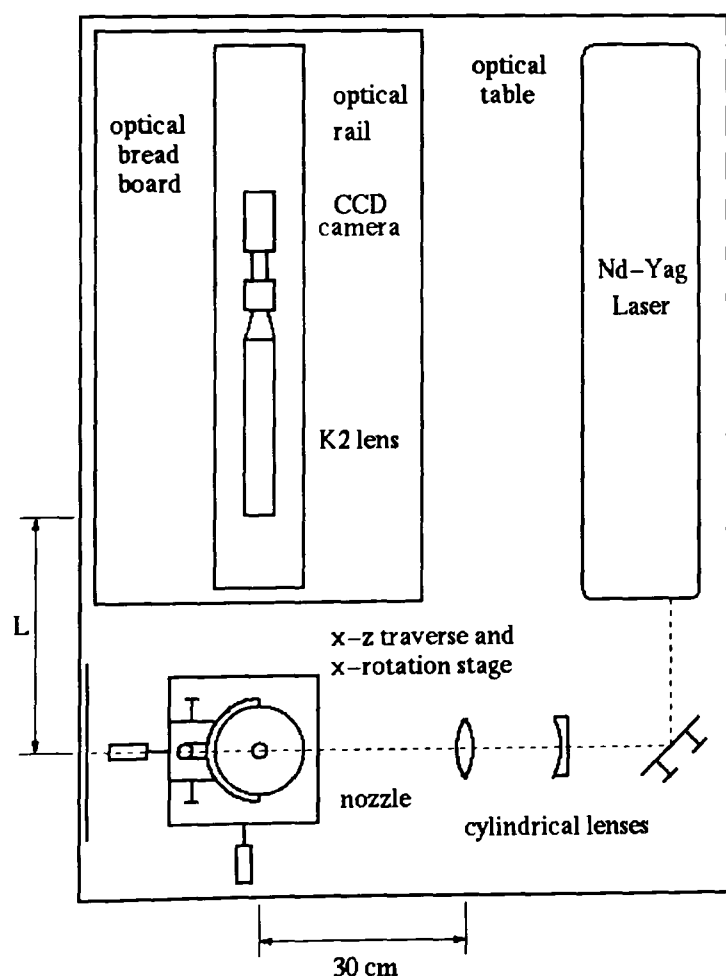


Figure 5.1. The optical arrangement.

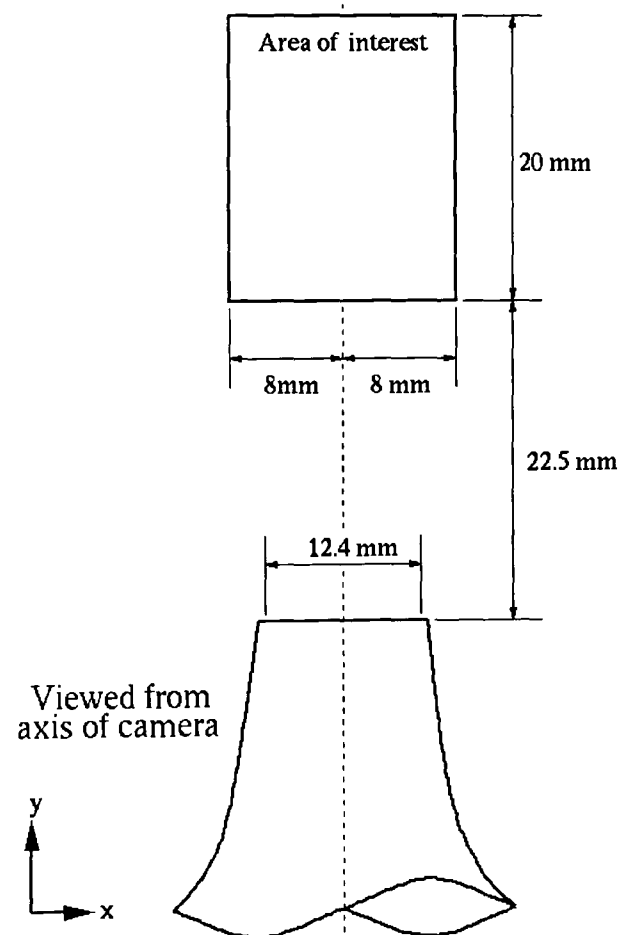


Figure 5.2. Field-of-view, 1400 mm from the nozzle.

The laser head was mounted on the optical table and the beam aligned with the nozzle using a series of dielectric mirrors. The beam was expanded into a sheet using a negative cylindrical lens and subsequently focused in the centre of the nozzle using a positive cylindrical lens. The light sheet was no more than an estimated 500  $\mu\text{m}$  thick throughout the region of interest. The laser was synchronised to the video frame signal to avoid interlaced images. The images were recorded using a single Pulnix CCD camera with a resolution of  $768 \times 576$ , looking through a K2 diffraction-limited lens [101]. The viewed area was calibrated by placing a graticule of indexed 1 mm by 1 mm squares in the region of interest.

Two sequences of data were recorded at a standoff distance of 1400 mm over a  $16 \times 20$  mm field-of-view. The pulse separation was 10  $\mu\text{s}$ . The first sequence of data yielded approximately 100 vectors per image using particle pairing. The seeding concentration was increased until the upper limit of the pairing algorithm was reached, approximately 400 vectors per image. As the light sheet did not intersect any mechanical surfaces there is very little noise in the images and the light intensity was adjusted so that the particle images intensities extended over the entire greyscale range of the camera (8 bit, 256 grey levels).



### 5.3.2 Results

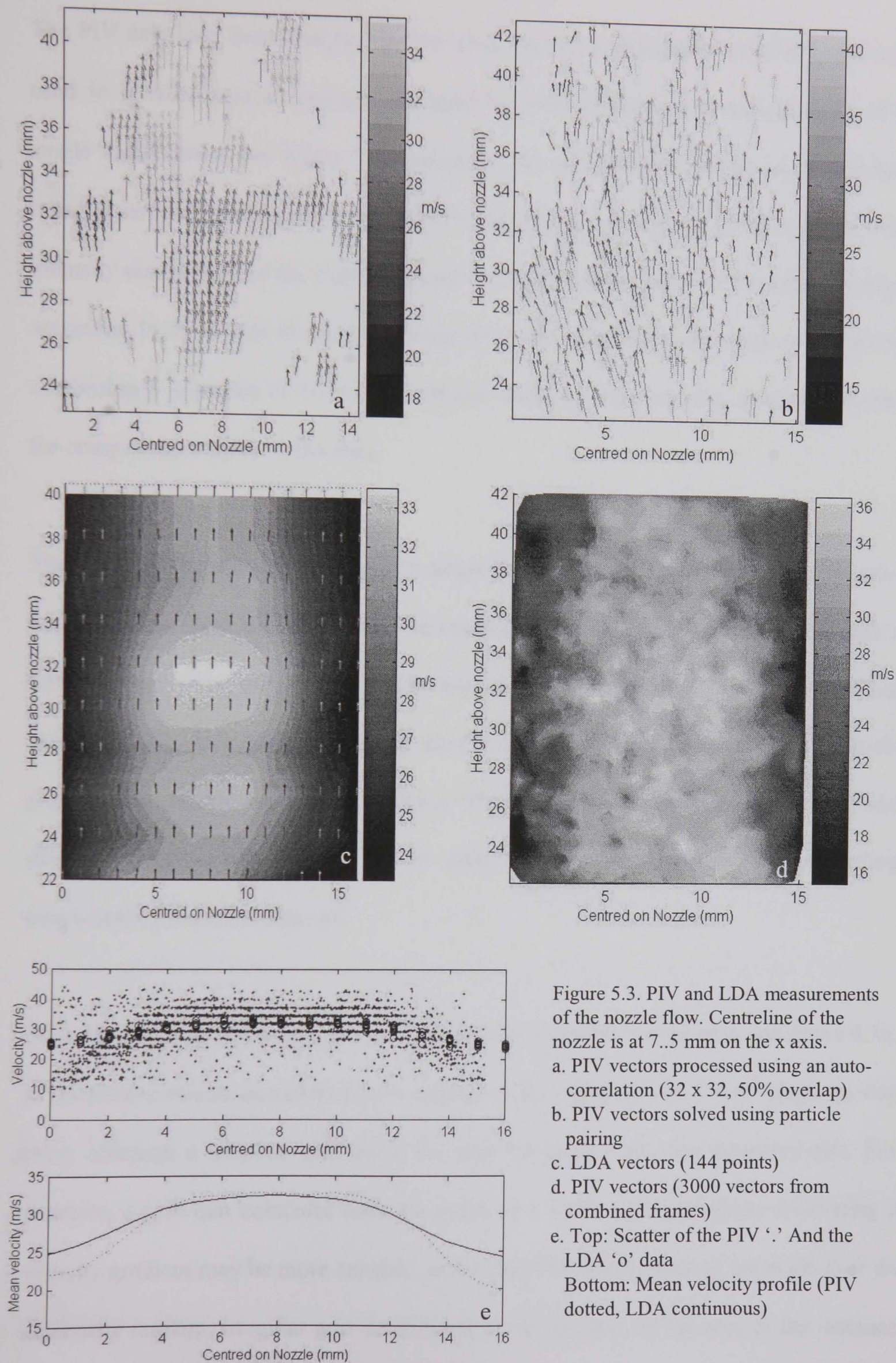


Figure 5.3. PIV and LDA measurements of the nozzle flow. Centreline of the nozzle is at 7.5 mm on the x axis.

a. PIV vectors processed using an auto-correlation (32 x 32, 50% overlap)  
 b. PIV vectors solved using particle pairing

c. LDA vectors (144 points)

d. PIV vectors (3000 vectors from combined frames)

e. Top: Scatter of the PIV '.' And the LDA 'o' data

Bottom: Mean velocity profile (PIV dotted, LDA continuous)

### 5.3.3 Discussion of Results

The PIV data have been analysed in two ways. Firstly, a correlation technique has been used to provide a local spatially averaged but near instantaneous measurement of a single video frame, see figure 5.3a. Secondly, the same frame has also been analysed using a particle tracking method to remove the spatial averaging, see figure 5.3b. The intensity distribution of the particle images has been used to estimate the image centres according to the centre-of-mass approximation. The time-averaged result, produced by combining a sequence of 16 frames analysed using particle tracking, is also presented for comparison with the LDA data.

The result of the auto-correlation of a single frame is shown in figure 5.3a. The auto-correlation has been carried out over an interrogation spot size of 32 x 32 pixels with a 50% overlap. Although the seeding concentration was increased to the upper limit that can be solved using particle tracking there are still an insufficient number of particle pairs to successfully apply the correlation. The outcome is holes in the vector map and identical neighbouring vectors due to peak locking. Unfortunately higher seeding concentration was not explored.

LDA allows point measurements to be made over a predetermined grid, see figure 5.3c. In the measurements described here a regular 16 by 9 grid of 1 by 2 mm<sup>2</sup> elements was used, although a bespoke grid could be used for more elaborate measurements. For example, a grid that coincides with the nodes of a CFD mesh or regions containing a velocity gradient may be more suitable. In contrast PIV measurements are made over an inherently random, irregular grid determined by the location of the seed at the instance of illumination.



The sample time in the order of seconds was used at each measurement point. In addition to the sample time, allowances need also to be made for the translation of the measurement volume between grid points. The LDA measurements are therefore temporally averaged to a greater extent than PIV, PIV's sampling period simply being the pulse separation for a single image. For the PIV measurement described here 16 images giving approximately 3000 points over an irregular grid were combined, Figure 5.3d. The total capture time for all the images was a fraction of a second.

To give a realistic 'between the points' measurement both the LDA and PIV data have been spatially averaged to give a continuous surface, figures 5.3c and 5.3d respectively. The LDA data was interpolated from a 16 x 10 grid of points to a continuous surface for display purposes using a Gaussian smoothing function whereby a surrounding measurement's contribution to a point on the continuous surface is weighted according to a Gaussian window. The amount of smoothing is adjusted by varying the standard deviation of the function (0.6 for the figure shown here). The velocity vectors have been plotted over the continuous surface to illustrate magnitude as well as direction. Owing to the irregular scattering of vectors produced by particle tracking an irregular Delaunay triangulation has been used to generate the continuous surface <sup>[110]</sup>. The Delaunay triangulation defines a grid where no data points are contained within a triangle's circumcircle. The original velocity vectors are preserved at the nodes of the mesh whilst a linear interpolation is used along the edges between the nodes to generate a continuous velocity map. A more detailed explanation of the application of the delaunay triangulation to sparse PIV data is included in chapter 8.

The continuous surfaces of Figures 5.3c and 5.3d show similar overall flow patterns but there are noticeable differences. The LDA measurements indicate that the flow shifts left to right between 22.5 and 27.5 mm above the nozzle. Figure 5.3c shows that some of the measurement points are missing in the lower corners of the plot. It is the absence of these entries that has distorted the results. The PIV data shows a reduction in the width of the core further from the nozzle exit, a feature that is also present on the LDA measurements to a lesser extent.

Figure 5.3e shows the scatter of both the particle tracking PIV and LDA velocities against  $x$ , and the mean velocities in  $y$ . PIV has captured a greater spread of velocities than LDA. This is expected as LDA returns the strongest velocity in the measurement volume over the sample time. PIV is an instantaneous measurement showing the entire range of velocities when the laser was fired. The data were intentionally recorded at the upper limit of the pairing algorithm, maximum of approximately 400 vector per image, the result of which is a large number of erroneous pairings. The spread of the PIV vectors appear to follow a common distribution with a scattering of random vectors. If the flow was assumed to follow a normal distribution, ie no shocks, the random vectors could be identified and removed from the solution.

The scatter of the PIV data is clustered into  $2 \text{ ms}^{-1}$  increments that gives an accuracy of  $\pm 7\%$  if the mean velocity is assumed to be  $30 \text{ ms}^{-1}$ . The image centroids have been located using the centre-of-mass approximation that is intended to give sub-pixel accuracy. The mean displacement between pairs is approximately 16 pixels and implies that the centroids have only been located to the nearest pixel. This is believed to be due to a peak-locking effect of the centre-of-mass algorithm that biases the centroid towards

and integer pixel value. This is despite the particle images being undistorted and clearly visible. The scatter of the LDA data is small in comparison to that of the PIV data. There are some rogue values in the plot. These would appear to be due to a transposition error in the post processing rather than erroneous measurements.

The mean velocities in the core of the jet are very similar, varying between 30 and 32  $\text{ms}^{-1}$ , although the LDA data's profile is smoother owing to the time averaging. There is some discrepancy in the periphery of the jet where PIV indicates a slower flow. The source of the error could be due to differences in the experimental set-up or the measurement techniques. Firstly, there could be some discrepancy between the areas measured and the flow conditions as the measurements were carried out by different operators at different sites at different times. Secondly, both LDA and PIV need to be set up for a range of velocities. With PIV, this is achieved by selecting the correct pulse separation. With LDA, the system has to be set to detect the correct range of frequencies. If the frequency corresponding to a given velocity is outside this range its signal will be attenuated.

#### 5.3.4 Conclusions of the 2-D PIV Measurements of the Nozzle Flow

The finite resolution of the image capture system discriminates against velocity in about 2  $\text{ms}^{-1}$  increments. For the PIV measurements considered here 2  $\text{ms}^{-1}$  corresponds to a 28  $\mu\text{m}$  displacement or 1 pixel. If the average separation between particle pairs is 16 pixels the accuracy of the measurement is  $\pm 7\%$ . The centre-of-mass approximation has not extended the *DVR* of the recording media. These figures assume that there are no further errors due to scaling, pulse separation, flow following ability of the seed etc.

The particle tracking has generated a large amount of spurious vectors owing to the ambiguous pairing process in a densely seeded flow. The upper limit on the vector yield per image was approximately 400 vectors over a 768 x 576 image. Unfortunately, higher seeding concentrations suitable for correlation analysis were not explored. The relatively low concentrations have created holes in the data and peak locking of neighbouring vectors. This problem could have been overcome by the introduction of more seed. The potential vector yield of the correlation would have been 48 x 36 vectors (1728 in total), approximately 4 times the upper limit of the pairing algorithm. It is therefore recommended that a high seeding concentration be used in the application on the ILPF to facilitate a correlation analysis, preferably with the use of a profile-fitting algorithm to the correlation peak to avoid the peak-locking effect of the centre-of-mass centroid estimation.

## 5.4 THIRD COMPONENT CHARACTERISATION

Two three-component PIV approaches have been evaluated, the first a stereo camera arrangement, the second recording the diffraction pattern and intensity profile of a defocused particle through a single camera.

### 5.4.1 Stereo PIV

The 2-D PIV measurements of the nozzle flow showed that the in-plane displacement of the exposures could be measured to an accuracy of  $\pm 7\%$ . A modest improvement in the sub-pixel accuracy of the centroid location would reduce this to a couple of percent. For the stereo camera approach the accuracy of the out-of-plane component is typically an order of magnitude worse than the in-plane measurement. Any non-corrected optical distortion between the two views further lowers the accuracy of the measurement. This hampers the application of this technique when the flow has to be viewed through a contoured window.

The stereo approach is inevitably a compromise as it is desirable to have a large angle between the cameras to increase the accuracy of the out-of-plane measurement, but also a small angle to allow for a shallower depth-of-field. By tolerating a shallower depth of field a wider aperture can be used to see smaller, dimmer particles. This compromise is relaxed where the Scheimpflug condition is satisfied, see section 4.5.2, but the magnification error still needs to be corrected.

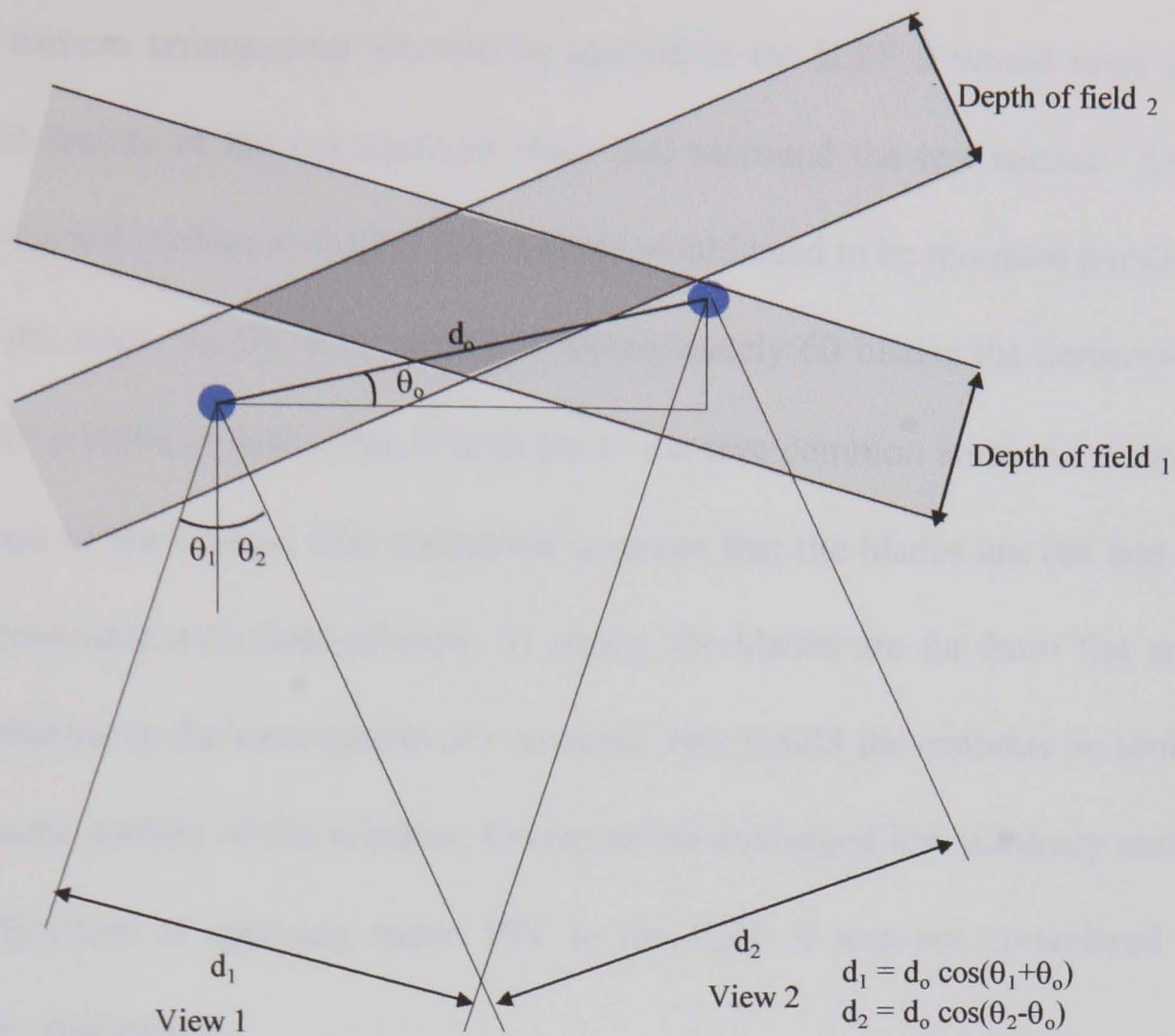


Figure 5.4. Disparity between particle pairs viewed through stereo cameras.

If a particle pair separated by displacement  $d_o$ , see figure 5.4, are viewed from angles  $\theta_1$  and  $\theta_2$  their viewed displacement is  $d_1$  and  $d_2$  respectively. As the angle increases the disparity between  $d_1$  and  $d_2$  also increases, but the overlap between the depth of field of the two decreases and particles at the extremities of the images fall out of focus, unless corrected by rotating the plane of the image array. The out-of-plane component is calculated trigonometrically from the disparity between  $d_1$  and  $d_2$ . It is typically the case that for particle pairing the particles are separated by 10 to 15 pixels. If the disparity is only 1 pixel the error can be up to 10%. For high-speed flows it is typical that the out-of-plane component of velocity may only be 10% of the mean velocity, the error therefore being as large as the component of flow being measured.

If the stereo camera arrangement were to be applied to the ILPF it would need to fit within the constraints of the containment rings that surround the test section. As the window into the test section is slender the cameras would need to be mounted parallel to the plane of the rotor. As the rotor contains approximately 60 blades the cameras can only be rotated  $6^\circ$  relative to each other if both are to observe common areas not obscured by the presence of the blades. This separation assumes that the blades are flat and that rotor phase coincides with field-of-view. In reality the blades are far from flat and a sequence of frames as the rotor passes are required. Nor would the cameras be looking through the same section of the window. Owing to the envisaged low accuracy and the technical difficulties of applying stereo PIV to the ILPF it was not considered any further for this application.

#### 5.4.2 Three-component PIV by Defocusing

Both the in and out-of-plane components of velocity of the flow from the nozzle unit have been measured using three-component PIV by defocusing. The apparatus used for the 2-D nozzle measurements was used for the 3-D measurements although the standoff distance, pulse separation etc. were adjusted accordingly. A calibration exercise was carried out prior to the experiment to establish a diffraction ring, intensity/depth relationship. The results for different flow angles are presented and show that it is possible to identify the particle position in three directions, within a turbulent flow, to a spatial accuracy of  $20\ \mu\text{m}$ .



A geometrical approximation of the impression a particle makes in the image plane is only valid when the particle's diameter is at least ten times larger than the effective resolution limit of the lens so that diffraction can be neglected. When a particle is smaller than the resolution length the intensity magnitude in the image plane is largely dependent on its scattering characteristics. The intensity profile is determined by the transfer function of the imaging system, which is influenced by the lens resolution and the degree of aberration. For the sizes of particles that are used in high-speed air flows ( $\leq 1 \mu\text{m}$ ) the intensity profile of the image is given by the point spread function (PSF) of the lens. The scattered intensity profile does not significantly affect the shape of the image.

The phase of the light scattered from the particle is delayed as it passes through the lens giving the diffraction ring patterns shown in Figure 5.5. If the pupil function of the lens is symmetrical, a symmetrical diffraction pattern will result. If the lens is astigmatic the ring pattern will be distorted accordingly.

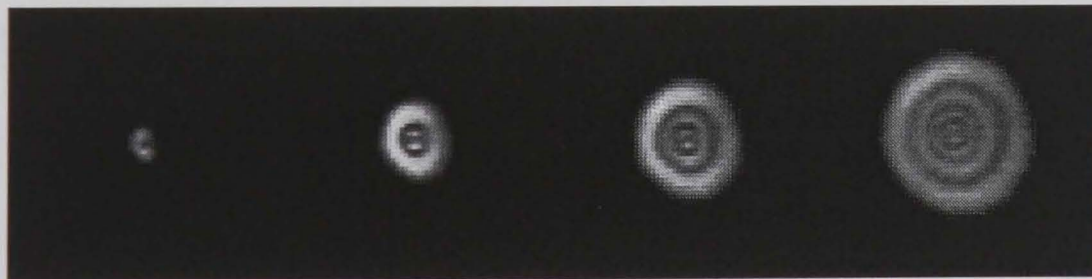


Figure 5.5 Diffraction rings at incremental depths

A point source at the origin of the object plane produces a spot image at the origin of the image plane. The image produced by the point source is called the point spread function, or *PSF* <sup>[138]</sup>. It will take on the smallest possible size when the system is in focus. If an illuminated particle is considered to be a point source it can be shown that the profile of



the particle image changes from an Airy function for a focused diffraction-limited image to a series of concentric rings for the defocused particle. The number of rings, the intensity profile, and the diameter of the outer ring depend on the amount of defocusing.

For an object amplitude distribution of  $U_o(x_o, y_o)$ , the image amplitude distribution,  $U_i(x_i, y_i)$ , is given by <sup>[125]</sup>

$$U_i(x_i, y_i) = \int_{-\infty}^{\infty} \int_{-\infty}^{\infty} h(x_i + Mx_o, y_i + My_o) \times U_o(x_o, y_o) dx_o dy_o \quad (5.1)$$

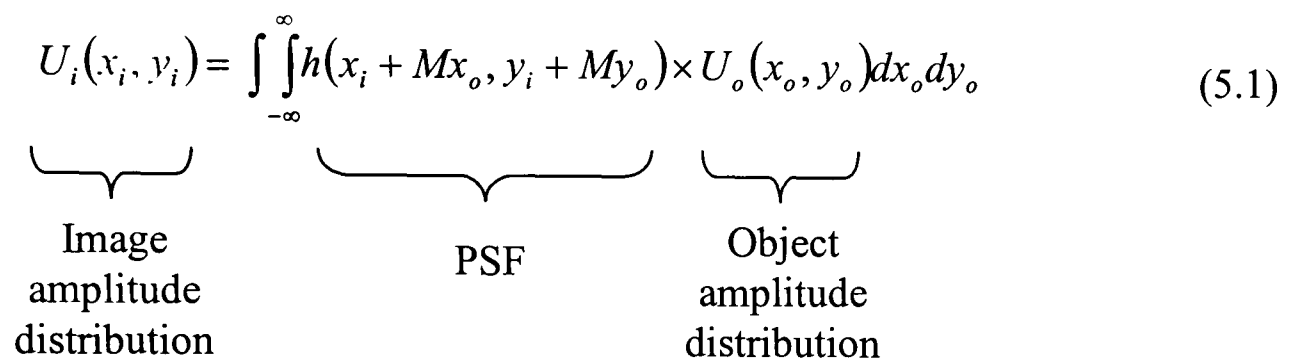


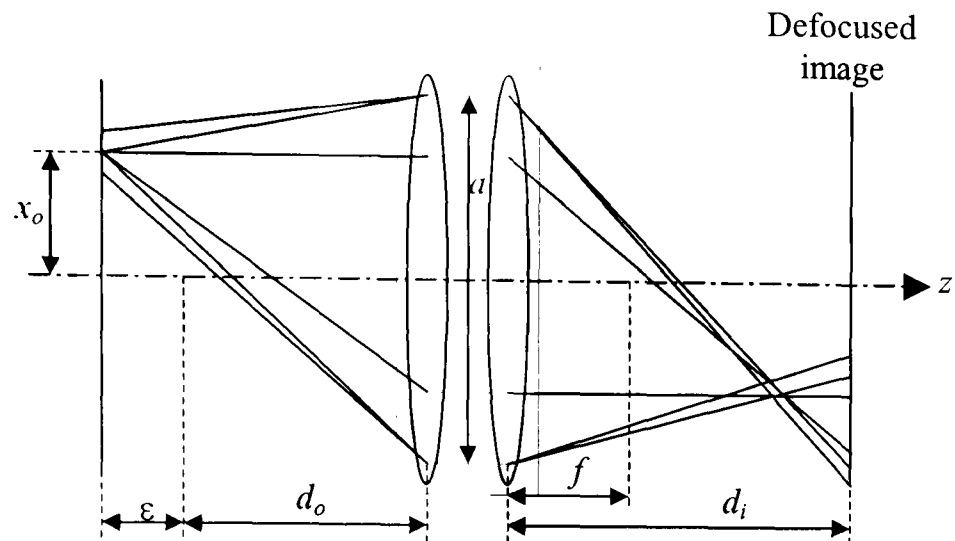
Image  
amplitude  
distribution

PSF

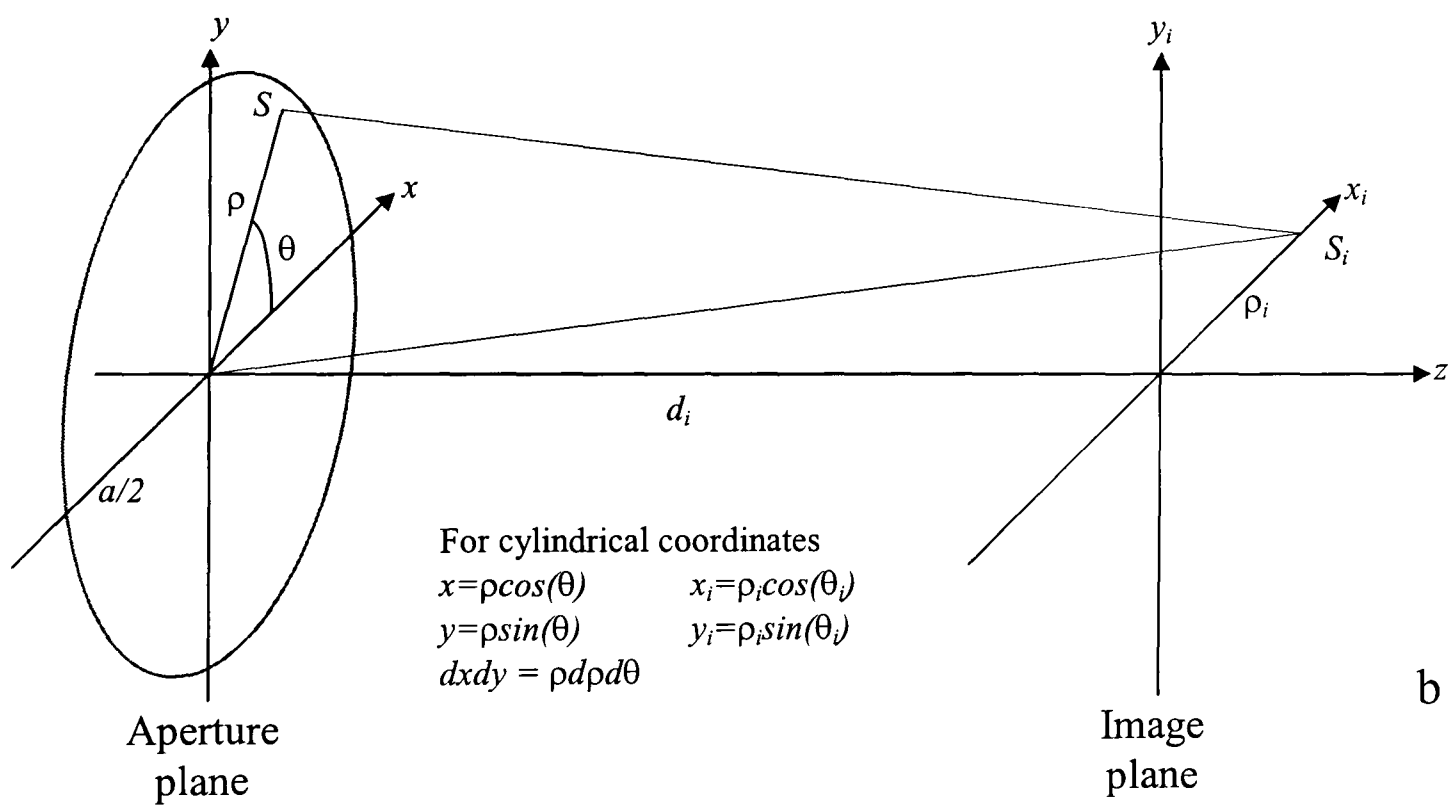
Object  
amplitude  
distribution

see figure 5.6. The image of a point source can be considered as the summation of spatially distributed *PSF* spots across the aperture (more precisely the exit pupil) of the system. The image amplitude distribution can be described by the convolution of the object amplitude distribution with the *PSF* of the optical system, hence equation 5.1 can be rewritten as a convolution,

$$U_i(x_i, y_i) = h(x_i, y_i) * U_o\left(-\frac{x_i}{M}, -\frac{y_i}{M}\right) \quad (5.2)$$



a



b

Figure 5.6. Schematics of dimensions for equations 5.1 to 5.10.

- a. Geometrical image for an out-of-focus particle.
- b. Geometry of an aberration free optical system

The point spread function of the system,  $h(x_i, y_i)$  is given by

$$h(x_i, y_i) = \frac{M}{\lambda^2 d_i^2} \int_{-\infty}^{\infty} \int_{-\infty}^{\infty} \underbrace{P(x, y)}_{\text{Pupil function}} \underbrace{e^{-j2\pi(x x_i + y y_i)/(\lambda d_i)}}_{\text{E-field of converging spherical wave}} dx dy \quad (5.3)$$

where  $d_i$  is the image distance (distance between the aperture plane and the image plane),  $x_i, y_i$  are coordinates in the image plane,  $M$  is the magnification and  $\lambda$  is the wavelength of the monochromatic light. The pupil function  $P(x, y)$  describes the extent of the spatial transmittance of the aperture. The PSF represents the Fourier transform of the pupil function,

$$h(f_{xi}, f_{yi}) = \frac{M}{\lambda^2 d_i^2} \mathfrak{F}\{P(x, y)\} \quad (5.4)$$

where  $f_{xi} = \frac{x_i}{\lambda d_i}$ ,  $f_{yi} = \frac{y_i}{\lambda d_i}$ , and  $\mathfrak{F}\{\}$  denotes a Fourier transform.

For coherent illumination, the image intensity is given by the square of the modulus of the image amplitude distribution,

$$I(x_i, y_i) = |U_i(x_i, y_i)|^2 \quad (5.5)$$

Udrea <sup>[125]</sup> presents a simplified model of the intensity pattern of a defocused sub-micron particle (that is considered to be a point source) imaged through a circular aperture. The normalised intensity of the particle centred on the origin is assumed to be an Airy distribution <sup>[99]</sup>. The defocusing of the particle is considered as a distortion in the optical path length because it introduces a relative delay and is considered as a

complex pupil function <sup>[99]</sup> (monochromatic illumination). As the pupil function of the lens is symmetrical a symmetrical diffraction pattern will result. The PSF of a defocused system in polar co-ordinates can be expressed as <sup>[125]</sup>

$$h_{\varepsilon}(\rho_i, \theta_i) = h(\rho_i) = \frac{2\pi M}{\lambda^2 d_i^2} \int_0^{\infty} r P(r) e^{j\pi \varepsilon r^2 / \lambda} J_0(2\pi r \rho_i / \lambda d_i) dr \quad (5.6)$$

where  $J_0(2\pi r \rho_i / \lambda d_i)$  represents a Bessel function of the zeroth order. Equation 5.6 describes the integration of the product of wave propagating through the aperture and Airy distribution in the field of the aperture. The pupil function also takes into account the difference in optical path owing to defocusing where

$$P_w(r) = P(r) e^{j\pi W(r) / \lambda} \quad (5.7)$$

$$W(r) \approx \varepsilon r^2 / 2 \quad (5.8)$$

$W(r)$  is called the aberration function. If the image plane is out of focus the amount of defocusing is given by

$$\varepsilon = \frac{1}{d_o} + \frac{1}{d_i} - \frac{1}{f} \quad (5.9)$$

The normalised distances for image and object defocusing are given by

$$\varepsilon_i = \frac{\varepsilon d_i}{(1 + \varepsilon d_i)} \quad \varepsilon_o = \frac{\varepsilon d_o}{(1 + \varepsilon d_o)} \quad (5.10)$$

Where  $d_i$  and  $d_o$  are the image and object distances respectively.

### 5.4.3 Defocusing calibration

In order to measure the out-of-plane component either the diffraction ring/depth relationship needed to be calculated or calibrated. As in practice the pupil function of the lens is not known and further aberrations may be present, a calibration exercise was conducted. The diffraction pattern emitted through a  $3\ \mu\text{m}$  pinhole illuminated from a 50mW continuous wave Nd-YAG laser was used as a point source for the calibration, see figure 5.7. The diameter of the pinhole was smaller than the  $3.9\ \mu\text{m}$  resolution of the optical system. The pinhole was mounted on a translation stage connected to a displacement transducer with a resolution of  $0.1\ \mu\text{m}$ . The diffraction-limited lens used for the calibration exercise was a long range microscope termed K2<sup>[101]</sup>. Working distances between 100 and 2500 mm can be achieved by using a range of objectives. The CF3 objective that gives varying magnification between 2 and 5, and  $f$ -numbers between 2.58 and 8, was used in the calibration exercise. The diffraction pattern was positioned in the centre of the field-of-view of the camera. Aperture of the K2 lens was fully open giving an  $f$ -number of 8 and a magnification of 3.2. The initial standoff distance of the pinhole was 139 mm. The pinhole was traversed from  $-500$  to  $1500\ \mu\text{m}$  (positive towards lens) in  $5\ \mu\text{m}$  increments with an estimated precision of  $0.1\ \mu\text{m}$  (least significant figure on traverse).

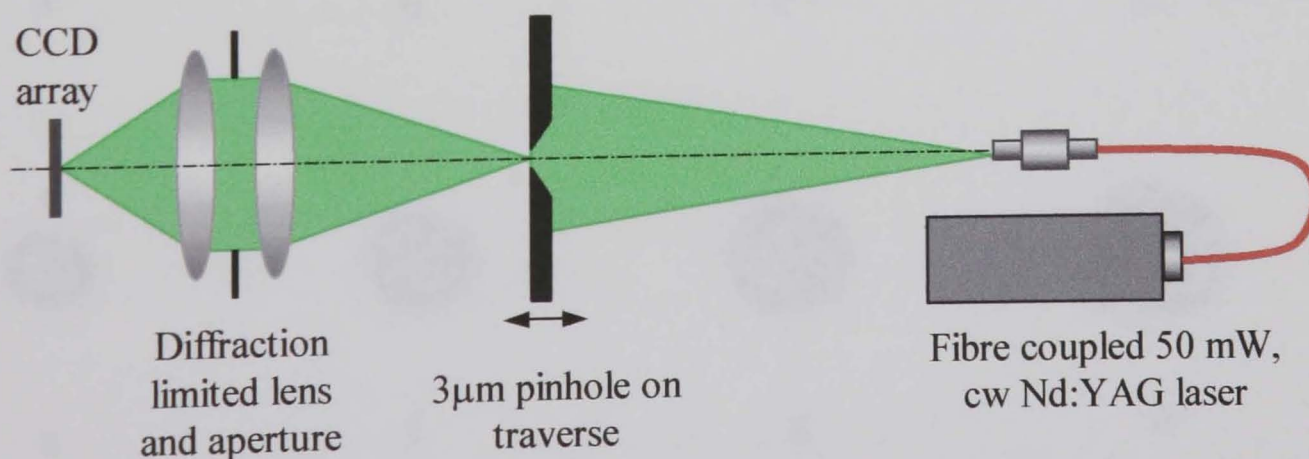


Figure 5.7. Experimental arrangement used in the 3-D calibration



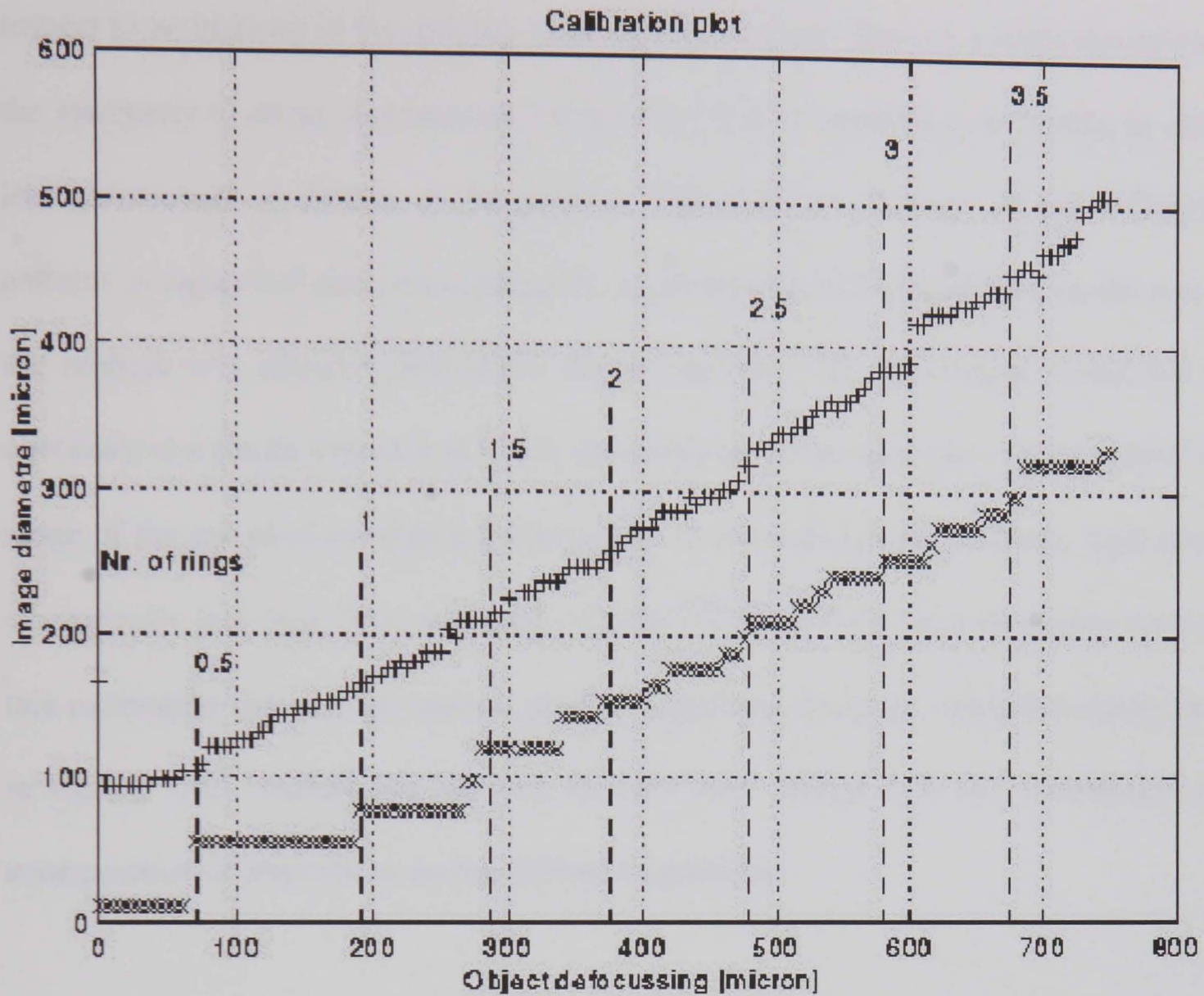


Figure 5.8. Calibration curves from measurements. (+) total image diameter, (x) diameter of the outer ring. (Figure taken from Udrea<sup>[125]</sup>)

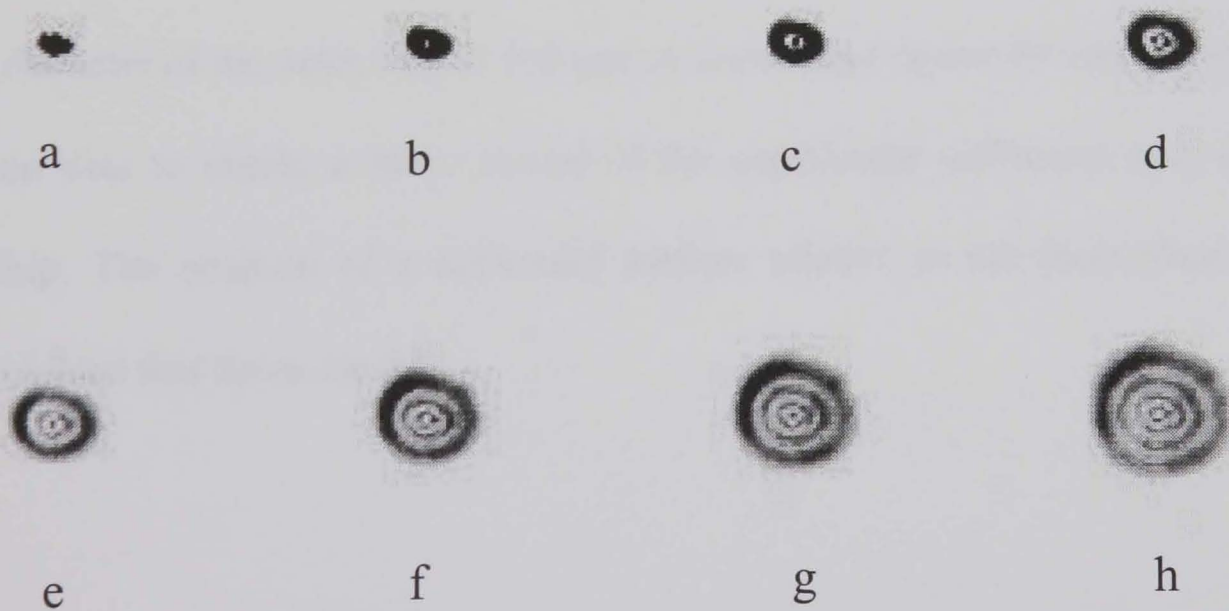


Figure 5.9. Experimental measurements of the defocused point source. A.  $\frac{1}{2}$  ring,  $\epsilon_o \approx 40 \mu\text{m}$  b. 1 ring,  $\epsilon_o \approx 120 \mu\text{m}$  c.  $1 \frac{1}{2}$  ring,  $\epsilon_o \approx 200 \mu\text{m}$  d. 2 rings,  $\epsilon_o \approx 300 \mu\text{m}$  e.  $2 \frac{1}{2}$  rings,  $\epsilon_o \approx 400 \mu\text{m}$  f. 3 rings,  $\epsilon_o \approx 500 \mu\text{m}$  g.  $3 \frac{1}{2}$  rings,  $\epsilon_o \approx 600 \mu\text{m}$  h. 4 rings,  $\epsilon_o \approx 700 \mu\text{m}$

The overall diameter, and diameter of the diffraction rings, is shown to increase with respect to an increase in the distance from the object plane. There is a slight deviation in the symmetry in shape and intensity of the rings that is expected to be owing to either lens aberrations or defects in the pinhole. The absolute intensity of the diffraction patterns in figure 5.9 cannot be compared, as the amount of light incident on the rear of the pinhole was adjusted throughout the experiment. This adjustment would not be necessary in a planar experiment where the thickness of the light sheet would restrict the range of the out-of-plane displacement (range of calibration was 2000  $\mu\text{m}$ , light sheets are typically less than 1000  $\mu\text{m}$  thick). Udrea <sup>[125]</sup> achieved a close similarity between this calibration data and theoretical profiles calculated using her modelled summarised in section 5.4.2. Differences between the two were attributed to the quantisation and superposition of aberrations on the diffraction patterns.

Figure 5.8 shows the total image and outer ring diameters plotted against object defocusing. The diameters have estimated to a resolution of 1 pixel. The total image diameter can be used to measure the object defocusing to an estimated accuracy of 20  $\mu\text{m}$ , the diameter of the outer ring to 100  $\mu\text{m}$ . A linear least-square fit was applied to the calibration data to obtain a linear model of the depth/outer diffraction ring diameter relationship. The position of a defocused particle relative to the focal plane can be calculated from this linear model.



## 5.5 3-D MEASUREMENTS OF A FREE AIR JET BY DEFOCUSING

### 5.5.1 Experimental method

The diffraction ring calibration data was used to measure the 3-D velocity field of the nozzle flow described earlier<sup>[126]</sup>. An optical system similar to that used for the 2-D PIV measurements was used for the three-component measurements. A standoff of 139 mm and  $f$ -number of 3.67 were used as in the calibration exercise. The focal plane was positioned 200  $\mu\text{m}$  behind the light sheet so that the ring structure started with one ring. Particles with no ring structure were discarded in the analysis. A mean out-of-plane component of velocity was introduced by tilting the nozzle 10°, 20° and 30° relative to the light sheet. The laser was configured to give triple exposures for the tilted measurements. This made it easier to identify the particle tracks and increased the observed seeding concentration, see figure 5.10. The light sheet was estimated to be between 500-600  $\mu\text{m}$  thick (measured from the burn mark produced by putting over exposed photographic paper in the path of the beam).

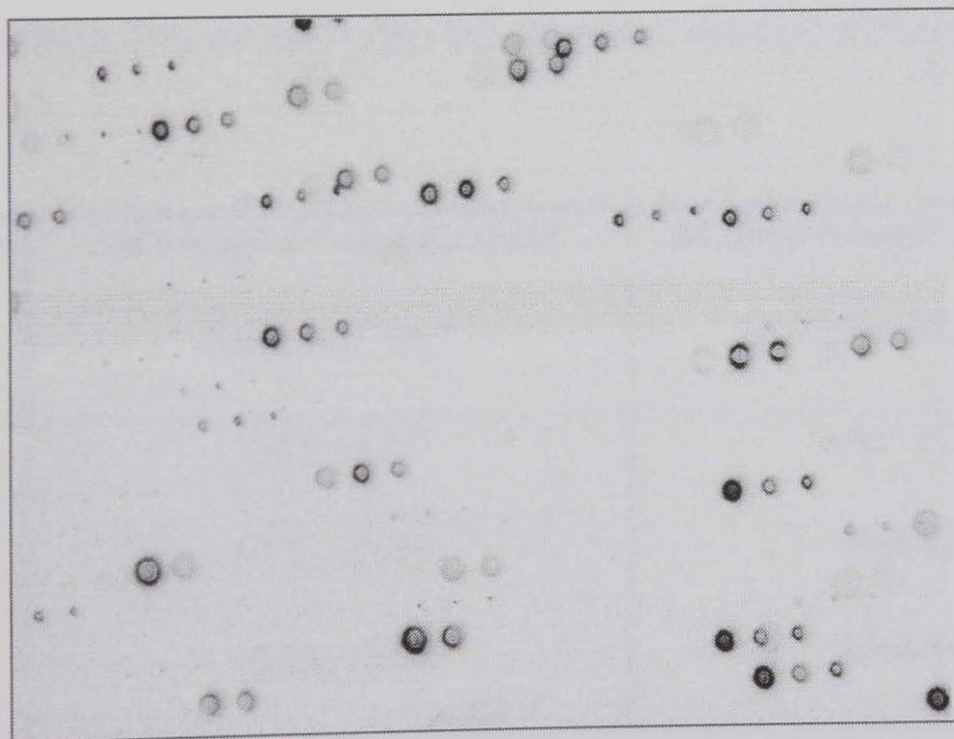


Figure 5.10. Defocused particles of the nozzle flow tilted at 30° to the plane of the light sheet. Triple exposure.



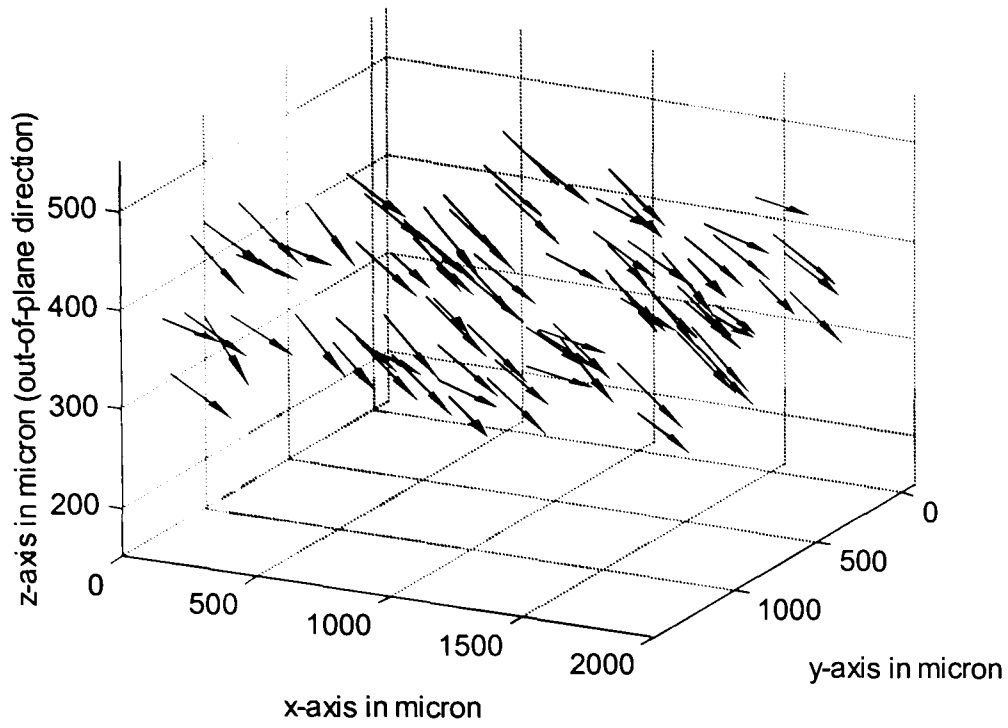
The 2-D PIV measurements taken prior to tilting the nozzle gave mean velocities of  $30.73 \text{ ms}^{-1}$  and  $-2.13 \text{ ms}^{-1}$  in  $y$  and  $x$  directions with standard deviations of  $2.60 \text{ ms}^{-1}$  and  $2.86 \text{ ms}^{-1}$  respectively over the field-of-view. Assuming the mean components and standard deviations of the velocity remain constant the calculated values of the out-of-plane component of velocity are shown in table 5.1. The measured components are shown for comparison.

It became apparent after the experiment that the nozzle flow has a bias of approximately  $2.13 \text{ ms}^{-1}$  in the plane orthogonal to the axis of the nozzle. Further to this, during the experiment it became apparent that the turbulence level changed according to the seeding pressures used. This problem was remedied by injecting the seeding through the same nozzle inlet as the main air supply, prior to the flow straightening honeycomb, rather than through an inlet further up the nozzle body. It is expected that a rotation of the nozzle body may account for the discrepancy between the calculations and measurements, although they do fall within the estimated standard deviations.

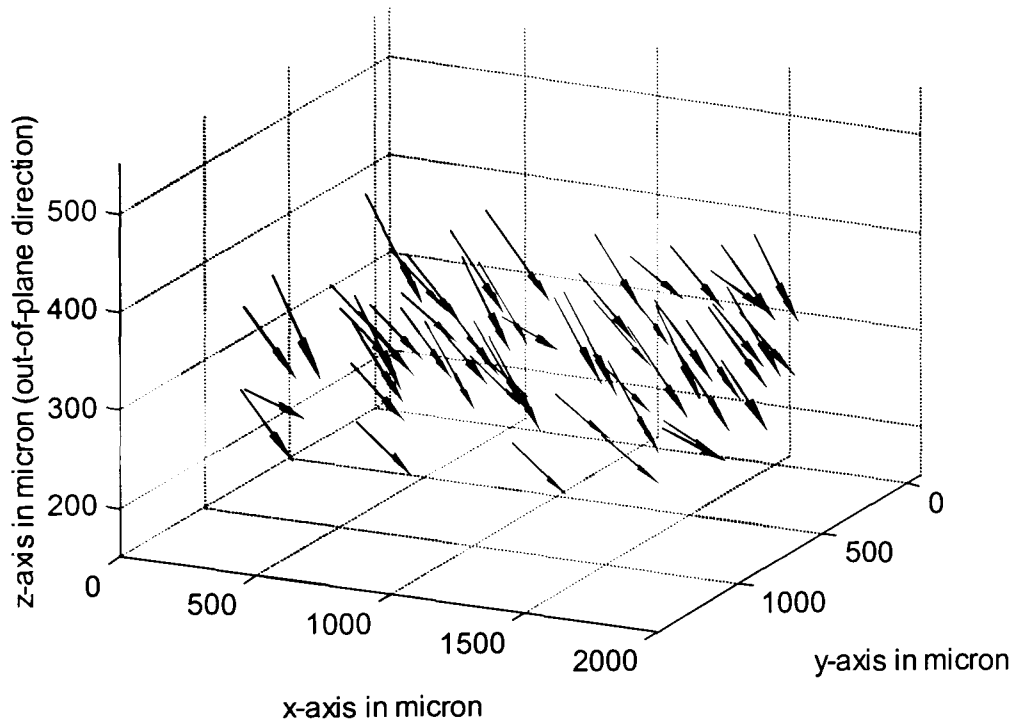
Tilting of nozzle	Calculated z- velocity & std. deviation, $\text{ms}^{-1}$	Measured mean z-velocity & std. Deviation, $\text{ms}^{-1}$
$10^\circ$	$7.42 \pm 3.27$	$6.7 \pm 2.2$
$20^\circ$	$12.51 \pm 3.58$	$10.4 \pm 3.3$
$30^\circ$	$17.21 \pm 3.78$	$13.6 \pm 4.7$

Table 5.1 Calculations and measurements of the out-of-plane component of the nozzle flow.

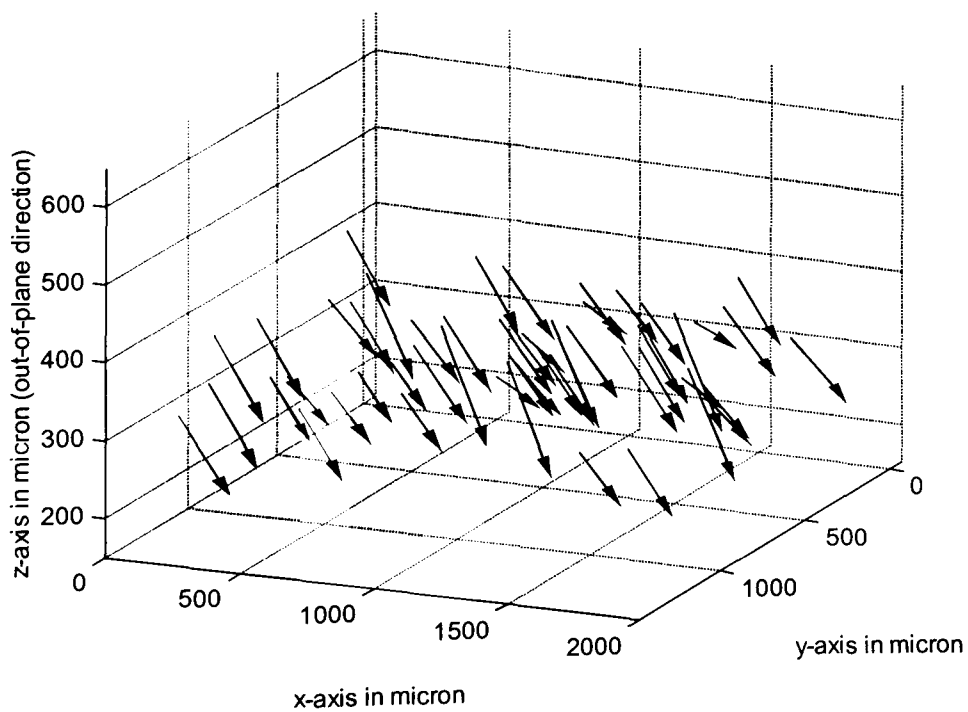
## 5.5.2 Results



a. Displacement vector plot of the nozzle flow tilted  $10^\circ$ .



b. Displacement vector plot of the nozzle flow tilted  $20^\circ$ .



c. Displacement vector plot of the nozzle flow tilted  $30^\circ$ .

Figure 5.11 3-D displacement between the first and third exposures of 8 overlaid frames. Nozzle tilted from y-axis.

### 5.5.3 Discussion of Results

The  $30 \text{ ms}^{-1}$  nozzle flow has been measured in three dimensions using PIV by defocusing. A calibration exercise was required to determine a depth/diffraction pattern relationship. The relation has been shown to compare well with a theoretical model. A spatial resolution of  $20 \text{ }\mu\text{m}$  in all three components, an accuracy of 4 %, has been achieved using the calibration data over a  $4 \text{ mm}^2$  field-of-view using a  $768 \times 576$  CCD camera. The technique removes the need for the wide angle of view traditionally required by stereo visualisation applications.

The defocusing technique has a number of advantages in comparison to a stereo camera arrangement. As only one camera is required the set-up is essentially the same as for 2-D, except that a smaller field-of-view is required if the diffraction patterns are to be resolved. The camera does not need to be aligned with a second camera or warping coefficients calculated, nor does a corresponding data set from the second camera need be recorded. The out-of-plane position is calculated for each individual particle from a single image. For stereo cameras a 2-D displacement recorded by each camera is calculated by correlation, a local averaging procedure. The 3-D displacement is calculated from corresponding local correlations. In other words, the 3-D velocity is determined from the disparity between two in-plane measurements. As the disparity is typically a fraction of the in-plane displacement the error on the out-of-plane will be higher than the in-plane.

The defocusing technique has a number of drawbacks primarily owing to the requirement to resolve the diffraction images. This necessitates a near diffraction-limited imaging system and a small field-of-view in comparison to an equivalent 2-D

arrangement. A  $4 \text{ mm}^2$  field-of-view was recorded by a CCD camera with a resolution of  $768 \times 576$  pixels in the calibration and nozzle measurements. The data also needs to be sparse to allow particle pairs to be identified.

As the diffraction image diameters are three to five times larger than an equivalent focussed particle, a more powerful light source is required to compensate for the drop in the particle's intensity profile as it becomes defocused. The seeding number density needs to be reduced if overlapping images are to be avoided.

Udrea <sup>[125]</sup> suggests the use of two cameras, looking along a common optical axis and sharing identical  $f$ -numbers and magnification but different distances from the in-focus image plane, to determine the out-of-plane component from the difference in the peak and total intensity within the first ring structure. The advantage of the technique is that the accuracy in the out-of-plane could be maintained whilst realising a larger field-of-view. The drawback of this approach, apart from the additional complexity of the set-up, is that the depth of the light sheet needs to correspond to the defocusing required to achieve a single diffraction ring. The variation between intensity and defocusing within this region is assumed to be linear.

#### 5.5.4 3-D PIV by Defocusing Through a Contoured Test Section Window

Having successfully measured all three components of velocity of the free air jet, the test was repeated with the inclusion of the test-section window from the turbine cascade placed between the camera and flow. This Perspex window is machined to the contours of the section's outer casing. It contains a compound curvature surface and is of

approximately uniform thickness. The window has been hand polished to remove the cusps left by the machining process. This window acts as an additional lens that can be considered to act like two cylindrical lenses representing the difference in radii of curvature in each plane.

The diffraction images, viewed through the test-section window without any attempt to correct distortions, were highly stigmatised. The process was repeated with the addition of a couple of weak cylindrical lenses in front of the camera lens. These lenses were rotated relative to each other to minimise the larger scale distortions in the window. Figure 5.12 shows a typical image. Despite these two lenses the diffraction images remained distorted beyond a limit that was acceptable from an analysis point-of-view. The distortion is not uniform across the field-of-view and the intensity of the particle images varies, presumably dependent on the particle's position in the light sheet and the diameter of the diffraction image. It was found during the calibration procedure, albeit over a large depth/diameter range, that the illumination intensity had to be increased as the diffraction ring pattern became larger in the image plane. No three-dimensional velocity measurements were attempted during the limited time available on the turbine cascade. Instead the emphasis was placed on gathering an extensive set of two-dimensional data.

It is believed that this three-component technique is applicable to this turbine, given more time and effort. From a qualitative viewpoint the optical correction that could be quickly achieved by rotating a pair of cylindrical lenses between the imaging lens and window was very significant. This correction alone may be sufficient where the out-of-plane component can be inferred from an aberrated data set recorded by looking through

the test-section window. Where only the number of rings can be identified the resolution of the out-of-plane component is likely to drop from  $20\ \mu\text{m}$  to  $100\ \mu\text{m}$  <sup>[125]</sup>.

The aberrations through the test-section window can be thought of as an additional complex amplitude function owing to the coherent illumination. The function could be corrected with a conjugate function recorded in a holographic optical element. A simple solution to the stigmatism problem would have been to fit an optically flat window into the test section. Such a solution may alter the aerodynamic qualities of the flow to be measured although the window would not need to be large owing to the finite resolution of the camera restricting the field-of-view.





Figure 5.12 a. Diffraction image recorded through test-section window of turbine cascade (inverted).  
b. Single diffraction image recorded through window after partial correction with cylindrical lenses (inverted).  
c. Diffraction image taken from calibration for comparison (inverted).

## 5.6 SUMMARY OF CHAPTER

The velocity of a nozzle flow ( $\approx 30 \text{ ms}^{-1}$ ) has been measured using 2-D PIV and LDA. The results exhibit a close similarity although the PIV data contains a wider scatter of vectors. The PIV data was processed using particle tracking and the particle centroids estimated using the centre-of-mass algorithm. This algorithm was shown not to improve the accuracy of the measurement, the accuracy of  $\pm 7 \%$  corresponding to integer pixel displacements. The seeding concentration was insufficient for auto-correlation analysis, resulting in holes in the vector grid and peak locking. The upper limit on vector yield per image using particle tracking was approximately 300 vectors per image. The potential vector yield for auto-correlation using  $32 \times 32$  pixel interrogation spot with a 50 % overlap is 1728 vectors.

Three-component PIV measurements have been made of the nozzle flow to a resolution of 20 microns in each direction. This translates to an estimated accuracy of 4% for velocity. The measurements were made over a  $4 \text{ mm}^2$  field-of-view at a standoff distance of 139 mm using a single camera. The out-of-plane component of velocity was determined from the diffraction pattern and intensity profile of a defocused particle. The application of stereo PIV to the ILPF has been dismissed owing to limited optical access in the axial direction and blade shadowing in the tangential direction of the rotor.

The same experiment was repeated with a curved perspex window placed between the camera and airflow. Owing to the distortions present in the window the third component of velocity could not be resolved. Possible solutions to this problem have been



discussed. This technique cannot realistically be applied to the turbine cascade until this problem is addressed.

Although the application of a cross-correlation camera failed, it does represent a potentially very powerful tool for PIV measurements. The ability to capture two frames in quick succession not only allows the directional ambiguity in recirculating flows to be solved but also allows the use of a higher seeding concentration to resolve smaller features in a flow. The camera is also triggerable and non-interlaced. The ability to trigger the camera would allow the same blade passage to be sampled to facilitate a statistical analysis of the mean and fluctuating aspects of the flow.

## *Chapter 6*

# APPLICATION OF PIV TO A SPINNING TURBINE CASCADE

-

## EXPERIMENTAL ARRANGEMENT

### *Description of Chapter*

*This chapter describes the optical arrangement applied to the ILPF. It covers optical access, light sheet delivery and the PIV system itself. The choice of seeding and seeding procedure are also explained.*

## 6.1 OPTICAL ACCESS

Gaining optical access into turbomachinery is not a trivial issue if the flow is not to be significantly disturbed. To give a line of sight a perspex window was fitted into one of the removable cassettes that make up the outer casing of the turbine stage. The inner contours of the window matched the compound curvature of the test section to preserve the characteristics of the flow.

The Perspex window, made by Osney laboratories, Oxford University, was approximately 300 by 200 mm<sup>2</sup> in size although only an area of approximately 200 by 100 mm<sup>2</sup> was of uniform thickness ( $\approx 12$  mm). The window extended from upstream of the nozzle guide vanes to downstream of the trailing edge of the rotor, see figure 6.1. Despite being formed on a high precision 5-axis CNC machine and being stress relieved to remove any internal changes in refractive index the window still contained an 'orange peel' surface finish. This was removed by a small amount of hand polishing at the expense of the geometric qualities of the window.

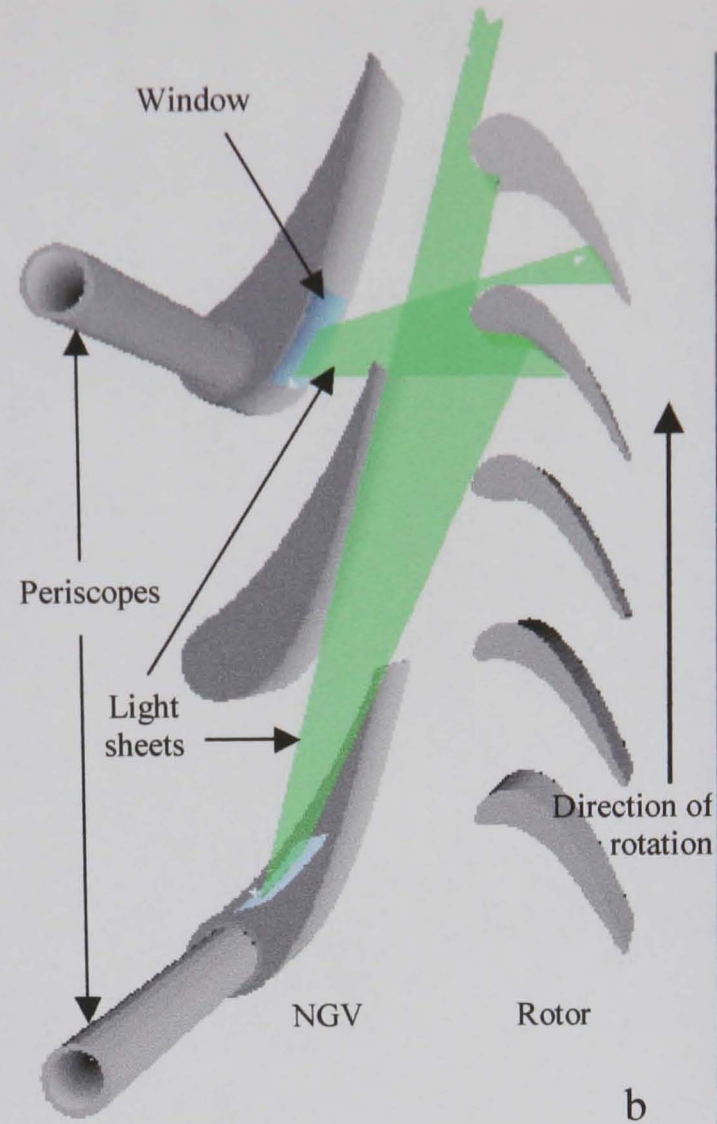
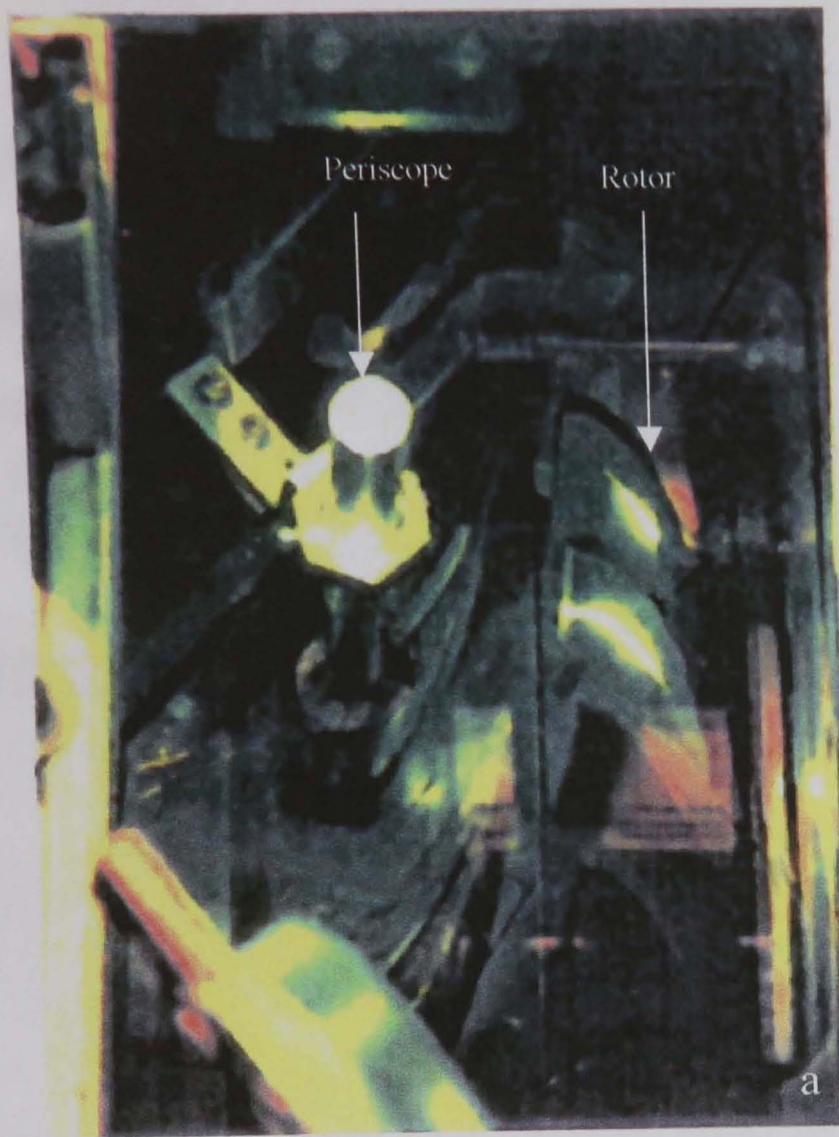


Figure 6.1 The test section window

- a. Photograph of window, periscope and light sheet incident on the rotor.
- b. The periscopes and windows fitted to the cavities within the nozzle guide vanes.
- c. Window removed from facility. Note ngvs form part of the window assembly. Rule included for scale.

A calibration grid was placed in the plane of the light sheet in order to establish the number of pixels per mm and to assess the gross distortions generated by the window.

The maximum possible depth-of-field is required to allow for the changes in optical path length through the window. This is in conflict with the amount of light required to detect a particle. Diffraction-limited particle images were achieved at an  $f$ -number of  $f^{\#}11$ . Acceptable particle images were also achieved at  $f^{\#}8$ , although astigmatic distortions were observed in the areas of high window curvature. An  $f$ -number of  $f^{\#}11$  was used throughout all the experiments described here in order to minimise distortions and to avoid misleading particle detection algorithms.

## 6.2 LIGHT SHEET DELIVERY

The test-section only contained one optical access port. In previous studies optical periscopes have been introduced into the flow to launch the light sheet <sup>[112 &121]</sup>. The insertion of such probes obviously perturbs the flow, so they are typically mounted many tens of probe diameters further up or down stream. The geometry of the stage was such that it became difficult to illuminate sufficient areas of both the stator passage and the stator-rotor gap, as the blades obstructed the beam. A novel solution was found by launching the light sheets from within the nozzle guide vanes. Four removable nozzle guide vanes were fitted to the inner surface of the window using keyways. Although only loosely fitted to the window, the vanes became trapped into position once the window was bolted to the test section. Two of the nozzle guide vanes were hollowed out and fitted with flat windows in the pressure and suction surfaces. Slender optical periscopes of 8 mm in external diameter, which contained the light sheet



forming optics, were inserted into vane cavities allowing the illumination of both the stator passage and stator-rotor gap.

The periscope contained two positive cylindrical lenses that could be rotated and translated relative to each other to alter the focal length and orientation of the light sheet, see figure 6.2. The lenses were not at  $90^\circ$  relative to each other, so did not define individual orthogonal components of the light sheet. Relative rotation between the lenses adjusted the focus of the light sheet, rotating them together altered the orientation of the light sheet. This gave a larger range of adjustment in the light sheet forming properties of a single probe that could be used to illuminate multiple regions of interest simply by rotating the lens.

A broad-band dielectric mirror was fitted within the end of the probe. Three mirrors were available,  $40^\circ$ ,  $45^\circ$  and  $50^\circ$ . A light sheet can only be tangential to the circumference of the test section at one point. The mirror was chosen so that this point occurred as near to the centre of the region of interest as possible.

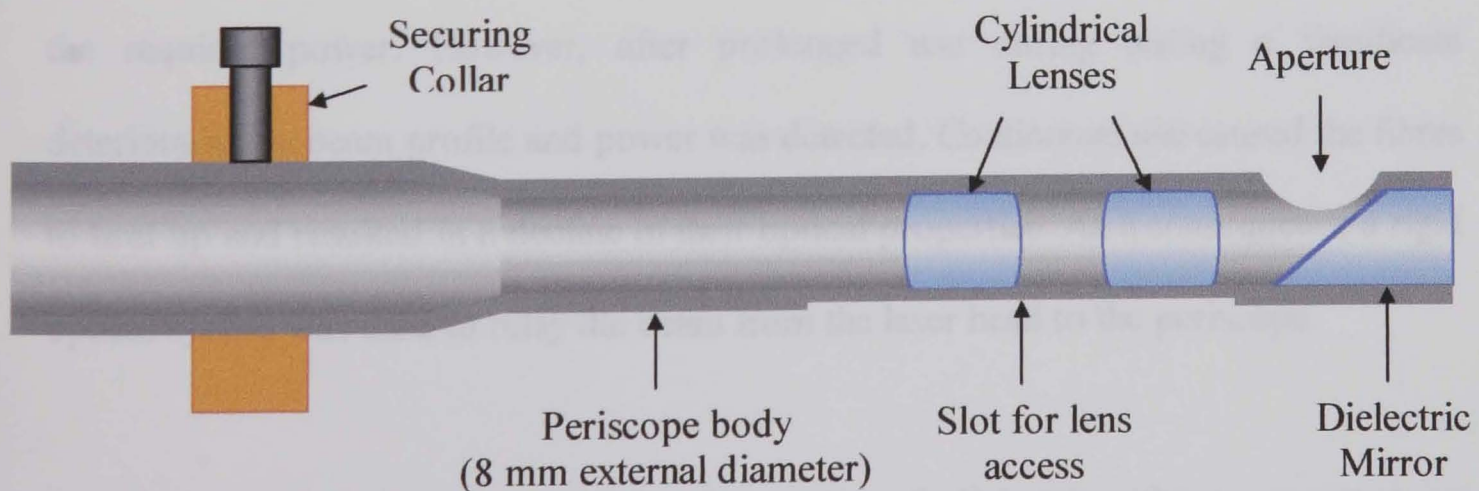


Figure 6.2 Schematic of the periscopes inserted into hollowed out nozzle guide vanes. Used to form and project a light sheet into the test section.



The periscope also catered for the fitment of a fibre optic delivery system. The fibre system, developed by Heriot-Watt University, was made up of 19 multi-mode step index fibres, see figure 6.3. The 100  $\mu\text{m}$  core diameter fibres were bonded together to form a fibre bundle 2 metres long. The faces of each of the fibres were polished prior to bonding. At the delaunch head the fibres were bonded in a round bundle whilst at the launch end the fibres were mounted side by side to form a sheet like structure. The delaunch and launch ends of the bundle were housed in steel cylindrical and brass D-section fittings respectively. The non-transparent cladding was bonded to these fittings.

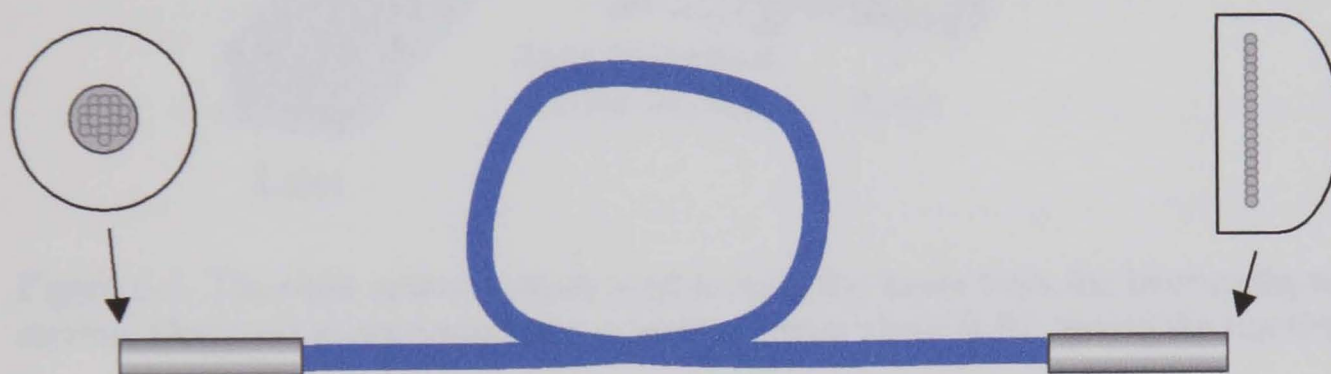


Figure 6.3. Fibre delivery system with circular bundle at input and fibres stacked in a line at the output to project a light sheet.

The fibre delivery system was initially successful in delivering a good quality beam of the required power. However, after prolonged use during testing a significant deterioration in beam profile and power was detected. Continuous use caused the fibres to heat up and resulted in a decline in their optical properties. As a consequence a rigid optical system was used to relay the beam from the laser head to the periscope.

The rigid optical system consisted of a series of dielectric mirrors mounted on kinematic supports, see figure 6.4. The beam was projected parallel to the principal axis



of the facility. This allowed the facility to move in this axis without affecting the alignment of the beam. The movement only resulted in a change in the optical path length of the beam. This was important as the entire facility does move along this axis during the run, hence the sliding joint between the test section and exhaust tank.

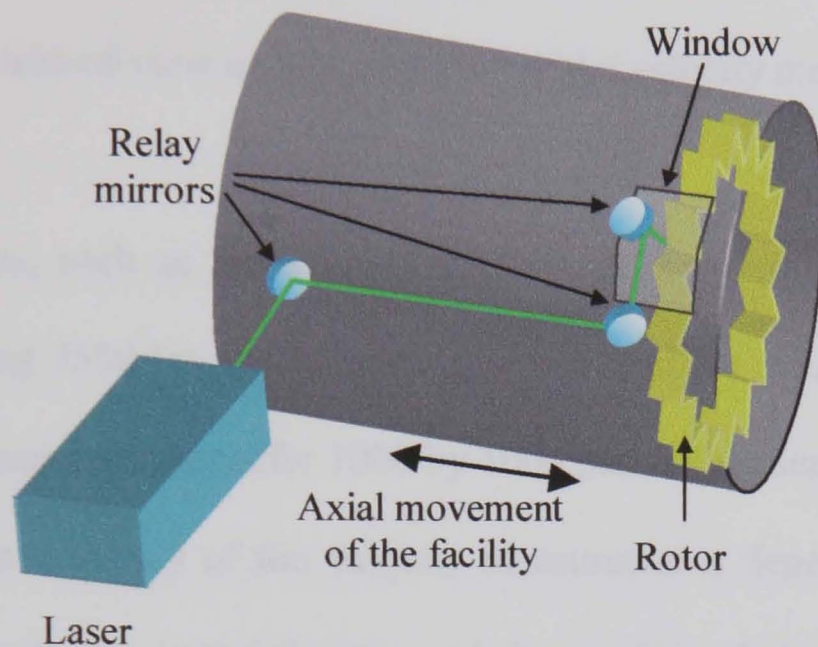


Figure 6.4 The rigid optical system used to relay the beam from the laser to the test section. Designed to accommodate axial movement of the ILPF during the run time.

The camera system was also mounted onto a framework attached to the removable cassette. By adopting this approach the complete optical assembly, periscope, camera and ngvs, could be lined up and tested prior to fitment to the facility. This greatly simplified the setting up of the optical system, which could be carried out remote from the facility.



### 6.3 IMAGE ACQUISITION

A strong emphasis was placed on the digital acquisition of the data, as this allowed an on-line assessment of the experiment. It also negated the requirement for time consuming wet processing. The low spatial resolution of CCD arrays in comparison to photographic film dictated that a lack of picture elements would be the limiting factor to the size of the field-of-view and the accuracy of the velocity measurements.

Photographic films, such as Kodak T-Max 3200, offer approximately 100 lines/mm over 35 mm giving 3500 by 3500 picture elements with an ASA/ISO rating of 3200. Digital 8-bit cameras typically offer 1000 by 1000 picture elements with a similar light sensitivity. As the accuracy of the velocity measurements depend on the number of picture elements between a particle pair, and the number of elements describing each particle, photographic film offers a far better resolution-to-range ratio than a CCD camera. However, in many applications it may not be possible to fully exploit the resolution of photographic media. Light levels or optical access may limit the field-of-view, optical aberrations and the flow following abilities of a particle may limit the accuracy that can be appended to a measurement. If the spatial resolution cannot be realised, the real-time feedback, storage and archiving advantages, and processing and image manipulation options that are available to digital media are far more desirable.

For the measurements described here the geometry of the test section restricted the size of the plane of illumination. Difficulties in launching a light sheet from a slender probe and the stagger angle of the stator vanes dictated that only segments of the stator passage and stator-rotor gap could be illuminated from a single optical probe. As only a small area could be illuminated at once a digital camera with a resolution of 1000 by

1000 pixels was initially chosen. As the distance from the trailing edge of the stator vanes to the crown of the rotor blades was only 15 mm the entire stator-rotor gap could be imaged with a 15  $\mu\text{m}/\text{pixel}$  resolution. The minimum resolvable spot size (Rayleigh distance  $\approx 1.22\lambda f^\#$ ) for an  $f$ -number of  $f-11$ , as used in the experiments described here is 7  $\mu\text{m}$ , larger than the  $\mu\text{m}/\text{picture}$  element resolution achievable with photographic film over this field-of-view. The approximate particle diffraction-limited spot diameter, from equation 4.9, is 18  $\mu\text{m}$  [77]. If a particle pair was separated by 200  $\mu\text{m}$  and the particle centres were estimated to 5  $\mu\text{m}$ , one pixel, the particle displacement can be measured to an accuracy of 2.5% in the absence of other errors.

With both particle pairing and auto-correlations there is a sign ambiguity in the direction of a velocity vector. In both cases a convention has to be defined prior to the analysis. If a flow contains recirculating regions, local rather than global conventions need to be defined, a process which normally requires human interaction. By capturing the first and second exposures on separate frames and either cross-correlating or pairing between the frames the directional ambiguity is removed. Capturing the data on two frames also allows higher seeding densities, and hence higher vector yield, to be used, an important compensation for not taking the high-resolution photographic route.

A bespoke digital camera for PIV applications, a PIV-Cam 10-30 RS-170 digital camera, operating in the 'frame-straddle' configuration, was to be used for image acquisition. The frame-straddle configuration allows two frames to be captured in quick succession, separated only by a few microseconds to allow the charge on the CCD chip to be discharged, a period called the transfer time. The first and second frames integrate over 255 microseconds and 33 milliseconds respectively. Short pulse separations can be

achieved by timing the first and second laser pulses to coincide with the end of the first and beginning of the second frames respectively. This cycle is triggerable and can be repeated at up to 15 Hz. The transfer time is a function of the amount of charge on the CCD chip. If the image is brightly illuminated and saturated the transfer time can be in excess of 10 microseconds. If the mean background grey level is low and the image is sparsely seeded the transfer time can be reduced to less than a microsecond, although intensity may be lost and the first image may bleed into the second.

At the time of the test the PIV-Cam 10-30 failed and an alternative camera system had to be found at short notice. A standard CCIR interlaced camera with a resolution of 576 by 768 pixels was used in its place. To achieve a non-interlaced image the laser has to be fired when both the odd and even fields of the camera are integrating. As the delay until between the asynchronous reset pulse and this non-interlaced integration time was approximately 20 milliseconds the camera was considered to be non-triggerable in this high-speed application. As a result the camera was used as a timing master and hence the image acquisition was not locked to the rotor phase. Judicious use of the camera's field-of-view allowed a resolution of 26  $\mu\text{m}/\text{pixel}$  to be achieved across the stator-rotor gap.

The camera and lens, a Sigma 90 macro lens, were mounted on the framework attached to the optical cassette. The camera has a split body where the CCD housing and lens is remote from main camera body, so could be easily be accommodated on the mounts of the larger PIV-Cam. Despite this, the region of interest still had to be imaged off a front-silvered mirror owing to the space restrictions within containment rings of the facility.

### 6.4 THE PIV SYSTEM

A Lumonics HY400 Q-switched Nd:YAG double pulsed laser was used as the light source. A doubler crystal was fitted to the laser to provide 532 nm wavelength (green) light. The laser output is 50 mJ pulses with duration of 8 nanoseconds at 25 Hz. As the laser contains a single oscillator the pulse separations can only range from a few tens of nanoseconds to about 250  $\mu$ s after which the power diminishes. The laser can also generate triple pulses although this was not explored in this experiment.

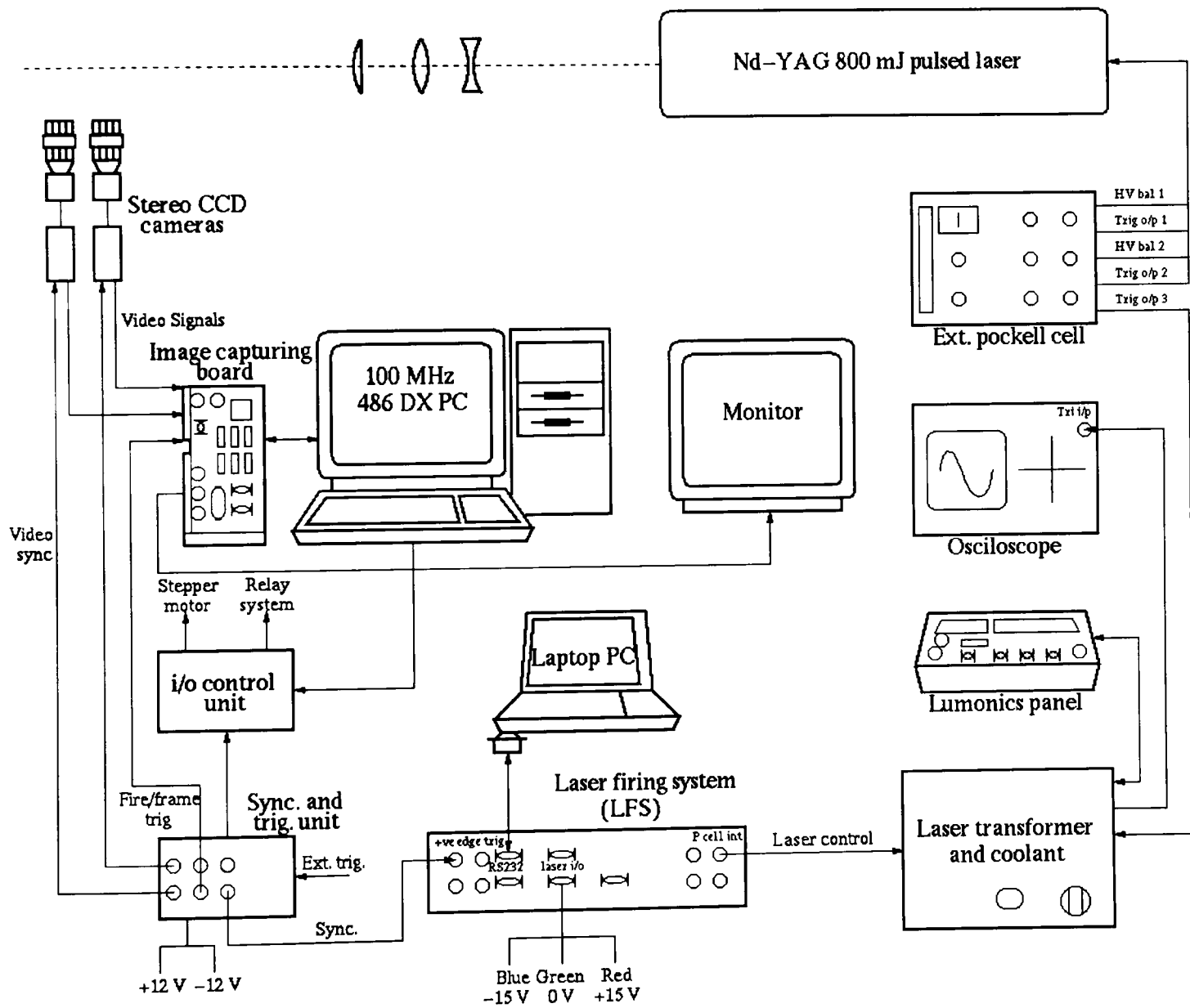


Figure 6.5 Schematic of the PIV system

The camera was connected to a frame-grabber board within a 486DX 100MHz PC, see figure 6.5. This allowed up to 72 frames to be captured at 25 Hz in the grabber board's memory prior to being written to the hard disk. A second camera can be connected to the PIV system to facilitate stereo recording although it was not explored in this application.

The raw data were archived rather than real-time processed to allow the data to be post processed. Although real-time processing systems are commercially available, the preferred in-house processing and presentation algorithms are not suited to real-time use, as they are computationally intensive and not fully automated. Further to this, archiving of the raw data allows spurious results to be investigated and the data recovery to be maximised, even in the presence of varying signal-to-noise ratios.

The laser and image capture systems were synchronised using an external triggering system referred to as the LFS (Laser Firing System). The LFS is an embedded computer system containing precision digital counters, signal conditioning and isolation circuits and digital-to-analogue converters. Upon receiving a remote trigger from the facility the LFS took complete control of the laser firing and video sequence, double pulsing the laser during the full field integration period of the interlaced camera.

## 6.5 SEEDING

A seeding procedure almost identical to that described by Towers [113] was adopted. 0.5  $\mu\text{m}$  styrene seed, suspended in water, was injected into the pump tube prior to pressurising it to the pre-run condition. Towers showed that this combination of seed

and seeder produced a size distribution ranging from 0.4 to 0.65  $\mu\text{m}$  with a mean size of 0.5  $\mu\text{m}$ . The 0.6  $\mu\text{m}$  particles were shown to take approximately 2.2 mm to a step change in velocity (normal shock) or 641 to 114  $\text{ms}^{-1}$ .

The pump tube was seeded for a period of 25 minutes whilst all the jets of the seeder were in operation. The pressure in the pump tube was dropped to 0.9 bar during the seeding process and the run was initiated as quickly as possible after the seeding procedure to minimise the amount of settling of the seed.

## 6.6 SUMMARY OF CHAPTER

The test section window of the ILPF, supplied by Osney Labs., is mounted into a removable cassette that makes up part of the outer casing. It is approximately  $300 \times 200 \text{ mm}^2$  although only of uniform thickness over  $300 \times 100 \text{ mm}^2$ . The contours of the window are matched to the profile of the outer casing to avoid perturbing the flow. The window provides optical access from upstream of the leading edge of the NGVs to beyond the trailing edge of the rotor.

8 mm external diameter optical periscopes inserted into hollow NGVs were used to project light sheets into both the stator passage and stator-rotor gap through windows in both the suction and pressure surfaces. The beam was relayed to the periscopes using a rigid optical system that allowed the ILPF to move in the axial direction without disturbing the beam. A fibre optic beam delivery system was tried but found to be incapable of delivering 50 mJ pulses (8 ns pulse width) for prolonged periods. A frequency doubled Nd:YAG laser (532 nm) was used as the light source.

A CCD camera of resolution  $768 \times 576$  pixels (8 bit) was used to record the PIV data after the cross-correlation camera failed and could not be replaced in time for the test. A resolution of  $26 \mu\text{m}$  per pixel was achieved over the stator-rotor gap. The estimated diffraction limited particle diameter is  $18 \mu\text{m}$ .

$0.5 \mu\text{m}$  styrene seed have been used. In a previous study  $0.6 \mu\text{m}$  styrene seed was shown to take 2.2 mm to respond to a step change in velocity from  $641$  to  $114 \text{ ms}^{-1}$ . The seeder was shown to give a size distribution from  $0.4$  to  $0.65 \mu\text{m}$  with a mean of  $0.5 \mu\text{m}$ . The pump tube of the ILPF was seeded for 25 minutes prior to each run.



## Chapter 7

# APPLICATION OF PIV TO A SPINNING TURBINE CASCADE

-

## RESULTS

### *Description of Chapter*

*This chapter shows the PIV data processed using an auto-correlation. The description of the results, discussion on the choice of processing method, accuracy etc is included in chapter 8.*

*Results for three separate runs of the ILPF are presented although the total data set consists of 20 runs, each with approximately 20 valid frames of data. Figures 7.1 to 7.5 are all made in the region of the trailing edge of the NGVs to the leading edge of the passing rotor. The figures show the effect the passing rotor has on the velocity distribution. Figures 7.6 and 7.7 show measurements in the stator passage and between the suction surface of the NGV and the leading edge of the rotor. Figure 7.1 to 7.7 use a common colour bar for comparison. Figures 7.1 to 7.7 have been subjected to one 'centroid-node' smoothing iteration, described in chapter 8. Figure 7.8 shows vectors combined from the stator passage and stator-rotor gap for comparison against a CFD prediction. These data have not been smoothed. All data are of single instantaneous frames. The discussion of these results appears in chapter 8.*

*The Reynolds number for all the measurements is  $2.8 \times 10^6$ , based on the axial chord on the NGVs and downstream conditions.*

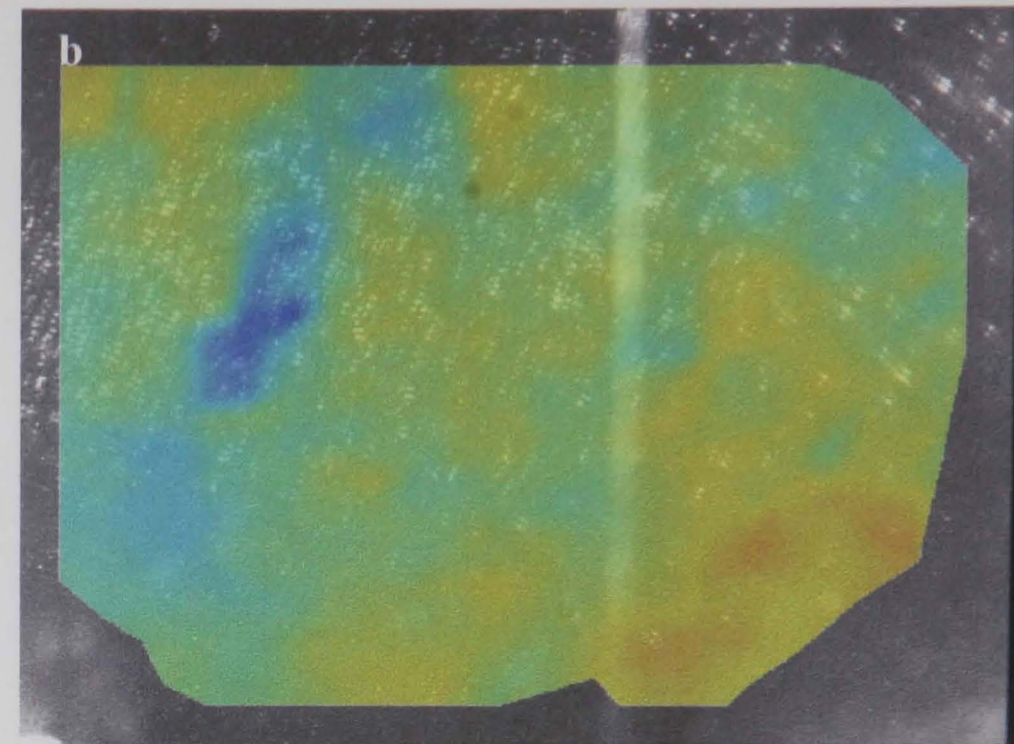
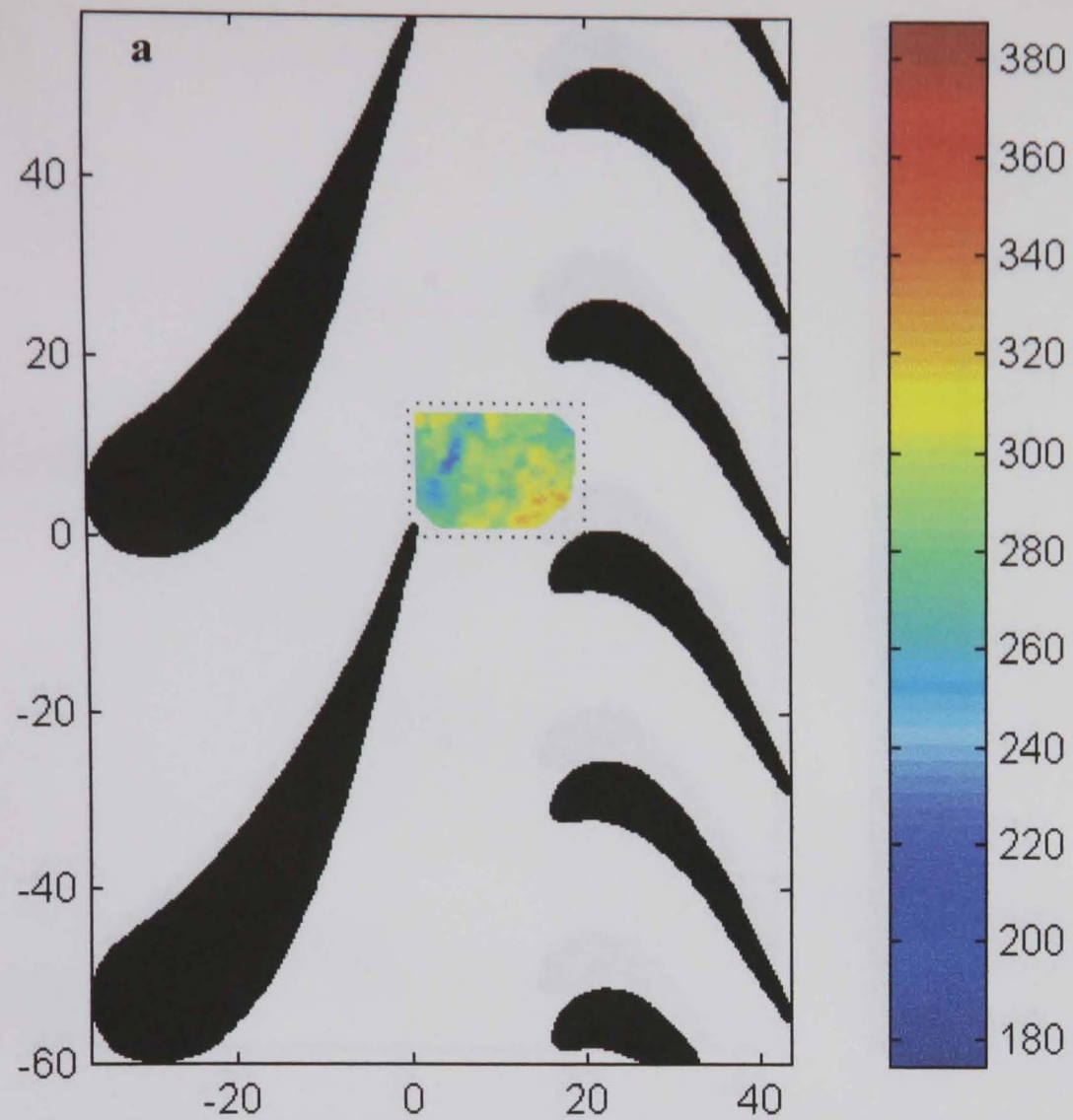


Figure 7.1. Example of the data set recorded between the ngvs. Colour bar is in  $\text{ms}^{-1}$ , Coordinates are in mm. Processed using autocorrelation (64 x 64 pixels).

- a. Region of interest between the ngvs
- b. Velocity surface generated using a Delaunay triangulation overlaying the raw piv image
- c. Velocity vectors overlaying the raw piv image. Colour and magnitude represent the magnitude of the velocity



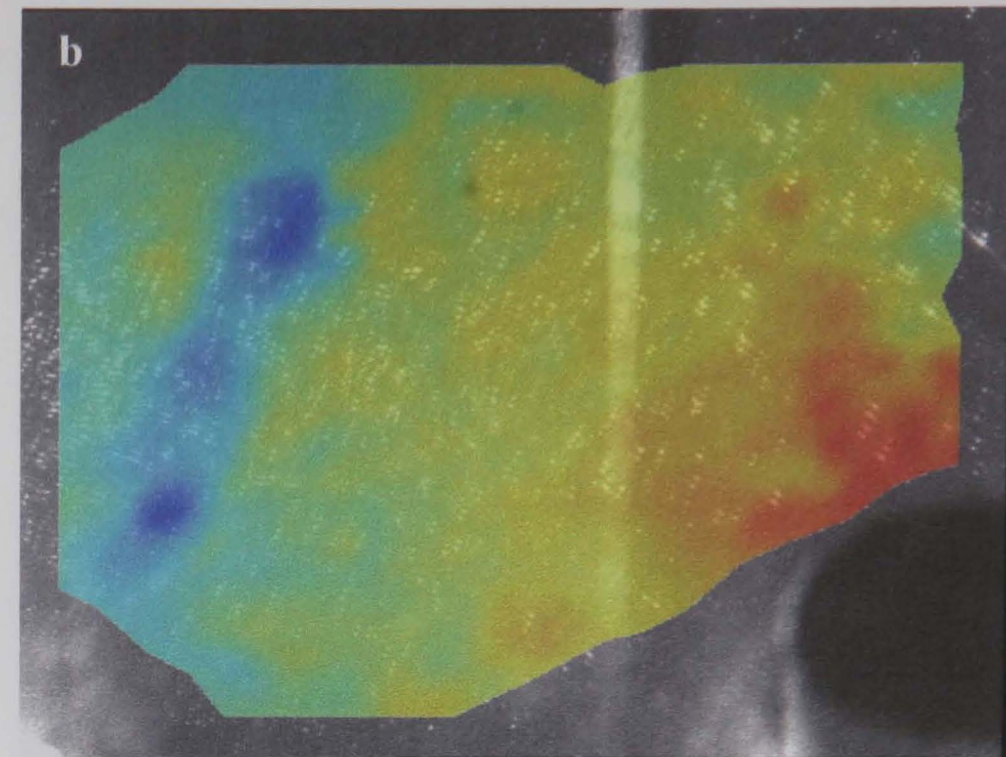
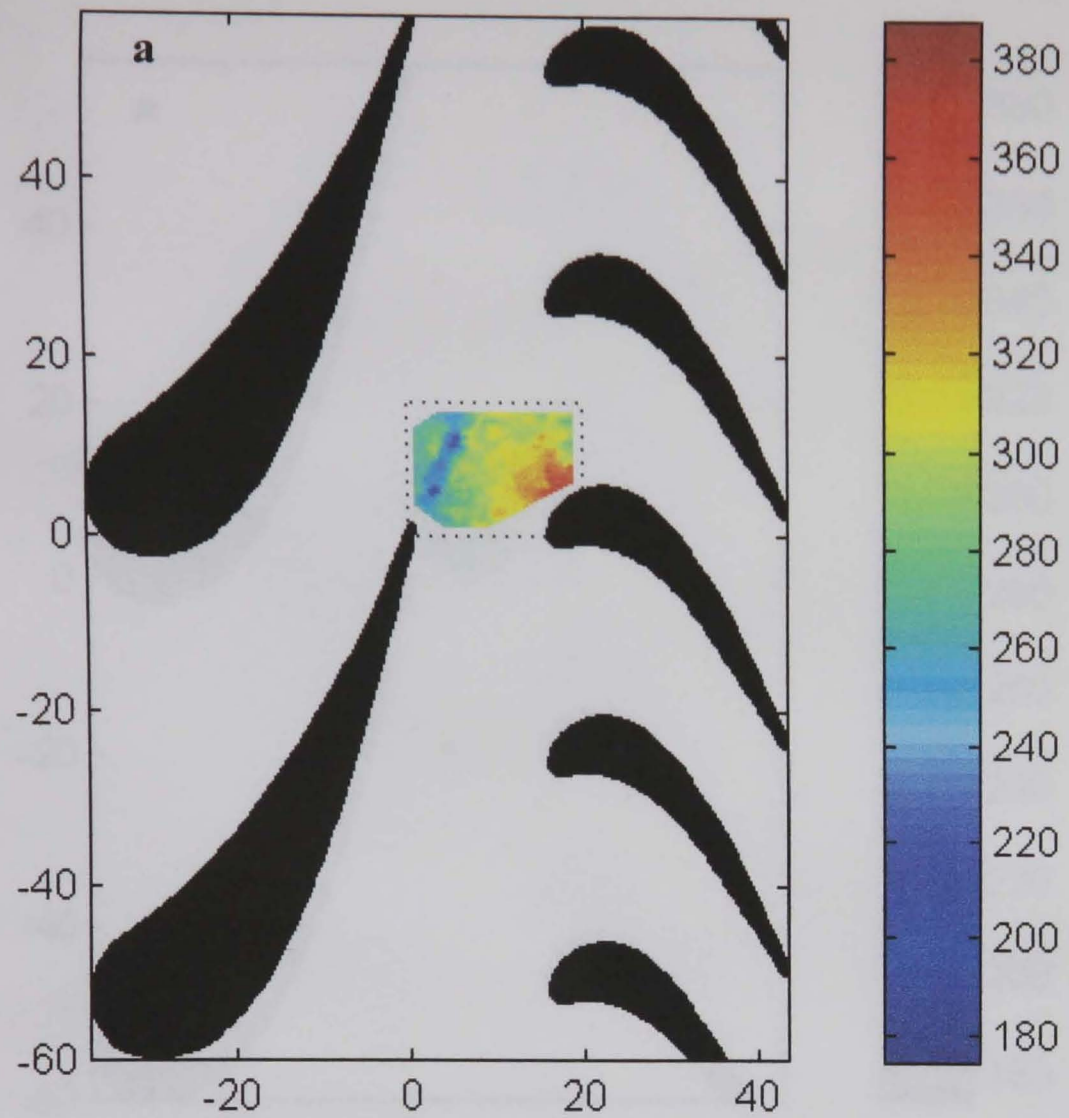


Figure 7.2. Example of the data set recorded between the ngvs. Colour bar is in  $\text{ms}^{-1}$ , Coordinates are in mm. Processed using autocorrelation (64 x 64 pixels).

- a. Region of interest between the ngvs
- b. Velocity surface generated using a Delaunay triangulation overlaying the raw piv image
- c. Velocity vectors overlaying the raw piv image. Colour and magnitude represent the magnitude of the velocity



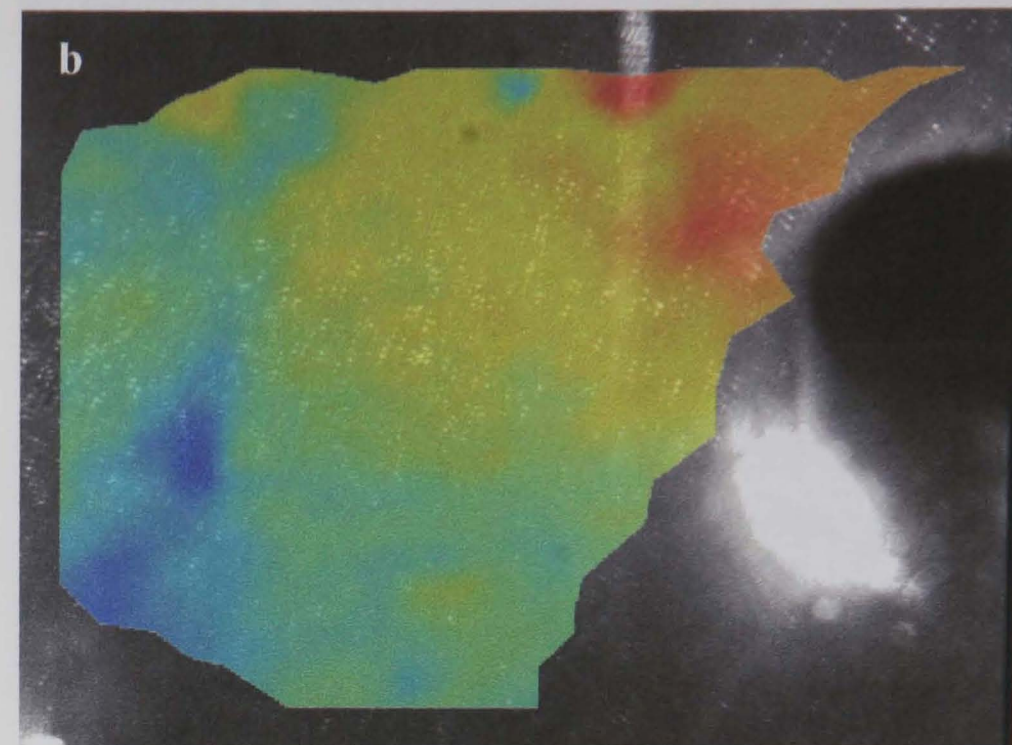
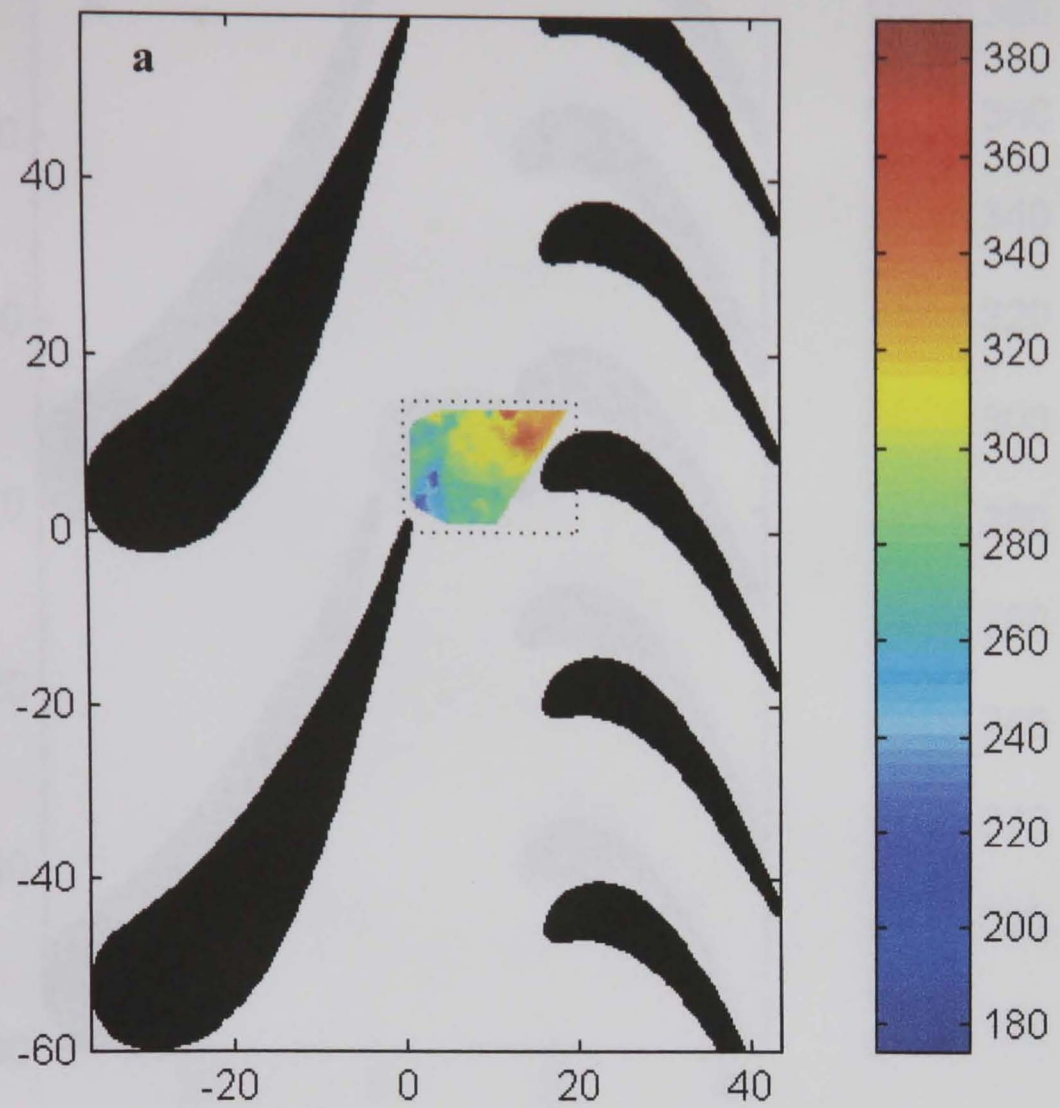


Figure 7.3. Example of the data set recorded between the ngvs. Colour bar is in  $\text{ms}^{-1}$ , Coordinates are in mm. Processed using autocorrelation (64 x 64 pixels).

- a. Region of interest between the ngvs
- b. Velocity surface generated using a Delaunay triangulation overlaying the raw piv image
- c. Velocity vectors overlaying the raw piv image. Colour and magnitude represent the magnitude of the velocity



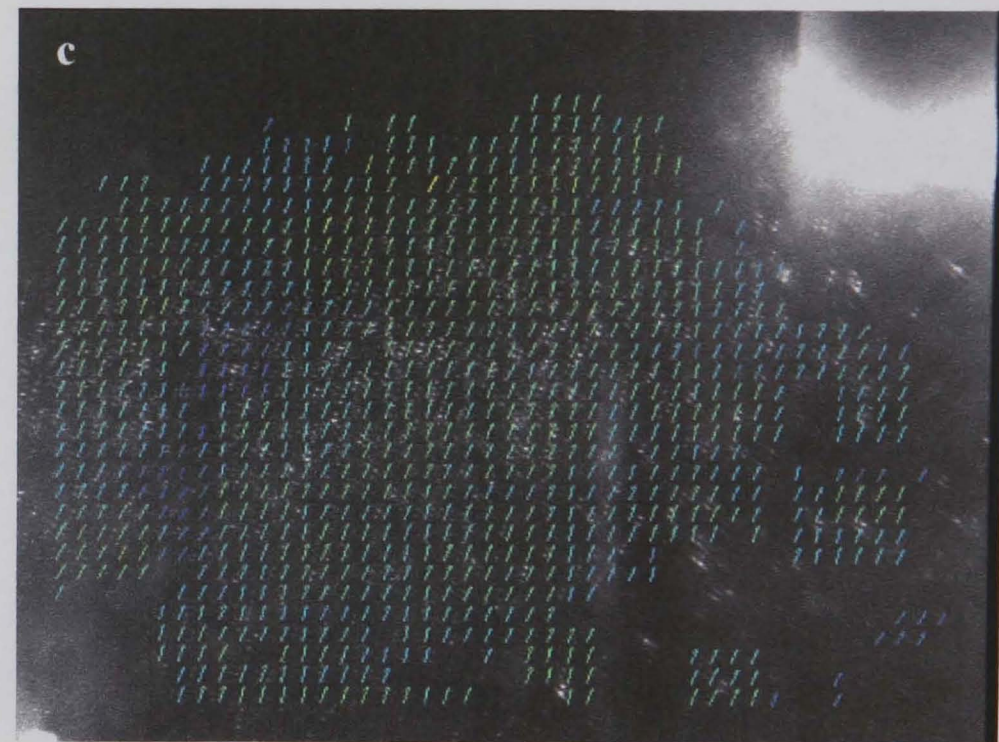
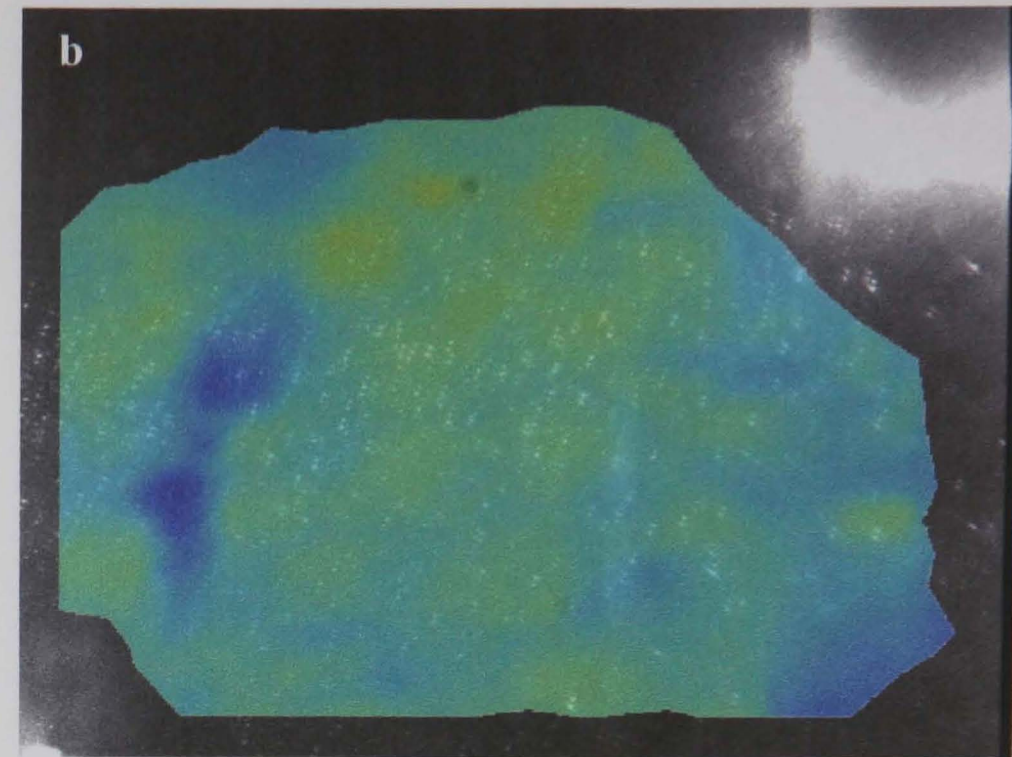
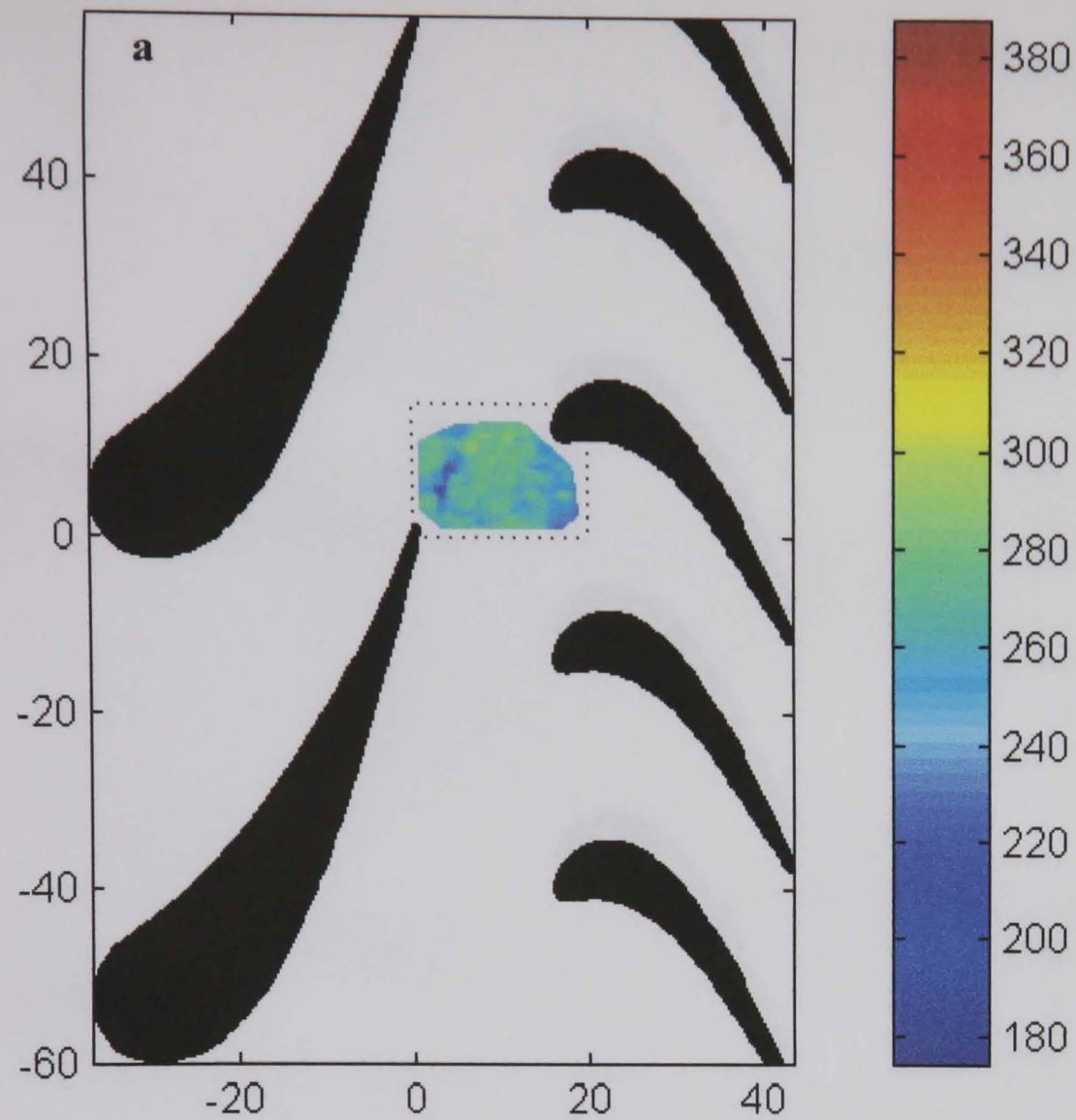


Figure 7.4. Example of the data set recorded between the ngvs. Colour bar is in  $\text{ms}^{-1}$ , Coordinates are in mm. Processed using autocorrelation (64 x 64 pixels).

- a.** Region of interest between the ngvs
- b.** Velocity surface generated using a Delaunay triangulation overlaying the raw piv image
- c.** Velocity vectors overlaying the raw piv image. Colour and magnitude represent the magnitude of the velocity



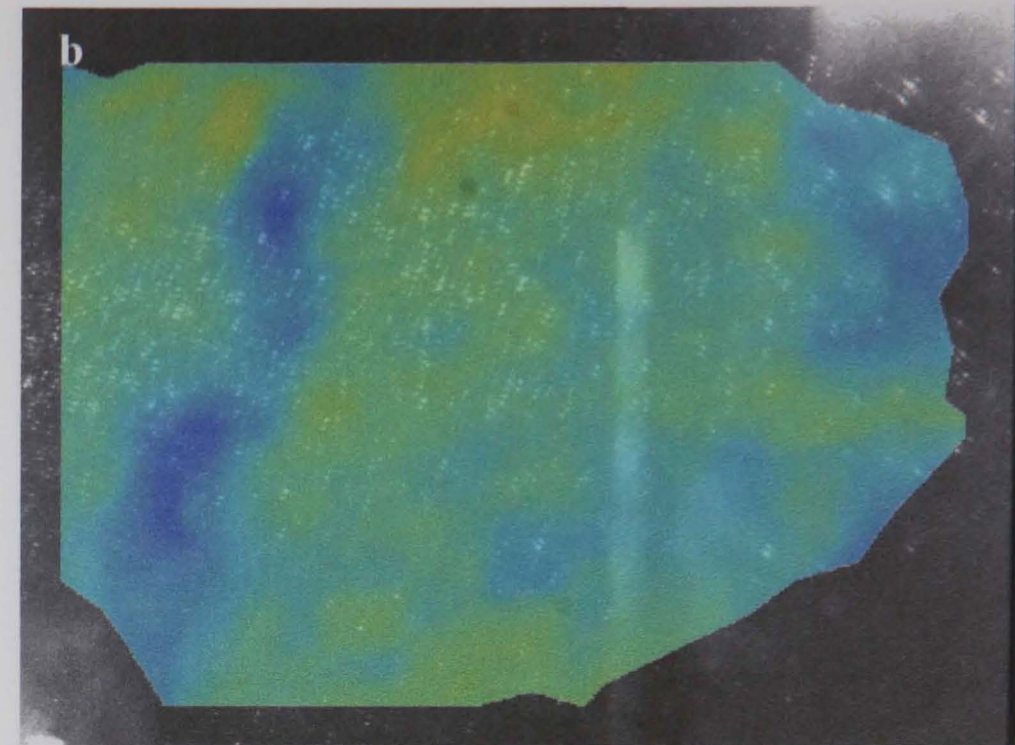
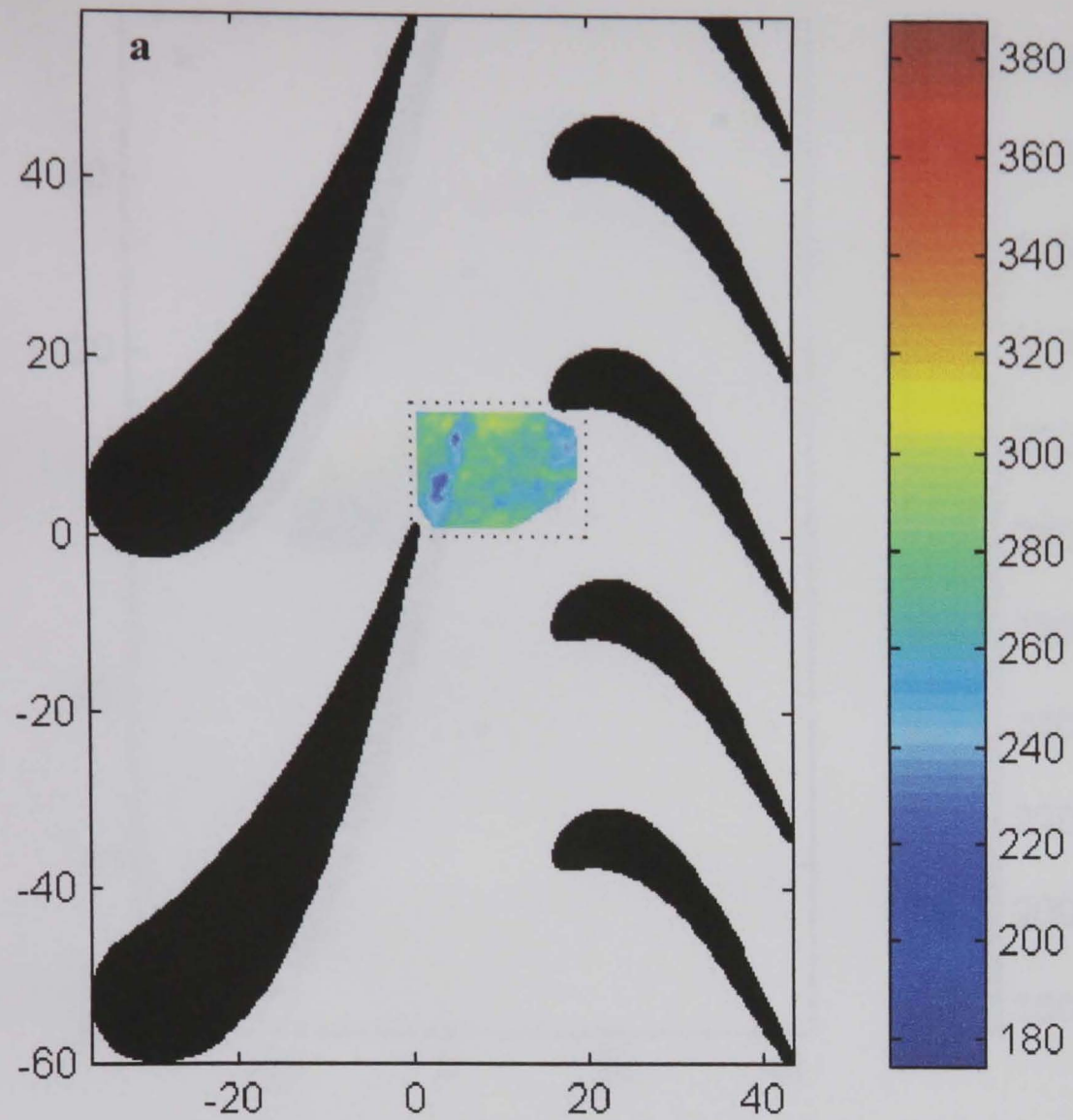


Figure 7.5. Example of the data set recorded between the ngvs. Colour bar is in  $\text{ms}^{-1}$ , Coordinates are in mm. Processed using autocorrelation (64 x 64 pixels).

**a.** Region of interest between the ngvs

**b.** Velocity surface generated using a Delaunay triangulation overlaying the raw piv image

**c.** Velocity vectors overlaying the raw piv image. Colour and magnitude represent the magnitude of the velocity



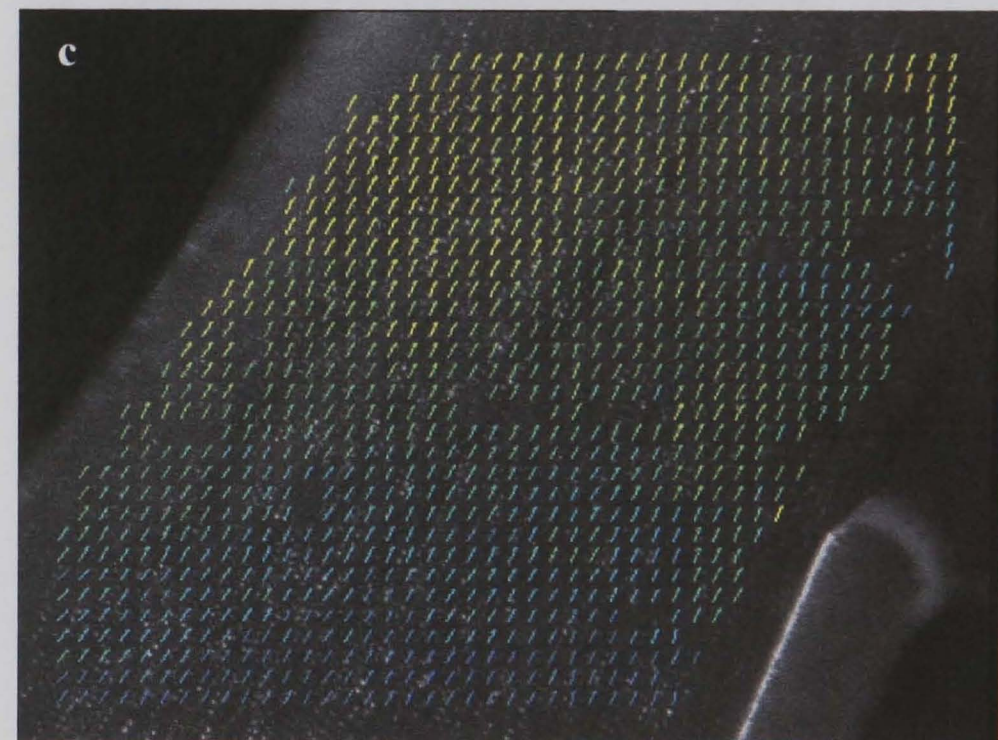
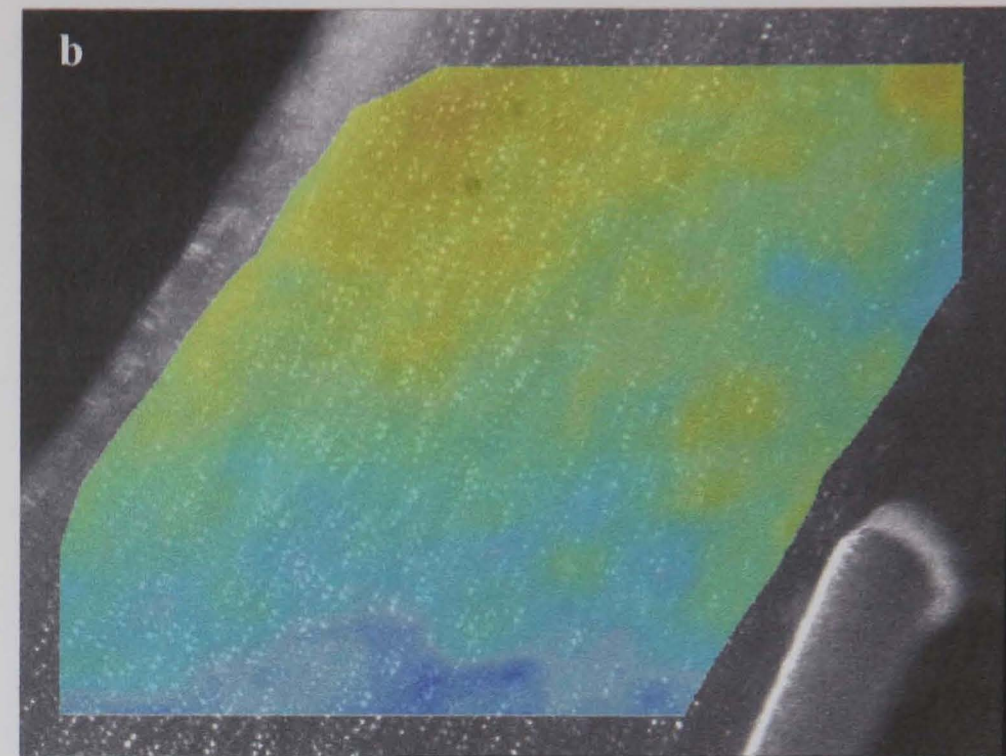
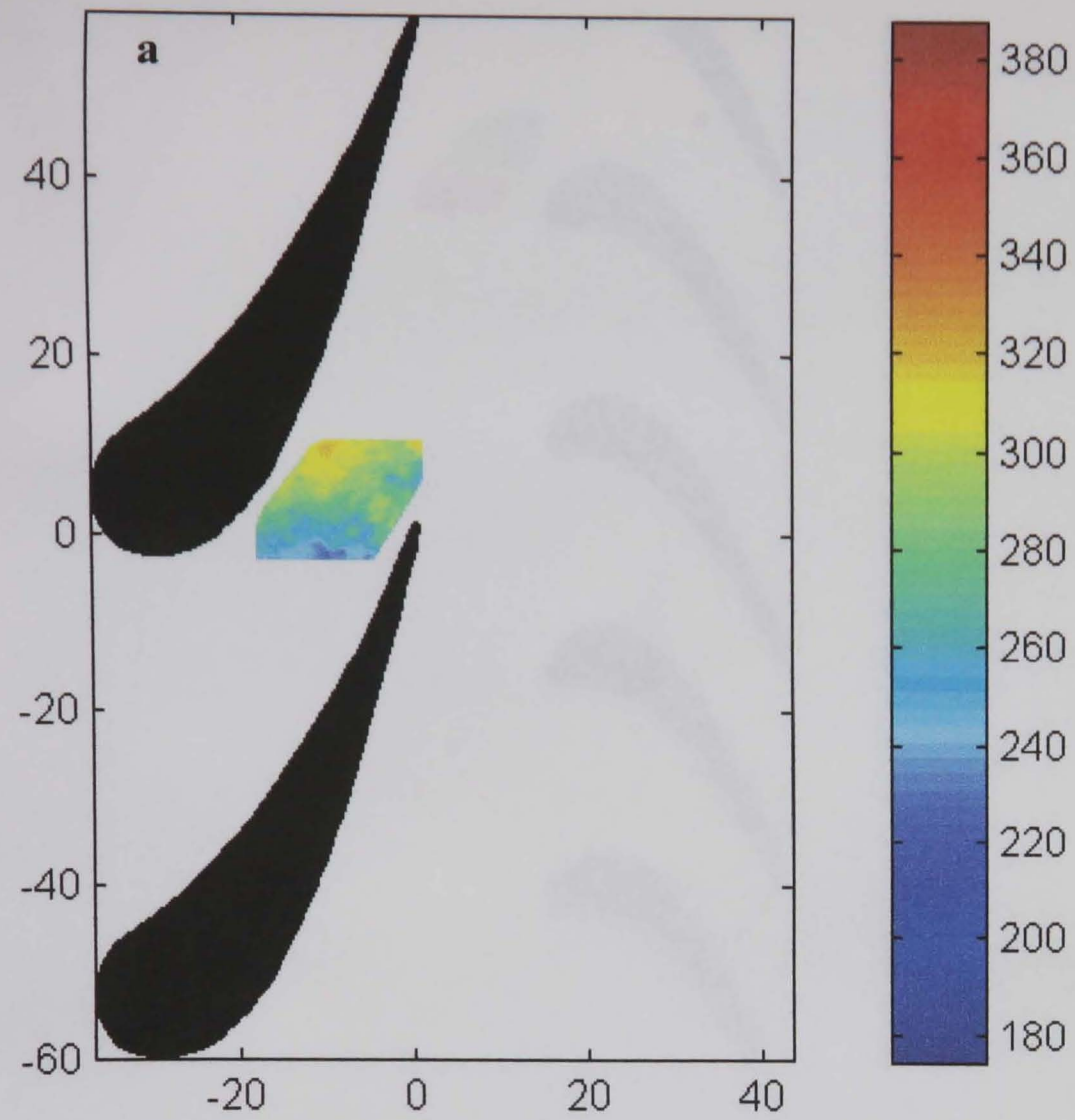


Figure 7.6. Example of the data set recorded between the ngvs. Colour bar is in  $\text{ms}^{-1}$ , Coordinates are in mm. Processed using autocorrelation (64 x 64 pixels).

- a. Region of interest between the ngvs
- b. Velocity surface generated using a Delaunay triangulation overlaying the raw piv image
- c. Velocity vectors overlaying the raw piv image. Colour and magnitude represent the magnitude of the velocity



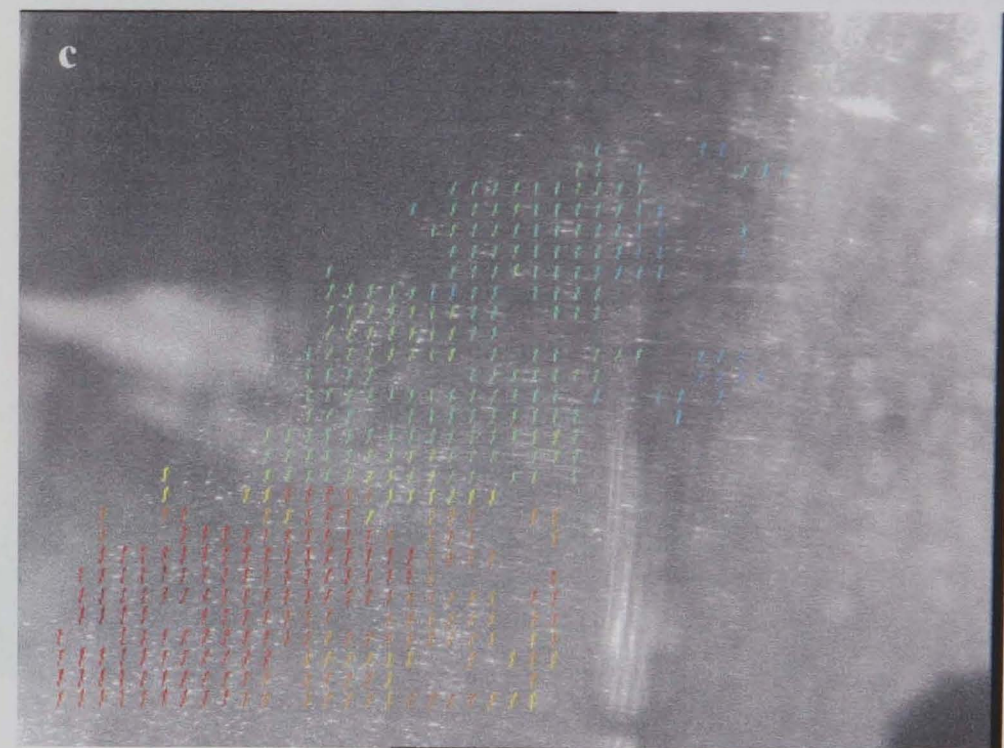
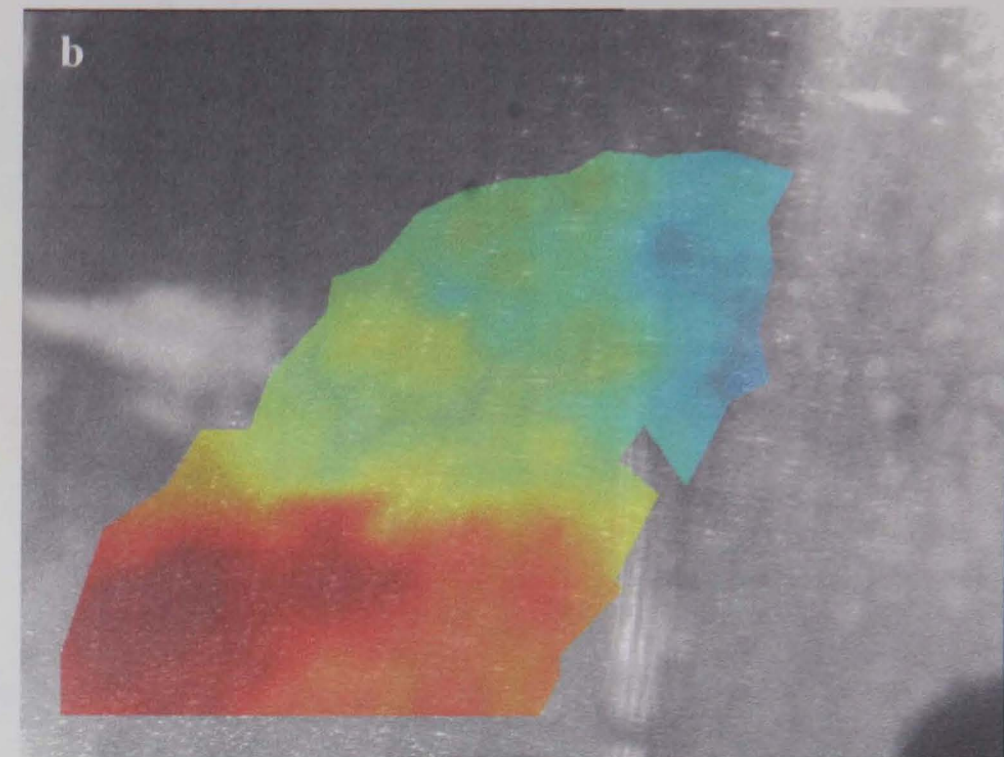
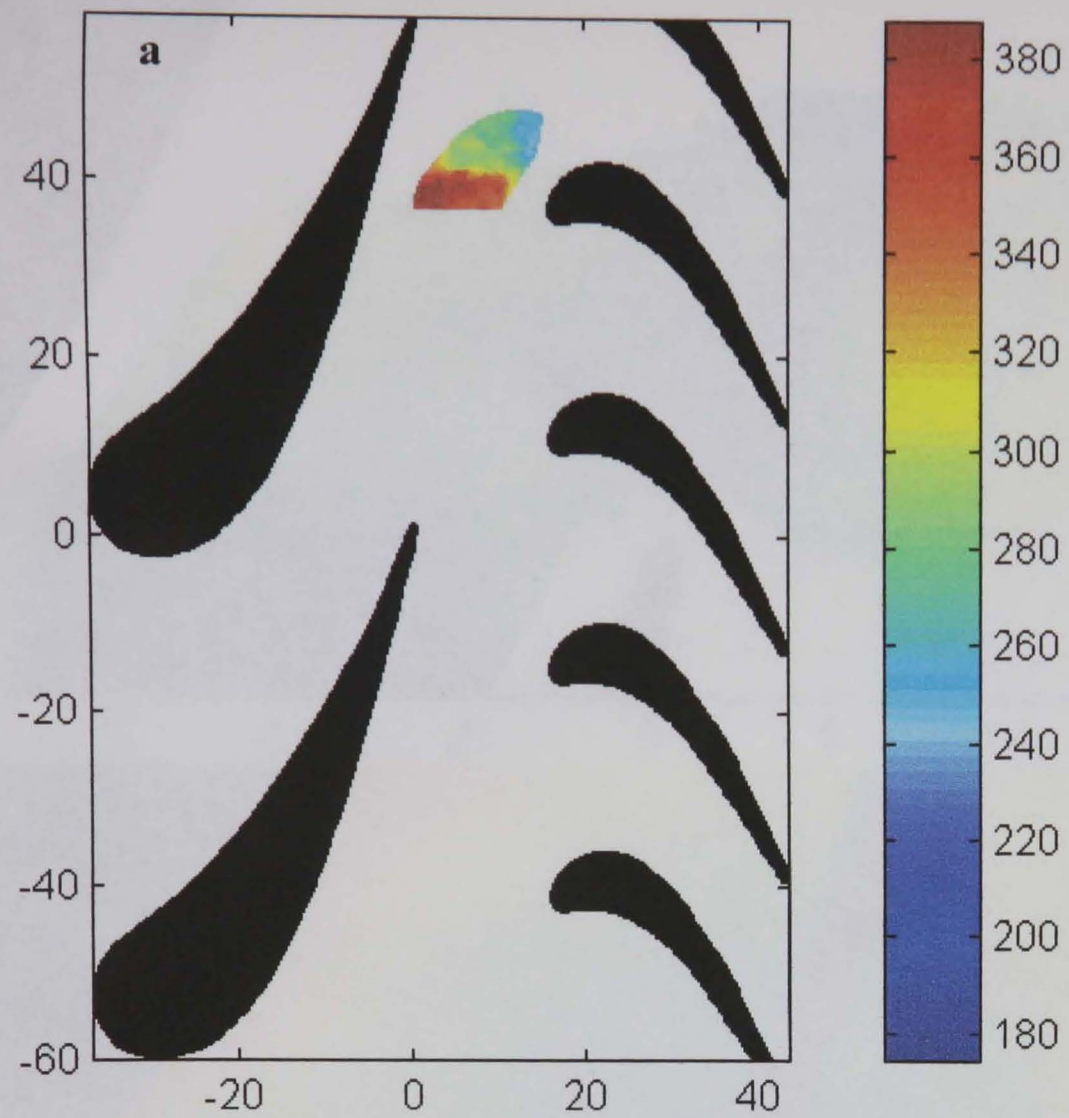


Figure 7.7. Example from the brief data set recorded from the higher of the two optical periscopes. Solutions from a single image shown in the background. Colour bar in  $\text{ms}^{-1}$

- a. The region of interest and the approximate rotor phase
- b. Velocity surface generated using a Delaunay triangulation overlaid the raw piv image
- c. Velocity vectors overlaid the raw piv image. Colour and magnitude represent the magnitude of the velocity



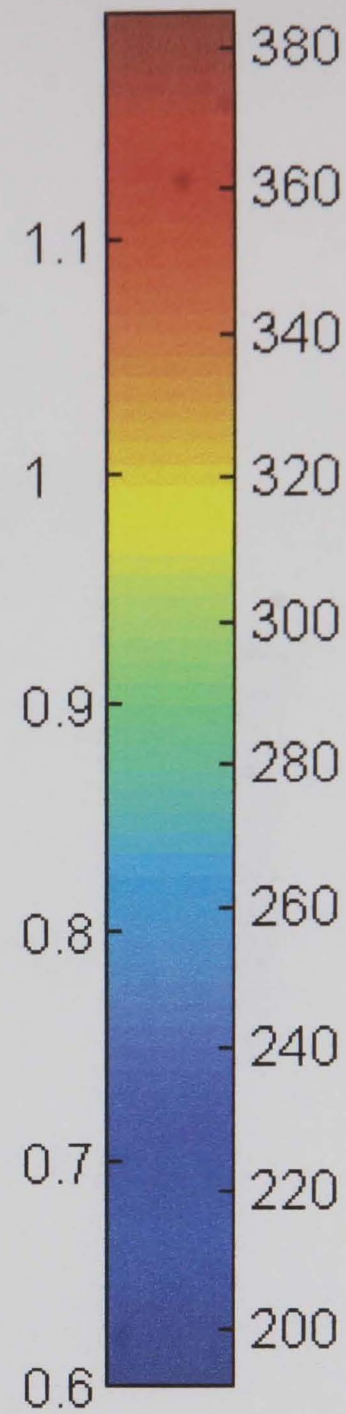
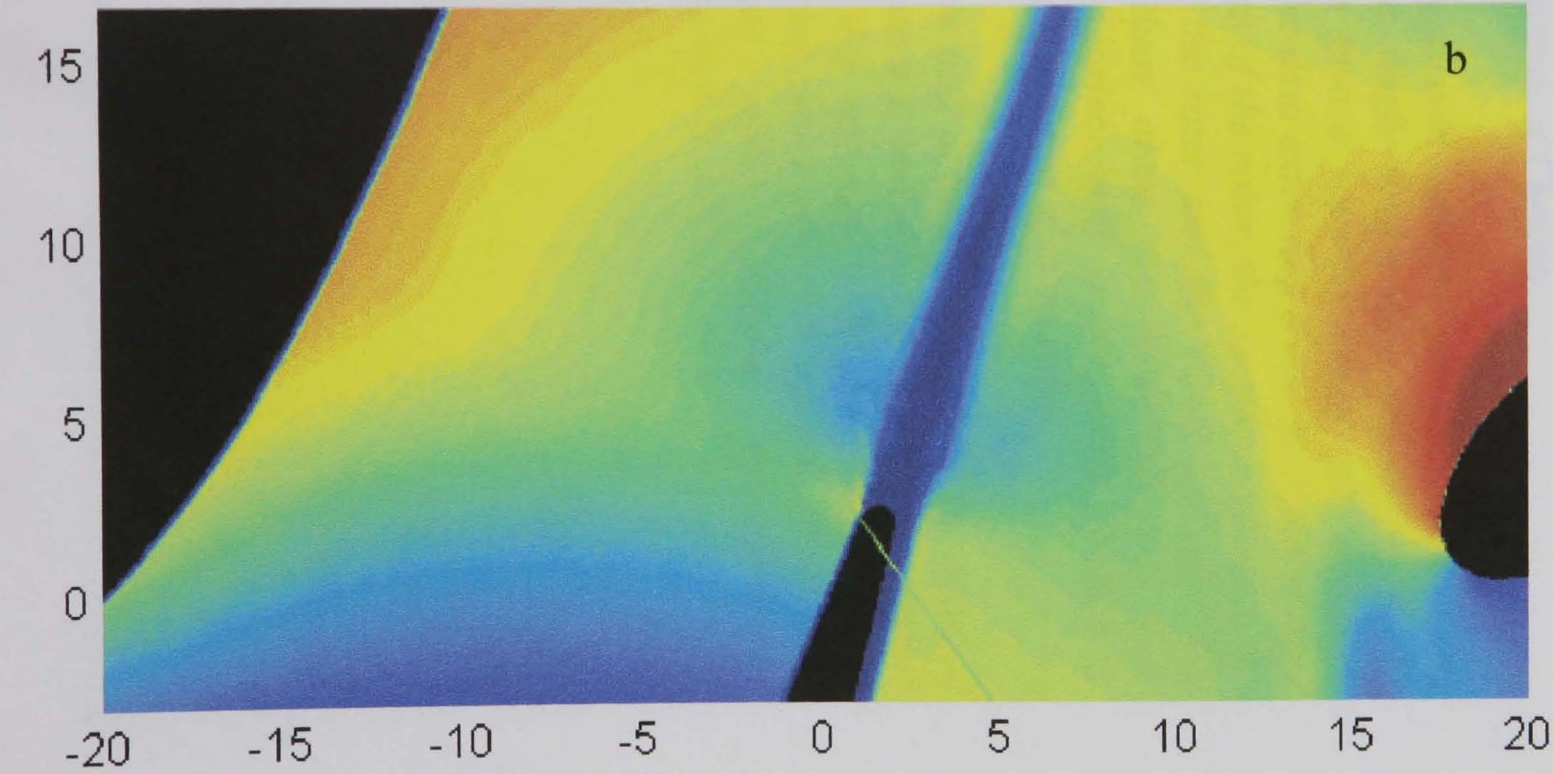
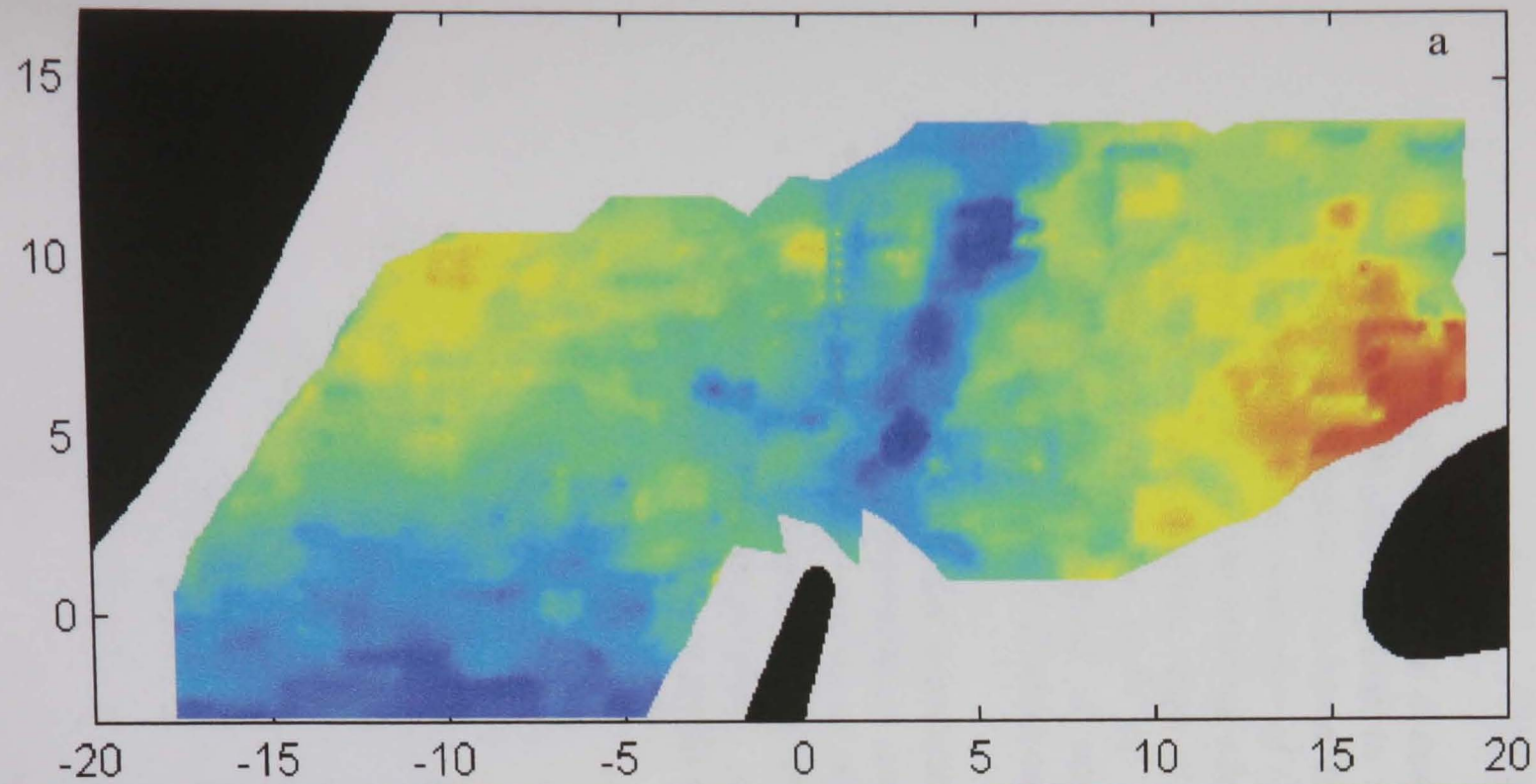


Figure 7.8 Measurement and prediction. Colour bar shows both Mach number and velocity in ms<sup>-1</sup>.

- a. Measured, two combined frames that slightly overlap. Individual images shown in figures 7.2 and 7.6
- b. Predicted, unsteady and 2-D.(Unflow). Taken from Giles<sup>[128]</sup>.

## Chapter 8

# THE APPLICATION OF PIV TO A SPINNING TURBINE CASCADE

-

## DISCUSSION

### *Description of Chapter*

*This chapter describes a comparison between particle tracking and auto-correlation applied to a single image recorded in the ILPF. Auto-correlation is shown to give a superior result and has been applied to the remainder of the data extending from the trailing edge of the NGV to the leading edge of the rotor, the suction surface of the NGV to the leading edge of the rotor and the stator passage. The measurements in each of these areas are described and their accuracies quantified. A comparison with a numerical prediction, produced using a 2-D unsteady solver, is also included.*

*The relative spatial resolution and accuracy that could be attained with the cross-correlation camera is included for comparison against the camera that was used in this application. Recommendations are also made towards optimising accuracy and spatial resolution, making time-averaged and phase stepped measurements, measurements close to surfaces and 3-D PIV.*

## 8.1 VECTOR EXTRACTION

A single representative image has been processed using both particle tracking and auto-correlation in order to identify the optimum vector yield and accuracy per image. This task was embarked upon after tests on the nozzle flow indicated that a correlation approach may be superior to the tried and tested particle tracking software that had previously been used at Warwick.

### 8.1.1 Particle Tracking

The particle tracking software applied to the test image, figure 7.5 (turb5\_27.tif), was AP2D <sup>[125]</sup>, a development of Judge's APWin program <sup>[109]</sup>. AP2D uses a centre-of-mass centroid estimation to ascertain the particle centres.

The pairing process consists of identifying individual particles and their centroids. Minimum and maximum velocities and approximate direction are required to identify a segment within which the second exposure must fall. Erroneous vectors will be generated if multiple exposures exist in the segment. This prerequisite defines the upper limit on the seeding concentration and is therefore only applicable to sparse data.

### 8.1.2 Auto-Correlation

The auto-correlation software was PIV Proc, kindly supplied by Wernet <sup>[127]</sup>. PIVProc uses a 3-point Gaussian estimator to locate the centre of the satellite peaks in the auto-correlation plane. The estimated accuracy of the centroid location is  $1/10^{\text{th}}$  pixel assuming that the particle image diameters are 1 to 2 pixels in diameter and each

interrogation spot contains about 10 particle pairs. A high seeding concentration is required to satisfy this prerequisite.

### 8.1.3 Comparison of Results generated using Particle Tracking & Auto-Correlation

Figure 8.1 shows the scatter of the components of particle displacement in pixels. It is immediately obvious that the tracking vectors are grouped into bands. This is believed to be due to a bias in the centre-of-mass estimation to integer pixel values. As the mean displacement between successive exposures is only 5.6 pixels the accuracy is only 18 %. The vector yield is 501 vectors. The scatter of the data indicates a large number of spurious vectors.

The auto-correlated data contains 1020 vectors with displacements that do not appear to be banded into discrete displacements or randomly scattered. The location of the vectors is banded owing to the regular grid interrogation spots of 64 x 64 pixels with a 75 % overlap. The auto-correlation software offers both the highest vector yield and accuracy in the displacement, albeit by calculating a local average velocity rather than an individual pairing.



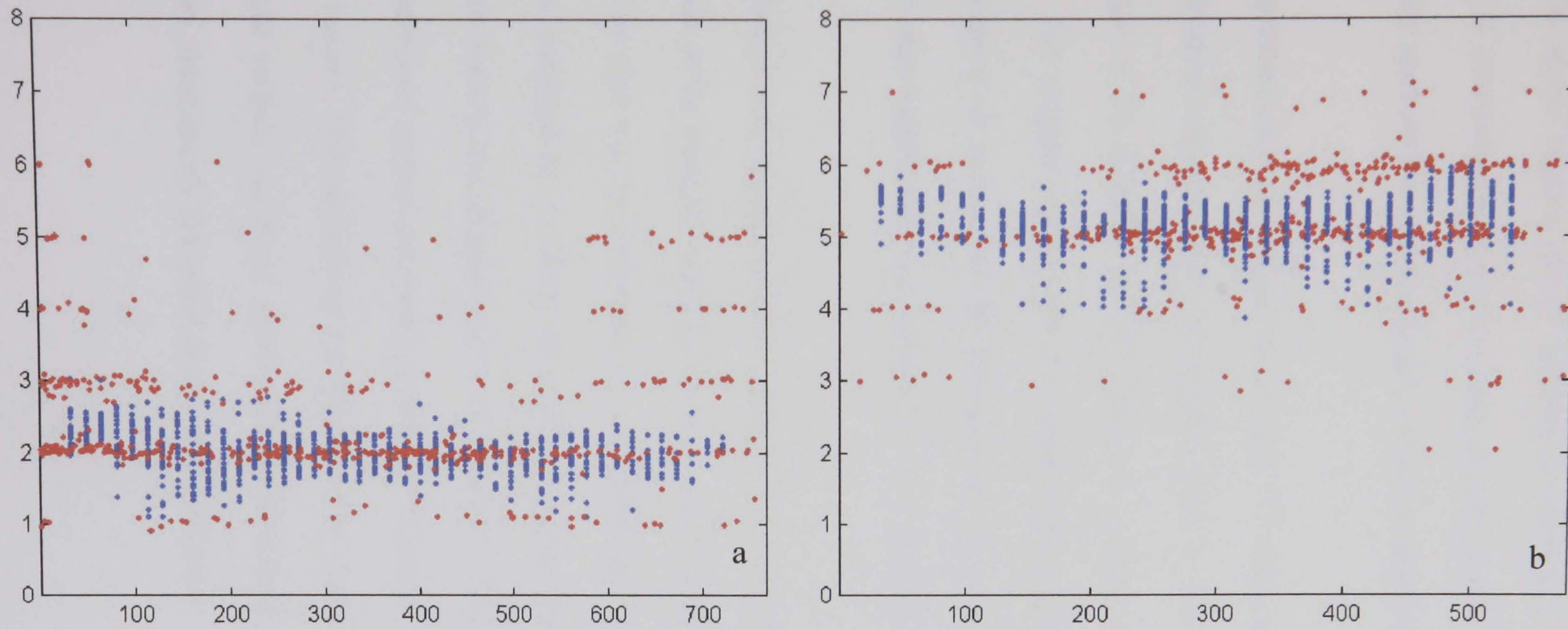


Figure 8.1 Scatter of the PIV data processed by **particle tracking** and **auto-correlation**  
 a. 'x' component of displacement in pixels versus 'x' co-ordinate  
 b. 'y' component of displacement in pixels versus 'y' co-ordinate



## 8.1.4 POST PROCESSING

A novel meshing algorithm has been written to produce a continuous velocity surface from the sparse vectors (script included in appendix). The algorithm was originally written to interpolate between the sparse vectors produced during particle tracking, but is equally applicable to the regular grid of vectors produced by auto-correlation.

The algorithm uses a Delaunay triangulation<sup>[110]</sup> where the nodes of the mesh represent the individual velocity vectors, see figure 8.3a & b. A linear interpolation is used along the edges of the triangles and the surface is a linear interpolation between the three nodes. The original vectors are not compromised as they are kept in the solution. Extrapolation is avoided as the triangulation only links existing vectors. Excessive triangle edge lengths can also be identified and removed automatically.

The interpolation procedure can be extended to calculate a further vector, or node, at the centroids of the triangles weighted according to the three surrounding nodes, see figure 8.3c. The data can be smoothed by calculating the velocity at the centroid of each triangle weighted by its three surrounding neighbours and interpolating between the centroids back to the original nodes, see figure 8.2. This smoothing operation has been frequently used on data produced by particle tracking as it crops the peaks of individual rogue vectors. This smoothing procedure is less applicable to correlated data as the erroneous vectors, which are usually readily identifiable due to extreme magnitude or direction, are routinely discarded at the correlation stage.

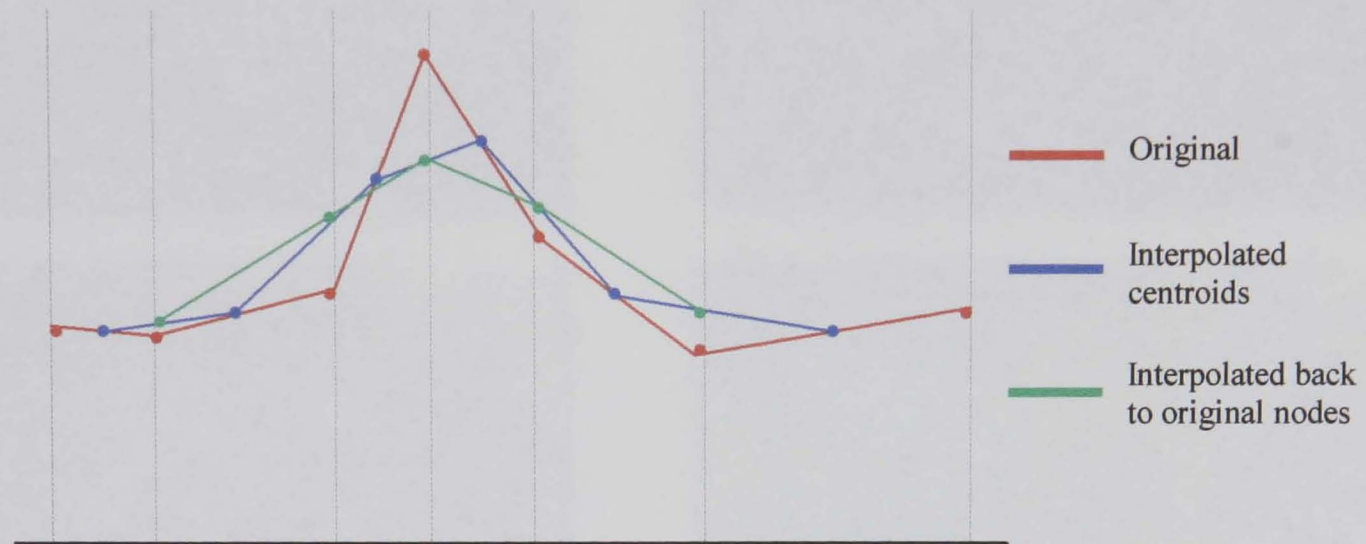


Figure 8.2 The affect of the smoothing over a velocity plot. Red line is the interpolation between red dots that represent the original vectors. Blue dots represent interpolated velocity at centroids. Green dots represent interpolation between centroids at the original vector locations.



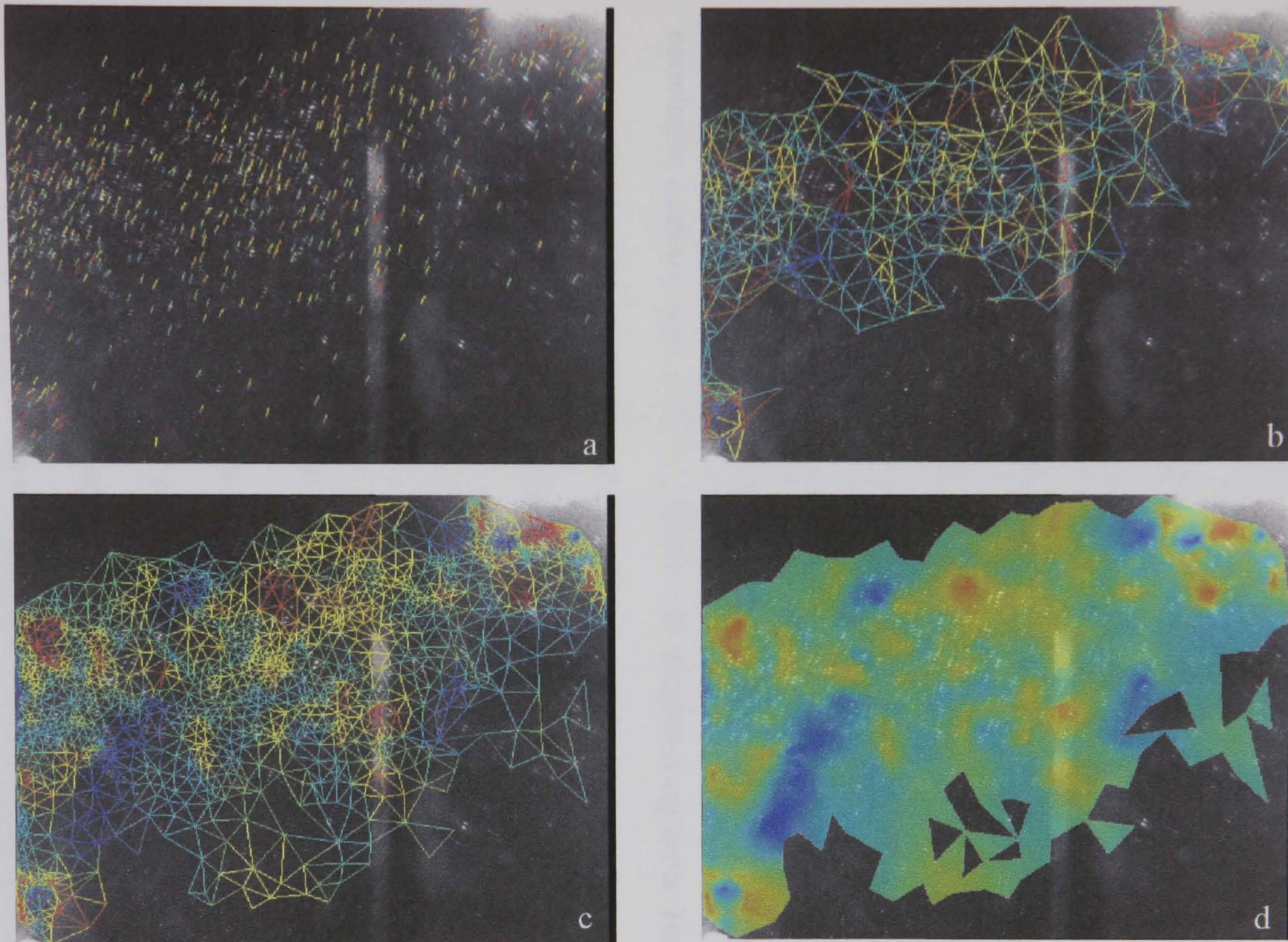


Figure 8.3. Post processing of the velocity data (taken from figure 7.5)

- a. Location of the sparse vectors produced using particle pairing (turb5\_27)
- b. Delaunay triangulation of the sparse vectors (edges over 50 pixels removed).
- c. Refined Delaunay mesh. Additional nodes at centroids of original triangles.
- d. Linear interpolation along triangle edges, Surface interpolated with respect to all three nodes

## 8.2 DESCRIPTION OF RESULTS

Figures 7.1 to 7.7 show single, instantaneous, images plotted in three different ways to expedite the representation of the velocity distribution and the underlying particle concentration. The first of the plots is used to show the region of interest and the approximate rotor phase. The rotor phase is estimated from the position of the rotor in the raw image. In the second plot the interpolated velocity distribution, produced using Delaunay triangulation, one smoothing iteration and one centroid-node iteration, has been plotted over the original raw image. The velocity distribution is slightly transparent so that the underlying seeding concentration or noise can be used to ascertain the confidence of the local velocity. Sparsely seeded or noisy areas can produce erroneous or inaccurate vectors. Finally, a vector plot, again overlaying the original raw image, shows the output from the auto-correlation analysis. The regular grid of vectors correspond to the 64 x 64 pixel interrogation spots used in the auto-correlation analysis, with a 75 % overlap with neighbouring spots. Holes in the grid occur owing to noise and a lack of seed. Both the colour and magnitude of the vectors are used to represent the magnitude of the velocity.

### 8.2.1 Trailing edge of NGV to leading edge of rotor

Figures 7.1 to 7.5 show the velocity distribution between trailing edge of the NGV and the leading edge of the rotor as the rotor passes upwards through the field-of-view. The sequence also shows the scanning of the light sheet between frames as the laser comes up to temperature. The parameters of the analysis, errors etc. are summarised in table

8.1

The wake of the NGV can be clearly seen in all of the images in the sequence. The wake of the lower NGV can also be seen in figures 7.4 and 7.5 in the absence of the rotor. Where the rotor is present the flow accelerates over its crown to a velocity of  $380 \text{ ms}^{-1}$ . Two thirds of the way across field-of-view is a gap between the stationary NGV inner annulus and the rotor hub. A small amount of oil seeps from this gap during the run and gathers on the downstream side of the window, aberrating the image. The test section window was removed after every two runs for cleaning and to treat it with a coating of car windscreen demisting agent. It is difficult to get seeding in boundary layers and wakes. Holes in vector grid round the trailing edge of the NGV are common in all of the images in the sequence. All the images clearly show the slow NGV wake, but in most the interpolation algorithm has spanned across the gaps in the vector grid and artificially generated holes in the wake. Nevertheless, the cells in the wake are present in every picture of the sequence and are consistent with the expected position and size of the wake. The spacing of the cells does not coincide with the nodes of the correlation grid implying that they are not a feature of the vector extraction algorithm.



Figure	7.1	7.2	7.3	7.4	7.5
Filename	Turb5_25	Turb5_28	Turb5_26	Turb5_29	Turb5_27
Estimated Relative Rotor Phase	0°	1.3°	2.5°	4.2°	4.9°
Run Number	1943				
Reynolds Number	$2.8 \times 10^6$				
Height	Mid-span				
Total temperature	315 K				
Number of vectors	1073	1052	798	914	1020
Pulse separation (ns)	539				
Y scaling	26.12 $\mu\text{m}/\text{pixel}$				
X scaling	25.97 $\mu\text{m}/\text{pixel}$				
Scaling used	26.04 $\mu\text{m}/\text{pixel}$				
Scaling error	0.3 %				
Field-of-view	20 x 15 mm				
Interrogation spot size	64 x 64 pixels, 1.66 x 1.66 mm				
Interrogation spot overlap	75 %				
Mean particle displ.	5.6 pixels, 146 $\mu\text{m}$				
Image displ. accuracy	5.40 %				
Estimated total accuracy (scaling + image displ.)	5.70 %				

Table 8.1 Parameters for PIV data in stator-rotor gap



## 8.2.2 Stator passage

Figure 7.6 shows the velocity distribution in the stator passage. As the rotor phase is unknown its silhouette has been excluded from figure 7.6a. The direction of the light sheet propagation is approximately in the direction of the walls of the neighbouring NGVs. There is, therefore, little glare in the image and the seed is clearly visible. The seed is also visible in high concentrations, thus giving very few holes in the grid of vectors. The parameters of the analysis, errors etc. are summarised in table 8.2.

The flow is accelerating through the stator passage except for adjacent to the trailing edge of the lower NGV where the flow decelerates from  $300$  to  $250 \text{ ms}^{-1}$  in a line normal to the vane's chord. The velocity is recovered 2 to 3 mm downstream.

Figure	7.6
Filename	Stat2_26
Run number	1953
Reynolds Number	$2.8 \times 10^6$
Height	Mid-span
Total temperature	315 K
Number of vectors	1016
Pulse separation	840 ns
Scaling (parallel to chord)	26.66 $\mu\text{m}/\text{pixel}$
Scaling (normal to chord)	28.15 $\mu\text{m}/\text{pixel}$
Scaling used	27.40 $\mu\text{m}/\text{pixel}$
Scaling error	2.7 %
Field-of-view	21 x 15.7 mm
Interrogation spot size	64 x 64 pixels, 1.75 x 1.75 mm
Interrogation spot overlap	75 %
Mean particle displ.	8.5 pixels, 233 $\mu\text{m}$
Image displ. Accuracy	3.60%
Estimated total accuracy (scaling + image displ.)	6.3%

Table 8.2 Parameters for the PIV data in the stator passage.

### 8.2.3 Suction surface of NGV to leading edge of rotor

Figure 7.7 shows the velocity distribution three-quarters of the way down the suction side of an NGV with the field-of-view extending to the leading edge of the rotor. This field-of-view was only measured over two runs, therefore the data set in this area is limited. The light sheet launch position was common to that used for the stator passage measurements shown in figure 7.6. This is essentially the same light sheet, but further downstream, and is limited in width due to the walls of the NGVs (the beam originated from the leading edge of an NGV). The parameters of the analysis, errors etc. are summarised in table 8.3.

The visible seeding concentration is low and the background noise is high owing to glare from a rotor that has passed through the field-of-view and the oil that has gathered on the window downstream of the rotor hub gap. The silhouette of the next rotor can just be seen in the bottom right hand corner. There is a further feature, expected to be a shock, in the background image that appears to be emanating from the NGV and gets wider but dimmer towards the centre of the image. The line of action of this shock coincides with the rapid deceleration in the velocity data from  $370$  to  $300 \text{ ms}^{-1}$ .

There is an ambiguity in location in the velocity distribution on the rotor phase diagram, figure 7.7a. All the previous images had a stationary datum, the trailing edge of the NGV, which could be used to locate the velocity distribution precisely relative to the NGVs. This region of interest does not have such a datum and the positioning of the velocity distribution has been approximated from the distance between the line of action of the rotor and suction surface of the NGV.

Figure	7.7
Filename	Turu1_33
Estimated Relative Rotor Phase	3.3°
Run number	1959
Reynolds Number	$2.8 \times 10^6$
Height	Mid-span
Total temperature	315 K
Number of vectors	418
Pulse separation	640 ns
Scaling (parallel to chord)	25.74 $\mu\text{m}/\text{pixel}$
Scaling (normal to chord)	25.48 $\mu\text{m}/\text{pixel}$
Scaling used	25.61 $\mu\text{m}/\text{pixel}$
Scaling error	0.5 %
Field-of-view	19.7 x 14.8 mm
Interrogation spot size	64 x 64 pixels, 1.64 x 1.64 mm
Interrogation spot overlap	75 %
Mean particle displ.	8.0 pixels, 205 $\mu\text{m}$
Image displ. Accuracy	3.75 %
Estimated total accuracy (scaling + image displ.)	4.25%

Table 8.3 Parameters for the PIV data between the suction surface of the NGV and the leading edge of the rotor.

## 8.2.4 Comparison with Numerical Prediction

Figure 7.8 shows a PIV measurement and a CFD prediction of the velocity distribution from the stator passage to the leading edge of the rotor. The PIV result is made up from the two images of data shown in figures 7.2 and 7.6. The two have been combined so that the region of interest extends to the area of the prediction. There is a small overlap in the two occurring at the trailing edge of the NGV. The PIV data has not been smoothed and each of the frames represents one, instantaneous result. In the absence of smoothing the velocity surface appears to consist of blocks, a feature of the interrogation spot size used in the auto-correlation. The 2-D, unsteady prediction, supplied by DERA Pyestock, was performed using the UNSFLO code by Giles <sup>[128]</sup>.

The measurement and prediction are in very close agreement for the majority of the region of interest but there are significant differences, the reasons for which becoming apparent once the shortcomings of the two are explained. The prediction was created using a 2-D unsteady solver. The solver uses separate grids for the inviscid and viscous regions that are interfaced together to produce a continuous result. The viscous regions are modelled using an ‘O’ grid that, as the name suggests, surround the mechanical surfaces to describe the boundary layers. The remainder of the flow is modelled using an inviscid ‘H’ grid made up of sheared quadrilaterals. Problems occur where the boundary layer separates and the interface between the two grids moves, and in the modelling of the wake. The wake exists in the inviscid grid in the absence of viscous dissipation. In reality the wake will mix out quicker than in the prediction. This effect is evident in the prediction where the wake neither contains vortical structures nor broadens with distance from the trailing edge.

In contrast the wake shown in the measurement broadens with distance from the trailing edge and contain cells that would appear to be consistent with a Karman vortex street. Caution should be emphasised, as the measured velocity surface is an interpolation of a grid of coarsely spaced vectors. However, the cell like structure is present in all the measurements of the wake and does not coincide with the spacing of this grid although its extent maybe accentuated by its finite spatial resolution.

Both the measurement and prediction show a deceleration of approximately  $50 \text{ ms}^{-1}$  either side of the trailing edge, which seems to extend in a direction normal to its chord. In neither case does the deceleration extend to the suction surface of the adjacent NGV were the flow accelerates to approximately  $320 \text{ ms}^{-1}$ . The velocity is recovered 5 mm downstream. In each case the flow accelerates over the rotor crown to in excess of  $360 \text{ ms}^{-1}$ . Again the pattern of acceleration is similar between the two.

Unfortunately, the measurement does not extend to close to the mechanical surfaces or to the areas that are not served by a light sheet. As a result it does not cover the complete area of the prediction.

### 8.2.5 Accuracy, Resolution & Sources of Errors

The errors in the measurements come from a combination of five sources, laser timing, estimation of particle image displacements, scaling from pixels to real world dimensions, the ability of the particle to follow the flow and the accuracy to which the location of the light sheet is known. All of the measured displacements are assumed to be in the plane of the light sheet. The variation in the timing of the laser, and hence the pulse separation, is minimal and was logged during the experiment for verification. The



error from timing is therefore negligible. The accuracy of the particle image displacements is expected to be in the region of 3 % depending on the distance between exposures, the mean diameter of the exposures and the number of pairs in the interrogation spot relative to the background noise. Areas that contain too few pairs have been removed from the solution. The accuracy of the centroid location is estimated to be  $1/10^{\text{th}}$  of the particle image diameter. As the particle image diameters range from 2 to 4 pixels the accuracy is estimated to be 0.3 of a pixel. The average accuracy on the particle image displacement is 4.25%. The scaling errors result from the conversion from pixels to meters. The scaling factor will not be uniform across the images owing to the curvature of the windows. However, orthogonal scaling components, calculated from a reference grid in the field-of-view, show that the variation is of the order of 1 %. As this error is small, compared to the error in determining the particle image displacements, the mean of the two orthogonal scaling factors for each region of interest has been used.

Towers <sup>[113]</sup> showed that the 0.6  $\mu\text{m}$  styrene seed takes 2.2 mm to assume the downstream velocity of a normal shock of step change from 641 to 114  $\text{ms}^{-1}$ . The difference in the minimum and maximum velocities over all the measurements in the ILPF is 200  $\text{ms}^{-1}$ . The lag of the 0.6 styrene seed used in this experiment is likely to be a fraction of a millimetre and therefore a fraction of the interrogation spot size of 1.6 mm. It is expected that the errors owing to particle lag will be small compared to scaling and particle image displacement errors. It will, however, have an effect on the distribution of the seeding, evidence of which can be seen in the NGV wakes.

The plane of the light sheets was initially reconstructed from the depths of the optical periscopes inserted into the NGVs. This approach was found to be inaccurate as the depth of the light sheet depended on the alignment of the beam with the axis of the periscope. The planes were eventually reconstructed from the light sheet burn marks on the NGVs and rotors that had been coated with a matt black paint to avoid glare prior to running. The depth of the light sheet is known only to the nearest mm. The light sheet was projected from periscopes in NGVs at different angular positions to the field-of-view and is flat rather than cylindrical. The light sheet is therefore at the approximate mid-span only along the centreline of the images. The peripheries of the images deviate from mid-span by approximately 1/5<sup>th</sup> mm.

The use of a 64 x 64 pixel interrogation spot size gives a vector every 1.66 mm and a smallest resolvable length scale of the same size. A 75 % overlap has been used to give a vector every 0.415 mm. The Dynamic Velocity Range (*DVR*), the ratio of the maximum and minimum resolvable velocities from equation 4.1, for a maximum displacement defined by Adrian's ¼ rule <sup>[77]</sup> of 16 pixels and centroid location to 0.3 pixels is

$$DVR = \frac{16}{0.3 \times 3} = 17.8$$

This ratio is somewhat misleading in that it assumes that overlapping particle images separated by 0.3 pixels can be resolved. With cross-correlation they can be resolved, but for auto-correlation the minimum separation would be the same as the mean particle image diameter that gives a DVR of 1.8. The Dynamic Spatial Ratio (*DSR*), the ratio of the minimum and maximum resolvable length scales given by equation 4.2, is

$$DSR = \frac{768}{16} = 48$$

where the image contains 768 pixels in one dimension and 16 pixels is defined by Adrian's <sup>[77]</sup> ¼ rule. The product of the DVR and DSR, which is often used as a benchmark with which to compare combinations of recording media and analysis algorithm, is 854.

## 8.3 RECOMMENDATIONS FOR FURTHER WORK

### 8.3.1 Optimisation for a Cross-Correlation Camera

The original intention was to apply a triggerable cross-correlation camera to the ILPF rather than a non-triggerable, non-cross-correlation camera. Unfortunately, the cross-correlation camera failed and could not be replaced in time for the test. With the benefit of the results presented here, hindsight allows the optimal configuration for such a cross-correlation camera to be defined.

The camera has a resolution of 1000 x 1000 pixels that would give 20  $\mu\text{m}$  per pixel over the 20 x 20  $\text{mm}^2$  field-of-view required to observe both the trailing edge of the NGV and the leading edge of the rotor. The accuracy of the measurement, excluding that corresponding to the displacement between exposures, is of the order of 1 %. If the particle images are only 1 to 2 pixels in diameter the minimum displacement required to achieve a comparable accuracy of 1 % is 10 pixels between exposures. A pulse separation of 1.18  $\mu\text{s}$  would give a 10 pixel displacement of the minimum recorded velocity of approximately 170  $\text{ms}^{-1}$ . The maximum velocity would give a displacement of 23 pixels. If there were a 16 pixels shift, in the direction of the mean flow, between cross-correlated areas the interrogation spot size could be reduced to 32 x 32 pixels, an area of 640 x 640  $\mu\text{m}^2$  and still satisfy Adrian's  $\frac{1}{4}$  rule<sup>[77]</sup>. If the light sheet were 0.5 mm thick a seeding concentration of 50 seed  $\text{mm}^{-3}$  would be required to give 10 particle pairs per interrogation spot, a requirement that is only just satisfied in the most densely seeded areas in the results presented here. The *DVR* would be

$$DVR = \frac{(32/4)+16}{0.1 \times 2} = 120$$

The DSR and product of the DVR and DSR would be

$$DSR = \frac{1000}{(32/4) + 16} = 42$$

$$(DVR)(DSR) = 5040$$

The spatial resolution could be extended still further by cross-correlating in an iterative manner so that the shift between cross-correlated regions can be defined locally to allow the interrogation spot size to be as small as possible. The limit of such an approach would involve cross-correlating individual pairs, assuming that the cross-correlation peak can be identified in the presence of noise.

### 8.3.2 Measurements Close to Mechanical Surfaces

Glare and blade shadowing hamper measurements close to mechanical surfaces. Schodl<sup>[18]</sup> adapted his L2F system to collect light through two apertures and a spatial filter. The approach is similar to the 3-D PIV technique described in section 4.5.3 except that the spatial filter allowed light to be collected only from a narrow axial region. Schodl also explored the use of an unnamed fluorescent seed of 1 μm in diameter in a high-speed turbomachinery application, but later rejected them owing to the inability to follow the flow sufficiently.

Fluorescent seed could also be used in the ILPF assuming they adequately follow the flow and can be seen. The excitation wavelength must also not make any of the surrounding surfaces or gas within which they are suspended fluoresce. Fluorescent polystyrene microspheres, loaded with a variety of dyes, are available in sizes ranging from 0.02 to 4  $\mu\text{m}$  in diameter <sup>[129]</sup>. A range of excitation wavelengths are available, most notably at 488 and 354 nm which coincide with the emission lines of argon ion and frequency tripled Nd:YAG lasers respectively. As the emission line can be easily filtered from the excitation line the image of the seed can be separated from that of its surroundings. As the fluorescent signal is typically much smaller than Mie-scattered signal an image intensifier would be needed in front of cross-correlation camera explored here.

### 8.3.3 Time Averaged Measurements

The PIV data presented here give a spatial velocity distribution at an instant in time. None of the results have been combined to give a time-averaged result, as the camera acquisition could not be locked to the rotor phase. If the acquisition could be locked, the same rotor position could be resampled over multiple revolutions to give time-averaged quantities at each of spatial locations of the vector grid. Phase locking of the acquisition would also allow the rotor position to be phase stepped between acquisitions to show how the flow develops as the rotor passes.

A time-averaged velocity error is composed of both statistical and systematic contributions. Increasing the number of samples reduces the statistical error. Reducing the systematic error involves minimising errors from particle image displacement,



timing, scaling etc. described in the previous section. The systematic error needs to be smaller than the fluctuating aspect of the flow if turbulent intensities are to be identified. The acquisition of the time-averaged aspect of the flow therefore necessitates a very rigorous experimental procedure.

An alternative to phase stepping over multiple revolutions would be to acquire a quick succession of images as the rotor passes the field on the same revolution. High speed, intensified cameras originally designed for ballistics studies are available, an example of which is described in [130]. This intensified imaging system allows up to 24 frames to be recorded at an equivalent frame rate of up to 20 000 000 frames per second. Output is either to photographic film or 16 bit cooled CCD of ISO 30 000 equivalent sensitivity (camera used here was approximately ISO 3000 equivalent, 8 bit). The period for a rotor to traverse a stator passage is approximately 300  $\mu$ s. The system described in [130] would allow 12 frame pairs, for cross-correlation, to be recorded over this period. A light source that could be double pulsed at 50 kHz would be required.

#### 8.3.4 3-D PIV in the ILPF

Three-dimensional measurements are of importance close to, and in the wake of, mechanical surfaces as these regions determine the heat transfer to and from the blades and can contain flow with a large out-of-plane component of velocity.

The application of stereo PIV to the ILPF has already been discussed in section 5.4.1 and was dismissed owing to the restricted optical access and blade shadowing. 3-D PIV by defocusing through a diffraction-limited lens was also presented in section 5.4.2 but

was not applied to the ILPF due to the aberrations present in the window. Possible remedies to this problem have been discussed, as has a two camera defocusing approach that potentially allows a field-of-view of similar dimensions to that used in 2-D PIV to be achieved.

An alternative approach would be to exploit defocusing through an aperture mask as presented by Gharib <sup>[124]</sup> and discussed in section 4.5.3. The use of a single camera with an aperture mask neither suffers from the blade shadowing effects of stereo cameras nor requires a diffraction-limit optical arrangement between the scatterer and the image plane. Equation 4.18 can be used to assess the resolution in out-of-plane displacement for a given optical arrangement. For the optical arrangement summarised in table 8.4, an out-of-plane displacement of 40  $\mu\text{m}$  would correspond to a 1 pixel separation between exposures. The in-plane resolution would be 20  $\mu\text{m}$  per pixel. The out-of-plane resolution could, as could the in-plane, be extended by adopting sub-pixel accuracy. It is expected that the replacement of three circular apertures, as used by Gharib, by a couple of parallel slits at the periphery of the aperture would give an improved resolution (parallel markers are often used when visually recording tensile testing data).

Field-of-view	20 × 20 mm
Distance between apertures, $d$	50 mm
Focal length of lens, $f$	23 mm
Distance to object plane, $d_o$	100 mm
# pixels, pixel size	1000 × 1000, 6 × 6 μm
Out-of-plane displacement for 1 pixel separation	40 μm
In-plane displacement for 1 pixel displacement	20 μm

Table 8.4. Parameters used to assess resolution of 3-D PIV by defocusing through aperture masks

## 8.4 SUMMARY OF CHAPTER

Both particle tracking and auto-correlation have been applied to a single image recorded in the ILPF. Particle tracking gave 501 vectors, many of which were spurious. The centre-of-mass centroid approximation was applied but was found not to improve the accuracy of the measurement. The accuracy was estimated to be  $\pm 18\%$ , which corresponds to integer pixel displacements with an average separation of 5 to 6 pixels. The auto-correlation gave 1020 vectors using a  $64 \times 64$  interrogation spot size with a 75% overlap. The particle centres are conservatively estimated to be located to 0.3 of a pixel, giving an accuracy of  $\pm 5.4\%$  for the image displacement. Auto-correlation was used for the remainder of the images.

The velocity distributions have been plotted using a Delaunay triangulation to produce a non-smoothed, non-extrapolated but interpolated surface that contains all of the original velocity vectors. Smoothing can be applied if necessary.

Velocity distributions extending from the trailing edge of the NGV to the leading edge of the rotor, the suction surface of the NGV to the leading edge of the rotor and stator passage have been presented and described. A single, instantaneous, non-smoothed measurement has also been shown to have very close similarity with a numerical prediction produced using a 2-D unsteady solver.

The velocity vectors are expected to be accurate to approximately  $\pm 5\%$  when scaling errors and image displacement errors are combined. The particle response is less than the interrogation spot size for all the flow features in the regions of interest. The plane

of the light sheet has a  $1/5^{\text{th}}$  mm deviation from mid-span height at the periphery of the images.

The auto-correlation gave a vector every 1.66 mm and the same resolvable length scale. A 75% overlap was used to give a vector every 0.415 mm. The *DVR* is 17.8, the *DSR* 48, the product of which is 854. An optimal arrangement based on the cross-correlation camera would give a vector every 0.64 mm for an interrogation spot size of  $32 \times 32$  pixels. The *DVR* would be 120, the *DSR* 42, the product of which is 5040 whilst maintaining an estimated accuracy of 1 % for the image displacement.

Recommendations have been made for further work. The first recommendation is for the iterative cross-correlation of two images with the shift between cross-correlated regions converging on the mean displacement within the interrogation spot. This would allow the interrogation spot size to be reduced to give a greater vector yield and spatial resolution. The use of fluorescent seed has been recommended for measurements close to surfaces, the emission wavelength being separated from the excitation wavelength to remove glare and background illumination. Time-averaged and phase stepped measurements have also been discussed with the emphasis being placed on reducing systematic errors below the levels of the fluctuating aspect of the flow. The investigation of 3-D PIV by defocusing through the aperture mask of a single camera is also recommended in preference to other 3-D PIV techniques.

## *Chapter 9*

# SHEARING INTERFEROMETER

—

# THEORY FOR APPLICATION

### *Description of Chapter*

*The operating principle and theory behind applying the shearing interferometer to compressible flow fields is presented. To achieve this it has been necessary to review the fringe analysis software that has been used and the tomographic theory applicable to reconstructing refractive index distributions from a limited number of projections.*

*The review of the tomographic theory has been extended to example reconstructions of synthetic distributions modelled in the MatLab environment. Their application has not been applied further here but they are subjects of a further project outside the realms of the thesis.*



## 9.1 INTRODUCTION

Although the range and accuracy of measurement instrumentation is constantly improving there is still a requirement for simple, quick to apply, maybe qualitative visualisations of fluid flow. The shearing interferometer is means of achieving, in the first instance, a qualitative visualisation. By analysing the visualisation with the necessary algorithms it can be extended to a quantitative measurement of density.

The shearing interferometer differs from beam splitting interferometers in that the interfering beams occupy common optical paths and are incident on the same components. It is therefore far less sensitive to relative movement between the components. It is envisaged that the shearing interferometer would be used where either a schlieren or shadowgraph would normally be used.

In chapters 10 and 11 the application of the shearing interferometer to 2-D wind tunnel containing a compressor representative flow, and a shock tube used for the acoustic testing of jet noise suppressor nozzles, are described. In the former the measurement is a first pass characterisation of the flow prior to the evaluation of anemometry equipment. In the latter the visualisation was secondary to, and must not interfere with, the acoustic testing of the suppressor nozzles. In each case either a visualisation or a quantitative density measurement has been accomplished. The relevant theory for the successful application of the shearing interferometer is presented in the remainder of this chapter.

## 9.2 OPTICAL PATH DIFFERENCE

At velocities below 0.3 of the speed of sound air density can be assumed to be constant.

As the velocity increases this assumption becomes no longer valid and the density distribution becomes inhomogeneous. As the air density within the flow field changes, its refractive index changes with an approximately linear relationship unless extreme temperature or pressures are encountered. This relationship is described by the Gladstone-Dale equation <sup>[91]</sup>,

$$\mu - 1 = C\rho \quad (9.1)$$

where  $\mu$  is the refractive index,  $\rho$  is the density and  $C$  is the Gladstone-Dale constant ( $2.256 \times 10^{-4} \text{ m}^3/\text{kg}$  for light of 632 nm in wavelength).

As a light ray is transmitted through a region of higher refractive index it becomes retarded relative to a ray that has not passed through such a region. The retarded ray experiences a longer optical path length than that of the unretarded ray. By measuring the difference in optical path lengths the difference in refractive index, and hence the differences in density along the optical paths can be calculated. Assuming refractive index bending to be negligible the optical path difference between the two rays is given by

$$\begin{aligned} \Delta\psi(x, y) &= \int \mu(x_1, y_1, z_1) - \mu(x_2, y_2, z_2) dz \\ &= \int \Delta\mu(x, y, z) dz = N\lambda \end{aligned} \quad (9.2)$$

where  $\lambda$  is the wavelength of the illuminating light and the fringe order number,  $N=0, \pm 1, \pm 2, \dots$  for positive (additive) interference, ie bright points and  $N= \pm 1/2, \pm 3/2, \dots$  for dark points. Assuming two-dimensionality  $dz$  becomes a constant, say  $l$ . Combining equations 9.1 and 9.2 the change in density at point  $x,y$  is given by

$$\Delta\rho(x,y) = \frac{\lambda N(x,y)}{Cl} \quad (9.3)$$

### 9.3 INTERFEROMETRY

The human eye and most forms of recording media are sensitive to light intensity (amplitude) but not phase. Interferometry is a successful means of transforming the phase information into an amplitude object that can be observed and recorded. This is achieved by combining two coherent beams to generate an interference pattern of light and dark fringes that represent the phase difference (optical path difference) between the two beams.

### 9.4 THE SHEARING INTERFEROMETER

An interference pattern can be created using a beam-splitting interferometer such as the Mach-Zehnder. This kind of interferometer is susceptible to noise as the reference and object beams occupy separate optical paths. A fraction of a wavelength movement between the two beams can generate a whole wavelength phase shift at the interferogram.

For a shearing interferometer a single beam is projected through the flow-field of interest onto a shearing device, which splits it into two beams that are slightly displaced

relative to each other but still occupy common optical paths. The two beams interfere to produce lines of constant phase difference between two overlapping points separated by the direction and magnitude of the shear. The beam is sheared after the flow-field, rather than before, otherwise the interfering beams would occupy the same path through the flow-field and undergo the same phase change to no net effect.

Figure 9.1 shows a simple beam shearing arrangement consisting of a cube beam splitter and a couple of front-silvered mirrors. One of the mirrors is slightly tilted relative to the normal of the second mirror so that the recombined beams at the exit of the beam splitter are misaligned. The displacement between the two beams is called the shear distance that, for this arrangement, increases with  $x$ . As the emergent beams overlap they interfere to produce lines of constant phase difference.

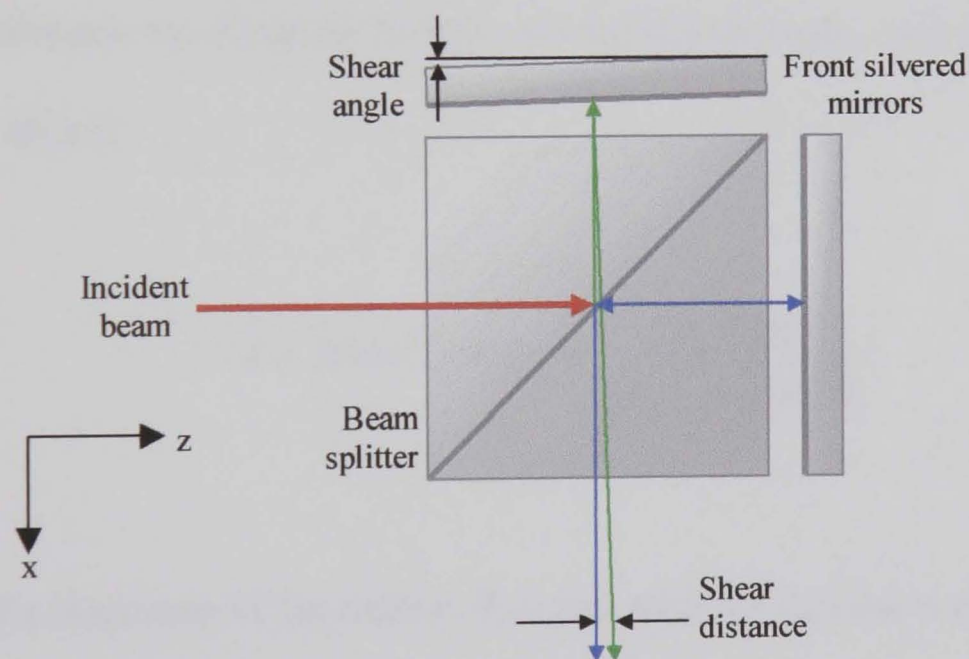


Figure 9.1. Using mirrors and a beam splitter as a beam-shearing device.

Figure 9.2 shows an alternative shearing arrangement where a back-silvered mirror is used as the shearing device. The initial glass surface of the mirror and its back silvering each reflect a portion of the light along slightly displaced but common optical paths.



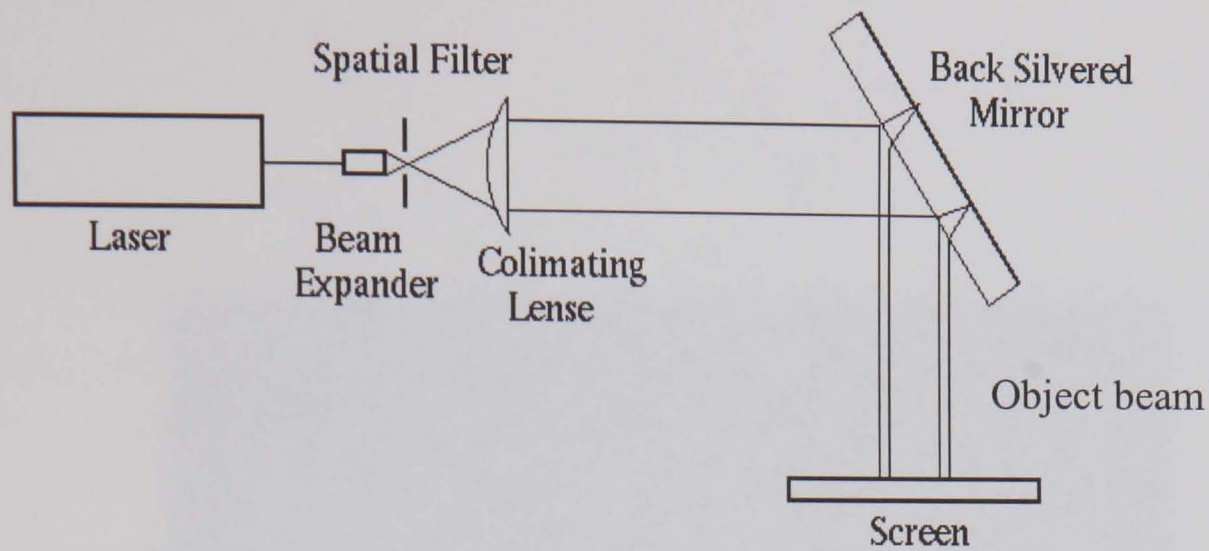


Figure 9.2. The Shearing Interferometer

The two sheared beams interfere to produce a finite fringe interferogram (straight fringes). The fringe deformation represents optical path difference, and hence the change in density, between two sheared points in the object beam that coincide at a point  $(x,y)$  on the screen. The amount and direction of shear is a function of the angle of incidence between the shearing mirror and the object beam, and the thickness of the glass of the mirror

$$d = 2t \tan \theta_i \cos \theta_t = \frac{t \mu_i \sin \theta_i}{\sqrt{\mu_i^2 - \mu_t^2 \sin^2 \theta_i}} \quad (9.4)$$

where  $t$  is the thickness of the mirror,  $\theta_i$  is the angle of incidence and  $\theta_t$  is the angle of transmissivity and  $\mu_t$  is the refractive index of air (or the medium in which the mirror is suspended), see figure 9.3. Increasing the amount of shear increases the number of fringes (carrier frequency) and the distance between the two points over which the change in density is calculated.



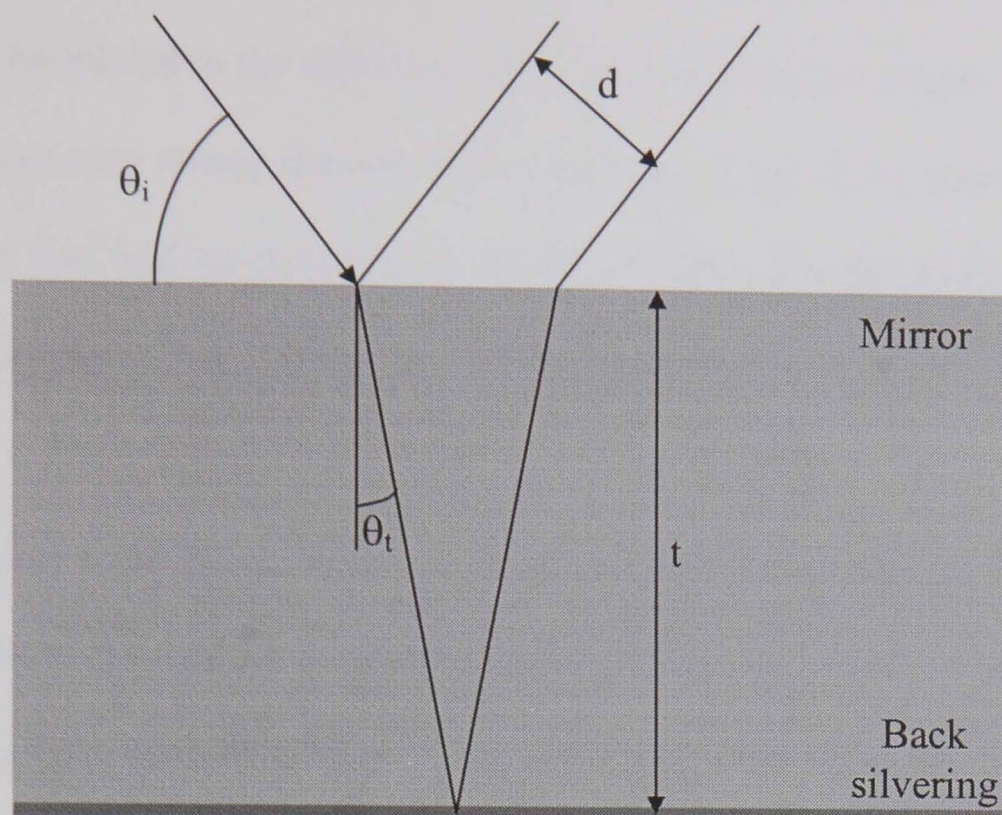


Figure 9.3. Beam shear 'd' produced using a back-silvered mirror

The back-silvered mirror was used in preference to the beam splitter arrangement for several reasons. As the beams originate from the same optical component it is less susceptible to relative motion between the components. Large back-silvered mirrors are inexpensive and allow large fields of view to be measured. If a divergent beam is sheared the shear distance remains constant in size relative to the size of the field-of-view. There will also be a small magnification difference between the sheared beams owing to the optical path length through the thickness of the shearing mirror. The compromise that has to be made for these favourable attributes is one of adjustability. Adjusting the amount of shear (rotating the mirror) meant that the screen and camera needed to be relocated in accordance with the position of the projected fringe pattern.

Figure 9.4a shows the lines of constant phase produced by a shearing interferometer. A  $\text{CO}_2$  jet of higher refractive index than its surroundings, 1.00045 for  $\text{CO}_2$  and 1.00014 for ambient air, has been positioned in the optical path of the beam. The optical path



difference generated by the CO<sub>2</sub> jet manifests itself as bending of the lines of constant phase that can be related to the refractive index profile of the jet. Figure 9.4b shows the unwrapped phase map where the bending of the fringes has been quantified using the FFT technique that will be described in a later section. The greyscale represents the number of wavelengths delay, or fringe order number, that the beam has experienced.

Figure 9.4c shows a plot of the fringe order number across the CO<sub>2</sub> jet. The fringe order number represents the difference in optical path relative to a sheared point rather than the absolute optical path difference. An integrating in the direction of shear from a known datum can be used to derive the absolute optical path difference.

The shearing interferometer can also be used as a fringe projection device for surface contouring. Figure 9.5a shows the fringes projected onto the eye of a manikin. The surface contours can be determined from triangulation if the camera is at an angle to the optical path of the projected fringes. The grey scales of figure 9.5b represent the contours of the surface.

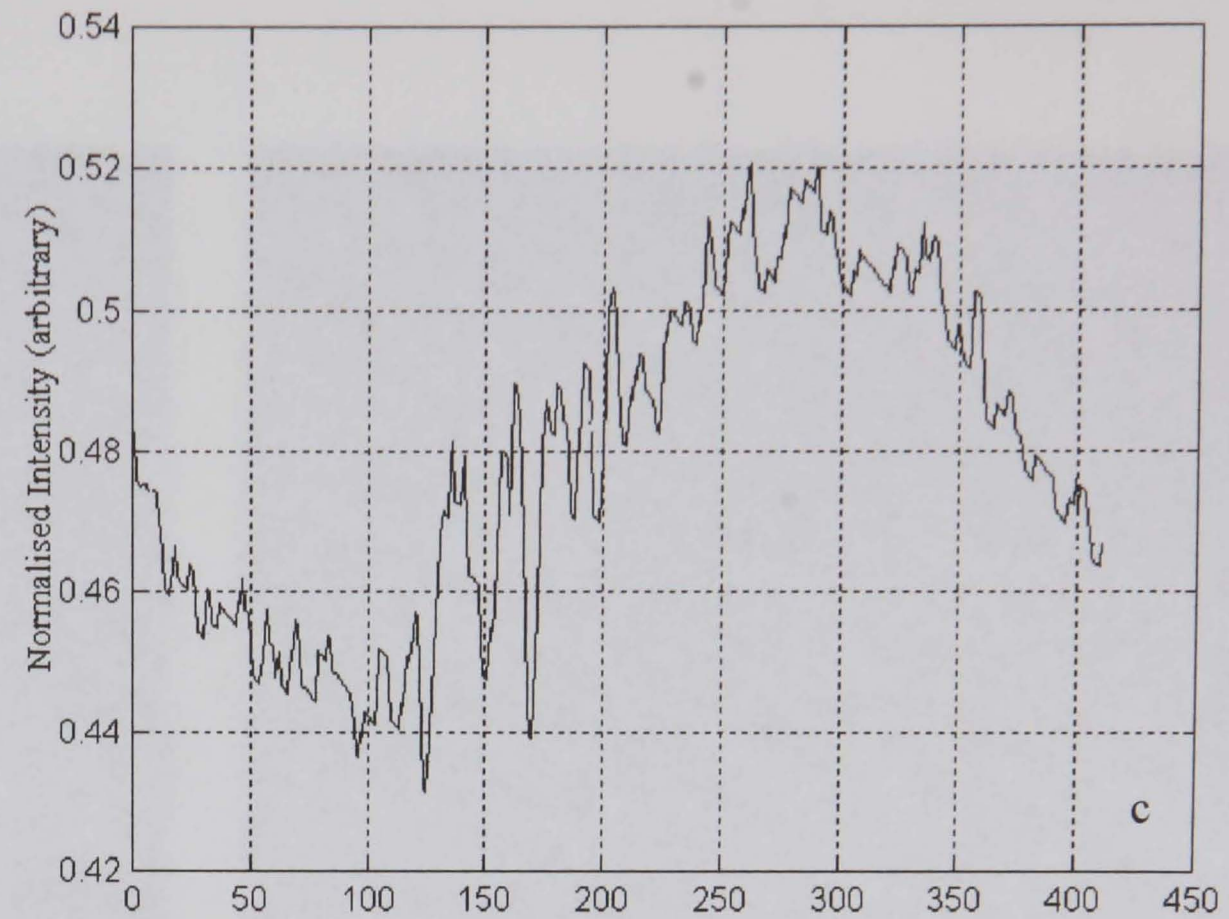
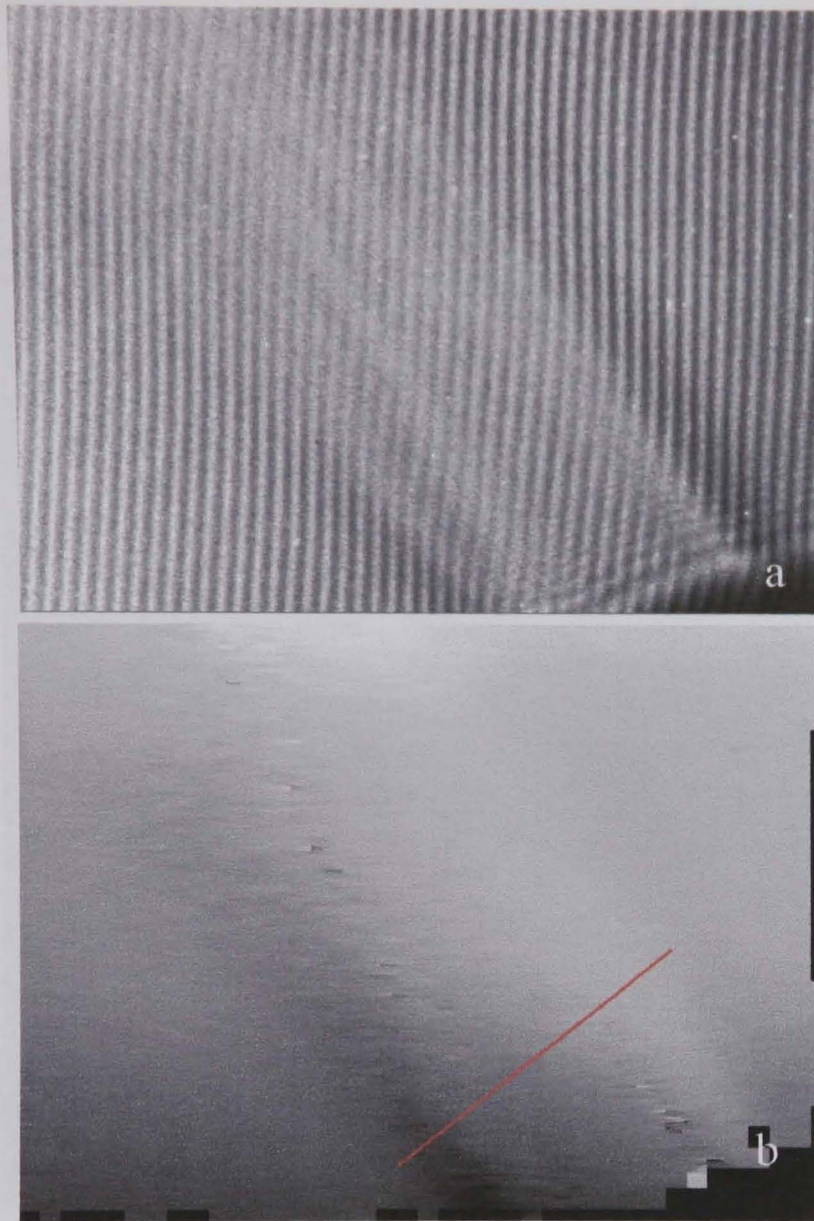


Figure 9.4. Measurement of a CO<sub>2</sub> jet using a shearing interferometer  
 a. The raw interferogram  
 b. The unwrapped phase map of the interferogram  
 c. Plot of the normalised intensity, equivalent to fringe order number, through the cross-section of the CO<sub>2</sub> jet indicated in 'b'.



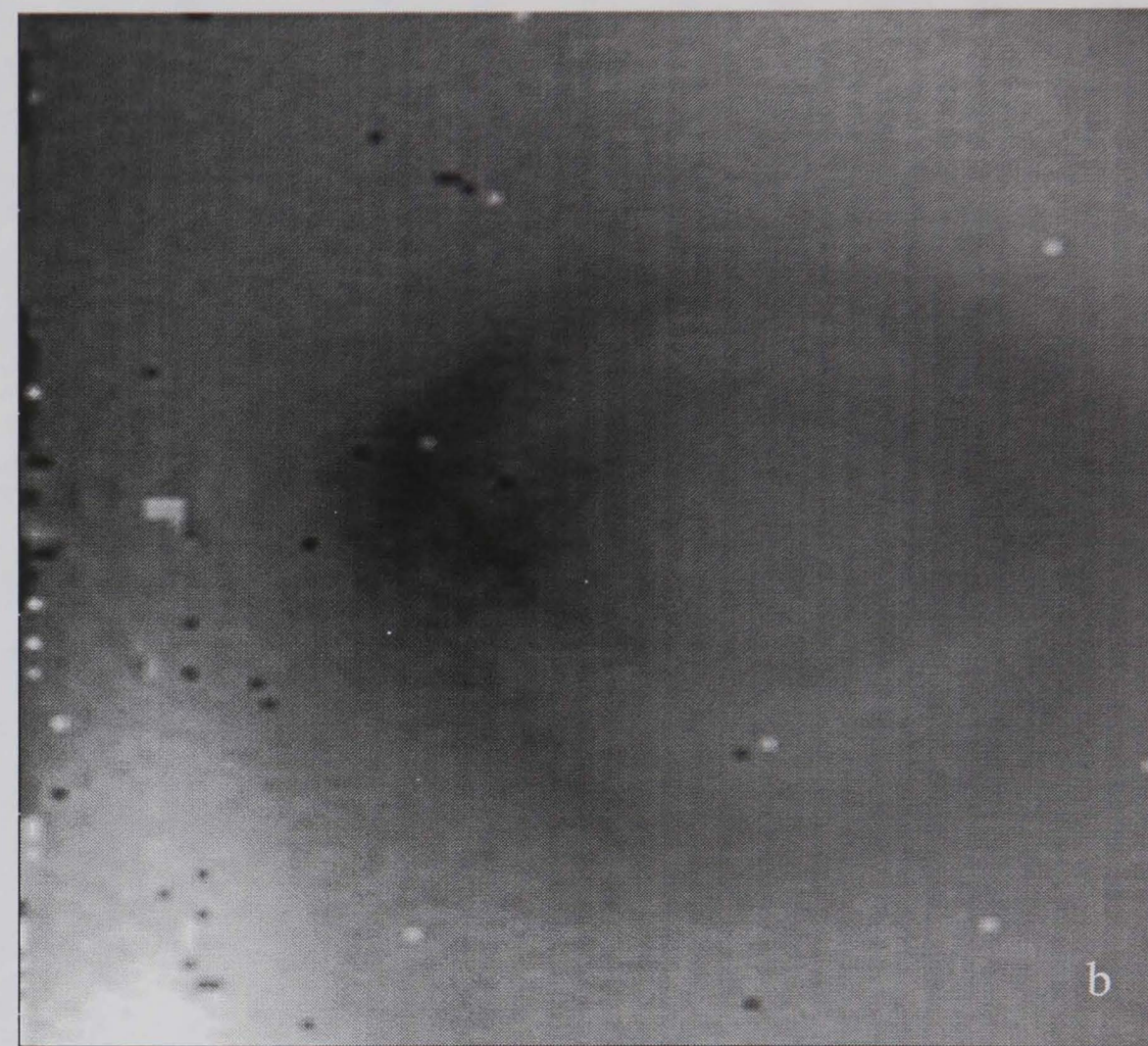
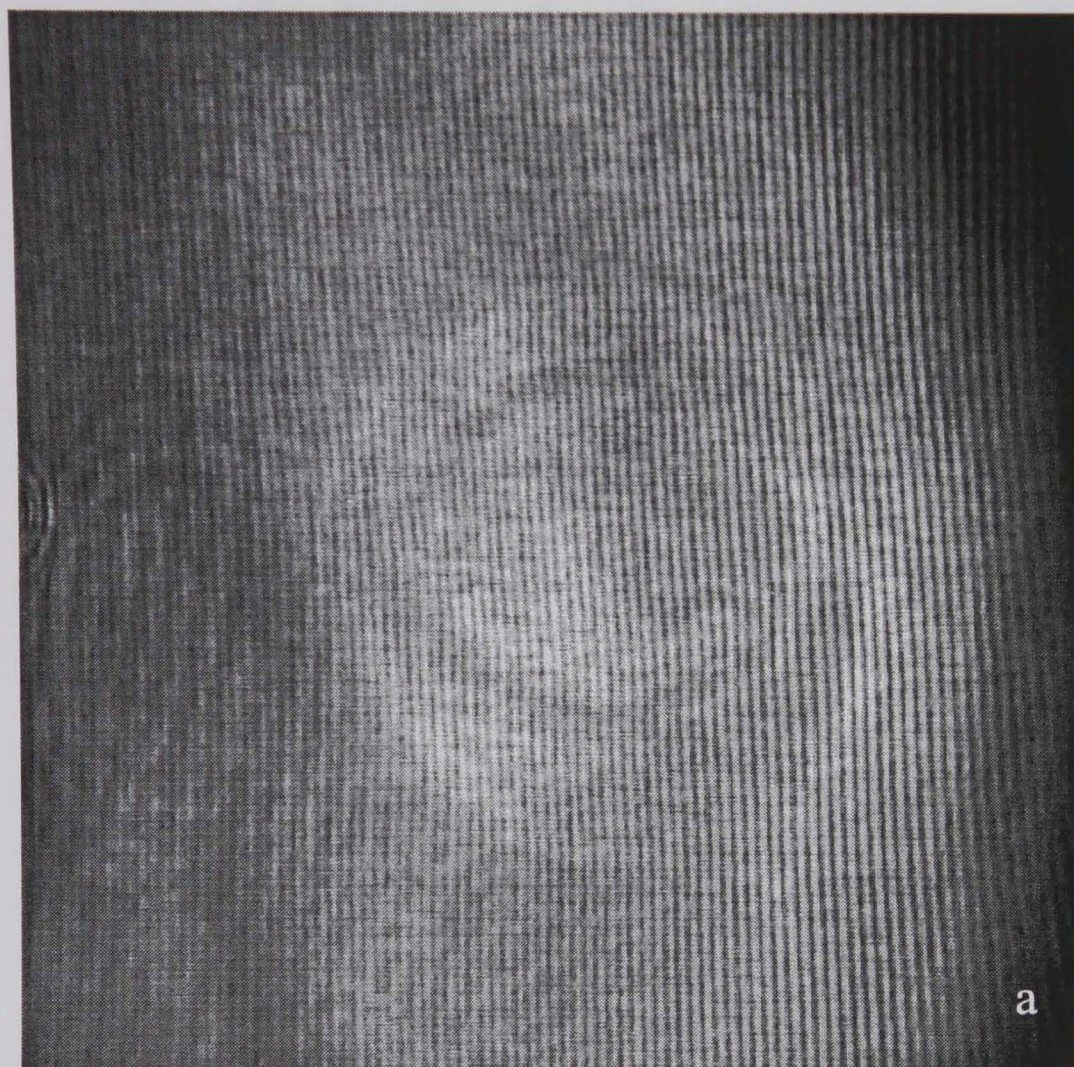


Figure 9.5. The shearing interferometer used as a fringe projection system for surface contouring.

a. The fringes projected onto the eye of a manikin. Camera placed at an angle to the optical path of the illumination.

b. The fringe pattern solved using the FFT approach. A reference image (fringes projected onto a flat surface) has been subtracted to remove distortions in the image due to non-straight reference fringes.



## 9.5 THE FOURIER TRANSFORM METHOD OF FRINGE ANALYSIS

The Fast Fourier Transform (FFT) method of extracting the phase information from finite fringe interferograms is described. The phase information, extracted using the FFT, is presented as arctan fringes. The arctan fringes give a phase distribution with  $2\pi$  discontinuities from which the sign of phase changes can be determined. A largely noise-immune approach to unwrapping the modulus  $2\pi$  phase information into a continuous surface is also described. The description broadly follows the treatments given by both Judge <sup>[109]</sup> and Bryanston-Cross <sup>[111]</sup>.

Both algorithms are embodied into a software package called FRAN <sup>[109]</sup> that has been used to process the data included herein. The preconditions and ambiguities in using FRAN are discussed. MatLab <sup>[110]</sup> has been used to demonstrate the FFT approach and highlight the uncertainties in this implementation.

The phase information is encoded into the interferogram in the form of bending of the fringes. As the fringes are deformed the uniform spacing between the fringes is lost, generating localised areas of compressed and expanded fringe spacing. Scanning across these areas would reveal changes in the fringe frequency corresponding to the change in fringe spacing. By extracting this fringe frequency from the dominant carrier frequency the required phase information is isolated. This is achieved by using a Fourier transform <sup>[111 & 112]</sup>, equations 9.5 and 9.6 giving the Fourier and inverse Fourier transforms respectively.

$$G(u) = \int_{-\infty}^{\infty} g(x) e^{-j2\pi ux} dx \quad (9.5)$$

$$g(x) = \int_{-\infty}^{\infty} G(u) e^{j2\pi ux} du \quad (9.6)$$

The discrete Fourier transform is more suitable to computational methods, the discrete transform pair being defined as

$$G(n) = \frac{1}{N} \sum_{k=0}^{N-1} g(k) e^{-\frac{j2\pi nk}{N}} \quad (9.7)$$

$$g(k) = \sum_{n=0}^{N-1} G(n) e^{\frac{j2\pi nk}{N}} \quad (9.8)$$

where  $n=0,1,2,3,\dots,N-1$ .

The interferogram can be described by <sup>[111 & 112]</sup>

$$g(x,y) = a(x,y) + b(x,y) \cos[2\pi f_o x + \phi(x,y)] \quad (9.9)$$

where  $a(x,y)$  is the background amplitude and  $b(x,y)$  the modulation noise.  $f_o$  is the carrier frequency in the  $x$  direction and  $\phi(x,y)$  is the phase information of interest.

Equation 9.9 is written in its complex form as

$$\begin{aligned} g(x,y) = & a(x,y) + 1/2 b(x,y) (\cos [2\pi f_o x + \phi(x,y)] + j \sin [2\pi f_o x + \phi(x,y)] \\ & + \cos [2\pi f_o x + \phi(x,y)] - j \sin [2\pi f_o x + \phi(x,y)]) \end{aligned} \quad (9.10)$$

where  $\cos[2\pi f_0 x + \phi(x,y)] - j\sin[2\pi f_0 x + \phi(x,y)]$  is the complex conjugate.

Equation 9.10 can be written in a more convenient form thus

$$g(x,y) = a(x,y) + b(x,y)/2 (e^{j\phi(x,y)} e^{j2\pi f_0 x} + e^{-j\phi(x,y)} e^{-j2\pi f_0 x}) \quad (9.11)$$

Letting  $c(x,y) = b(x,y)e^{j\phi(x,y)}/2$  and  $c^*(x,y)$  be its complex conjugate, equation 9.11 becomes

$$g(x,y) = a(x,y) + c(x,y)e^{j2\pi f_0 x} + c^*(x,y)e^{-j2\pi f_0 x} \quad (9.12)$$

The FFT assumes that the raster of pixels is a periodic part of a continuous signal. The periodicity is removed by weighting the intensity of the raster of pixels using a Papoulis window <sup>[111]</sup>, see figures 9.6 a and b. If the raster was not weighted in this way a ringing phenomena associated with the length of the raster would be generated in the frequency domain. The Fourier transform of the intensity distribution is given by

$$G(f,y) = A(f,y) + C(f-f_0,y) + C^*(f+f_0,y) \quad (9.13)$$

The power spectrum of the raster consists of two spectral side lobes corresponding to the second and third terms of equation 9.13, centred round the carrier frequency, see figure 9.6c.



As the side lobes are symmetric about the carrier frequency only one needs to be considered. It is desirable for  $\phi(x,y)$  to be a slowly varying function compared to the carrier frequency. The carrier frequency needs to be higher than the phase frequency in the entire image, lower than the maximum frequency that is resolvable. If this is achieved the peaks in frequency space will be clearly separated. By weighting one of the side lobes using a Hanning window <sup>[111]</sup>, see figure 9.6c, and translating it to the origin, see figure 9.6d, by the carrier frequency,  $C(f,y)$  is obtained. A Hanning window is used to prevent the creation of periodic noise in the filtered data. The phase map is calculated using the inverse transform of  $C(f,y)$ . The phase distribution is given by

$$\phi(x,y) = \arctan \left[ \frac{\Im[c(x,y)]}{\Re[c(x,y)]} \right] \quad (9.14)$$

where  $\Im[c(x,y)]$  and  $\Re[c(x,y)]$  are the imaginary and real components of  $c(x,y)$  respectively. The use of the arctan function gives a discontinuous phase map wrapped in a modulus of  $2\pi$ , figure 9.6e and f. The discontinuous form of the arctan function removes the directional ambiguity in unwrapping the phase. The sign convention, although arbitrary in FRAN, can later be corrected from the direction of shear.

Figures 9.6 e and f show the wrapped maps of the same raster of pixels processed using the FFT approach. In each case a different carrier frequency has been specified resulting in a gradient in the phase information between the two. The carrier frequency is inevitably inhomogeneous over the spatial extent of the interferogram owing to divergent beams, misalignments etc. In FRAN the carrier frequency is calculated from one raster of pixels but used globally over the entire image. The outcome is a gradient on the unwrapped phase owing to the distortions present in the reference state. The

solution is to process both a reference, in the absence of the flow, and subject images using identical carrier frequencies. The reference unwrapped phase map is subtracted from the subject's to remove the distortions. In practice obtaining an unwrapped phase map is difficult owing to ambiguities in the fringe data, speckle noise and the resolution of the imaging system.

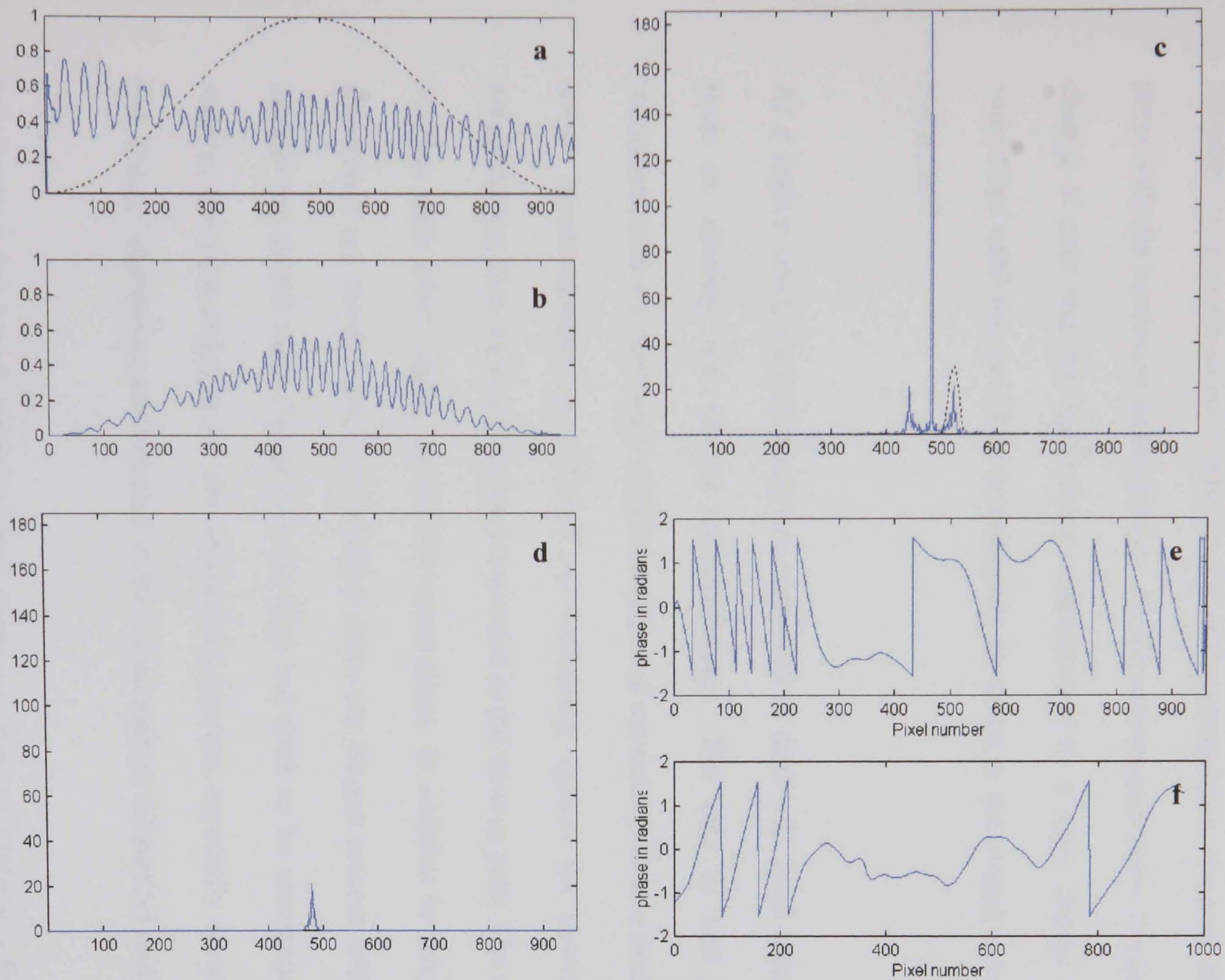


Figure 9.6. The FFT method of extracting the phase information from finite fringe interferograms

**a.** Intensity data of one raster of pixels and weighting window.      **b.** Intensity data weighted by window.

**c.** Power spectrum of raster with carrier frequency and deformation.

**d.** Side lobe after weighting by Hanning window and translated by the carrier frequency to the origin.

**e & f.** Wrapped phase produced by selecting different carrier frequencies, **f** is correct, **e** has a gradient due to incorrect carrier frequency

FRAN uses a minimum spanning tree as a mechanism for computing the consistency of possible phase-unwrapping routes <sup>[109 &111]</sup>. An unwrapping path is constructed in order to maximise confidence, confidence being weighted according to a minimum spanning tree. At its lowest level paths between pixels are compared to circumvent spike noise. Neighbouring pixels to each individual pixel are considered, the path progressing to the pixel with the minimum phase change. As the unwrap path seeks to minimise the phase change at each step the spike noise, characterised by a rapid change in phase, is not considered until the end of an unwrap path. Its threat to the overall solution is therefore minimised.

At a higher level, tiles of pixels are compared to deal with local area inconsistencies such as aliasing and natural inconsistencies. The aim is that areas of local inconsistencies are contained within the tiles and are dealt with in a similar way to spike noise. Inconsistencies are detected by comparing against the unwrapped edges of neighbouring tiles. Inconsistencies are avoided in the unwrap path. The tiles are made to overlap each other slightly to aid the comparison. In addition to this, edge-detection algorithms are used to find out whether there are fringes present within a tile. If no fringes are found then clearly the tile does not need to be unwrapped. This greatly reduces the time required for the unwrapping process, especially where large areas of non-fringe information are included in the image such as silhouettes and boundaries.

By adopting this largely noise-immune phase-unwrapping strategy, a fringe pattern can be solved despite the presence of spike noise and local area inconsistencies. Their threat

to the overall solution is minimised by only including them at the end of an unwrap path or excluding them from the solution.

## 9.6 TOMOGRAPHIC RECONSTRUCTION OF DENSITY FIELDS

Interferometry can give the projection of a density field. The optical path length is a convolution of the density and its spatial extent within the optical path. For a two-dimensional flow field this spatial extent is known and only one projection is required to calculate the density distribution in the flow field. Multiple projections are required to spatially resolve three-dimensional density distributions.

Where the number of projections is limited, assumptions need to be made about the refractive index distribution to facilitate a reconstruction. Equation 9.3 can be used if the flow is assumed to be two-dimensional. An Abel inversion can be used if the flow is assumed to be axis-symmetric whilst an algebraic reconstruction can be applied where there are limited data of a three-dimensional flow. Descriptions of the Abel inversion and Algebraic Reconstruction Technique (ART), the latter following the pragmatic overview given by Lawton <sup>[29]</sup>, are included to facilitate the three-dimensional reconstruction. Brief overviews of Fourier Slice theory, filtered, and convolution back-projection methods are also included, although their application to the limited data presented here is questionable (typically projections every 2° to 6° steps over 180° are required).

### 9.6.1 Axial Tomography

Axial tomography refers to the reconstruction of a cross-section, or slice, through an object. The slice is reconstructed by means of a mathematical manipulation of the data gathered by passing many beams through the slice. The first medical applications of axial tomography used X-rays to map areas of constant absorption coefficient. Whilst



X-rays are used for solids, UV, visible and near IR radiation are normally used for gasses and liquids.

Most of the tomography texts are understandably biased towards the reconstruction of absorption coefficient <sup>[29 & 114]</sup> through a two-dimensional slice, as they are geared towards medical applications. Interferometry is concerned with the phase difference through a transmitting object rather than the beam attenuation. The analysis is essentially the same in that the refractive index field, not the absorption coefficient, is reconstructed.

Figure 9.7 shows a typical arrangement used for axial tomography where a line of radiation sources emit a parallel set of rays through the test object onto a linear array of detectors. A projection at a given angle,  $\theta$ , is made up of many individual paths. A complete scan is typically made up of many projections at increments of  $2^\circ$  to  $6^\circ$  over  $180^\circ$ . A three-dimensional object can be reconstructed by stacking the individual slices.

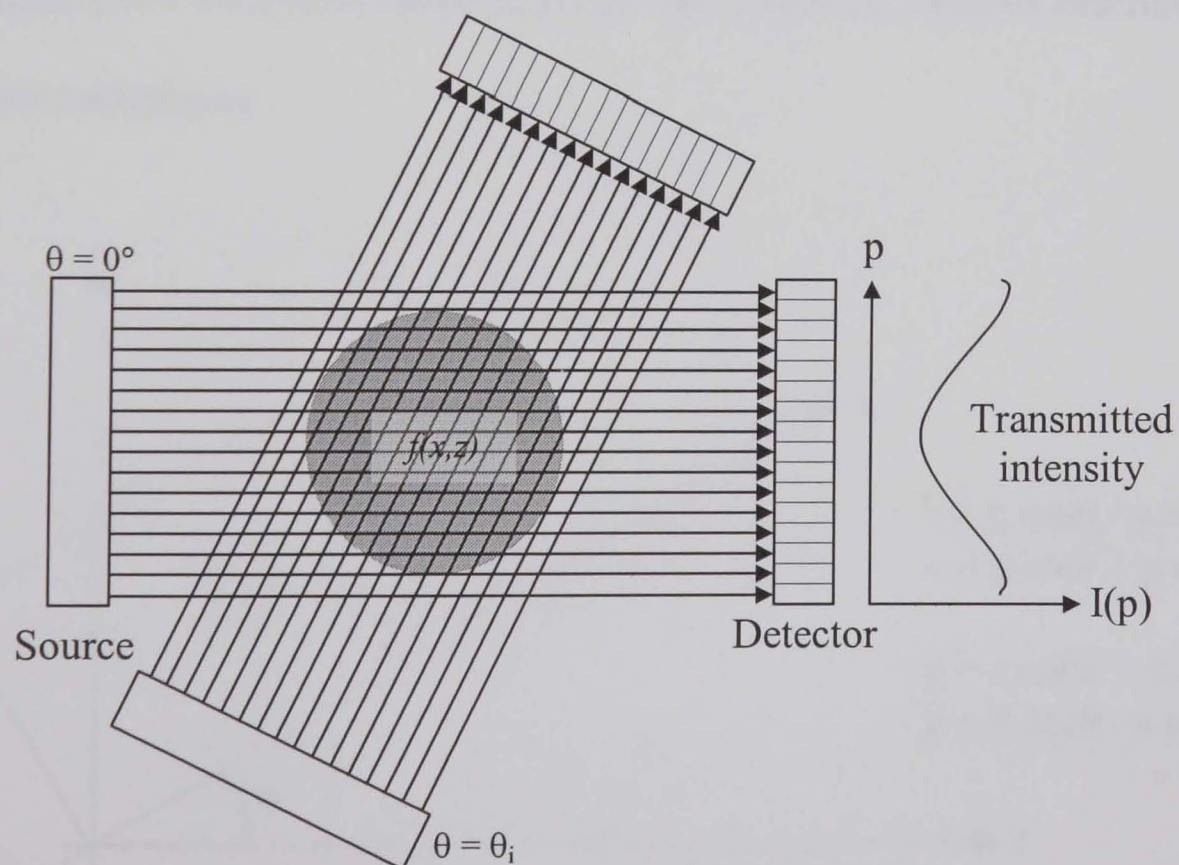


Figure 9.7. Axial tomography



The projection process, the coordinate system of which is shown in figure 9.8, can be described analytically using the Radon Transform <sup>[19]</sup>,

$$f_r(p, \theta) = \int f(x(q), z(q)) dq$$

$$= \int f(x, z) \delta(x - p \cos \theta - q \sin \theta, z - q \cos \theta + p \sin \theta) dq \quad (9.15)$$

where  $f(x, z)$  is the source function,  $\theta$  is the beam angle from the  $z$  axis,  $p$  is the transverse coordinate,  $\delta$  is the Dirac delta function and  $q$  is the coordinate along the ray path.  $f_r(p, \theta)$  represents the one-dimensional projection of  $f(x, z)$  onto a line orientated at an angle  $\theta$  with the  $z$  axis.

The integration is idealized into a line integration rather than a strip integration that accommodates the finite thickness of the rays or detector element pitch. Inverting the Radon transform gives the source function,  $f(x, y)$ . The following sections describe some of the inversion techniques.

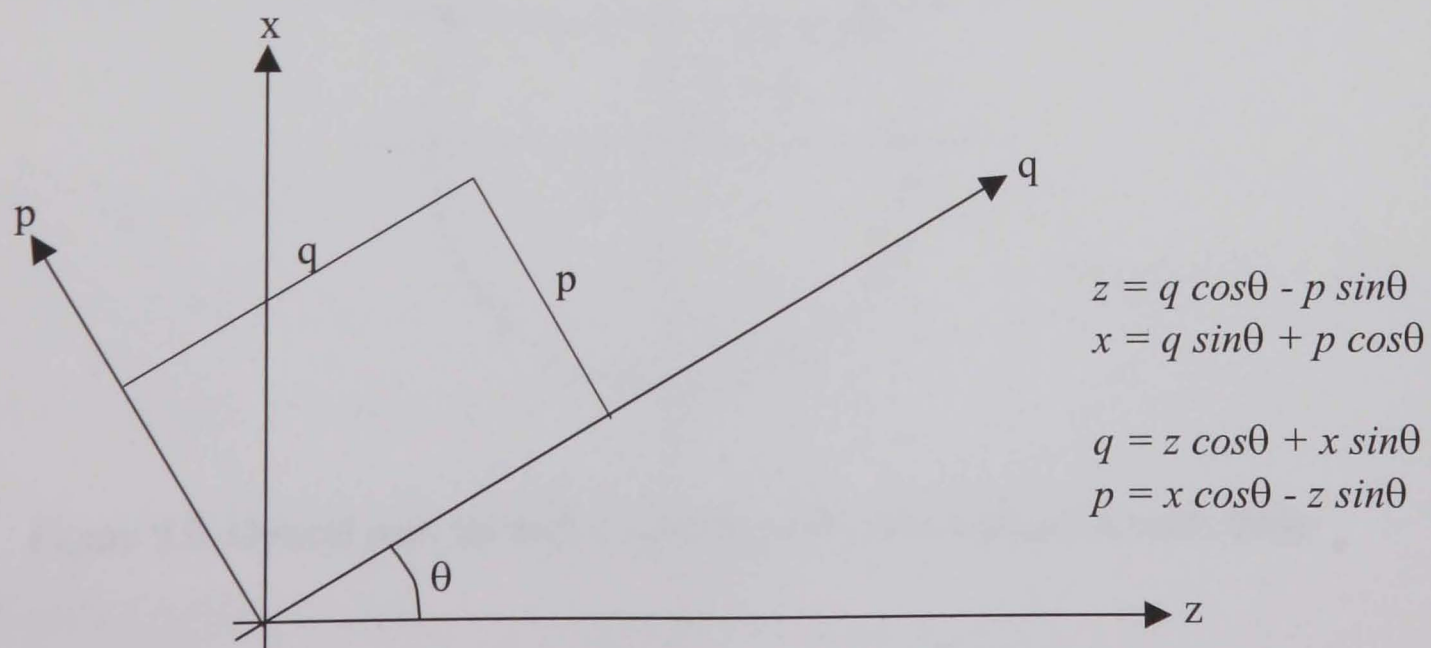


Figure 9.8. Projection coordinate system

### 9.6.2 Abel Inversion

In the case of radial symmetry the two-dimensional slice can be determined from one projection. The premiss of the Abel inversion is that a refractive index distribution can be divided into a series of constant refractive index, concentric rings. The inversion process involves *onion peeling* the distribution layer by layer. Figure 9.9 shows a ray passing through a refractive index field. Neglecting refraction the optical path difference may be written as <sup>[19]</sup>

$$\psi(x) = 2 \int_0^{z_1} n(r) dz \quad (9.16)$$

Differentiating along the optical path,  $x$  is constant gives  $rdr = zdz$  and substituting

$z = \sqrt{r^2 - x^2}$  gives

$$dz = \frac{rdr}{\sqrt{r^2 - x^2}} \quad (9.17)$$

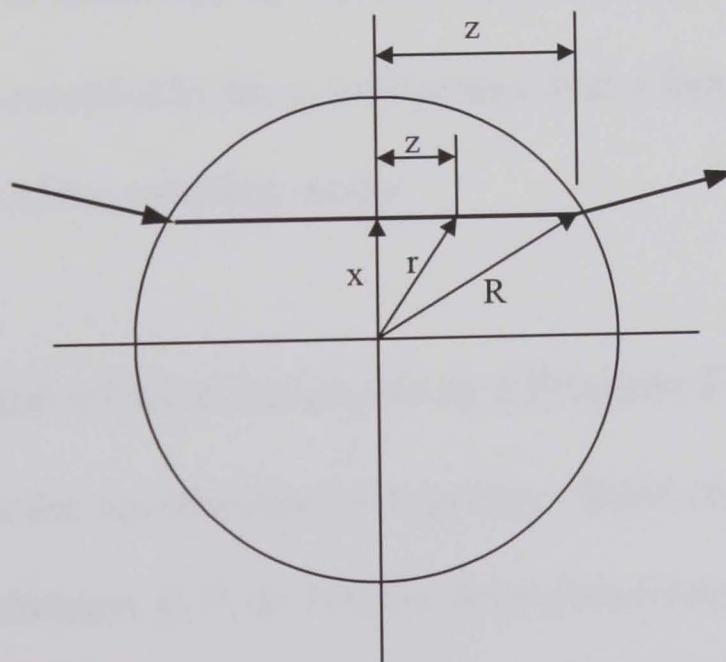


Figure 9.9. Optical path through a radially symmetric refractive index field

Therefore equation 9.16 can be written

$$\psi(x) = 2 \int_x^R \frac{n(r)r}{\sqrt{r^2 - x^2}} dr \quad (9.17)$$

If the optical path difference is recorded by the interferometer for all values  $0 < x < R$ , or preferably further than  $R$  to include areas outside the flow, then equation 9.17 may be inverted to give the refractive index in the range  $0 < r < R$  [19 & 29].

$$n(r) = -\frac{1}{\pi} \int_r^R \frac{\psi_x}{\sqrt{x^2 - r^2}} dx \quad (9.18)$$

where

$$\psi_x = \frac{d}{dx} \psi(x)$$

Such an inversion is known as an Abel Inversion.  $\psi(x)$  is not usually an analytical function of  $x$ , but is recorded by the interferometer over a finite number of rays owing to the finite resolution of the recording media.

### 9.6.3 Application of Abel Inversion to a Propane Flame

Figure 9.10a shows the interferogram of a propane flame emitted from a radial burner taken from both references [111 & 115] by Bryanston-Cross. The interferogram is not the result of a sheared beam but the interference of a plane wave with a tilted wave front to produce carrier fringes.

Figure 9.10b shows the unwrapped phase map produced using the FFT technique. The solution contains localized tile failures but the Minimum Spanning Tree phase unwrapping algorithm has preserved the overall integrity of the global solution. As the flame is assumed to be radially symmetric the Abel Inversion algorithm need include only one half of the flame. The left-hand side of the flame contains the least tile failures so will be the subject of the remainder of the analysis. Neither the angle of tilt between the plane and reference beams nor the dimensions of the flame are known so the analysis remains dimensionless and all axis coordinates refer to pixels only.



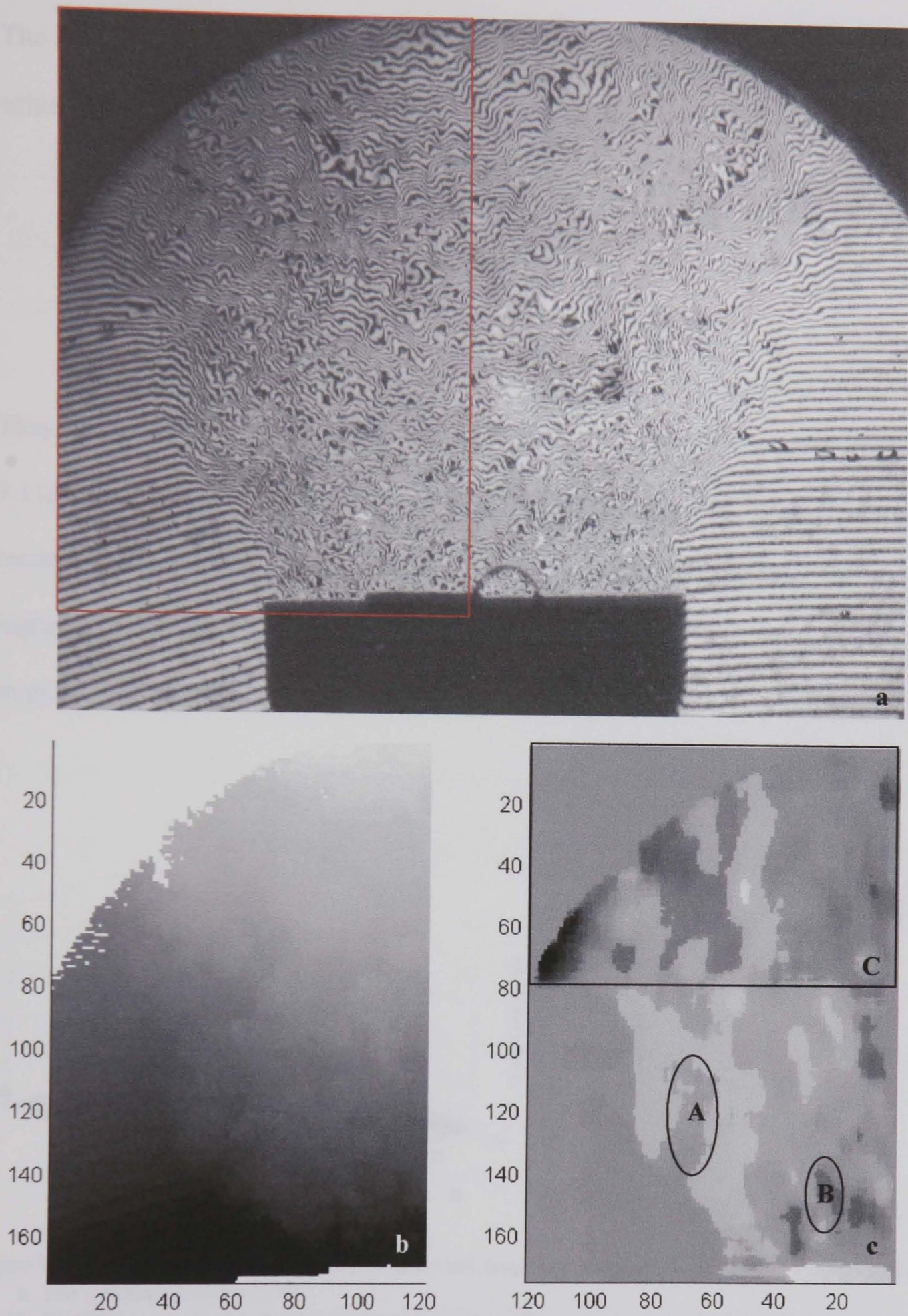


Figure 9.10. The analysis of a tilted wave interferogram projected through a propane flame.  
**a.** The tilted wave interferogram.  
**b.** The unwrapped phase map of half the interferogram (highlighted in red).  
**c.** Cross section through the propane flame calculated using an Abel inversion.  
 Highlighted areas contain localized failures discussed in text.



The integration and differentiation in equation 9.18 is to be carried out numerically. To achieve this the equation can be discretised as follows,

$$n(r) = -\frac{1}{\pi} \sum_r^R \frac{\psi_x}{\sqrt{x^2 - r^2}} \Delta x \quad (9.19)$$

This discretisation has been implemented and tested in the MatLab environment. Figure 9.11a shows a synthetic density field with a Gaussian profile. Figure 9.11b shows the reconstructed profile plotted against the original synthetic profile for successively higher resolutions of 100, 300 and 500 square pixels. The reconstructed solution improves as the resolution increases.

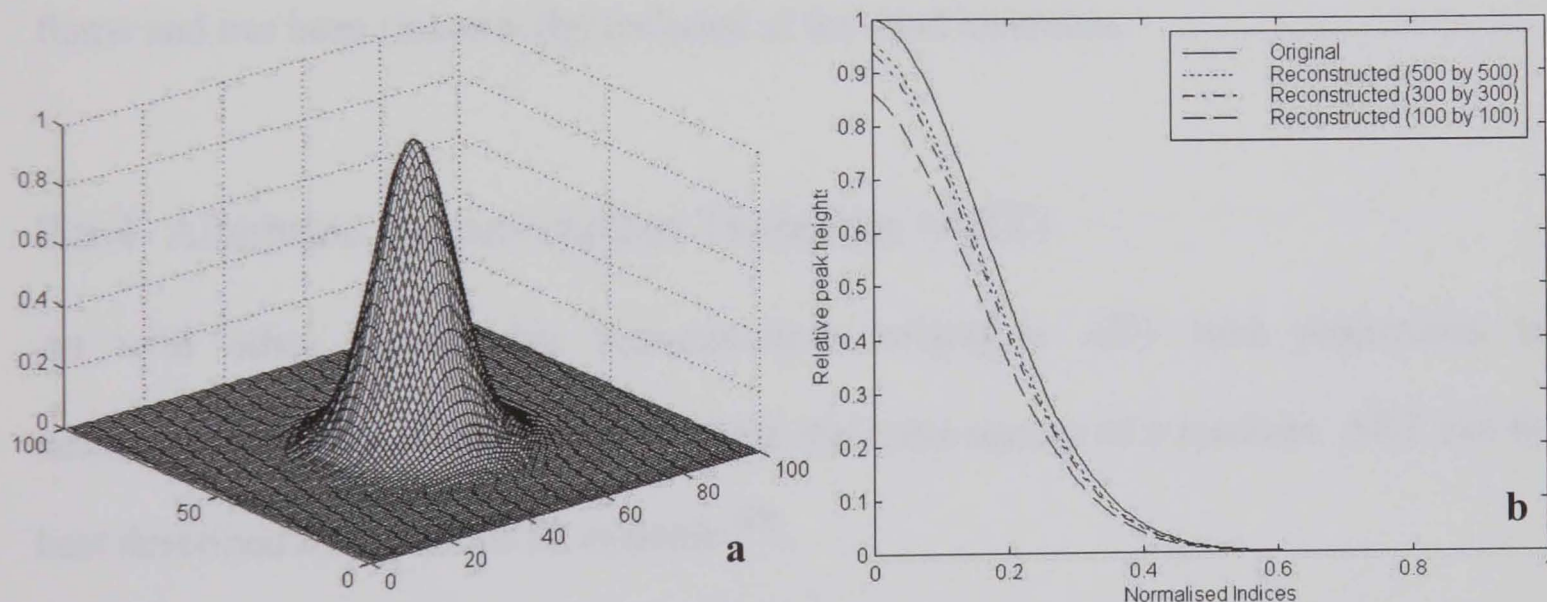


Figure 9.11. Testing of the discretisation of the Abel Inversion, equation 9.19, using a synthetic density field  
**a.** The synthetic density field  
**b.** Original cross section plotted against reconstructions at successively higher resolutions

The discretisation has been successfully applied to the unwrapped phase map of the propane jet, figure 9.10c. The solution has been subjected to a 9 x 9 median filter to reduce the spike noise. Figure 9.10c shows a ring of higher refractive index of similar

diameter to the burner exit that grows in diameter further downstream. The profile is similar to that measured by Bryanston-Cross <sup>[115]</sup> using thermocouples and coincides with the hottest part of the flame ( $\approx 1000$  °C). However, some of the features of figure 9.10c are artifacts of the analysis and noise. Areas A and B coincide with localized tile failures. The tile failures occur for two reasons. Firstly, the resolution of the interferogram has been reduced owing to computational limitations (insufficient memory). As a result the resampled interferogram may simply not have sufficient resolution to resolve the compressed fringes. Secondly, the phase information encoded within the deformation of the fringes needs to be a slowly varying function in comparison to the carrier frequency. This is necessary to successfully discriminate between the phase information and the carrier frequency in the frequency domain. The top third of the solution, area C, seems to have an offset in comparison with the rest of the image. This is because the silhouette in the top left-hand corner obscures part of flame and has been (incorrectly) included in the Abel inversion.

#### 9.6.4 Algebraic Reconstruction Technique (ART)

As with other tomographic reconstruction techniques ART uses projections to determine the unknown coefficients within the cross-section of a medium. ART can be best described by the use of an example <sup>[29]</sup>.

Figure 9.12a shows a three by three grid of coefficients. The grid elements, or pixels, are assumed to have unit dimension and the coefficient is uniform within its pixel. Adjacent to the grid are shown the vertical and horizontal ray sums that make up the projections. The grid contains 9 entries whilst we have 6 ray sums. The problem is therefore, as is typical of tomography, indeterminate.

			$\Sigma x$	
	1	3	2	6
	1	1	3	5
	2	1	2	5
$\Sigma y$	4	5	7	

**a.** Initial 3 by 3 problem and the projections of the rows and columns (the sum of the entries).

				$\Sigma x$
	6/3	6/3	6/3	6
	5/3	5/3	5/3	5
	5/3	5/3	5/3	5
$\Sigma y$	4	5	7	

**b.** Reconstruction, step 1. All grid entries are assumed to be unity. Elements first scaled by the row sum divided by the number of elements in the row.

				$\Sigma x$
	2	2	2	6
	1.67	1.67	1.67	5
	1.67	1.67	1.67	5
$\Sigma y$	5.33	5.33	5.33	

**c.** Reconstruction, step 2. Columns of reconstructed grid are summed.

				$\Sigma x$
	1.50	1.88	2.63	6.01
	1.25	1.57	2.19	5.01
	1.25	1.57	2.19	5.01
$\Sigma y$	4	5.02	7.01	

**d.** Reconstruction, step 3. Column elements are multiplied by column sum given in part a divided by the column sum calculated in part c. E.g. The elements in column 1 would be multiplied by 4/5.33, column 2 by 5/5.33 etc. After just one iteration the reconstructed grid gives row and column sums that are converging on those given in part a.

Figure 9.12. Example of the multiplicative algebraic reconstruction technique.

Initially the entries of the reconstructed grid are assumed to be unity. The rows are first multiplied by their respective row sum divided by the number of pixels in the row, figure 9.12b. The columns are then multiplied by the sum of the elements in the reconstructed column and divided by the column ray sum given in figure 9.12a. Several iterations of this scaling process may be required before the sum of the scaled rows or columns converge to a steady solution. As the problem is indeterminate the reconstructed grid converges to a solution, not necessarily the correct solution.

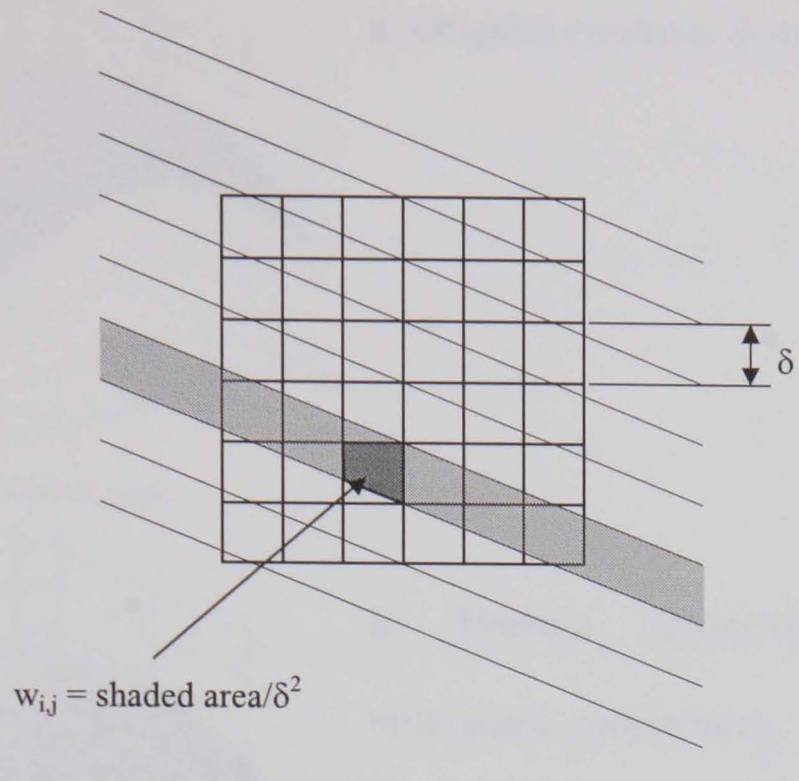
In the example shown in figure 9.12, multiplicative ART (MART) was used to scale the rows and columns by multiplication. An alternative to MART is to use addition ART (AART) to scale the rows and columns. With AART the difference between the reconstructed and original ray sum, divided by the number of pixels in the ray sum, is added to each of the entries. MART is often used in preference to AART as it cannot produce negative coefficients.

In the example only two orthogonal projections corresponding to the  $x,y$  coordinate system were used. In practical measurements the use of two orthogonal projections may not be possible or sufficient to reconstruct the domain. In such situations projections that do not coincide with the  $x,y$  coordinate system need to be considered.

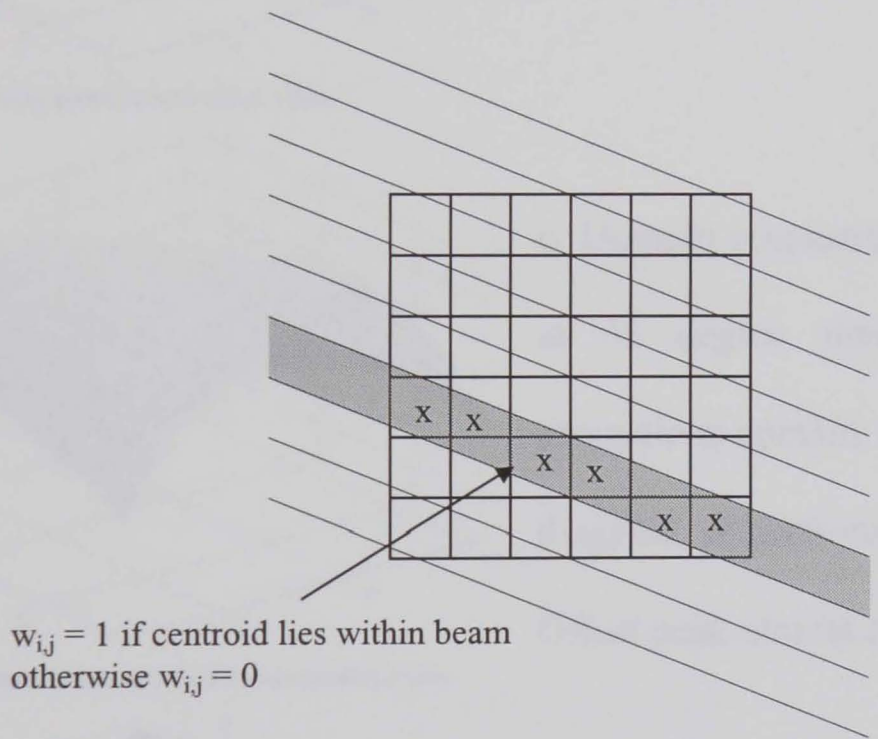
Figure 9.13 shows an arbitrary ray passing across a domain from a source to a detector. The ray has a finite thickness that will overlap both whole and part elements. The multiplicative or arithmetic scaling needs to be weighted either according to the area of this overlap or on a binary basis according to the presence of the centroid of the element within the ray.

Figure 9.14 shows an application of MART to a synthetic domain generated in the MatLab environment. The domain has been reconstructed using both 2 and 4 projections with 16 ray sums per projection. The use of 4 projections produces an obvious dividend in terms of reconstructing the offset peak.





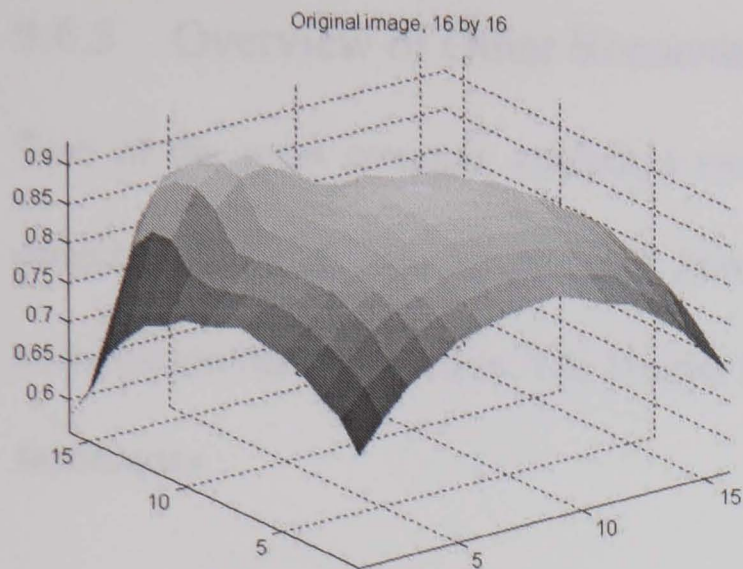
**a.**



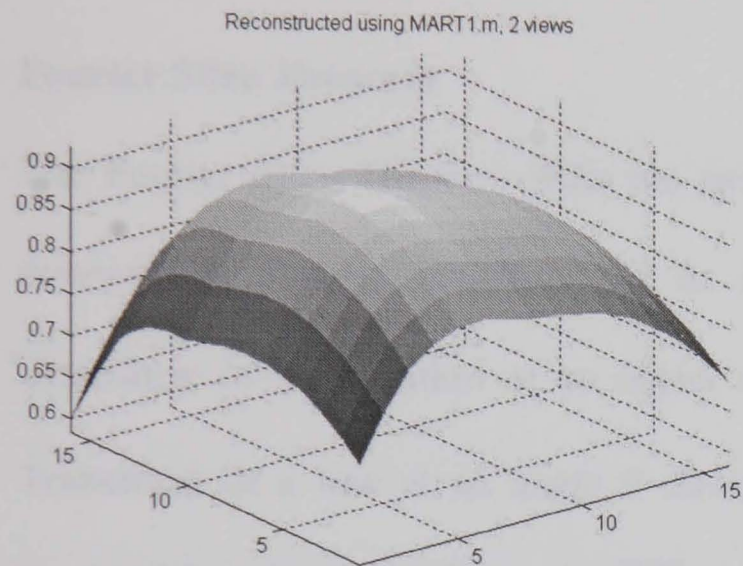
**b.**

Figure 9.13. A ray passing through a domain, partially overlapping some of the elements

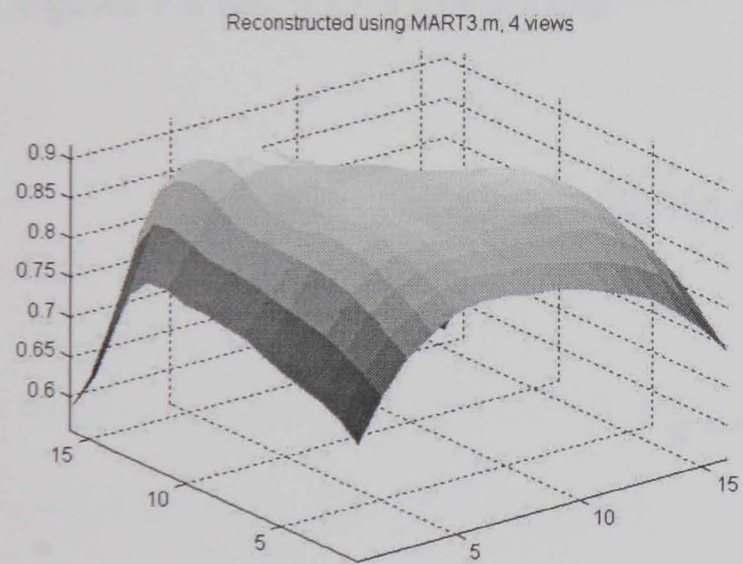




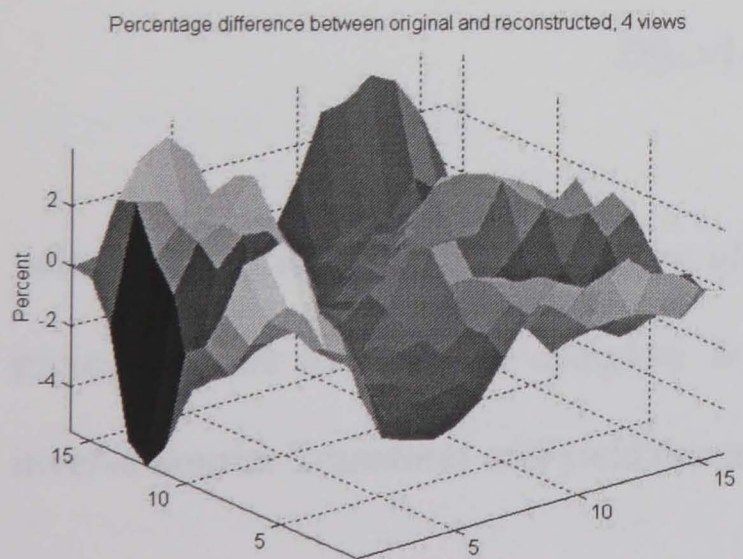
a. Original synthetic domain



b. Domain reconstructed from two orthogonal projections, each consisting of 16 ray sums. Single iteration. Offset peak only partially reconstructed



c. Domain reconstructed from 4 projections at 45 degree intervals. The orthogonal projections contain 16 ray sums, each of the diagonal projections contains 31 ray sums. Offset peak almost complete. 1 iteration.



d. Error  $\cong \pm 5\%$  as a percentage of the original amplitude based on the 4 projection reconstruction

Figure 9.14. Comparison of multiplicative reconstructions of a synthetic domain using two and four views.

### 9.6.5 Overview of Other Reconstruction Techniques

Two of the most common analytical reconstruction methods that are used where the object under study can be accessed from a full 180° are filtered back projection and convolution back projection. The Fourier Slice theorem forms the basis for both of these techniques.

#### Fourier Slice Theorem

The Fourier Slice Theorem links the two-dimensional Fourier Transform to the one-dimensional Fourier Transform of its projection <sup>[19,29 & 113]</sup>. It states the Fourier Transform of a projection of an object at angle  $\theta$ ,  $\mathfrak{F}\{f_r(p,\theta)\}$ , is equal to the Fourier Transform of a line at an angle  $\theta$  through an object,  $F_r(q,\theta)$  <sup>[19]</sup>. With reference to figures 9.8 and 9.15 it follows that <sup>[138]</sup>

$$\mathfrak{F}\{f_r(p,\theta)\} = F_r(q,\theta) \quad (9.20)$$

$$q = \sqrt{u^2 + v^2} \quad (9.21)$$

$$D(u,v) = \mathfrak{F}\{f(x,z)\} \quad (9.22)$$

where  $D(u,v)$  is the Fourier transform of the object in Cartesian coordinates. If all the projections are known, the complete frequency field can be built, from which the inverse Fourier Transform will yield the original object.



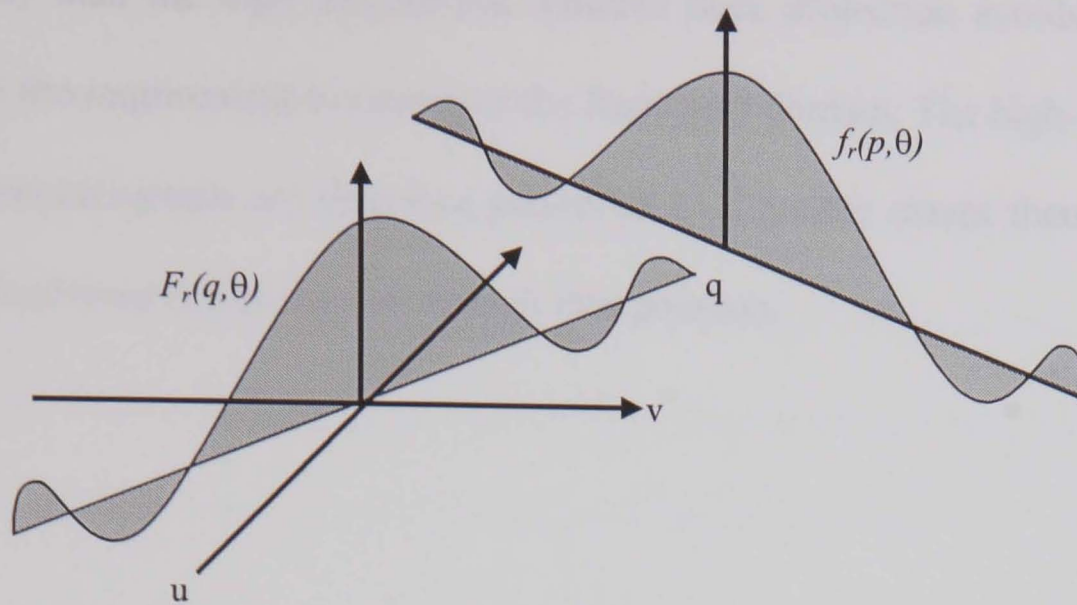


Figure 9.15. Diagrammatic explanation of Fourier Slice theorem

### Back Projection

Back projection is a simple, inexact, but less computationally intensive method of reconstructing the object. The back projection is described by <sup>[138]</sup>

$$b(x, z) = \int_0^\pi f_r(p, \theta) d\theta \quad (9.23)$$

Each projection is expanded (back projected) along the beam axis and the superimposed (summed) back projections produce an approximate reconstruction

### Filtered Back Projection

For the filtered back projection method the filtered inverse Fourier Transforms of the projections are determined individually <sup>[19]</sup>. As the frequency domain is reconstructed from lines radiating from its origin it will never be fully defined from a limited number of projections. Furthermore, in order to carry out a Fast Fourier Transform the radial frequency values need to be interpolated to a Cartesian grid. As the interpolation error increases with distance from the origin the lower frequencies will be reconstructed more

accurately than the high frequencies. Filtered back projection avoids this problem by negating the requirement to construct the frequency domain. The high frequency aspects of the reconstruction are therefore preserved to a greater extent than if the frequency domain had been reconstructed through interpolation.

## 9.7 SUMMARY OF CHAPTER

Refractive index changes approximately linearly with density. A ray of light that is transmitted through a region of high refractive index will be retarded relative to a ray that has not. The optical path difference is the difference in the path integrals, a convolution between refractive index and its thickness along the optical path, of the two rays (line integral in the absence of refractive bending).

The shearing interferometer is a simple means of recording optical path difference. The interferometer is used to shear a coherent beam that has passed through a phase object into two slightly displaced beams that occupy common optical paths. The two sheared beams interfere to produce a finite fringe interferogram. The optical path difference between overlapping sheared points manifests itself as a bending of the fringes. A one wavelength shift of a fringe represents an optical path difference of 1 wavelength. The measurement is relative to the sheared point rather than absolute. As all the beams are incident off common components and occupy common optical paths the interferometer is no more sensitive to vibration than an equivalent schlieren set-up.

The phase information can be automatically extracted from the interferogram by the FFT approach. The wrapped phase map can be unwrapped using the minimum spanning tree algorithm that unwraps round localised noise, either excluding it from the solution or only including it at the end of an unwrap path.

The carrier fringes produced by the shearing interferometer are typically not uniform across the extent of the image. The phase distribution of the reference state needs to be subtracted from disturbed state to remove these non-uniformities. The carrier frequency

needs to be higher than the phase frequency, but low enough to be resolved by the camera, to enable the segregation the phase information.

The distribution of refractive index, or density, within a phase object can be reconstructed by tomographic means. The reconstruction is typically indeterminate where the number of projections is limited. Assumptions are made about the geometry of the refractive index distribution to facilitate a reconstruction. Radially symmetric phase objects can be reconstructed using an Abel transform whilst a 3-D solution can be generated from a limited number of projections by using an algebraic reconstruction.



## *Chapter 10*

# APPLICATION OF THE SHEARING INTERFEROMETER TO A 2-D TRANSONIC AIR FLOW

### *Description of Chapter*

*This chapter describes the application of the shearing interferometer to a two-dimensional transonic wind tunnel at Rolls Royce, Derby.*

*A single, collimated beam has been projected through the flow field and sheared using a back-silvered mirror to produce a fringe pattern. The fringe pattern has been analysed using the Fast Fourier Transform (FFT) method <sup>[109 & 111]</sup>. The subsequent 'wrapped' phase map is 'unwrapped' using the largely noise immune Minimum Spanning Tree (MST) technique. This allows the flow field to be solved despite the presence of discontinuities such as shocks.*

*The shock structures were observed to be similar to those revealed by a holographic interferometer <sup>[22]</sup>.*

## 10.1 INTRODUCTION

Calculating the inter-passage flow in turbomachinery is difficult because of the existence of shock structures and turbulent regions. As numerical techniques increase in their sophistication experimental methods are required to validate them. Bryanston-Cross and Denton <sup>[22]</sup> made a 2-D quantitative visualisation of the density and Mach number distribution of the 2-D wedge rig, as it shall now be referred to, at Rolls-Royce, Derby. The measurements were made using a holographic interferometer at a compressor representative flow condition of inlet Mach number 1.45 and compared against an inviscid prediction. Bryanston-Cross's measurements were made in the early 1980s. 2-D measurements integrated over the line of sight are no longer considered to be sufficiently accurate to reveal the flow between highly three-dimensional compressor blades.

The measurements presented here are also 2-D and integrated over the line of sight. The purpose of these measurements differs from those described by Bryanston-Cross in that they were to be used as a quick, first pass characterisation of the flow field prior to the testing of a new 3-D anemometry system. To achieve this the optical arrangement had to be simple to set up and negate the requirement for excessive vibration isolation. The use of the shearing interferometer allowed measurements covering one half of the test section (symmetrical about the centreline of the wedge) to be made at mass flow rates from 0.6 to 1.0 kg/s in increments of 0.02 kg/s in the space of one day. Only the results of the 0.66 kg/s mass flow rate will be presented here.

## 10.2 TWO-DIMENSIONAL WEDGE RIG

The wedge rig is designed to maintain transonic flow continually through the test section. To achieve transonic flow a two-dimensional convergent-divergent nozzle was used to accelerate the flow through the 35.6 mm wide tunnel section containing the test body, from which it was then exhausted to atmosphere. Although the test section is very narrow the flow through it was assumed to exhibit two-dimensionality as described in [22]. A nine degree wedge was introduced into the test body to create a transonic compression of the flow, figure 10.1. The wedge and test body were designed to produce a strong leading edge shock that at speeds of approximately Mach 1.5 was considered to be similar to that generated in the first stage compressor of a typical commercial gas turbine engine. A summary of the operating conditions is given in table 10.1.

Unfortunately, on the day of the test one of the test section windows was found to be broken. The upper right-hand corner of the window can be seen to be missing in figure 10.1. As the missing fragment is downstream of the leading edge of the wedge and only extends to one side the decision was made to only consider the lower side of the wedge, downstream of its leading edge. The asymmetry affected the flow at the wedge tip where the air was found to be slower and denser than expected.

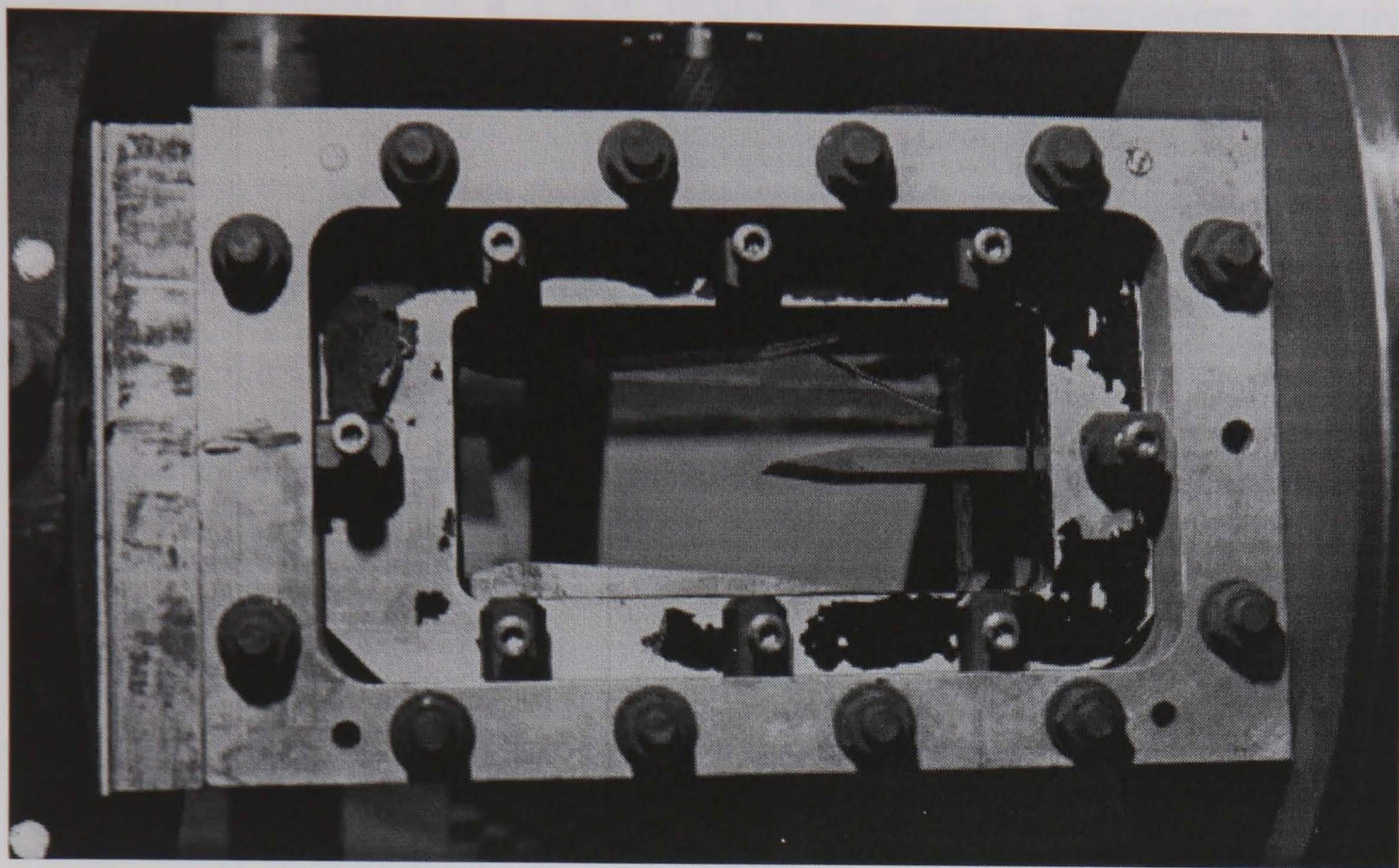


Figure 10.1 The test section of the wedge rig

Continuously running tunnel	
Exhaust to ambient air	
Reynolds number based on the tunnel width	$5 \times 10^5$
Width of tunnel	35.6 mm
Height of tunnel	68.5 mm
Angle of wedge	$9^\circ$
Thickness of wedge.	7 mm

Table 10.1 Dimensions of the wedge rig

### 10.3 EXPERIMENTAL ARRANGEMENT

The optics consisted of a 5 mW Helium Neon laser, a microscope objective of numerical aperture 0.4, a plano-convex lens of diameter 100 mm, focal length 150 mm and a 150 mm square, 3 mm thick back silvered mirror. The laser, microscope objective and plano-convex lens were mounted on an optical rail placed approximately one metre in front of the wind tunnel, see figures 10.2 and 10.2. The beam was expanded using the microscope objective and collimated into a beam of approximately 75 mm using the plano-convex lens. Efforts were made to make the beam as perpendicular to the wind tunnel as possible. The back-silvered mirror was mounted approximately 20 cm behind the wind tunnel on a scaffolding frame using a temporary mount. The mirror was rotated about the x-axis until the fringes were parallel with the direction of flow, thus being in a suitable alignment for the proposed FFT analysis. The proximity of the laboratory wall prevented the mirror from being rotated to an ideal angle. As a result each fringe was described by approximately ten pixels across its width rather than the optimum figure of five. The reflected beam was projected on to a piece of white paper wrapped round a piece of flat sheet metal. This gave a grain free image with little glare from the dull surface of the paper. The screen was positioned to be as near as possible to the normal of both the reflected beam and the view from the CCD camera. The reason for this was to avoid distorting the image due to a sloping screen and to allow the CCD camera to focus on the entirety of the image. The images were recorded with an 8 bit monochrome CCD camera with 560 by 450 pixels.

Results were gathered from flow rates of 0.6 kg/s to 1.0 kg/s in increments of 0.02 kg/s as within this region an interesting shock structure developed. Four reference shots were



taken before, after and during the capture sequence. Only the measurement at 0.66 kg/s is considered here.

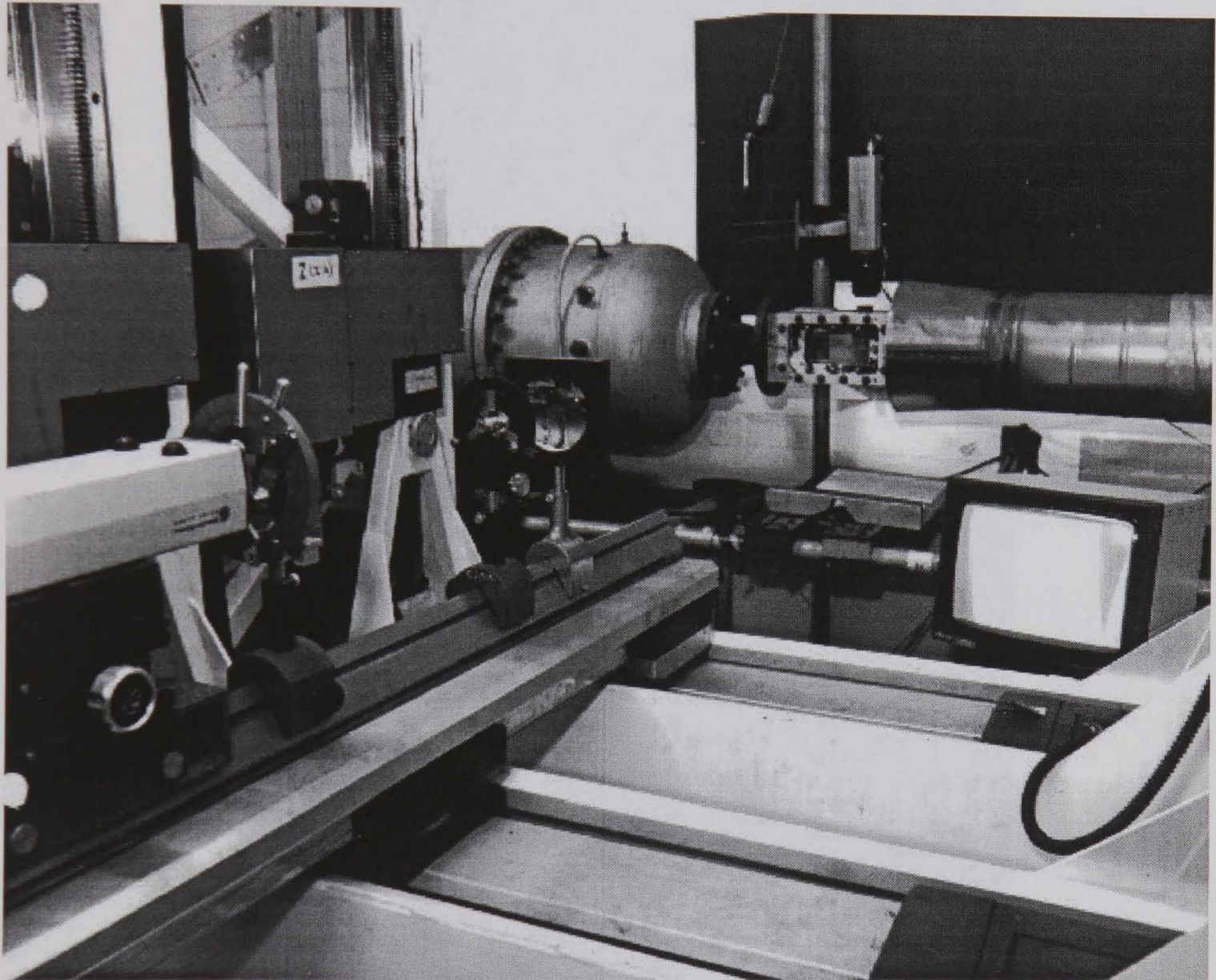


Figure 10.2 The shearing interferometer applied to the wedge rig.



## 10.4 RESULTS

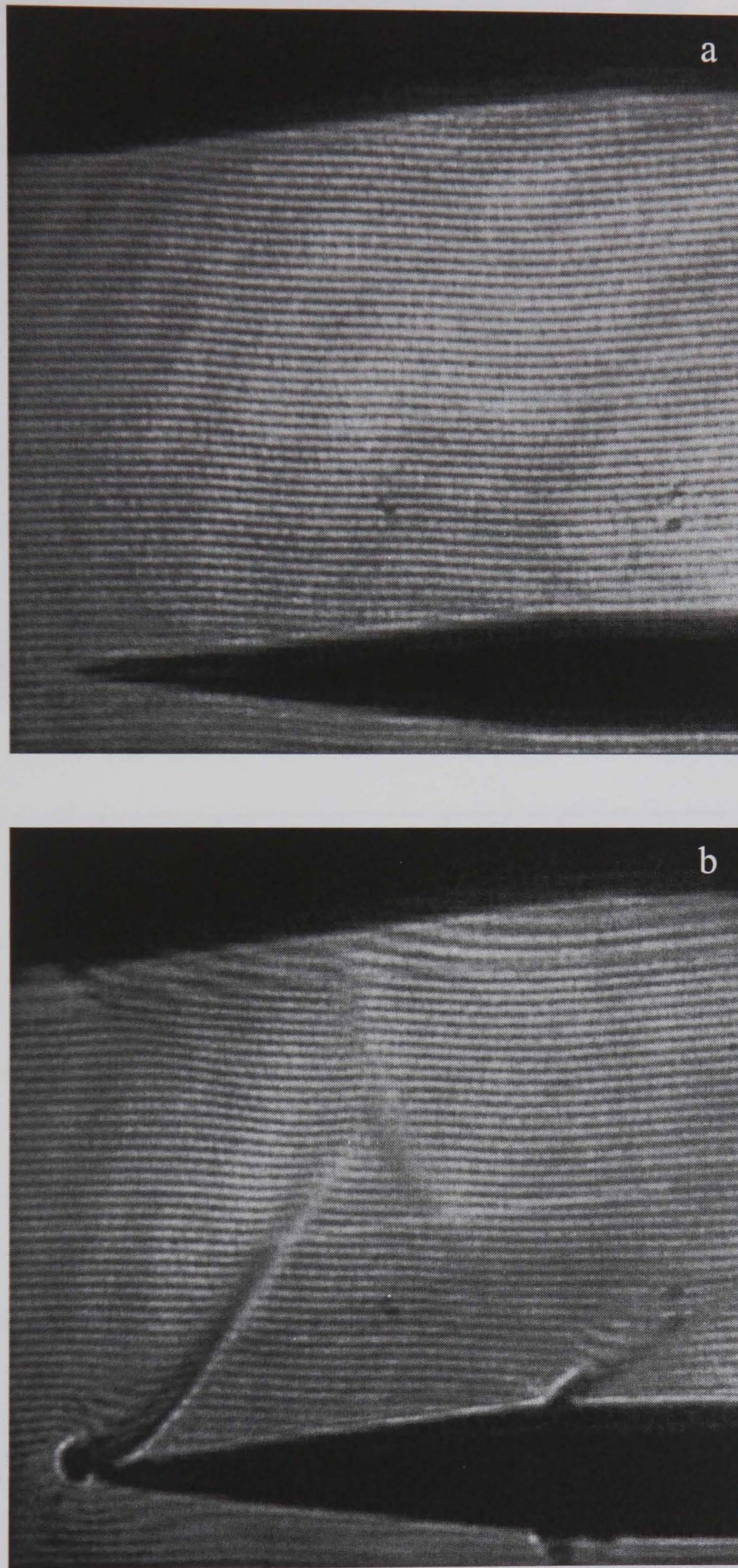


Figure 10.3 Fringes projected through the wedge rig  
a. Reference image in the absence of the flow  
b. Flow on, mass flow rate of 0.66 kg/s, Mach 1.5 at inlet, flow from left to right



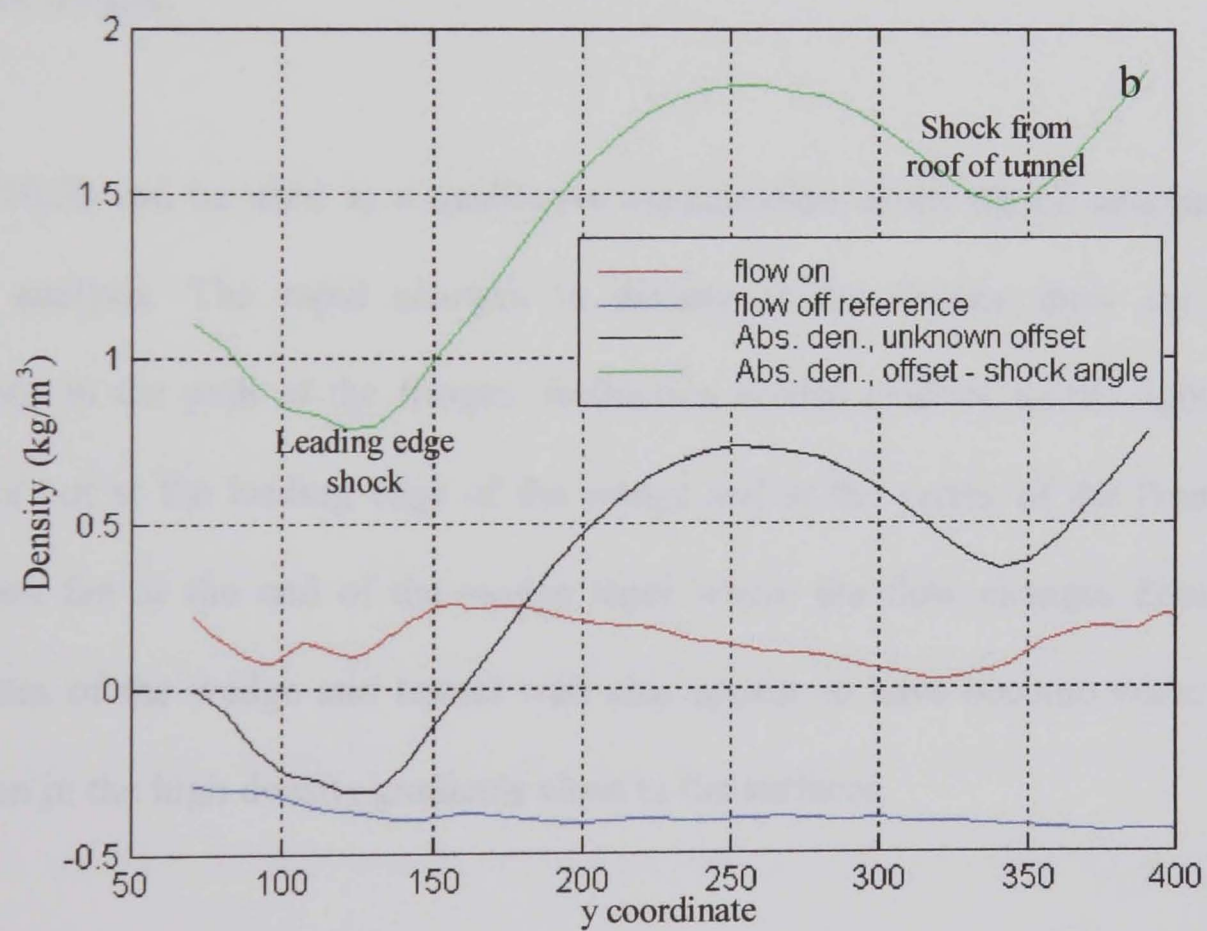
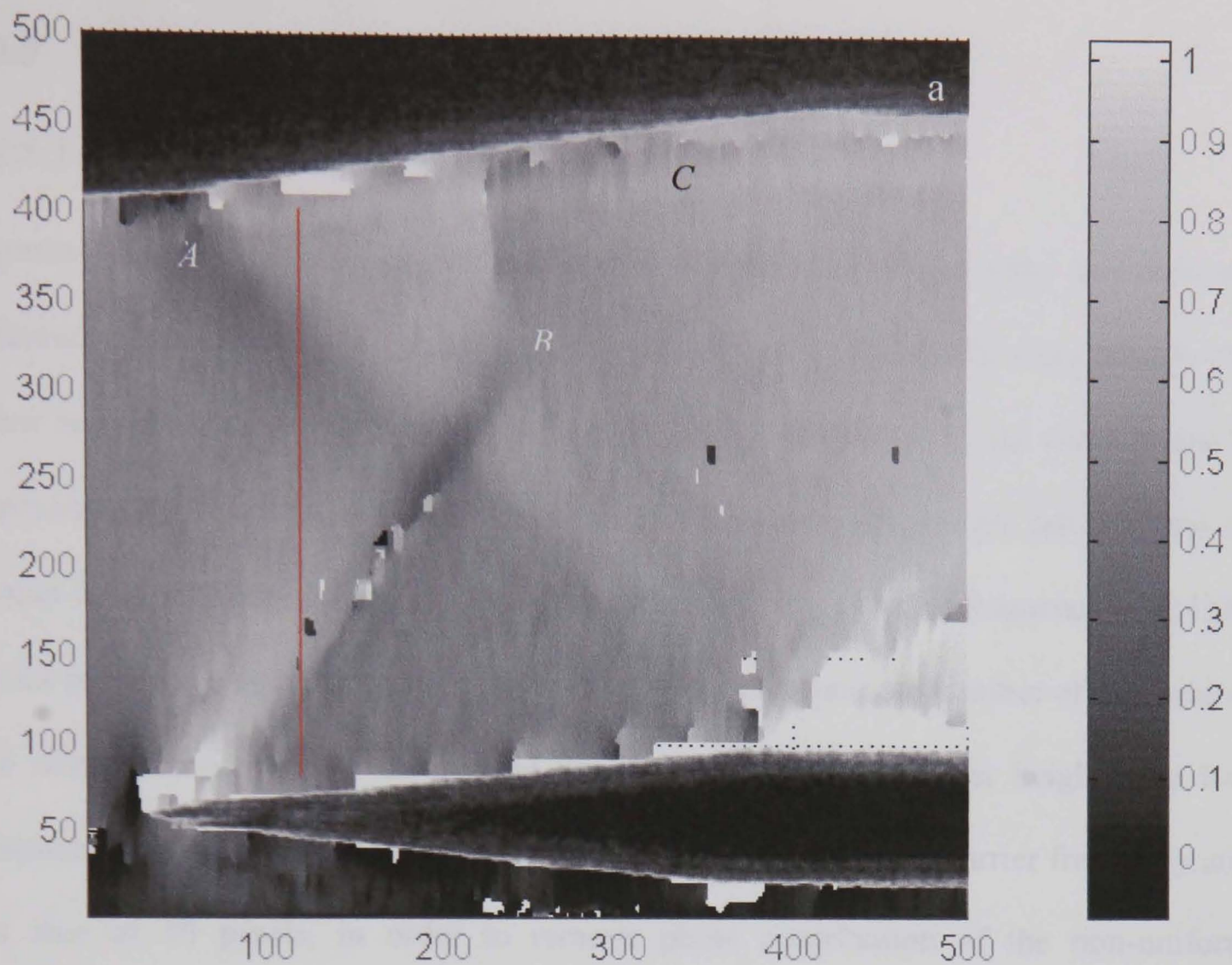


Figure 10.4 Processed fringe pattern from the wedge rig

- a. Unwrapped phase map. Colour bar in  $\text{kg/m}^3$  relative to sheared point (refer to text for description of highlighted regions)
- b. Solution for raster of pixels highlighted in 'a'. Flow on and off relative densities, and integrated density with unknown offset and offset estimated from oblique shock theory.

## 10.5 INTERPRETATION OF RESULTS

### 10.5.1 Analysis of the Fringe Patterns

Figures 10.3a and b show the flow off and flow on results respectively. The flow off reference image shows the fringes running parallel to the axis of the wind tunnel. The shear is in the orthogonal direction with a magnitude of  $\frac{3}{4}$  mm, which corresponds to approximately 9 pixels in the y-direction. The reference fringes are not uniform so cannot be described by a single carrier frequency. A single carrier frequency of 0.1289 cycles per pixel was chosen as it gave a solution with a minimum number of tile failures and discontinuities in the unwrapped phase map. The fringe order height map was subtracted from that of the flow on state, processed with the same carrier frequency and tile size of 10 pixels, in order to remove phase contribution of the non-uniform reference fringes.

Figure 10.3b can be used as a qualitative visualisation of the shock structure without further analysis. The rapid changes in density at the shocks show up as abrupt deviations in the path of the fringes. Refraction is also evident, as the light has been *squeezed* out at the leading edge of the wedge and at the vertex of the Prandtl-Meyer expansion fan at the end of the wedge taper where the flow changes direction. The silhouettes of the wedge and tunnel wall also appear to have become wider owing to refraction in the high density gradients close to the surfaces.

Figure 10.4a shows the density distribution relative to a sheared point in  $\text{kg/m}^3$ . The solution has been produced by subtracting the fringe order height map of the flow off condition from that of the flow on. The change in density has been calculated using

equation 10.3 as two-dimensionality has been assumed. Holes in the solution occur where a silhouettes or noise interrupt the tiles.

Figure 10.4b illustrates the integration of the raster of pixels from figure 10.4a, indicated by a red line, in order to calculate the absolute density. This raster of pixels was chosen as it crosses both the leading edge shock and what appears to be an expansion wave emanating from a change in direction of the tunnel wall. The blue and red lines of figure 10.4b show the relative changes in density of flow on and off conditions respectively. The flow off has been subtracted from the flow on and the offset removed. The changes in density of sheared points, separated by 9 pixels, have been summed along the raster to determine the absolute density with an unknown offset, shown by the black line. For the green line the offset has been estimated using oblique shock theory <sup>[106]</sup>

$$\frac{\rho_2}{\rho_1} = \frac{\tan \theta}{\tan(\theta - \beta)} \quad (10.1)$$

where  $\beta$  is half the angle of the wedge,  $\theta$  is the angle of the oblique shock,  $\rho_1$  and  $\rho_2$  are the pre and post shock densities respectively. The absolute density could also be calculated from points of known stagnation and the isentropic relations either side of the leading edge shock. From figure 10.4b the change in density across the shock (between pixels 70 and 125 on the x-axis) is  $0.3 \text{ kg/m}^3$ . Substituting  $\rho_2 - \rho_1 = 0.3$  into equation 10.1 gives  $\rho_1 = 0.803 \text{ kg/m}^3$  and  $\rho_2 = 1.103 \text{ kg/m}^3$ . The density ratio across the shock is 1.37 for a shock angle of  $53^\circ \pm 1^\circ$ . If the pre and post shock densities are known the pre and post shock Mach numbers can also be calculated from the following equations taken from White <sup>[106]</sup>

$$M_1 = \left[ \frac{2}{\sin^2 \theta \left( \frac{\rho_1 (\gamma + 1)}{\rho_2} - (\gamma - 1) \right)} \right]^{\frac{1}{2}} \quad (10.2)$$

$$M_2 = \left[ \frac{(\gamma - 1)M_1^2 \sin^2 \theta + 2}{2\gamma M_1^2 \sin^2 \theta - (\gamma - 1)} \times \frac{1}{\sin^2(\theta - \beta)} \right]^{1/2} \quad (10.3)$$

where  $M_1$  and  $M_2$  are the pre and post shock numbers respectively and  $\gamma=1.4$  for air. The calculations are summarised in table 10.2.

	Pre shock	Post Shock
Measured density, kg/m <sup>3</sup>	0.803	1.103
Density ratio	1.374	
Mach number	1.526	1.196

Table 10.2 Pre and post shock densities and Mach numbers.

### 10.5.2 Description of Results. Mass flow rate 0.66 kg/s.

#### **Close to the wedge.**

The flow approaches the leading edge with a Mach number of 1.53. A shock is formed at the leading edge of the wedge that slows the flow down to Mach 1.20 and turns the flow to run parallel with the profile of the wedge. At the end of the wedge taper a Prandtl-Meyer expansion accelerates the flow to its pre shock Mach number.

#### **Close to the tunnel wall surface.**

The abrupt change in direction at the tunnel wall at  $A$  creates a weak shock wave. The post shock Mach number quickly recovers to its pre-shock value of 1.3 only to

encounter another weak shock that appears to originate from the tunnel wall at *B*. The region immediately above *B* appears to contain a break in the unwrapped map that coincides with a region of poor fringe definition in figure 10.3b. The flow close to the tunnel wall from here on, *C*, contains noise where the silhouette has encroached into the tiles used in the unwrapping process. There is, however, a change in density along a line that continues downstream beyond the field-of-view that may be a separated region originating at *A*.

### 10.5.3 Resolution in Density

The fringe number corresponds to a convolution between the density change and the optical path length through the region. As the wind tunnel is two-dimensional the change in density between two sheared points required to produce a single fringe shift can be calculated using equation 10.3,

$$\Delta\rho = \frac{\lambda}{lC} = \frac{6.3 * 10^{-7}}{35.6 * 10^{-3} * 2.256 * 10^{-4}} = 0.078 \text{ kg / m}^3$$

### 10.5.4 First Order Approximation of Refraction

The incident beam will always be normal to the interface of the change in refractive index if the flow is assumed to be two-dimensional and the beam is aligned to the normal to the test section windows. From Snell's law the refractive bending will therefore be zero. Although the flow is assumed to be two-dimensional Bryanston-Cross [22] observed that although the features exhibited two-dimensionality across the major span of the tunnel the foot of shocks broadened close to the windows.



The amount of refractive bending can be measured by sending a beam of light through the wind tunnel and recording its displacement between the flow off and on conditions. Unfortunately, this test was not carried out. The refractive bending is expected to be significant close to the surfaces owing to the density gradient of the boundary layers. The refractive effect will extend to the corresponding sheared point. The apparent broadening of the silhouette of the wedge between the flow off and on conditions is believed to be due to refractive bending.

## 10.6 DISCUSSION

The fringe patterns presented here represent a challenging application for interferometry as the flow contains gradual changes in density followed by abrupt changes owing to the shocks. The carrier frequency needs to be higher than the phase frequency, so that they can be separated from the low frequency information in frequency space. The presence of shocks therefore dictates that a high carrier frequency is used. In this application the carrier frequency was approximately 0.13 cycles per pixel, the maximum that could be achieved at the time of the experiment. Figure 10.5 shows the power spectrum of the raster of pixels considered in figure 10.4b. It is not clear where the low frequency information from silhouettes etc ends and where the required side lobe begins. However, the ambiguity is not believed to be the cause of the tile failure in figure 10.4a as the failures correspond to regions in the original fringe pattern, figure 10.3b, where the fringes cannot be resolved either due to insufficient spatial resolution or a blurring of time variant aspects of the flow. A simple solution to the blurring effects would be to reduce the camera's integration time. The number of carrier fringes can be

increased by using more shear and opening up the camera's aperture to reduce the speckle size if it is larger than the pixel size.

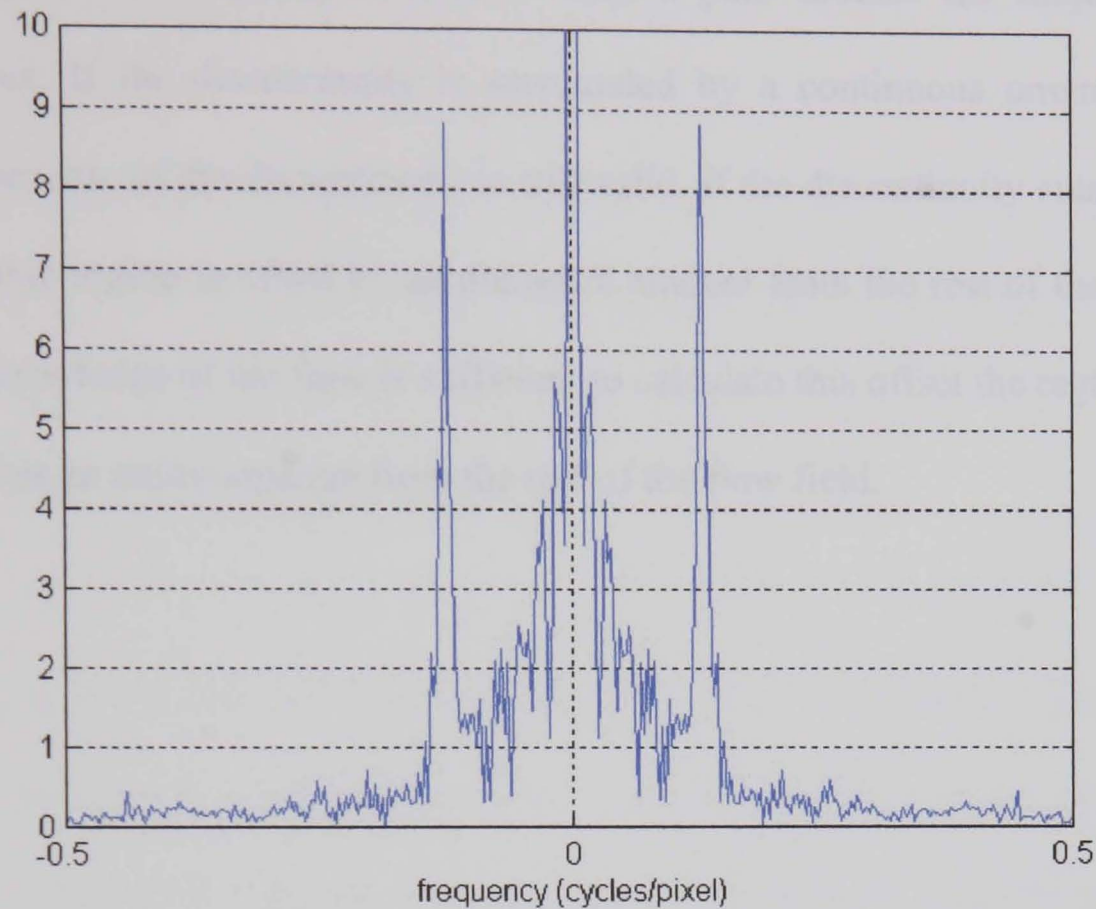


Figure 10.5 The power spectrum of the raster of pixels considered in figure 10.4b

The density close to the surfaces is hidden by the stepped edges of the tiles used in the unwrap path. The tile size of 10 x 10 pixels used here was the lower limit that can be achieved with the FRAN software. Even in the absence of the tile obscuration these regions are likely to be dominated by refractive bending owing to the steep density gradients of the boundary layers.

It is imperative that the analysis technique is robust enough to find a path around the discontinuities without jeopardising the overall solution. Shock waves or other abrupt changes in the flow field can cause a discontinuity in the fringe field. The discontinuities appear as a jagged, stepped transition between grey levels. Shocks are to

be expected in transonic flows so it is important that they are allowed for in the analysis whilst still solving the continuous surface. With FRAN the minimum spanning tree method of phase unwrapping is able to find a path around the majority of the discontinuities. If the discontinuity is surrounded by a continuous unwrap path the solution either side of the discontinuity is still valid. If the discontinuity cuts off an area the flow in this region is offset by an unknown amount from the rest of the flow field. Unless the knowledge of the flow is sufficient to calculate this offset the region can only be described as an entity separate from the rest of the flow field.

## 10.7 SUMMARY OF CHAPTER

Density measurements have been made in a 2-D wind tunnel with an inlet Mach number of 1.5 using the shearing interferometer. The test section of the 35.6 mm wide, 68.5 mm high wind tunnel contains a wedge profile with a half angle of  $9^\circ$ . The measurements were used as a first pass characterisation of the flow through the tunnel in preparation for the evaluation of anemometry equipment. Measurements were made at mass flow rates from 0.6 to 1 kg/s in 0.02 kg/s increments within the space of one day. Only the 0.6 kg/s mass flow rate has been considered here.

The shearing interferometer can be used to provide either a qualitative visualisation or quantitative information about density if the phase information is extracted from the interferograms. The FFT method of fringe analysis and the MST phase unwrapper have been used to get this information in the presence of discontinuities in the fringe data and spike noise. A back-silvered mirror was used to give a shear of  $\frac{3}{4}$  mm (9 pixels) in a direction orthogonal to the axis of the facility. The carrier frequency was approximately 0.13 cycles per pixel.

The unwrapped map shows a strong leading edge shock from the leading edge of the wedge and a Prandtl-Meyer expansion fan at the end of the wedge taper. The pre and post shock Mach numbers are 1.526 and 1.196 respectively. Oblique shock theory has been used to calibrate the relative density measurements for absolute density.

## Chapter 11

# APPLICATION OF THE SHEARING INTERFEROMETER TO A SHOCK-TUBE EXHAUSTING INTO AMBIENT AIR

### *Description of Chapter*

*The chapter describes the application of a simple interferometric shearing device to a shock tube used to evaluate noise-suppressor nozzles relevant to the High-Speed Civil Transport programme. The problems in making such an aircraft fit within modern certification standards and the rationale of the reflection-type shock tube is also discussed with regard to testing time and economics relative to an equivalent continuous running facility. A brief overview of the gas dynamics, function and dimensions of the facility is also included.*

*The shearing interferometer allows a projection of the change in refractive index of a medium to be measured. The change in refractive index can either be due to a change in density of the fluid or the presence of a gas of differing Gladstone-Dale constant. The Fourier Transform method of fringe analysis and a largely noise-immune phase-unwrapping algorithm are described.*

*The analysis of a single result recorded on the shock tube is also included. Recommendations are made regarding the future application of the shearing interferometer to this facility.*



## 11.1 INTRODUCTION

### 11.1.1 Introducing the Problem

Airport regulations and aircraft noise certification requirements govern the maximum noise level that an aircraft is permitted to produce. The principal source of noise is the aircraft's engine <sup>[102]</sup>. The compressor, turbine and exhaust jets all produce noise levels that increase, to varying degrees, with the relative airflow velocity. Of these it is the exhaust jet that is likely to be dominant, so a reduction in the exhaust jet velocity will have the strongest influence on the overall noise level.

The exhaust jet noise is due to the mixing of the exhaust gases with the atmosphere and is influenced by the shearing action and relative velocity between the two. The small eddies which are found near the exhaust duct generate high frequency noise, see figure 11.1. These eddies coalesce and grow into larger eddies that generate low frequency noise. If the jet speed exceeds the speed of sound the jet core will contain a criss-crossing shock pattern that may produce a single tone under certain circumstances and can amplify the mixing noise at certain frequencies.

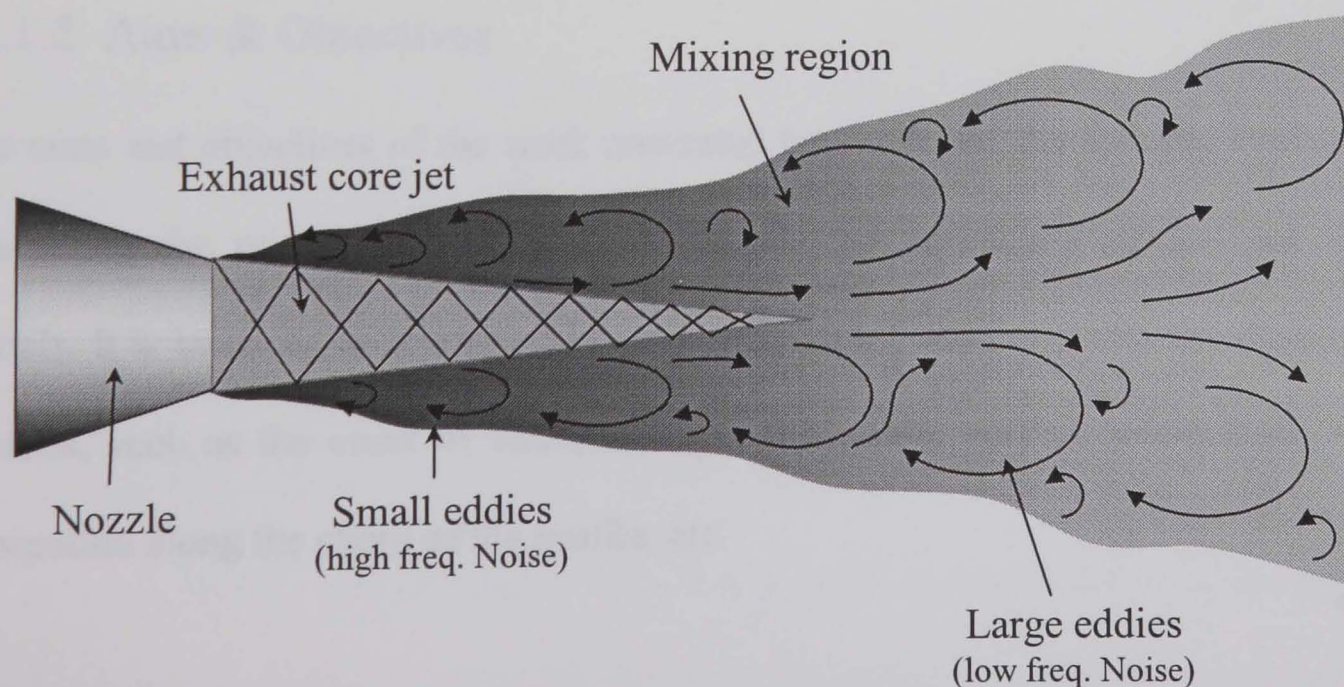


Figure 11.1. Exhaust core jet and mixing region of a compressible jet



The noise level can be reduced if the mixing rate is accelerated or the relative velocity is reduced. Corrugated-lobe-type suppressors, see figure 11.2, promote mixing by increasing the contact area between the exhaust jet and the atmosphere but deep lobes can have performance penalties in terms of thrust, weight and drag.

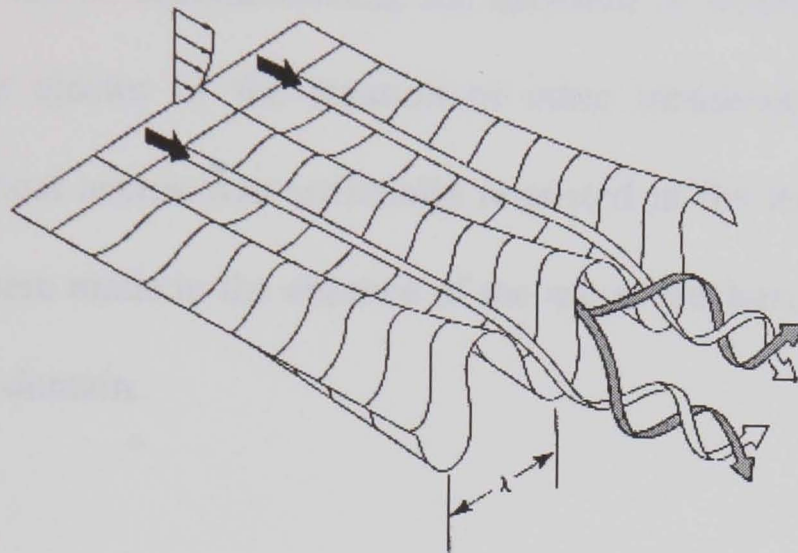


Figure 11.2. Lobe type suppressor nozzle <sup>[103]</sup>

The purpose of the MIT shock tube is the acoustic evaluation of noise suppressors, or mixer-ejectors, relevant to the HSCT programme.

### 11.1.2 Aims & Objectives

The aims and objectives of the work presented here is to aid the acoustic evaluation by visualising the mixing and other flow features for correlation against the acoustic signals. It is intended to reveal information that can be used to revise the design of the profiles, such as the onset of boundary-layer separation, vortical interactions, viscous dissipation along the chord of the profile, etc.

A qualitative indication of mixing integrated over the entire run time is the primary requirement of the visualisation. Snapshots of the jet development, velocity, spatial density distributions and the location of shock structures are desirable but not essential.

The optical access must not interfere with the acoustic tests. Whilst optical access from three directions can be accommodated, the insertion of windows can compromise the geometry of the ejector or the location of other instrumentation such as pressure transducers. Optical access was artificially restricted in the tests described here as the measurements were made in the absence of the mixer-ejectors, because their details are not in the public domain.

### 11.1.3 Overview of Experiments

These measurements were made when the shock-tube facility had only recently come online. The acoustic testing completed prior to this visualisation contained unexpected features that were believed to be due to an incomplete jet development within the quasi-steady runtime.

A troubleshooting stage was embarked upon that diagnosed inconsistent firing and jet development. A high-speed camera was used to show that the plug, that was used to close the shock-tube during priming, was only a couple of diameters downstream of the nozzle exit by the end of the quasi-steady runtime. Cut-down plugs that were projected beyond the field-of-view within the runtime were used for subsequent tests, although the plug can still be seen in some of the results. Low weight plugs were manufactured but were not available in time for the tests described here. Despite this, only one representative result was recorded with the shearing interferometer in the time available

after the troubleshooting stage. Its acquisition can largely be attributed to chance owing to the inconsistent firing of the facility. As a consequence, the result has not been subjected to a tomographic reconstruction, as the dimensions and centreline of the jet in the field-of-view are unknown. Despite this, the result has been solved for unwrapped phase and demonstrates the suitability of the shearing interferometer to this application.

Some of the results recorded during the troubleshooting stage, Mie-scattering and focused schlieren, are included for comparison against the interferometric measurement.

## 11.2 THE MIT SHOCK TUBE <sup>[103,104 &105]</sup>

Combustion or electric-arc-heated steady-flow facilities are the primary means used to gather fluid mechanics and acoustical data from noise-suppression nozzles. Such facilities have high running costs requiring nozzle designs that are both mechanically and thermally robust. Subscale nozzles can cost between \$10 000 and \$100 000 dollars and take several months to design and fabricate. Time and fiscal constraints provide the motivation for a more flexible and efficient method of investigating nozzle design concepts <sup>[105]</sup>.

The MIT shock tube is a mechanically simple, versatile, and low-cost means of generating a supersonic free jet over a wide range of total pressures and temperatures comparable to steady-state facilities. Moreover, the isentropic shock heating provides a near-uniform total temperature and pressure profile at the nozzle inlet.

The isentropic compression allows nozzle pressure ratios (NPR) and total temperature ratios (TTR) relevant to the HSCT ejector programme to be achieved without the additional heating requirement of a continuously running facility. As the nozzles are only subjected to high temperatures for a few tens of milliseconds the nozzles can be made from cast aluminium or stereo lithographic resins rather than more thermally robust materials that typically cost an order of magnitude more to manufacture. The compromise for this mechanical simplicity is the brief, quasi-steady, test time.



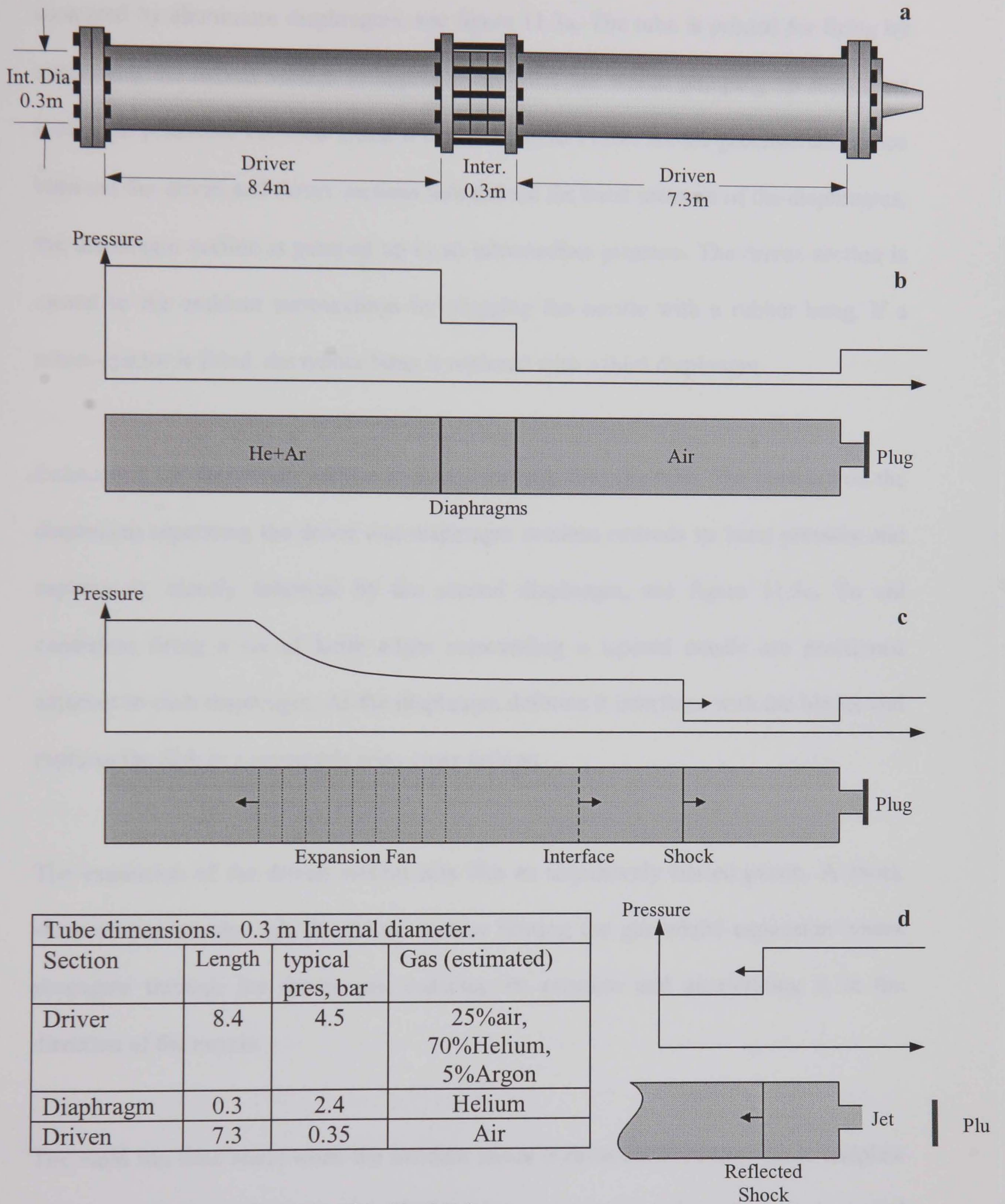


Figure 11.3. The Gas Dynamics of the Shock Tube

- The three sections of the Shock Tube
- Primed for firing
- Diaphragms rupture and shock wave progresses towards exhaust nozzle
- Shock is reflected, leaving a high pressure, high temperature reservoir in its wake

The shock tube consists of three zones, the driver, diaphragm and driven sections, each separated by aluminium diaphragms, see figure 11.3a. The tube is primed for firing by evacuating the driven section to approximately 0.2 bar whilst pumping up the driver section to pressures between 2 and 6 bar, see figure 11.3b. As the pressure difference between the driven and driver sections will exceed the burst pressure of the diaphragms, the diaphragm section is pumped up to an intermediate pressure. The driven section is closed to the ambient surroundings by plugging the nozzle with a rubber bung. If a mixer-ejector is fitted, the rubber bung is replaced with a third diaphragm.

Exhausting the diaphragm section to a vacuum tank fires the tube. The pressure on the diaphragm separating the driver and diaphragm sections exceeds its burst pressure and ruptures it, closely followed by the second diaphragm, see figure 11.3c. To aid consistent firing a set of knife edges surrounding a tapered needle are positioned adjacent to each diaphragm. As the diaphragm deforms it interferes with the blades and ruptures the disk in a repeatable criss-cross fashion.

The expansion of the driven section acts like an impulsively started piston. A shock wave propagates through the driven section heating the gas whilst expansion waves propagate through the driver gas, reducing its pressure and accelerating it in the direction of the nozzle.

The valid run time starts when the incident shock is reflected from the nozzle endplate leaving a volume of high-pressure, high-enthalpy gas in its wake, which is expanded through the nozzle. The pressure ratio between the driver and driven sections allows the stagnation temperature and pressure behind the reflected shock to be regulated <sup>[105]</sup>.

It is assumed that the driver and driven gases do not mix and their contact faces are analogous to the surface of a piston. The gas composition of the driver section is defined so that the speed of sound is constant across this interface. This avoids the production of extraneous waves as the reflected shock passes through it. The arrival of a second shock at the nozzle endplate determines the end of the valid run time. The required gas composition is achieved by evacuating the driver section prior to filling with a mixture of helium and air, the quantities of each is a function of the pressure ratio between the driven and driver sections.

The driven section contains four flush-fitting pressure transducers that are used to determine the primary nozzle pressure, the shock speed and the valid run time. The duration of the valid, steady run time is limited either by the exhaustion of the test gas or the arrival of a second shock at the nozzle endplate. Figure 11.4 shows the shock propagation along the length of the shock tube with respect to time.  $T_I$  represents the period between the first shock and its reflection from the contact interface between the driver and driven gases. As mentioned before this phenomenon can be avoided by matching the speed of sound across the interface.  $T_{wave}$  represents the period between the arrival of the first shock and the reflected head of the primary expansion, or the weak secondary expansion generated by the reflected shock overtaking the tail of the primary expansion, at the nozzle endplate. The net test time is  $t_I$  or  $t_{wave}$ , whichever is shorter, minus the time required to initiate a flow through the nozzle and to achieve a quasi-steady state.

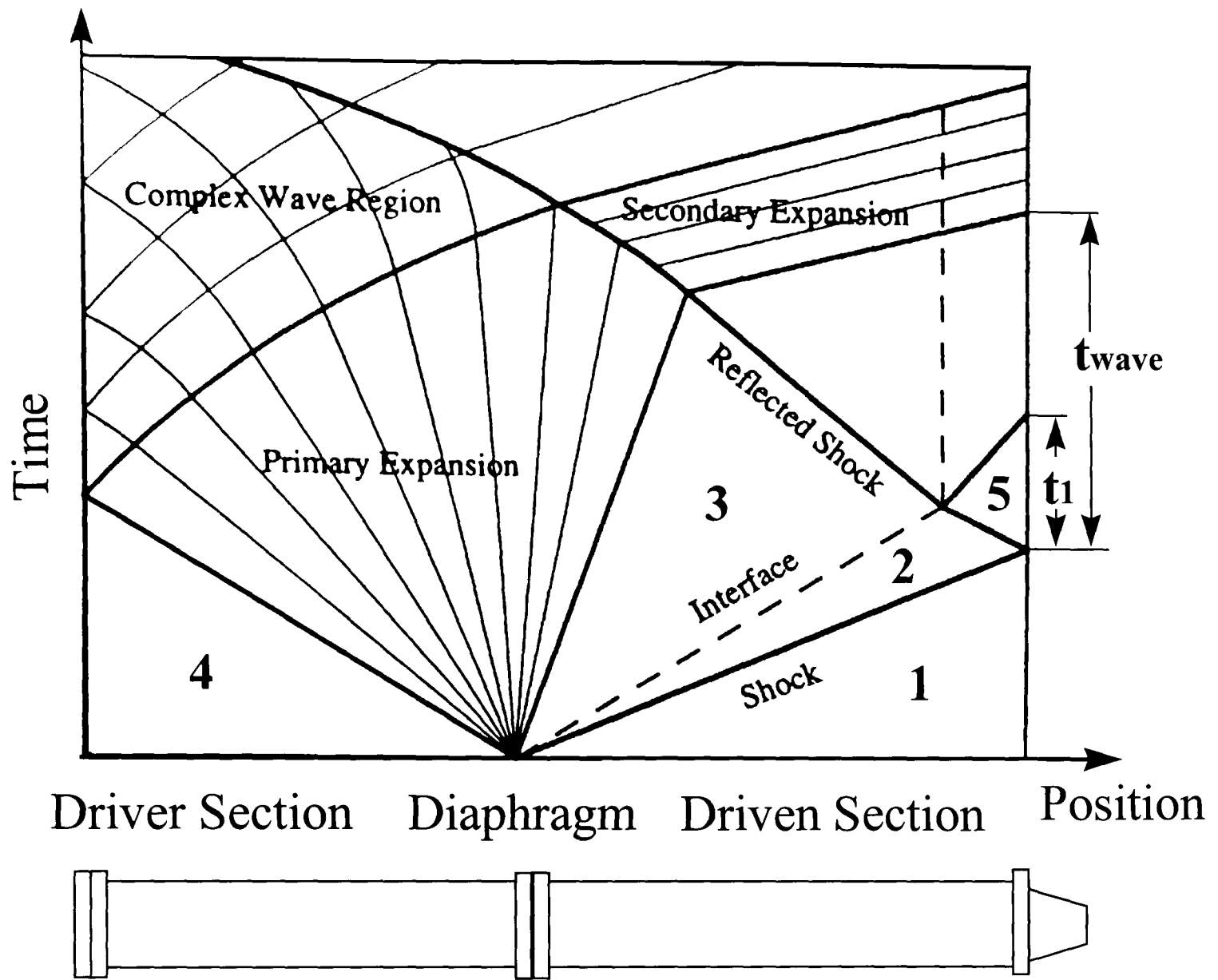


Figure 11.4. Shock propagation in the shock tube with respect to time <sup>[105]</sup>.

This reflection-type tube is designed to produce a flow at total temperatures and pressures analogous to those at the exit of a gas-turbine engine. Using air as the test gas, total pressures up to 38 bar and total temperatures up to 1750 K can be achieved.

### 11.3 EXPERIMENTAL ARRANGEMENT

A common optical system was used for the measurements of a CO<sub>2</sub> jet, shown in figure 9.2, and the Shock Tube. The optics consisted of a 5 mW Helium Neon laser, a microscope objective of numerical aperture 0.25, a spatial filter, a plano-convex lens of diameter 100 mm, focal length 150 mm and a 150 mm<sup>2</sup>, 3 mm-thick back-silvered mirror. The beam was projected through the objective and spatially filtered with a 3 μm pinhole. The divergent beam was collimated using the plano-convex lens to give a beam diameter of approximately 70 mm. The beam was incident on the back-silvered mirror approximately 50 cm away from the lens. The nozzle exit was positioned between the plano-convex lens and the mirror. The angle of incidence between the beam and mirror was adjusted to achieve a suitable compromise between fringe contrast and resolution when the fringes were projected on to a sheet of over-exposed bromide paper (photographic paper). The bromide paper was only used as a screen onto which the fringes could be projected. A CCD camera was used to record the image projected onto this screen. The blackened bromide paper was used as a screen as it appeared to give a smaller speckle size through the imaging lens and gave good fringe contrast in comparison to the under-exposed, white, bromide paper. The smaller speckle size allowed a higher carrier frequency to be used.

Both the beam from the interferometer and view from the camera were positioned as close as possible to the normal of the screen. The images were captured using a CCD camera with a resolution of 1000 × 1000 and exposure time of 30 milliseconds. The camera was coupled to a frame grabber within a PC that also contained the FRAN fringe-analysis software. The camera standoff was adjusted to give approximately 10 pixels per fringe through the Macro 90 lens. The departure of the plug from the nozzle



was used as a trigger for the camera. No trigger was required for the laser as it was continuous wave.

## 11.4 RESULTS – SHOCK TUBE

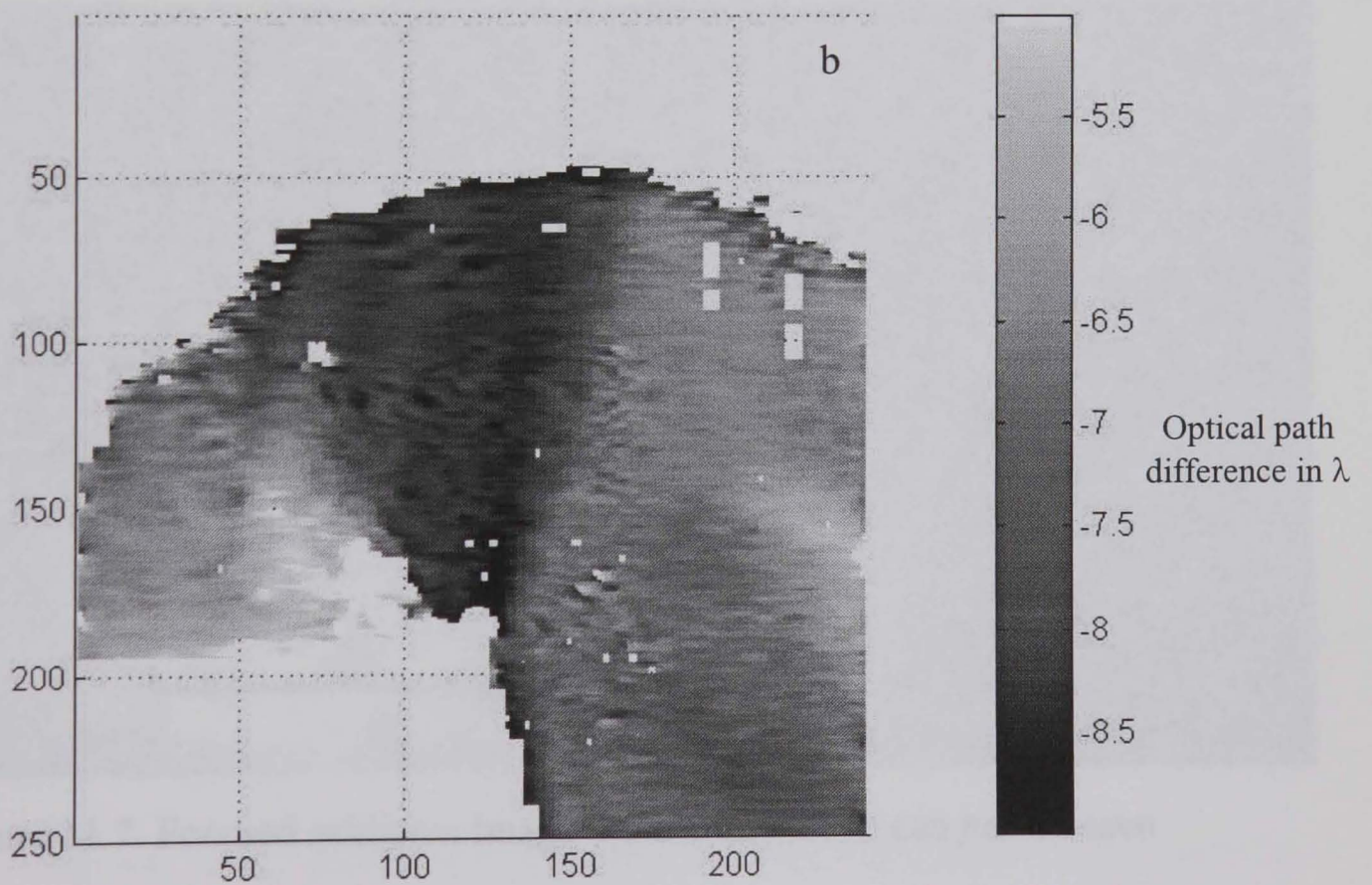
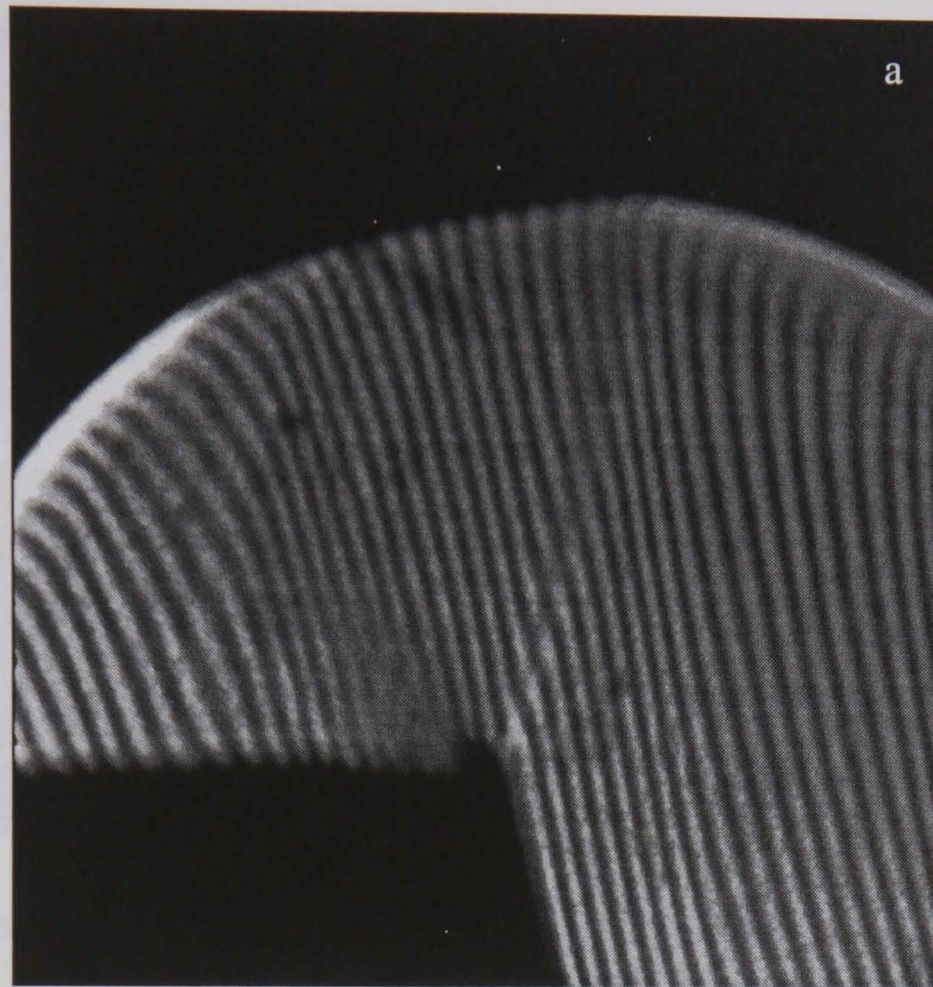


Figure 11.5a. The raw interferogram of the 20<sup>th</sup> scale (2 inch diameter) nozzle, NPR=2.3, TTR=2.3.

b. The fringe order height map representing the bending of the fringes relative to a reference picture (reference not shown).



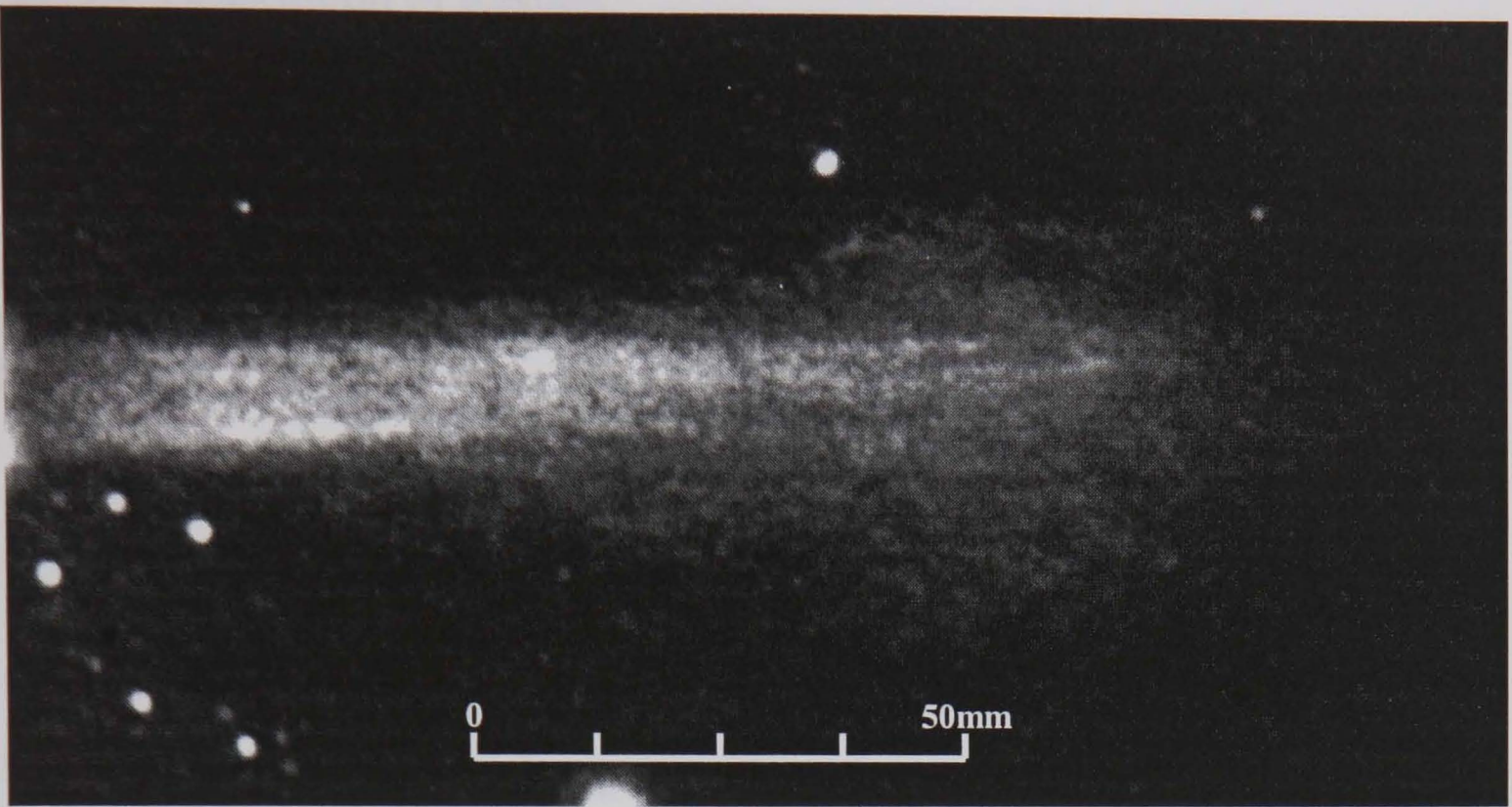


Figure 11.6. Seeded with  $0.59\ \mu\text{m}$  seed, NPR 2.5, 12 millisecond delay from pressure transducer trigger.

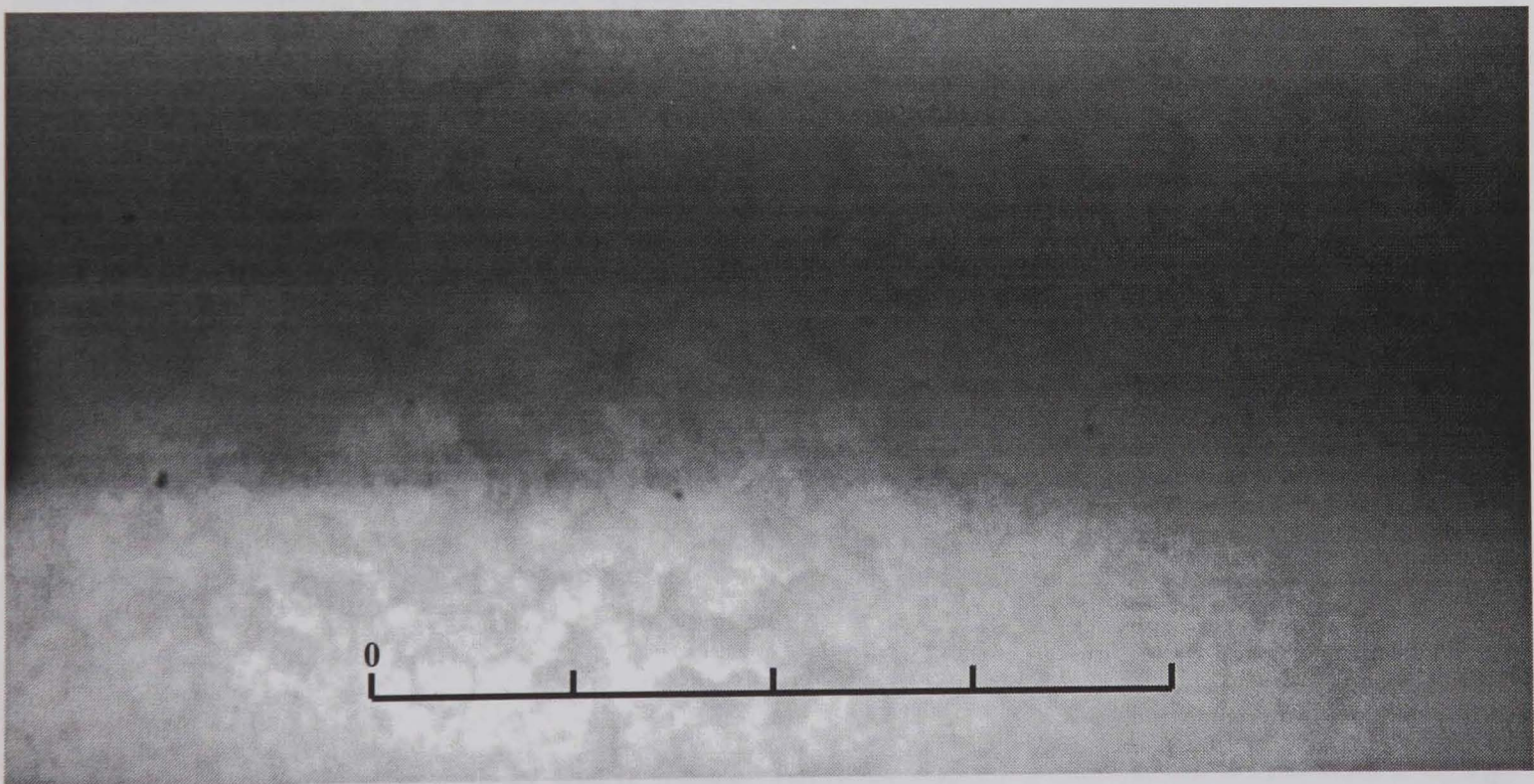


Figure 11.7. Focused schlieren image. Diamond pattern can just be seen.

## 11.5 INTERPRETATION OF RESULTS

### 11.5.1 Description of Results

The shock tube was fired many times before the measurement shown in figure 11.5 was obtained. As its acquisition can be put down to chance the application of the shearing interferometer to the shock tube was far from optimised. The timing of the acquisition cannot be verified against the valid run time, nor is its scale or location relative to the shock tube certain.

Figure 11.5a shows the fringe pattern projected through the flow field. The silhouette half the 20<sup>th</sup> scale nozzle (50 mm diameter) is in the bottom left-hand corner of the image. The otherwise straight fringes have been disturbed by the change in refractive index of the jet relative to the surroundings. A shock can be seen dissecting the fringes from the corner of the nozzle. Unfortunately the shock appears as a break in the fringes rather than bending and so is not apparent in the solution. A refraction 'bubble' has also occurred at the nozzle's edge due to the extreme refractive index gradient.

Figure 11.5b shows the fringe order height map of a projection through the nozzle flow. The figure clearly shows three distinct areas, an expansion fan originating from the edge of the nozzle, its ambient surroundings and the core of the jet. The nozzle flow is choked and therefore under expanded.

Figure 11.5b shows the fringe order height map of figure 11.5a after a reference fringe order height map has been subtracted. The reference was subtracted to allow for the non-uniform carrier frequency of the undisturbed state. The reference was recorded in the absence of the nozzle silhouette to get a datum for every point as the nozzle moves

rearward during the run. The fringe order numbers are relative rather than absolute and their sign is a function of the convention used in the analysis, ie whether a fringe bending to the left or right is positive.

The holes in the fringe order height map correspond either to the silhouette, spike noise or tile failures. Tile failures are apparent adjacent to the periphery of the nozzle which correspond with a region of poor fringe definition in figure 11.5a. The tile failures have been contained in the unwrap path and their threat to the overall solution has been minimized. This is a corollary of the Minimum Spanning Tree phase unwrapper that unwraps in the direction of the minimum phase change. Abrupt changes in phase, such as noise and discontinuities, are only considered at the end of an unwrap path.

### 11.5.2 Comparison with Mie-Scattering & Schlieren Measurements

Figure 11.6 shows the jet emitted from the quarter inch nozzle for a nozzle pressure ratio of 2.5. The flow has been seeded with 0.6 $\mu$ m diameter styrene particles, which are illuminated as they pass through a light sheet provided by a 10 Watt all channels, continuous wave, Argon Ion laser. The image was recorded using a 1000 by 1000 pixel camera coupled to an image intensifier. The camera shutter has been opened 11 milliseconds after the trigger to capture the last 5 milliseconds of the valid run time. The figure shows the bright core being engulfed by the shear layer approximately 5 diameters down stream. The small saturated areas surrounding the jet are fragments of the sound insulation of the anechoic chambers (fibre glass) stirred up by successive firing of the shock tube.



The focused Schlieren, similar to that described by Weinstein <sup>[108]</sup>, provides a qualitative visualization of the strongly refracting features of the flow but unfortunately its sensitivity is insufficient for the mixer-ejector representative flows. Figure 11.7 shows the criss-crossing expansion and compression waves at the nozzle exit.

### 11.5.3 Tomographic Reconstruction

An Abel Transform can be used to reconstruct the nozzle flow if it is assumed to be radially symmetric. This approach was successfully applied to the propane burner shown in section 10.5.3. In theory the application of the Abel Inversion, equation 10.18, would be simpler as the shearing interferometer gives the differential of density relative to a sheared point that would otherwise need to be calculated computationally. Unfortunately the scale, but more importantly the centerline and hence the line of symmetry, is not known. A tomographic reconstruction can therefore not be accurately applied in this case. However, the contrast and minimal noise in figure 11.5b implies that a tomographic reconstruction could have been applied to those rasters of pixels that stretch from the periphery to the centerline of the jet without being broken by tile failures.

### 11.5.4 Optical Path Difference at Nozzle Exit

Before the optical path difference between a ray passing through the nozzle jet and ambient can be calculated an estimation of the jet geometry and density is required. This has been achieved using the isentropic flow relations <sup>[106]</sup> and assuming that the density profile across the jet is uniform at the exit.

The nozzle pressure and total temperature ratio for the result shown in figure 11.5 were both 2.3. This gives a (static) density of  $0.66 \text{ kg/m}^3$  in the jet. Ambient (stagnation) density is assumed to be  $1.19 \text{ kg/m}^3$  giving a difference in density of  $0.53 \text{ kg/m}^3$ .

The optical path difference through the centerline of the jet relative to ambient using equation 10.3,  $N(x,z) = \frac{C\Delta\rho(x,z)l}{\lambda} = 9.5$  wavelengths relative to ambient. At the centerline of the jet the optical path difference between sheared points will be small if the diameter of the jet is much larger than the amount of shear ( $dN/dr \approx 0$ ).

The maximum optical path difference relative to a sheared point will occur at the periphery of the jet. The shear was approximately 1.7 mm normal to the axial direction of the nozzle. The nozzle was 50 mm in diameter. The maximum optical path difference of a jet of uniform core will occur at a radius of 23.3 mm at the exit. Using equation 10.3 the optical path difference is 3.4 wavelengths. The measured optical path difference at the periphery of the nozzle exit, shown in figure 11.5b, is approximately 2.5 wavelengths. This smaller optical path difference is expected as the jet expands at the nozzle exit.

### 11.5.5 Resolution in Density

The optical path difference is a function of the change in density and optical path length. The resolution in density is estimated at a radius of 23.3 across the jet relative to an ambient ray. Along this path a change in density of  $0.15 \text{ kg/m}^3$  will give an optical path difference of one wavelength. Assuming ten pixels per cycle and satisfying the Nyquist

criterion this gives a resolution in density relative to a sheared point of  $0.03 \text{ kg/m}^3$ , neglecting refraction.

### 11.5.6 First Order Approximation of Refraction

Using trigonometry and Snell's Law <sup>[107]</sup>, from figure 11.8 its can be shown that

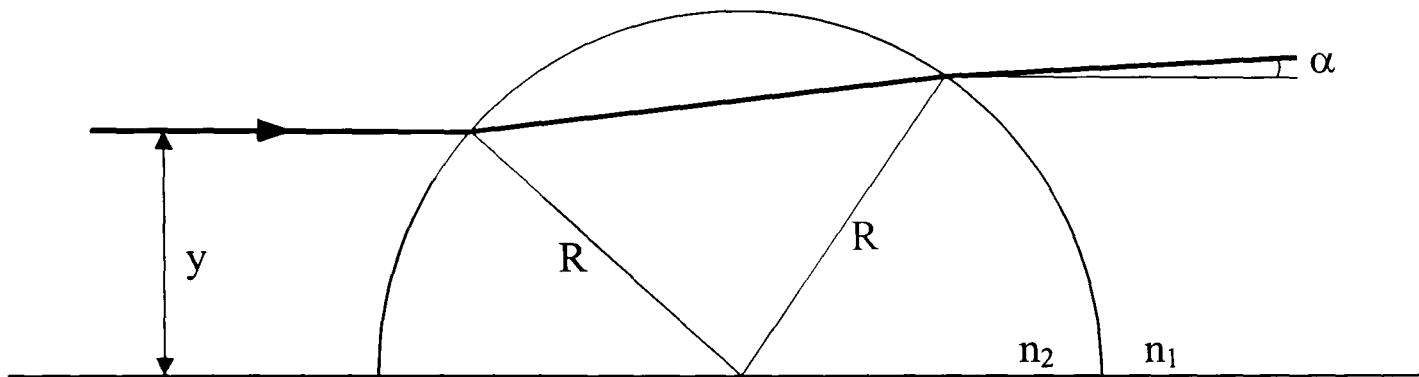


Figure 11.8. Refraction of a ray passing through a circular region of higher refractive index than its surroundings

$$\alpha = 2 \left\{ \sin^{-1} \left( \frac{n_1 y}{n_2 R} \right) - \sin^{-1} \left( \frac{y}{R} \right) \right\} \quad (11.1)$$

At a radius of 23.3 mm, a jet density of  $0.66 \text{ kg/m}^3$ , ambient density of  $1.19 \text{ kg/m}^3$ , jet radius,  $R$ , of 25 mm, the deviation of the transmitted ray from its original path,  $\alpha$ , is  $0.035^\circ$  ( $6.17 \times 10^{-4}$  radians). Over a further path length of 1 m gives a ray displacement of 0.6 mm from its unrefracted path. This is 36% percent of the shear distance (1.7 mm) so is not negligible at the jet periphery.

## 11.6 DISCUSSION

The result shown in figure 11.5 implies that the shearing interferometer could be used to provide a quantitative visualisation of the nozzle flow at exit of the shock tube. However, its applicability for revealing the flow further downstream is unknown. The successive expansion and compression waves will cease and the density change will reduce as viscous damping takes effect.

A possible solution would be to seed the driven volume of the shock tube with a gas of lower refractive index to accentuate a change in optical path length even if the flow was assumed to be incompressible. For instance, a change from air to argon in the driven section would be equivalent to a change in density relative to ambient of  $-0.36 \text{ kg/m}^3$ . This would be in addition to the change in density of the jet due to velocity (assuming it is less dense than ambient).

A correction in the makeup of the driver gas would be needed to compensate for the difference in speed of sound between the driven and driver sections if a seed gas was used. This correction would be needed to avoid the creation of erroneous reflected shocks within the tube that would terminate the valid run time.

If such a solution were permissible the shearing interferometer could be used to measure the mixing at the exit of the chute racks. Axial symmetry could be assumed in a reconstruction if lines of sight were available from two directions. Refraction could also be greatly reduced if the flow was contained within windows orthogonal to the optical path.

## 11.7 SUMMARY OF CHAPTER

A shearing interferometer has been used to visualise the flow emitted from a shock tube designed to simulate the flow conditions relevant to the HSCT mixer-ejector programme. The primary purpose of the shock tube is the acoustic testing of jet noise suppressor nozzles, or mixer-ejectors. The visualisation is secondary to, and must not interfere with, the acoustic testing. The measurements presented in this chapter were made at a nozzle pressure ratio of 2.3, total temperature ratio of 2.3, in the absence of a mixer-ejector. The shock tube exit consists of a 50 mm diameter conical nozzle.

The measurements were made when the shock tube had only recently become operational and its successful firing had not been verified. The visualisation diagnosed incorrect jet development in the quasi-steady run-time ( $\approx 10$  ms) owing to the interference of the plug that was used to close the driven volume with the flow. This problem was remedied but only in time to allow one on-condition result to be acquired with the shearing interferometer. This single result, integrated over the entire quasi-steady run-time, has not been subjected to a tomographic reconstruction, as the scale and exact position of the measurement are unknown. The result does, however, provide a qualitative visualisation that indicates the suitability of the shearing interferometer for this application.

The optical path difference and hence density through a cross-section exit has been compared with that which would be produced from a jet of uniform density of  $0.66 \text{ kg/m}^3$  (calculated from the NPR and TTR). The measured optical path difference at the periphery of the jet is 2.5 wavelengths. A uniform top-hat profile would give a 3.5



wavelength optical path difference. This difference is expected as the shear layer reduces the density gradient between the core and ambient.

The change in density required at the periphery of the jet to give 1 wavelength optical path difference relative to ambient is  $0.15 \text{ kg/m}^3$ . The refraction at the periphery of the jet was expected to be 36 % of the shear (1.7 mm) by the time the beam was incident on the screen.

As the density change diminishes downstream of the nozzle it is recommended that the driven volume be doped with argon to increase the density change. The addition of the argon would be equivalent to a change in density of  $0.36 \text{ kg/m}^3$  that would be in addition to changes due to velocity. The mixture of the driver section would need to be adjusted accordingly to prevent the creation of erroneous reflected shocks within the tube that may prematurely terminate the quasi-steady run-time.

*Chapter 12*

CONCLUSIONS

-

OPTICAL INSTRUMENTATION FOR  
FLUID FLOW IN GAS TURBINES

## 13.0 CONCLUSIONS

Two optical diagnostic techniques have been demonstrated in gas turbine representative flows. The simpler of these, a novel shearing interferometer, has first been applied to a two-dimensional wind tunnel operating at a compressor representative condition and, secondly, a simulated jet exhaust flow. The second technique, particle image velocimetry, has been applied to a turbine representative flow, again operating in the transonic region.

Although described in the latter half of the thesis the shearing interferometer is described as a *first pass* technique that is used to characterise a flow in preparation for a more sophisticated anemometry technique (LDA). It will therefore be described here first.

The shearing interferometer has first been used to make density measurements in a 2-D wind tunnel operating at an inlet Mach number of 1.5. The interferometer measures the optical path difference, and hence density, relative to a sheared point. The optical path difference manifests itself as rarefied or compressed fringes that have been analysed using the Fourier Transform method to extract the phase information. The phase distribution has been unwrapped using a technique that unwraps round the noise, either excluding or only including it at the end of an unwrap path. The result is a continuous phase distribution that can be calibrated for absolute density. The measurements in the 2-D wind tunnel were converted to absolute density using oblique shock theory. This theory was also used to determine the pre and post leading shock Mach Numbers of 1.20 and 1.53. The resolution in density through the 35.6 mm thick wind tunnel was

found to be  $0.078 \text{ kg/m}^3$  for an optical path difference of 1 wavelength (1 wavelength fringe shift).

The shearing interferometer has also been used to visualise the jet emitted from a shock tube operating at a nozzle pressure ratio of 2.3, total temperature ratio of 2.3. The shock tube is designed for the acoustic evaluation of jet exhaust noise suppressor nozzles, or mixer-ejectors, relevant to the high-speed civil transport programme. The visualisations were secondary to, and therefore couldn't interfere with, the acoustic testing. The mixer-ejectors were not fitted for these tests. The testing occurred at a time when the shock tube had only recently come on line. The visualisations diagnosed incorrect development in the quasi-steady run time (shock tube corking mechanism interfering with the flow). The one on-condition image that was acquired has been processed to reveal an under expanded jet. The unwrapped phase map has not been calibrated for density as the scale and alignment of the field-of-view relative to the nozzle exit is unknown. The unwrapped map does, however, provide a qualitative visualisation that illustrates the suitability of the shearing interferometer for this application. As the density change diminishes downstream of the nozzle, it is recommended that the flow be doped with argon to increase the refractive index change. The use of argon will give a change refractive index equivalent to a change in density of  $0.36 \text{ kg/m}^3$  that will be in addition to any changes due to velocity. This will allow the mixing of the argon with the ambient air to be visualised downstream of the mixer-ejectors.

The shearing interferometer is simple and was quick to apply in each application. For example, the measurements on the wind tunnel made at mass flow rates from 0.6 to 1 kg/s in 0.02 kg/s increments were made in the space of one working day. The

interferometer consists of only a few inexpensive optical components. Large regions of interest can be investigated, as the shearing device is merely a back-silvered mirror. As the sheared beams are incident on common optical components it is no more sensitive to vibration than a schlieren or shadowgraph arrangement. The shearing interferometer has the obvious advantage over these techniques in that it can be used to give accurate information of the density distribution. As the measurement is encoded in phase rather than amplitude its accuracy is not compromised by background illumination. The shearing interferometer cannot be applied where there is no line of sight through the flow or where the flow is contained within a complex 3-D geometry such as an annular compressor or turbine.

2-D planar velocity measurements have been made in the stator-rotor gap and stator passage of a short duration spinning turbine cascade. The cascade was operated at an engine representative Reynolds number of  $2.8 \times 10^6$  based on the axial chord of the nozzle guide vanes. The measurements have been made using a technique called particle image velocimetry, the individual frames of which represent an instantaneous 2-D description of the spatial velocity distribution. Although a development of those presented by Bryanston-Cross<sup>[139]</sup>, they represent the first to be made in the presence of a spinning rotor. These measurements also differ from Bryanston-Cross's in that the data have been recorded using a CCD camera rather than by photographic means. Automatic vector extraction algorithms and novel post processing algorithms have been used to increase the vector yield per image by an order of magnitude ( $\approx 1000$  vectors per image) and achieve an estimated accuracy of  $\pm 5\%$ . A close agreement has been achieved between instantaneous, non-smoothed measurements and a numerical prediction generated using a 2-D unsteady flow solver (prediction supplied by DERA).



The measurements show evidence of a Karman vortex street in the wake of the NGVs and wake broadening that has not be predicted by the flow solver.

An evaluation exercise was embarked upon prior to testing on the turbine cascade to assess the hardware and analysis routines that were available. A 1000 x 1000 pixel camera with the ability to capture two frames of data only a microsecond apart was evaluated but failed and could not be replaced in time for testing on the facility. A back-up camera system was used for testing on the turbine cascade. The acquisition could not be locked to the rotor phase, as the back-up camera was not triggerable. Neither could the frames be cross-correlated, as their exposures were tens of milliseconds apart. As a consequence, no statistical analysis of the time-mean aspect of the flow has been embarked upon. A pseudo phase-stepped sequence of frames, of the rotor passing through the region of interest, has been constructed from the large volume of data (20 runs, 20 useful images per run).

Particle tracking and correlation analysis have been compared both on a nozzle flow and on the data from the turbine cascade. The particle tracking software was found to produce many ( $\approx 30\%$ ) erroneous vectors for high seeding concentrations (upper limit of 400 vectors over a 768 x 576 image). Despite using the centre-of-mass algorithm to determine the particle centres the vectors were banded into increments of velocity that corresponded to integer pixel displacements. An auto-correlation algorithm with a 3 point Gaussian estimator for determining the centroid of the satellite peak in the correlation plane was found to give an accuracy of  $1/10^{\text{th}}$  if the seeding concentration was sufficiently high (15 pairs per interrogation spot) <sup>[127]</sup>.

A novel 3-D PIV technique that determines the out-of-plane component of velocity from the defocusing of a particle viewed through a single camera has also been investigated. A calibration exercise showed that the out-of-plane component could be determined to a resolution of 20  $\mu\text{m}$  over a field of view of 4  $\text{mm}^2$  from the total diameter of the diffraction pattern of a particle viewed through a diffraction limited lens ( $f$ -number 8, magnification of 3.2). The calibration data compared favourably with theoretical models of the defocused particle images supplied by Udrea <sup>[125]</sup>. An attempt to make 3-D velocity measurements through the test section window of the turbine cascade failed as the aberrations through the window could not be corrected in time for testing on the facility. Suggestions have been made to rectify this problem.

Recommendations have also been made towards improving the application of 2-D PIV to complex turbine geometries. The first is the use of fluorescent seed to allow measurements close to mechanical surfaces where glare would otherwise dominate. A suitable supply of dyed styrene microspheres available in a range of sub-micron size has been identified.

The possible improvements that could have been achieved with the cross-correlation camera, had it not failed, have been discussed in terms of improving accuracy and vector yield per image. It has been shown that a potential vector yield of 3900 vectors per image can be achieved at an accuracy of 1% ( $32 \times 32$  interrogation spot with a 50% overlap, 50 seed per  $\text{mm}^3$ ). A novel adaptation of the cross-correlation analysis has been suggested to iteratively cross-correlate with progressively smaller but shifted interrogation spots, thereby maximising the vector yield and increasing the spatial resolution. The acquisition of a sequence of images at a constant rotor phase to establish

time-averaged quantities has also been discussed, as has the acquisition of a sequence at phase-stepped increments in rotor position. For the former the emphasis has been placed on reducing systematic errors to a level significantly below those of the fluctuating components of velocity. For the latter a high speed intensified camera system with a frame rate of 20 000 000 frames per second has been suggested for recording the interaction of an individual rotor blade as it passes through the stator wake.

The path of this thesis goes from the concept of a simple, novel interferometric device for measuring density distributions, to the first application of a state-of-the-art anemometry technique to a spinning turbine cascade. In each case new knowledge is presented about the flow to which they are applied. Recommendations have been made towards attaining spatially and temporally resolved 3-D velocity vectors within turbomachinery representative flows.

## REFERENCES

- [1] Yeh Y., Cummins H.Z., *Localised Fluid Flow Measurements with a He-Ne Laser Spectrometer*, Applied Physics Letters, Vol. 4, pp.176-178, 1964
- [2] *Principles of Laser Doppler Anemometry*, Powerpoint presentation, Dantec measurement technology, [www.dantecmt.com](http://www.dantecmt.com), 1999
- [3] Menon R.K., *Three Component Velocity Measurements in the Interblade Region of a Fan*, TSI Incorporated, International Gas Turbine Conference, 87-GT-207, Anaheim, CA, June, 1987
- [4] Dantec Newsletter, Volume 5, No. 1, 1998
- [5] *Laser Doppler Velocimetry Systems*, TSI Incorporated, 1996
- [6] *FiberFlow 5-Beam Probe*, Dantec Newsletter, Volume 5, No. 2, 1998
- [7] Witze P.O., *Application of LDV to Spark-ignition Engines*, Flow Lines, L5.2. CRF Sandia National Laboratories. 1989
- [8] Jaffri K., Hascher H.G., Novak M., Lee K., and Schock H., Michigan State University; and Bonne M. and P. Keller P., Chrysler Corporation, *Tumble and Swirl Quantification within a Motored Four-Valve SI Engine Cylinder based on 3-D LDV*

*Measurements*, SAE Paper 970792, International Congress & Exposition, Detroit, Michigan, February 24 - 27, 1997

[9] Hascher H.G., Jaffri K., Novak M., Lee K., and Schock H., Michigan State University; and Bonne M., and Keller P., Chrysler Corporation, '*An Evaluation of Turbulent Kinetic Energy for the In-Cylinder Flow of a Four-Valve 3.5L SI Engine using 3-D LDV Measurements*', SAE Paper 970793, International Congress & Exposition, Detroit, Michigan, February 24 - 27, 1997

[10] Komine H., *System for measuring velocity field of fluid flow utilising a laser-Doppler spectral image converter*, US Patent 4 919 536, 1990

[11] Meyers J.F., Komine H., *Doppler Global Velocimetry – A New Way to Look at Velocity*, ASME Fourth International Conference on Laser Anemometry, Cleveland Ohio, August 1991.

[12] Roehle I., Willert C., Schodl R., *Recent Applications of Three-Dimensional Doppler Global Velocimetry in Turbo-Machinery*, 9<sup>th</sup> Int. Symp. On App. Of Laser Tech. To Fluid Mechanics, Vol. 2, pp: 34.2.1-34.2.8, July 1998.

[13] Roehle I., *Doppler Global Velocimetry*, VKI-Lecture, German Aerospace Research Establishment (DLR), Institute for Propulsion Technology, Linder Hohe, 51140 Cologne, Germany, 1998.

[14] Nelson E., *Hot Wire and Hot Film Anemometry*, TSI Inc, 1984.



- [15] *Principles of Constant Temperature Anemometry*, PowerPoint Presentation, [www.dantecmt.com](http://www.dantecmt.com), Dantec Measurement Technology, 1997-99
- [16] Cantwell B., Coles D., *An experimental study of entrainment and transport in the turbulent near wake of a circular cylinder*, J. Fluid Mech. 1983. Vol:136, pp: 321-374.
- [17] Schodl R., Forster W., *Multicolor Fiberoptic Laser-2-Focus Velocimeter For 3-Dimensional Flow-Analysis*, AIAA Journal, 1991, Vol.29, No.8, pp.1290-1297
- [18] Schodl R., *A Laser-2-Focus (L2F) Velocimeter For Automatic Flow Vector Measurements In The Rotating Components Of Turbomachines*, Journal Of Fluids Engineering-Transactions Of The ASME, 1980, Vol.102, No.4, pp.412-419
- [19] Timmerman B., *Holographic Interferometric Tomography for Unsteady Compressible Flows*, Thesis, 1997, ISBN 90-5651-044-4.
- [20] Bassett M.D., Pearson R.J., Winterbone D.E., Clough E., *Visualisation of wave propagation in a three pipe junction*, Int. Conf. On Optical methods and Data Processing in Heat and Fluid Flow, IMechE Conference Transactions, 1998, C541/044/98
- [21] Burnett M., Bryanston-Cross P.J., *Measurement of Transonic Shock Structures using Shearography*, Laser Interferometry VIII: Applications. Proceedings of SPIE [2861-19], July 1996

[22] Bryanston-Cross P.J., Denton J.D., *Comparison of Interferometric Measurements and Computed Flow Around a Wedge Profile in a Transonic Region*, ASME 82-GT-258, 1982

[23] Vest C.M., *Holographic Interferometry*, Wiley, 1979.

[24] Greenhalgh D.A., *Inelastic Scattering Laser Diagnostics; CARS, Planar LIF and Planar LII*, To appear in *Optical Diagnostics for Flow Processes*, Eds.: L. Lading, P. Buchave, G. Wigley, Plenum, N.Y. 1994

[25] Eckbreth A.C., *Laser Diagnostics for Combustion Temperature and Species*, Abacus Press 1988, ISBN 0-85626-344-3

[26] Goss L.P., *CARS Instrumentation for Combustion Applications*, Instrumentation for Flows with Combustion, Edited by A.M.P.K. Taylor, Chapter 4, pp: 251-322, 1993, ISBN 0-12-683920-4

[27] MSTB Measurement Technologies, NASA Langley Research Centre, <http://mstb/larc/nasa.gov/tech/listing.html>. 2000

[28] Brown M.S., Roberts W.L., *Single Point Thermometry in High Pressure, Sooting, Premixed Combustion Environments*, Journal of Propulsion and Power, Vol. 15, No. 1, Jan-Feb 1999, pp:110-118

[29] Lawton B., Klingenberg G., *Transient Temperature in Engineering and Science*, Oxford Science Publications, Oxford University Press, 1996, ISBN 0 19 856260 8

[30] Shoji H., Saima A., Sasao T., Arai J., Ikeda S., Iwasaki M., *Clarification of the Combustion Reaction Mechanism in a Spark Ignition Engine by Spectroscopic Analysis*, JSAE Review, Vol. 13, No. 2, pp: 4-9, April 1992.

[31] Shoji H., Sasao T., Saima A., Iwasaki M., *Measurement of Radical Luminescence Intensity in Abnormal Combustion in a Spark Ignition engine*, Proceedings of the ASME/JSME Thermal Engineering joint Conference, pp:495-502, Book No: I0309C – 1991.

[32] Huang Y., Yan Y., Lu G., Reed A., *Measurement of Temperature Distribution in a Model Furnace using the Two-Colour Method*, SPIE 3783-42, Oct. 1999

[33] Allison S.W., Gillies G.T., *Remote Thermometry with Thermographic Phosphors: Instrumentation and Applications*, Review of Scientific Instruments, 68(7), July 1997, pp: 2615-2650

[34] Zhang Z.Y., Grattan K.T.V., Palmer A.W., Meggitt B.T., *Potential for temperature sensor applications of highly neodymium-doped crystal and fibre at up to approximately 1000°C*, Review of Scientific Instruments, 68(7), July 1997, pp: 2759-2763.

- [35] Zhang Z.Y., Grattan K.T.V., Palmer A.W., Meggitt B.T., Sun T., *Fluorescence decay-time characteristics of erbium-doped optical fibre at elevated temperatures*, Review of Scientific Instruments, 68(7), July 1997, pp: 2764-2766.
- [36] McGee T.D., *Principles and Methods of Temperature Measurement*. Wiley-Interscience Publication, 1988, ISBN 0-471-62767-4
- [37] Private Communication, Dr. D. Harvey, SRC, Rolls-Royce, Derby. 2000
- [38] Campbell B.T., Liu T., Sullivan J.P., *Temperature Sensitive Fluorescent Paint Systems*, AIAA paper, 94-2483, June 1994
- [39] Schanze K.S., Carroll B.F., Korotkevitch S., Morris M. J., *Temperature Dependence Of Pressure Sensitive Paints*, AIAA Journal, 1997, Vol.35, No.2, pp.306-310
- [40] Cattafesta III L.N., Liu T., Sullivan J.P., *Uncertainty Estimates for Temperature-Sensitive Paint Measurements with Charge Coupled Device Cameras*, AIAA Journal, Vol. 36, No. 11, November 1998.
- [41] Thermographic Measurements Co. Ltd., Riverside Buildings, Dock Rd. Ind. Est., Connah's Quay, Flintshire, CH5 4DS, Web: [www.thermax.com](http://www.thermax.com)

[42] Hilton M., Lettington A.H., Wilson C.W., *Gas Turbine Exhaust Emissions Monitored Using Nonintrusive Infrared Spectroscopy*, Transactions of the ASME, July 1998, Vol. 120 pp:514-518.

[43] Hilton M., *Gas Turbine Exhaust Emission Monitoring using Passive Fourier Transform Infrared Spectroscopy*, University of Reading, September 1995.

[44] Heland J., Haus R., Schafer K., *Remote Sensing and Analysis of Trace Gases from Hot Aircraft Engine Plumes using FTIR Emission Spectroscopy*, Proc. 3<sup>rd</sup> Int. Symp. On Transport and Air Pollution, Avignon, 1994.

[45] Thompson D.M., Nattrass S.R., *Full Mid-IR Spectral Characterisation of Lubricant in the Ring Pack of a Running Diesel Engine by Time-Resolved FTIR Spectroscopy*, 1996, SAE 962003

[46] Edinburgh Instruments <http://www.edinst.com/>, 2000

[47] le Gal P., Farrugia N., Greenhalgh D.A., *Development of Laser Sheet Drop Sizing (LSD) for Spray Characterisation*, ImechE Conference Transactions, C541/048/98, 1998

[48] Locke R.J., Zaller M.M., Hicks Y.R., Anderson R.C., *Non-Intrusive Laser Induced Imaging for Speciation and Patternation in High pressure Gas Turbine Combustors*, SPIE September 16<sup>th</sup>-18<sup>th</sup> 1999, Santa Barbara, California.



[49] Seitzman J.M., Hanson R.K., *Two-Line Planar Fluorescence for Temporally Resolved Temperature Imaging in a Reacting Supersonic Flow over a Body*, Applied Physics B, 57, pp: 385-391, 1993.

[50] Seitzman J.M., Hanson R.K., *Comparison of Excitation Techniques for Quantitative Fluorescence Imaging of Reacting Flows*, AIAA Journal, Vol:31, No:3, pp: 513-519, March 1993

[51] McMillin B.K., Seitzman J.M., Hanson R.K., *Comparison of NO and OH Planar Fluorescence Temperature Measurements in Scramjet Model Flow fields*, AIAA Journal, Vol:32, No: 10, pp: 1945-1952, October 1994.

[52] Seitzman J.M., Hanson R.K., DeBarber P.A., Hess C.F., *Application of Two-Line Planar Laser Induced Fluorescence for temporally Resolved Planar Thermometry in Reacting Flows*, Applied Optics, Vol. 33, No. 18, 20<sup>th</sup> June 1994

[53] Greenhalgh D.A., *Inelastic Scattering Laser Diagnostics; CARS, Planar LIF and Planar LII*, To appear in Optical Diagnostics for Flow Processes, Eds.: L. Lading, P. Buchave, G. Wigley, Plenum, N.Y. 1994

[54] Dec J.E., Canaan R.E., Porter E.L., *PLIF Imaging of NO Formation in DI Diesel Engine*, Sandia Combustion Research, 1998 Technical Review, <http://www.ca.sandia.gov>

[55] Witze P.O., Green R.M., *LIF and Flame-Emission Imaging of Liquid Fuel Films and Pool Fires in an SI Engine*, Sandia Combustion Research, 1997 Technical Review, <http://www.ca.sandia.gov>

[56] Reeves R.M., Musculus M., *Two Laser Induced Fluorescence Techniques for Combustion Investigations*, Meeting on Engineering Applications of optical diagnostic techniques, NAC Stoneleigh Park, 20<sup>th</sup> October 1999.

[57] Mewes B., Seitzman J.M., *Soot Volume Fraction and Particle Size Measurements with Laser Induced Incandescence*, Applied Optics, Vol: 36, No: 3, January 1997

[58] Vander Wal R.L., Ticich T.M., Stephens A.B., *Optical and microscopy investigations of soot structure alterations by laser-induced incandescence*, Applied Physics B, 67, pp:115-123, 1998

[59] Vander Wal R.L., *LIF-LII measurements in a turbulent gas-jet flame*, Experiments in Fluids 23, pp:281-287, 1997.

[60] Greenhalgh D.A., *Inelastic Scattering Laser Diagnostics; CARS, Planar LIF and Planar LII*, To appear in Optical Diagnostics for Flow Processes, Eds.: L. Lading, P. Buchave, G. Wigley, Plenum, N.Y. 1994

[61] Vander Wal R.L., *LIF-LII measurements in a turbulent gas-jet flame*, Experiments in Fluids, 23, 1997, pp:281-287

[62] Naqwi A., *Sizing of Irregular Particles using a Phase Doppler System*, ASME 1995, HTD-Vol. 321/FED-Vol. 233, 1995 IMECE

[63] Naqwi A.A., Menon R., *A Rigorous Procedure for Design and Response Determination of Phase Doppler Systems*, *Developments in Laser Techniques and Applications to Fluid Mechanics*, Springer-Verlag, 1995

[64] Naqwi A.A., Durst F., *Light Scattering Applied to LDA and PDA Measurements Part 1: Theory and Numerical Treatments*, *Particle and Particle System Characterization* 8, 1991

[65] Naqwi A.A., Durst F., *Light Scattering Applied to LDA and PDA Measurements Part 2: Computational Results and their Discussion*, *Particle and Particle System Characterization* 9, 1992

[66] *Principles of Phase Doppler Anemometry*, Powerpoint presentation, Dantec Measurement technology, <http://www.dantecmt.com>, 2000

[67] Le Gal P., Farrugia N., Greenhalgh D.A., *Development of laser sheet drop sizing (LSD) for spray characterisation*, *ImechE* 1998, c541/048 p.p: 113-120.

[68] Sanker S.V., Maher K.E., Robart D.M., Barchalo W.D., 7<sup>th</sup> Int. Conf. On Liq. Atomisation and Spray Sys., Seoul, Korea, 1997

[69] (Ref: <http://www.dukescientific.com>), 2000

- [70] Private communication with Heather Booth, Oxford Lasers, (<http://www.oxfordlasers.com/>), 2000
- [71] Rawle A., *The Basic Principles of Particle Size Analysis*, Malvern Instruments, <http://www.malvern.co.uk/>, 1999
- [72] Rawle A., *Particle Sizing - An Introduction*, Malvern Instruments, <http://www.malvern.co.uk/>, 1999
- [73] TSI Incorporated, Particle Instrument Division, 2000
- [74] Jeung I.S., *Response Characteristics of the Knollenberg Active Scattering Aerosol Spectrometer to Light Absorbing Aerosols*, *Optical engineering*, 29(3), pp: 247-252, March 1990.
- [75] Particle Measuring Systems Inc. (<http://www.pmeasuring.com/>), 2000
- [76] Merzkirch W., *Flow Visualisation*, Academic press Inc., 2<sup>nd</sup> Edition, 1987
- [77] Adrian R.J., *Multi-point optical measurements of simultaneous vectors in unsteady flow, a review*, 1986, *Int. J. Of Heat and Fluid Flow*, Vol. 7, No. 2, pp: 127-143
- [78] Adrain R.J., *Statistical Properties of Particle Image Velocimetry Measurements in Turbulent Flow*, *Laser Anemometry in Fluid Mechanics*, 1988, pp: 115-129, Ladoan: Lisbon, Portugal.

[79] Lai W.T., *Particle image velocimetry: A new approach to experimental fluid research*, Th. Draco (ed.) Three dimensional velocity and vorticity measuring and image analysis techniques, 61-92, 1996, Kluwer Academic Publishers, Netherlands.

[80] Wernet M.P., *Digital PIV Measurements in the Diffuser of a High Speed Centrifugal Compressor*, 20<sup>th</sup> AIAA Advanced Measurement and Ground Testing Technology Conference, June 1998, AIAA-98-2777

[81] Barnhart D.H., Chan V.S.S., Garner C.P., Halliwell N.A., Coupland J.M., *Volumetric three dimensional flow measurements in IC engines using holographic recording and optical correlation analysis*, Int. Conf. On Optical methods and Data Processing in Heat and Fluid Flow, IMechE Conference Transactions, 1998, C541/007/98.

[82] Van Oord J., *The Design of a Stereoscopic DPIV-system*, MEAH-161, May 1997, Laboratory for Aero and Hydrodynamics, Rotterdamseweg 145, 2628 AL Delft, Netherlands.

[83] Liu Z.C., Adrian R.J., Meinhart C.D., Lai W., *Visualisation of Structure Within a Turbulent Boundary Layer using a Stereoscopic Particle Image Velocimeter*, 8<sup>th</sup> Int'l Symp Applications of Laser Techniques to Fluid Mechanics, Lisbon, July 8<sup>th</sup>-11<sup>th</sup>, 1996.

[84] Adrian R.J., *Particle imaging techniques for experimental fluid mechanics*, Annual Review of Fluid Mechanics, 23, pp: 261-304, 1991.

- [85] *PowerView Stereoscopic PIV System*, TSI Incorporated 1998.
- [86] Towers C.E., Bryanston-Cross P.J., Judge T.R., *Application of Particle Image Velocimetry to Large Scale Transonic Wind Tunnels*, 1991, *Opt. Laser Tech.*, 23(5).
- [87] Bryanston-Cross P.J., Epstein A.H., *The Application of Sub-Micron particle Visualisation for PIV (Particle Image Velocimetry) at Transonic Speeds*, 1990, *Prog. Aerospace Sci*, 27, pp: 237-265
- [88] Bryanston-Cross P.J., Judge T.R., Quan C., Pugh G., Corby N., *The Application of Digital Particle Image Velocimetry (DPIV) to Transonic Flows*, 1995, *Prog. Aerospace Sci.*, Vol: 31, pp: 273-290.
- [89] Bryanston-Cross P.J., Funes-Gallanzi M., Quan C., Judge T.R., *Holographic Particle Image Velocimetry*, OEL annual publications review 1995, University of Warwick.
- [90] Bryanston-Cross P.J., Denton J.D., *Comparison of Interferometric Measurements and Computed Flow around a Wedge Profile in a Transonic Region*, ASME, 82-GT-258, 1982
- [91] Vest C.M., *Holographic Interferometry*, John Wiley and Sons, 1979.



- [92] Towers C.E., Bryanston-Cross P.J., Towers D.P., *PIV in large scale transonic wind tunnels: seed particle detectability and flow following*, OEL annual publications review 1995, University of Warwick.
- [93] Towers C.E., *The Development of Whole Field Particle Imaging Techniques for Quantitative Velocity and Size Measurements Applied to Large Scale Transonic Aerodynamic Testing and Combustion Research*, Ph.D. Thesis, University of Warwick, May 1994
- [94] Adrian R.J., *Laser Velocimetry*, Fluid Mechanics Measurements, Second Edition, Edited by R.J. Goldstein, 1996, ISBN 1-56032-306-X, pp:175-293.
- [95] Hinze J.O., *Turbulence: An Introduction to its Mechanism and Theory*, McGraw-Hill Book Company Inc., 1959.
- [96] Durst F., Melling A., Whitelaw J.H., *Principles and Practice of Laser Doppler Anemometry*, Academic Press Inc., 1981.
- [97] Feller W.V., Meyers J.F., *Development of a controllable particle generator for LDV seeding in hypersonic wind tunnels*, pp.342-357, 1976, in E.R.G. Eckert (ed.), Minnesota Symp. On Laser Anemometry Proc., 1975, University of Minnesota, Department of Conferences, Minneapolis, 1976
- [98] Adrian R.J., *Laser Velocimetry*, in Fluid Mechanics Measurements, 2<sup>nd</sup> Edition, R.J. Goldstein (ed.) pp: 175-293, Taylor and Francis, 1996 ISBN 1-56032-306-X

- [99] Goodman J.W., *Introduction to Fourier Optics*, 1968, New York: McGraw-Hill pp: 287
- [100] Adrain R.J., Yao C.S., *Pulsed Laser Technique Application to Liquid and Gaseous Flows and the Scattering Power of seed Materials*, 1985, *Applied optics*, Vol. 24, No 1, 44-52.
- [101] *Infinity K2 Long Distance Microscope*, Infinity Photo-Optical Company, Boulder, Colorado 80303, USA
- [102] *The Jet Engine*, 4<sup>th</sup> Edition, Rolls-Royce, 1986, ISBN 0 902121 04 9
- [103] *Aero-Environmental Research Laboratory*, Web page, 1996, [www.mit.edu](http://www.mit.edu)
- [104] Kerwin, J.M., *Design of a Shock Tube for Jet Noise Research*. Master's Thesis, Massachusetts Institute of Technology, 1996.
- [105] Kirk D.R., Creviston D.O., Waitz I.A., *Aero-acoustic measurements of transient hot nozzle flows*, Aero-Environmental Research laboratory, Massachusetts Institute of technology, Cambridge, Massachusetts, MA 02139 – to be submitted.
- [106] White F.M., *Fluid Mechanics*, Fourth Edition, McGraw Hill, 1999, ISBN 0-07-116848-6

[107] Hecht E., *Optics*, Addison-Wesley, 1974

[108] Weinstein L.M., *Large Field High Brightness Focused Schlieren System*, AIAA Journal, Vol: 31, No: 7, pp: 1250-1255, July 1993

[109] Judge T.R., *Quantitative Digital Image Processing for Fringe Analysis and Particle Image Velocimetry*, Ph.D. Thesis, University of Warwick, 1992

[110] *MatLab 5*, MathWorks, Inc., 24 Prime Park Way, Natick, MA 01760, [www.mathworks.com](http://www.mathworks.com)

[111] Bryanston-Cross P.J., Quan C., Judge T.R., *The Application of the FFT Method for the Quantitative Extraction of Information from High-Resolution Interferometric and Photoelastic Data*, Optics and laser technology, Vol: 26, No: 3, 1994.

[112] Judge T.R., *FRANSYS fringe analysis system documentation*, Optical Engineering Laboratory, School of Engineering, University of Warwick. No date supplied.

[113] Towers C.E., *The Development of Whole Field Particle Imaging Techniques for Quantitative Velocity and Size Measurements Applied to Large Scale Transonic Aerodynamic Testing and Combustion Research*, Ph.D. thesis, University of Warwick 1994

[114] Herman G.T., *Image Reconstruction from Projections. The Fundamentals of Computer Tomography*, Academic Press, 1980, ISBN 0-12-342050-4.

- [115] Bryanston-Cross P.J., Towers D.P., *Quantitative Holographic Interferometry Applied to Combustion and Compressible Flow Research*, SPIE 1732-70, March 1993.
- [116] Edmunds J.D., Harvey D., Wiseall S.S., *Recent Developments in the Application of Laser Doppler Anemometry to Compressor Rigs*, May 1998, AGARD Conference Proceedings 598, Advanced Non-Intrusive Instrumentation for Propulsion Engines, Paper 16.
- [117] Thomas P.J., Butefisch K.A., Sauerland K.H., *On the motion of particles in a fluid under the influence of a large velocity gradient*, Experiments in Fluids 14, pp:42-48 (1993)
- [118] Udrea D.D., Bryantson-Cross P.J., Lee W.K., Funes-Gallanzi M., *Two sub-pixel processing algorithms for high accuracy particle centre estimation in low seeding density particle image velocimetry*, Optics and Laser Technology, Vol. 28, No. 5, pp. 389-396, 1996.
- [119] Oldfield M.L.G., Bryanston-Cross P.J., *A study of passage flow through a cascade of turbine blades using image plane holography*, AGARD Conference Proceedings, No. 399, Propulsion and Energetics Panel, 67<sup>th</sup> Symposium, Pennsylvania, May 1986, pp.31-1.32-15.
- [120] Gogineni S., Estevadeordal J., Sarka B., Goss L., Copenhaver W., *Application of Two-Colour Digital PIV for Turbomachinery Flows*, AGARD Conference Proceedings

- 598, Advanced Non-Intrusive Instrumentation for Propulsion Engines. pp. 49-1:49.12, 1998
- [121] Wernet M.P., *Demonstration of PIV in a Transonic compressor*, AGARD Conference Proceedings 598, Advanced Non-Intrusive Instrumentation for Propulsion Engines. pp. 51-1:51-13, 1999
- [122] Towers D.P., Buckberry C.H., Reeves M., *Development of a 2 colour PIV system from in-cylinder spark ignition engine flows*, 9<sup>th</sup> Int. Symp. On Applications of Laser Techniques to Fluid Mechanics, Vol. 1, pp. 12.5.1:12.5.8, 1998
- [123] Westerweel J., *Fundamentals of Digital Particle Image velocimetry*, Meas. Sci. Technol. Vol. 8, pp. 1379-1392, 1997
- [124] Gharib M., Modares D., Dabiri D., Pereira F., Taugwalder F., *Development and application of a Defocusing Three dimensional DPIV Technique for the Mapping of two-Phase Bubbly Flows*, 9<sup>th</sup> Int. Symp. On Applications of Laser Techniques to Fluid Mechanics, Vol. 1, pp. 16.5.1:16.5.7, 1998
- [125] Udrea D.D., *High Accuracy Flow Velocity Measurements Using Particle Image Velocimetry*, Ph.D. Thesis, University of Warwick, 1997
- [126] Judge L.S., Burnett M., Udrea D.D., Lee W.K., Bryanston-Cross P.J., *Whole-field instantaneous measurements in air*, Proceedings SPIE, Paper No. 3172.56, pp. 551-560, 1997

[127] Wernet M.P., *Particle Image Velocimetry Processing: PIVProc, PIVProc user manual*, 19<sup>th</sup> April 1999.

[128] Giles M.B., *Validation of a Numerical Method for Unsteady Flow Calculation*, ASME Journal of Turbomachinery, Vol. 115, pp.110-117, 1993

[129] *FluoSpheres Fluorescent Microspheres*, Product Information Sheet, March 1997, Molecular Probes Inc., 4849 Pitchford Ave., Eugene

[130] *Ultranac*. The Ultimate High Speed Imaging System, IMCO Electro-Optics Ltd., 14/16 Saffron Court, Southfields Ind. Pk., Basildon, Essex, SS15 6SS, UK

[131] Doukelis A., Mathioudakis K., Founti M., Papailiou K., *3-D LDA Measurements in an Annular Cascade for Studying Tip Clearance Effects*, May 1998, AGARD Conference Proceedings 598, Advanced Non-Intrusive Instrumentation for Propulsion Engines, Paper 4.

[132] Durst F., Melling A., Whitelaw J.H., *Principles and Practice of Laser Doppler Anemometry*, Academic Press, London, 1981.

[133] Goldstein R. J., Kreid D. K., *Measurement of Laminar Flow Development in a Square Duct using a Laser Doppler Flowmeter*, Journal of Applied Mechanics, Vol. 34, pp. 813-817, 1967.



- [134] Carpenter P. W., Private communication, August 2000.
- [135] Erf R. K., *Speckle Metrology*, ISBN 0-12-241360-1, Academic Press, London, 1978
- [136] Ardley S., Fottner L., Beversdorff M., Weyer H., *Laser-2-Focus Measurements on a Turbine Cascade with Leading Edge Film cooling*, May 1998, AGARD Conference Proceedings 598, Advanced Non-Intrusive Instrumentation for Propulsion Engines, paper 12.
- [137] Versteeg H. K., Malalasekera W., *An Introduction to Computational fluid Mechanics, The Finite Volume Method*, Longman, 1995
- [138] K.R. Castleman, *Digital Image Processing*, 1996, Prentice Hall, ISBN 0-13-211467-4.
- [139] Bryanston-Cross.P.J, Towers.C.E, Towers.D.P, Judge.T.R, Harasgama.S.P & Hopwood.S.T. *The Application of Particle Image Velocimetry (PIV) in a Short Duration Transonic Annular Turbine Cascade*. Journal of Turbomachinery (ASME), Vol 113 pp 504-510. July 1992 IS: 0402-1215
- [140] Hilditch M.J., Smith G.C., Anderson S.J., Charna K.S., Jones T.V., Ainsworth R.W., Oldfield M.L.G., 1996, *Unsteady Measurements in an Axial Flow Turbine*, AGARD-CP-571, Loss Mechanisms and Unsteady Flows in Turbomachines, Proc. PEP 85<sup>th</sup> Symp., Derby, May 1995, pp24-1: 24-9

[141] Moore C.J., Jones D.G., Haxell C.F., Bryanston-Cross P.J., Parker R.J., *Optical Methods of Flow Diagnostics in Turbomachinery*, 1981, proceedings of International Conference on Instrumentation in Aerospace Simulation Facilities, ICIASF81, pp:244-255

[142] Hilditch M.A., Fowler A., Jones T.V., Charna K.S., Oldfield M.L.G., Ainsworth R.W., Hogg S.I., Anderson S.J., Smith G.C., 1994, *Installation of a Turbine Stage in the Pyestock Isentropic Light Piston Tunnel*, 1994 ASME Turbo Expo, The Hague, Netherlands, ASME 94-GT-277

[143] Goodisman M.I., Oldfield M.L.G., Kingcombe R.C., Jones T.V., Ainsworth R.W., Brooks A.J., 1992, *An Axial Turbobrake*, ASME Journal of Turbomachinery, April 1992, Vol. 114, No. 2, pp. 419-425, (Also ASME paper 91-GT-1).

[144] Brooks A.J., Colbourne D.E., Wedlake E.T., Jones T.V., Oldfield M.L.G., Schultz D.L., Loftus P.J., 1985, *The Isentropic Light Piston Cascade Facility at RAe Pyestock*, AGARD PEP CP-390, Heat Transfer and Cooling in Gas Turbines, Bergen, 1985, (Also RAe Tech Memo P1053, 1985).

# Appendix A

MatLab script for plotting Delaunay triangulation  
of an irregular grid of vectors

-  
'deltri4.m'

```

% Delaunay Triangulation and interpolation smoothing
% Mark Burnett, 1997
%
% Subject is a 4 column matrix velfile of the form
%
%           [x;y;velocity magnitude;velocity angle]
%
% Before running the program define the velocity file, eg:
%
%   velfile=[x,y,v,a];
%
% Smoothing iterations - interpolates to centroids then interpolates
%                       back to nodes
%
% Centroid node iterations - Calculates values at element centroids
%                           and considers that as an additional
%                           node hence trebling the
%                           number of elements
%
% Maximum edge length - specify maximum edge length thus limiting
%                       element sizes
%
% 'velfile' is rewritten if any smoothing or centroid node iterations
% are specified. 'velfile' should be reassigned if the original
% velocities are to be restored. Otherwise processing time may increase
% as the interpolated nodes are considered as data points, increasing the
% size of the velocity file.
%-----

```

```

%GUI bit
prompt={'Number of smoothing iterations:','Centroid-Node iterations','Maximum edge
length:'};
def={'0','0','50'};
title='Delaunay Triangulation';
lineNo=1;
answer=inputdlg(prompt,title,lineNo,def);
iter=str2num(char(answer(1,1)));
cniter=str2num(char(answer(2,1)));
maxlen=str2num(char(answer(3,1)));

velfile=unique(velfile,'rows');
[a b c]=unique(velfile(:,1:2),'rows');
temp=velfile(b,:);
velfile=temp;

```

```

%constant=1/(38400*0.000000539);           % Velocity conversion for tart5 only
%constant=1/(39050*0.000000640);           % Velocity conversion for taru1_33 only
%constant=1/(36500*0.000000840);           % Velocity conversion for stat5 only
%velfile(:,3)=velfile(:,3).*constant;
%velfile(:,4)=velfile(:,4).*constant;

% Convert to magnitude and angle
velfile(:,3)=(sqrt((velfile(:,3).^2)+(velfile(:,4).^2))); % Converts dx dy to magnitude

% Usually commented out

% Convert from pixels to mm, tart5 only
%velfile(:,1)=velfile(:,1)./38.4;
%velfile(:,2)=velfile(:,2)./38.4;

% Convert from pixels to mm, taru1_33 only
%velfile(:,1)=velfile(:,1)./39.05;
%velfile(:,2)=velfile(:,2)./39.05;

% Convert from pixels to mm, stat5 only
%velfile(:,1)=velfile(:,1)./36.5;
%velfile(:,2)=velfile(:,2)./36.5;

% Velocity with no interpolation
e=[ 1 1 1 1 1 1 ]';
xy=velfile(:,1:2);
%xy(:,2)=xy(:,2)+22;
connecl=de-launay(velfile(:,1),velfile(:,2));

% Centroid-Node iterations
if cniter>0,
    for ctr1=1:cniter,

        [m,n]=size(connecl);
        vctr=pdeintrp(xy',connecl',velfile(:,3));
        actr=pdeintrp(xy',connecl',velfile(:,4));
        x=velfile(:,1);
        y=velfile(:,2);
        v=velfile(:,3);
        a=velfile(:,4);

        for ctr2=1:m,

% The xy coordinates of the triangles
            x1=velfile(connecl(ctr2,1),1);

```

```

y1=velfile(connec1(ctr2,1),2);
v1=velfile(connec1(ctr2,1),3);
x2=velfile(connec1(ctr2,2),1);
y2=velfile(connec1(ctr2,2),2);
v2=velfile(connec1(ctr2,2),3);
x3=velfile(connec1(ctr2,3),1);
y3=velfile(connec1(ctr2,3),2);
v3=velfile(connec1(ctr2,3),3);

% The mid-point between two nodes
xmid1=((x2-x1)/2) + x1;
ymid1=((y2-y1)/2) + y1;

% 2/3rd from node to mid-point
xctr=x3-((x3-xmid1)*(2/3));
yctr=y3-((y3-ymid1)*(2/3));

% Appending to xy coordinates
x=[x;xctr];
y=[y;yctr];

end;

v=[v;vctr'];
a=[a;actr'];
velfile=[x y v a];
connec1=delaunay(x,y);
xy=[x y];

end;
end;

trim

% Velocity smoothing
if iter>0,
for ctr=1:iter,
velocity=velfile(:,3);
velocity=pdeintrp(xy',connec1',velocity);
velfile(:,3)=pdeprtnti(xy',connec1',velocity);
ang=velfile(:,4);
ang=pdeintrp(xy',connec1',ang);
velfile(:,4)=pdeprtnti(xy',connec1',ang);
end;
end;

```



```

% Remove entries that contain a zero velocity
nonzero=find(velfile(:,3));          % Returns indices of non zero velocities
x=velfile(nonzero,1);
y=velfile(nonzero,2);
v=velfile(nonzero,3);
a=velfile(nonzero,4);
velfile=[x y v a];
connecl=delunay(x,y);
xy=[x y];
trim

% Plotting the velocity
%figure
pdeplot(xy,e,connecl,'xydata',velfile(:,3),'colormap','jet','colorbar','off')
axis('equal')
axis image;
%caxis([174 388]); % Used to make tart, stat and taru use same colourbars
caxis([min(velfile(:,3)) max(velfile(:,3))]);
%caxis([192 385]); % Used for cfd comparison
colorbar('v');
%axis([-36.6 43.5 -60 58.6])
hold off

```

# Appendix B

Papers published in journals and conference proceedings that contain work from this thesis

*Particle Image Velocimetry Measurements from the Stator-Rotor Interaction Region of a High pressure Transonic Turbine Stage at the DERA Isentropic Light Piston Facility, AGARD 90<sup>th</sup> Symp. Advanced Non-Intrusive Instrumentation for Propulsion Engines, 20-24<sup>th</sup> October 1997, Paper No. 46 (Unnamed author)*

*Measurements of Transonic Shock Structures using Shearography. Laser Interferometry VIII: Applications. Proceedings of SPIE [2861-19].*

*Measurements of a free air jet using Particle Image Velocimetry, (PIV), and Laser Doppler Anemometry, (LDA). ImechE 1998, C541/061/98*

*The instantaneous determination of a transonic stator wake and turbulent burst in a low speed boundary layer in air using particle image velocimetry (PIV). IMechE 1998, C541/035/98*

*Transonic PIV measurements made in the stator trailing edge and rotor region of the ILPF (Isentropic Light Piston Facility). Optical Technology in Fluid, Thermal, and Combustion Flow III. Proceedings of SPIE [3172-90]*

*Whole field instantaneous 3D PIV measurements in air. Optical Technology in Fluid, Thermal, and Combustion Flow III. Proceedings of SPIE [3172-56]*

PAGES NOT SCANNED AT THE  
REQUEST OF THE UNIVERSITY

SEE ORIGINAL COPY OF THE THESIS  
FOR THIS MATERIAL